Final Report

Design of a Low-ATR, Long-Range Aircraft Using Passive Flow Control

Group 15, Spring DSE 2021

N. Barner (4819624)
M. Camus Amorós (4857127)
O. Carpentier (4773624)
G. di Summa (4654870)
B. Galenkamp (4684354)
L. Ghafourpour (4772458)
M. S. Güverte (4548361)
V. Maes (4770706)
A. Ramanna (4663314)
P. Roeleveld (4654781)

Delft University of Technology

TUDelft

This page is intentionally left blank

Final Report

Design of a Low-ATR, Long-Range Aircraft Using Passive Flow Control

by Group 15, Spring DSE 2021

Student Name	Student Number
Nils Barner	4819624
Martín Camus Amorós	4857127
Oscar Carpentier	4773624
Gianni di Summa	4654870
Basthian Galenkamp	4684354
Luca Ghafourpour	4772458
Mustafa Sabri Güverte	4548361
Vincent Maes	4770706
Austin Ramana	4663314
Patrick Roeleveld	4654781

Tutors:	Steven Hulshoff, Davide Modesti
Coaches:	Barış Çağlar, Jingna Pan
Institution:	Delft University of Technology
Place:	Faculty of Aerospace Engineering, Delft
Project Duration:	April, 2021 - July, 2021
Date:	Tuesday 29th June, 2021

TU Delft

Preface

This final report marks the culmination of 11 weeks worth of conceptual and preliminary design work. The work has been conducted by a group of 10 TU Delft aerospace engineering students, as part of their final year design synthesis exercise (DSE). Each course of the bachelor program has to some extent played a key role in equipping every team member with the necessary skills to develop the envisioned aircraft. It has been extremely insightful to experience first hand the infancy stage of a real engineering design process, and shall undoubtedly prove to be an invaluable experience when further moving on in each team member's career.

With the 2050 EU climate regulations rapidly approaching, the relevance of the project brief has only further motivated the team to deliver an aircraft which has a sustainable design philosophy at its core. In this project we had the opportunity to investigate and implement innovative aerospace technologies, and determine their performance at reducing the aircraft's impact on climate emissions.

After countless late night sessions, lots of head scratching, a myriad of Python merge conflicts and LaTeXerrors, stress, but ultimately joy, we are proud to present the outcome of our design work. However, none of this would be possible without the continuous support and guidance from our coaches and tutors. We would like to thank Professor Steven Hulshoff, Dr. Davide Modesti, Dr. Bariş Çağlar and Jingna Pan for consistently challenging us to push further and strive for perfection with our design and analysis. We would also like to thank Liam Megill for his advice in improving our approach towards systems engineering and project management, as well as his willingness to help us in the technical aspects.

Group 15
Delft, June 2021

Contents

Nomenclature

Symbols

α	Angle of attack	°
$\bar{c}$	Mean aerodynamic chord	m
$\bar{c}$	Mean geometric chord	m
$\bar{x}$	MAC normalised distance in x direction	m
χ	Mass concentration	$\mathrm{kg\,m^{-3}}$
ΔU^+	Velocity shift	–
δ_f	Flap deflection angle	°
ϵ	Flap deflection angle	rad
η	Efficiency	
Γ	Dihedral angle	°
Λ	Sweep angle	°
λ	Climate sensitivity	-
λ	Taper ratio	-
Φ_0	Relative humidity	%
ρ	density	$\mathrm{kg\,m^{-3}}$
σ_y	Yield stress	Pa
A_O	Operational availability	%
A_g	Cross-sectional groove area	$\mathrm{m^2}$
Ar	Aspect ratio	-
b	Main wing span	m
C_H	Hinge moment coefficient	-
C_r	Root chord length	m
C_t	Tip chord length	m
C_D	Drag coefficient	-
C_d	Airfoil drag coefficient	-
c_f	Flap chord	m
C_L	Lift coefficient	-
C_l	Airfoil lift coefficient	-
C_M	Moment coefficient	-
C_m	Airfoil moment coefficient	-
$C_{f,e}$	Coefficient of skin-friction	–
C_{l_β}	Roll moment - sideslip derivative	-
C_{l_r}	Roll moment - yaw rate derivative	-
C_{n_β}	Yaw moment - sideslip derivative	-
C_{n_r}	Yaw moment - yaw rate derivative	-
DR	Drag reduction	%
E	Total emitted mass greenhouse agent	kg
Eff	Climate efficacy	-
f	Proportion of laminar-to-turbulent flow	–
FF	Form factor	–
h	Altitude above sea level	m
H_0	Specific humidity	%
i	Incidence angle	°
IF	Interference factor	–
K_{1c}	Fracture toughness	$\mathrm{MPa\,m^2}$
L	Nose ellipse semi-major axis	m
l_f	Fuselage length	m
l_g^+	Viscous scaled square-root of groove area	–
l_h	Horizontal tail arm	m
M	Mach number	–
m	Mass	kg
p	Pressure difference	Pa
p	Static pressure	Pa
P_v	A	psia
R	Nose ellipse semi-minor axis	m
Re	Reynold's number	–
S	Main wing area	$\mathrm{m^2}$
S_{wf}	Flapped wing surface	$\mathrm{m^2}$
T	Static temperature	K
V_h	Horizontal tail volume	-
V_v	Vertical tail volume	-
Vol	Volume	$\mathrm{m^3}$
x_h	Horizontal tail arm	m
x_v	Vertical tail arm	m
X_{tr}	Transition point	%
Y	Constant for the calculation of the LBBC	–
A	Aspect ratio	-
R	Outer radius of the fuselage	m
SFC	Specific Fuel Consumption	g/kNs
V	Velocity	$\mathrm{m\,s^{-1}}$

Sub- and superscripts

a	Aileron
A-h	Tailless aircraft
ac	Aerodynamic center
bag	baggage
e	Elevator
h	Horizontal tail
i	Integer
np	Neutral point
OEW	Operational Empty Weight
qc	Quarter chord
r	Rudder
v	Vertical tail
wet	Wetted area
x	In x direction
z	In z direction

Abbreviations

AC	Aircraft
AF	Airliner Financing
AM	Additive Manufacturing
AMNCC	aluminium matrix nano-composite
APU	Auxilliary Power Unit
ASM	Airliner Seat Mile
ATC	Air Traffic Control
ATR	Average Temperature Response

BPR By-Pass Ratio
CAA Civil Aviation Authority
CAD Computer Aided Design
CAD Computer-aided design
CAM Computer Aided Manufacturing
CAM Computer-aided manufacturing
CFD Computational Fluid Modelling
CG Centre of Gravity
CIM Computer Integrated Manufacturing
CIM Computer-integrated manufacturing
CORSIA Carbon Offsetting and Reduction Scheme for International Aviation
COVID Corona Virus Disease
CRB Counter blade rotating
DCpNM 2021 dollar cent per nautical mile
Depre Depreciation
DF Direct Flight
diff absolute difference
DOC Direct Operating Cost
DpG Dollar per Gallon
DSE Design Synthesis Exercise
EASA European Union Aviation Safety Agency
ECAM Electronic Centralised Aircraft Monitor
EI Emission Index
EIS Entry Into Service
EOL End of Life
EPNdB Effective Perceived Noise in decibels
ETS Electrical Taxiing System
FAA Federal Aviation Administration
FBD Free Body Diagram
FEM Finite Element Method
Fix Eqp Fixed Equipment Weight
GHG Green House Gasses
GLARE Glass laminate aluminium reinforced epoxy
Grp Gross reference Percentage
GW Gross Weight
HBPR High Bypass Ratio
HLD High Lift Device
HM High Modulus
HS High Strength
IAS Indicated Air Speed
ICAO International Civil Aviation Organisation
Ins Insurance
JAA Joint Aviation Authority
JIT Just in Time
LBBC Leak-before-break-criterion
LFN&T Landing fee, navigation and tax
Maint Maintenance
MEpY 2021 million euro per year
MLDT Mean Logistics Delay Time
MLDT Mean Logistics Down Time
MMT Mean Maintenance Time
MOI Moment Of Inertia
MRO Maintenace, Repair and Overhaul
MTBF Mean Time Between Failures
MTBM Mean Time Between Maintenance
MTBN Mean Time Before Maintenance
MTBPM Mean Time Between Preventive Maintenance
MTOM Maximum Take-Off Mass
MTOW Maximum Take-Off Weight
MTTF Mean Time to Failure
NLF Natural Laminar Flow
OEI One Engine Inoperative
OEM Operating Empty Mass
OEW Operational Empty Weight
Pwr Plt Power Plant Weight
QRH Quick Reference Handbook
RC Root Chord
RF Radiative Forcing
ROC Rate of Climb
ROD Rate of Descent
RoI Return on Investment
SM Safety Margin
SUAVE Stanford University Aerospace Vehicle Environment
TAS True Air Speed
TOM Take-Off Mass
TOW Take-Off Weight
TSFC Thrust Specific Fuel Consumption
TU Technical University
UD Uni Directional
UV Ultra Violet
WPF Wing Penalty Function

List of Figures

List of Tables

Executive Summary

This work reports on the results of the detailed (DSE) design phase which spanned the previous 5 weeks. The project objective is ”to design a long-range airliner employing laminar flow control and riblet technologies which achieves a low ATR”, where ATR is a metric for assessing an aircraft’s global warming impact. In particular, the aircraft should achieve a 40% ATR reduction compared to an Airbus A350-800 on an 8000 km mission, whilst minimising for DOC. As a starting point, this work considers the preliminary aircraft configuration which emerged from the rigorous trade-off process of four candidate concepts conducted as part of the foregoing Midterm design phase. The selected aircraft is of conventional configuration, meaning that it has a tube-and-wing layout with low-mounted wings and a fuselage-mounted horizontal tail, and features two open-rotor engines. The evolutionary technologies which shall be investigated in particular detail during this report are the following: open-rotor engines, riblets, NLF airfoils and synthetic fuels.

The first of three parts which this report is split into is concerned with the problem context and systems engineering aspects. Early during the detailed design phase, it was recognised that the chosen aircraft configuration would most likely be able to comply with the 40% ATR requirement rather easily, hence based on a comprehensive market analysis and in consultation with the project’s tutors and coaches, the updated project objective became ”to minimise ATR with no more than a 15% increase in DOC over an A330-200”. A chapter on technical risk assessment built up throughout the previous design phases follows, which provides the reader with insights into the motivation of various non-performance-related design choices. The subsequent functional analysis outlines the functionalities the envisioned low-ATR aircraft is supposed to inherit, whereas a list of user requirements summarises the most crucial design constraints.

The second part considers the detailed design of the various aircraft subsystems, as well as their synthesis and convergence into a coherent aircraft design. This includes an independent Class I and Class II weight estimation method, where the latter takes into account the subsystem/component weights and also serves in determining the center of gravity. It further represents the starting point for a number of subsystem design procedures, such as the aerodynamic design. Here, the airfoil, the wing planform and the fuselage nose shape are optimised to minimise the contributions of different drag components. A high-aspect-ratio-, zero-quarter-chord-sweep-wing design with an optimised taper ratio of 0.45 is chosen. By applying an NLF airfoil alone, a 10.3% overall drag reduction can be achieved with respect to the supercritical airfoil of the A330-200. Subsequently, the overall drag reduction potential of riblets applied to 70% of the wetted turbulent surface area is found to be 3.1%, which concludes the aerodynamic analysis.

The open-rotor propulsion system achieves a staggering 32% reduction in TSFC during cruise compared to an A330-200, which is largely due to the very high BPR of 30. A smaller contribution is due to the employed Fischer Tropsch synthetic kerosene, which has a heating value of 44.3 $\mathrm{MJ\,kg^{-1}}$ as opposed to the 43.0 $\mathrm{MJ\,kg^{-1}}$ of fossil-based Jet-A-1.

Stability and controllability, though not featuring as prominently in the overall ATR reduction efforts as other sub-systems, is crucial for the operability of an aircraft. In order to size for stability, a loading diagram (center-of-gravity-, or c.g.-, excursion during loading and unloading) and a wing placement diagram are produced, based on which the stable c.g.-range can be computed. In combination with controllability, a scissor plot can be made, based on which the required empennage and control surface dimensions can be derived. Moreover, the dynamic stability of the design is evaluated based on applicable military regulations, as well as the passenger ride comfort.

Next, the CO_2 footprints of the four main structural materials from which the envisioned low-ATR aircraft shall be manufactured are compared. It can be concluded that the engine structural material (Fe-9Ni-4Co-0.30C steel) has the lowest CO_2 footprint of 4.76 $\mathrm{kg\,kg^{-1}}$, whereas the wing and empennage material (Epoxy/HS carbon fiber,UD prepeg, UD lay-up) has the highest CO_2 footprint of 47.5 $\mathrm{kg\,kg^{-1}}$. Following the materials selection, the wing box ought to be sized in order to handle the loads encountered during flight. To round of the structural and material design, a brief note on aeroelasticity is provided, which turns out to be a constraint on the maximum permissible rotor diameter.

Part three of this report is concerned with the overall system’s performance analysis, primarily in terms of ATR and DOC relative to the A330-200. For a design cruise Mach number of 0.63 and altitude of 11 250 m, the relative ATR gain equals 80% at a relative DOC decrease of 7.5%, which have been computed by integrating the propfan and turbofan engines’ instantaneous performance over the mission profiles output by SUAVE (a preliminary aircraft mission design tool). Finally, the ATR reduction potential per technology (i.e., propfans, riblets, NLF airfoils and biofuel) is considered, which could be seen as the pinnacle of this project. This concludes part three of this report.

The following part touches upon a number of practical applications and implications, including an analysis of aircraft operations and logistics, a Reliability-Availability-Maintainability-Safety (RAMS) analysis, a production plan is devised and a financial overview is provided. Last but not least, a holistic sustainable development strategy is proposed, spanning all life-cycle phases from preliminary design until end of life, and including a life-cycle ATR assessment. The latter compares the absolute ATR emissions resulting from the manufacturing, operations and end-of-life plan of a single aircraft, both for the A330-200 and the envisioned low-ATR aircraft.

This report is concluded with a outlook to the potential post-DSE phase of this project, which includes a development logic and a Gantt chart, thus laying the foundation for a successful continuation of this promising long-haul airliner concept, which sets itself apart from its competitors due to its low climate impact and high economic profitability.

1. Introduction

Meeting the EU's 2050 climate goal puts enormous pressure on aircraft manufacturers, operators and regulatory authorities to decarbonise the aviation sector. Given the concurrent need for a short-term reduction of aviation's environmental footprint and a long-term road map towards carbon-neutral flight, a clever balance between technology readiness level, operational profitability and climate impact is sought. Whereas past engines and airframes were optimised for minimum Direct Operating Cost (DOC), a novel holistic design approach pursued by several authors suggests that aircraft optimised for minimum Average Temperature Response (ATR) achieve the lowest global warming impact. For the same tube-and-wing configuration as current DOC-targeted airliners, this new optimisation aim was shown to result in low-sweep, high-aspect-ratio wings and moderate bypass-ratio (BPR) turbofan engines, flying at lower cruise altitudes and Mach numbers. Particularly on long routes this will inevitably spawn an increase in airfare prices, which may however be limited by adding evolutionary technologies to the aforementioned aircraft redesign recipe. This project investigates the combined ATR reduction potential of propfan engines, synthetic fuels, riblets and Natural Laminar Flow (NLF) airfoils, whilst limiting the DOC increase to 15% relative to an Airbus A330-200. In particular, the project objective statement is "to design a long-range airliner employing laminar flow control and riblet technologies which achieves a low ATR". This final report concludes the detailed design phase of Group 15's Spring 2021 DSE by presenting and synthesising the detailed design of the major aircraft sub-systems, performing a comprehensive performance analysis and finally providing an outlook to (near-) future design work.

Part I
Problem Context and Systems Engineering

2. Mission Description

The mission description was written down in the project plan [40]: "The aim of this project is to design a 250 passenger trans-pacific, wide-body airliner optimised for minimum DOC, while offering a 40% ATR reduction relative to the Airbus A350-800. The aircraft shall be capable of performing shorter trans-pacific flights (e.g., Tokyo-Vancouver), comply with common regulatory requirements, at a competitive unit list price of 150 Million €. In terms of evolutionary technologies, the aircraft shall employ passive flow control, for example, in the form of riblets. These reduce the skin friction drag of turbulent boundary layers, and are therefore suitable for areas where the boundary layer cannot be kept laminar using laminar flow control. Also from a mission operations viewpoint, sustainability shall be at the focus of all design efforts; as was shown by Proesmans [78], minimising the airliner's ATR footprint will result in a lower flight altitude and speed, implying less passengers transported per unit of time. Combined with the designers' commitment to a sustainable End-Of-Life (EOL) plan, it will be both challenging and interesting to see how such an aircraft can be made profitable for its operators, and even outperform its competitors. Overall, this project team will employ a holistic approach in building up to their preliminary aircraft design, as presented during the Midterm Review, though with a clear focus on laminar flow technologies and sustainable design, manufacturing, operation and end-of-life planning.

In the following, the above paragraph shall be summarised in the form of a Mission Need Statement and a Project Objective Statement. It should be noted that the Project Objective Statement has been taken one-to-one from the Project Guide [47]."

- **Mission Need Statement:** "Meeting the EU's 2050 climate goals requires a short development time, competitively priced, long-range, wide-body aircraft achieving a significantly lower global warming footprint compared to current benchmark aircraft in its segment." [40]
- **Project Objective Statement:** "To design a long-range airliner employing laminar flow control and riblet technologies which achieves a low average temperature response."[47]

3. Market Analysis

In order to design a successful airplane. The design requirements and constrictions needs to be aligned with the market and future legislation. In this chapter, future legislation regarding aircraft emissions will be discussed, an analysis on market profitability is done. These analyses will lead to a new design requirement for the Low ATR Aircraft. Finally a SWOT

analysis of the aviation market is realized. Further analysis on production and manufacturing feasibility and costs will be discussed in future Sections 21 and 22.

3.1. International Climate Accords

The requirement for minimising ATR can be traced back all the way to the 2015 Paris climate Agreement. Here it was established that the global average temperature of 1.5° C compared to pre-industrial levels. Figure 3.1a shows that the average global temperature has been steadily increasing over the past decades and that the average temperature increase goal will be difficult to achieve. The temperature increase is primarily caused by man made green house gas emissions and these will have to be severely cut down by 45% in 2030 from 2010 to meet the requirement. One of the primary ways emissions are reduced is by implementing policies; which should catalyze technological transition. It is estimated that urban planning could reduce GHG emissions of public transport by 20-50% and carbon pricing has also been found promising. Aviation is identified as an especially difficult sector to decarbonize as a lot of energy is required. Nevertheless, the sector is expected to reduce $C0_2$ emissions by 56% with respect to 2005 levels before the year 2050. [63].

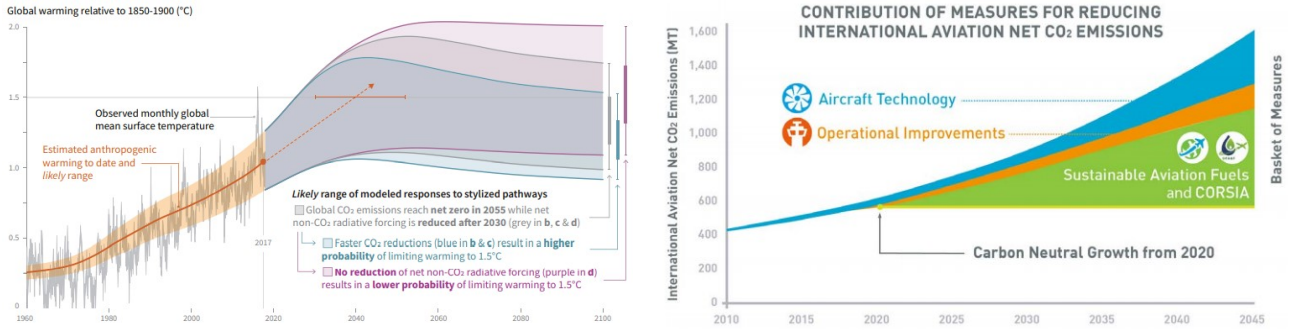

(a) Temperature increase [63]

(b) CO2 reduction in aviation [71]

Figure 3.1: Emissions trends & predictions

One of the main policy makers for aviation is the International Civil Aviation Organization (ICAO). Figure 3.1b shows how they believe GHG reduction will be achieved; the reduction will come from new aircraft technology, operational improvements, sustainable fuels and finally the Carbon Offsetting and Reduction Scheme for International Aviation (CORSIA) program. Some the new technology includes riblets, active flow control, more efficient propulsion systems and an increase in additive manufacturing and some of these technologies play a significant role in this design synthesis. The vast majority of emission reduction will however, come from changing aviation fuels and the CORSIA program which will later be discussed. This global program aims to increase energy efficiency by 2% a year, while leaving market forces untouched.

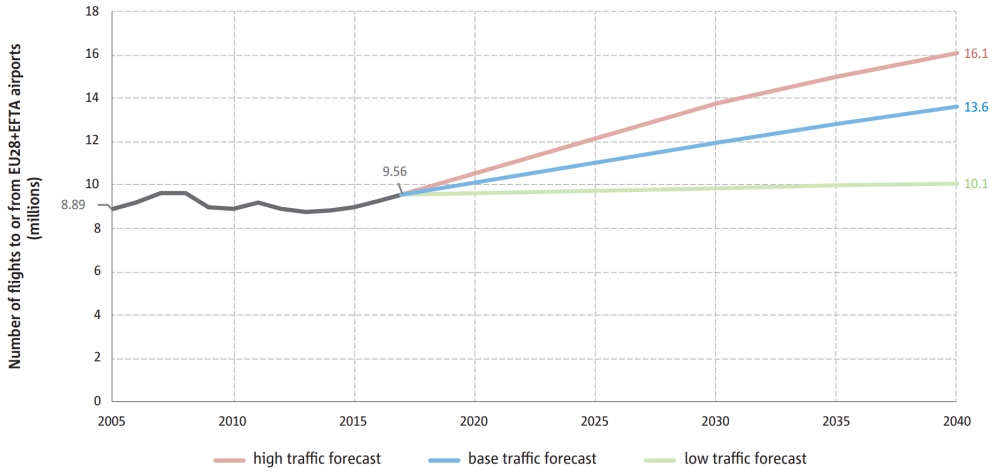

Figure 3.2: Forecasted Aviation Passenger Numbers [24]

3.2. Prospective ATR Reductions

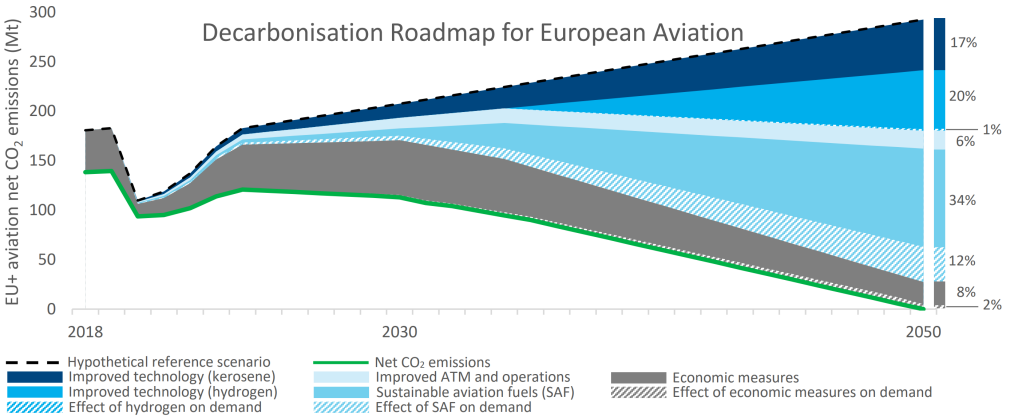

Figure 3.3: EU Destination 2050 roadmap [84]

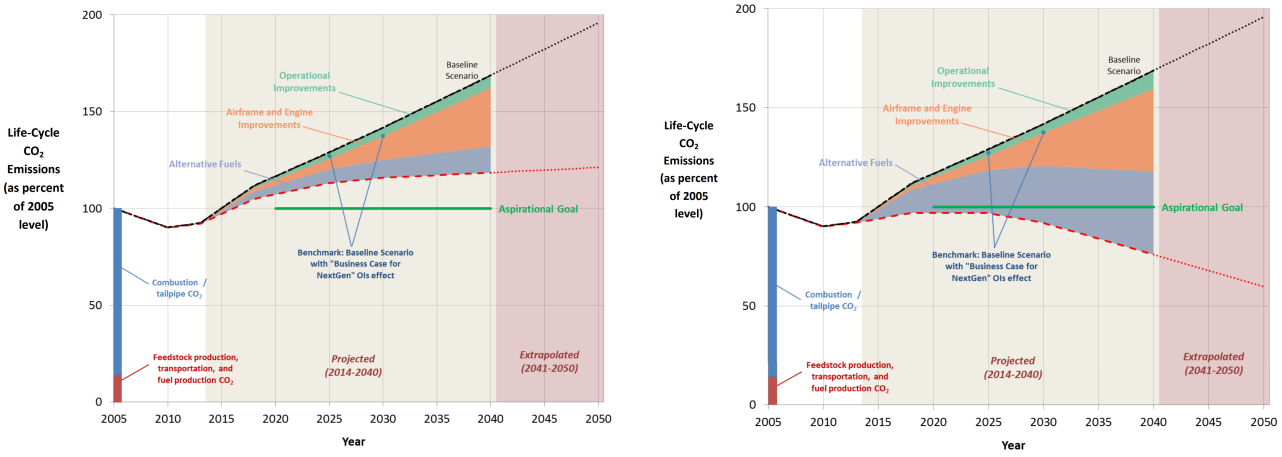

(a) American projected emissions roadmap moderate scenario

(b) American projected emissions roadmap aggressive scenario

Figure 3.4: American Emissions Roadmap [1]

In 2009, IATA; an association representing 293 airlines worldwide agreed on its first roadmap on an unified approach to emissions regulation. A plan to cap emissions by 2020 and reduce aviation's net carbon dioxide emissions to half of what they were in 2005, by 2050 [2]. This was followed by the European Union, whom in 2021 announced the plan: "Destination 2050". The plan aims for net zero emissions from the aviation sector by 2050 [84].

Furthermore, governments around the world, and especially the European Union have begun considering imposing carbon tax fines on the aviation industry to further curb. Two specific examples being the 2019 Swiss proposals for taxing European flights 12-30 CHF and international flights 30-48. This move was heavily criticized by IATA due to potential economic damage it could have on the aviation market, it is important to state that as IATA represents airliners directly, and as such, they have a vested interest against any carbon tax [3]. Another attempt by the Dutch government to tax carbon emissions in 2019 [4] failed after passengers switched to Belgian and German airports subsequently. This shows that governments are more inclined to take the approach to tax and increase costs but are currently trying to find a way to implement the law. Furthermore, a relatively new scheme that has been playing a major factor has been employing carbon off-setting to reduce the environmental effect of the aviation industry. This is done by two programs, the European Union's ETS scheme and the aforementioned Corsia. Airliners are able to buy carbon credits that offset their emissions when going over the legal limits. This is a temporary measure to allow airliners to readjust to new market demands while still decreasing their negative impact on the environment [24]. However, this measure is not a permanent one, as it does not directly decrease aviation emissions and the price of carbon has been increasing at an exponential rate. In 2013, the price of a tonne of carbon was 5 euros, which increased total operating costs by 0.3%. The cost at 2018 increased to 25

[2] https://www.iata.org/en/iata-repository/pressroom/fact-sheets/fact-sheet–climate-change/ accessed on 17-06-2021

[3] https://www.iata.org/contentassets/463a0063da9540d9a2501d2dde7cbb80/swiss-proposal-for-a-carbon-tax.pdf accessed on 17-06-2021

[4] https://www.government.nl/latest/news/2019/06/20/international-conference-on-carbon-pricing-and-aviation-taxes-is-starting accessed on 17-06-2021

euros and it is expected that by 2024 the price will be around 43 euros [109]. Furthermore the number of credits allocate for airliners is kept artificially low to spur optimization for emissions. Therefore, airliners cannot just rely on credits to meet industry goals for climate change. Thus, when considering a new DOC increase it is important to realize that DOC costs would increase regardless any policy change and what matters is the relative differences as well as whether the industry can bear the increases. Though different organizations have different policies for tackling climate change, it is evident that to achieve the most modest of climate goals, large changes in the industry are necessary.

3.3. Prospective Airliner Market Performance

In order to gain an understanding on what DOC requirements can be imposed on the airliner industry, one must analyse the current and prospective health of the aviation market. Until the 2019 Coronavirus pandemic, the airliner industry maintained a consistent 5-10% profit margin, which peaked at 2017 [5]. Though margins crashed to an almost -80% at the peak of the pandemic, profits are expected to return by 2021 [6].

Furthermore, prospective markets anticipate the onset of passengers from lesser economically developed countries (LEDC) especially in south east asia. It is expected that passenger activity from that region would increase ten fold in the long term [7]. For the short term, it is expected that by 2040, the number of flights will increase by 42% [24].

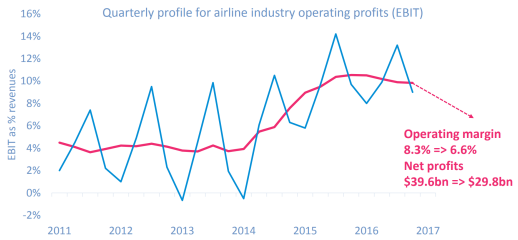

Figure 3.5: Aviation Industry Profit Margins [7]

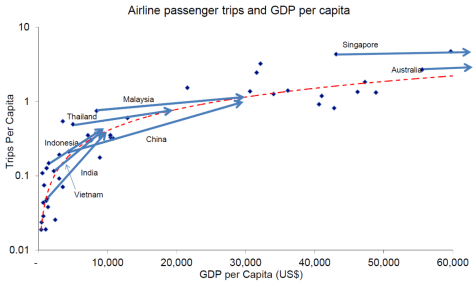

Figure 3.6: Expectatations of LEDC participation in global aviation travel [7]

3.4. Realizing New Design Requirements

As stated, IATA's requirement of dropping emissions by 50% by 2050, and the EU aiming for net zero emissions by then, makes it evident that a 40% ATR reduction does not make sense in the global time frame. An aircraft that only reduces ATR by 40% would not last long in the market before new emissions targets keep up with it. Therefore, it was evident that the current design requirements had to be changed to keep up with current market trends. Thus a new requirement was formulated as such:

The design is to minimise ATR with no more that a 15% increase in DOC over an A330-200.

This focuses the design back to minimising ATR and keeps DOC at an acceptable level which will explained and reasoned later on. It was important to keep the DOC as the limiting factor as the increase in ATR does not follow a completely linear path and it is important not to take an ATR value that could exponentially increase DOC and potentially bankrupt the industry, the reasoning behind this DOC values will be explained later.

3.5. Analysis of the New DOC Requirement

Having to decide a new DOC requirement, requires an understanding on the profit margins and tolerance of airliners and the industry as a whole to a DOC increase. It is important not to levy a cost increase that airliners cannot bear. Depending on the nature of the market, an increase in DOC can effect consumer demand for an aircraft. The pass on factor is a measure describing how much a DOC increase impact ticket prices and it depends on whether the aviation market is competitive or a monopoly. In a competitive market the pass on factor is 100% whereas in a monopoly it can be less and even 0% [45]. The reality would be that airliners and industries in general only pass on a fraction of their costs over an extended period of time, this is to soften any demand impacts due to a rice in operating costs. In the United States, it was observed that airliners reacted to an increased fuel price with a pass on rate of 10-50% spanning a period of five to six year [45]. In the very long term it would be expected that pass on rate would reach 100% as airliners are rarely profitable when taking into account the cost of capital. Next it is important to determine the demand elasticity of the aviation market. This is a measure that determines how much does demand change due to a change in costs and it gives an idea how much the market could shrink due to a DOC increase. The demand elasticity of the aviation market is set to revolve around -1.146 [22]. Thus, by taking the upper bound of the pass on rate it can be concluded that in a 5-6 year period the decrease the

[5] https://www.iata.org/en/iata-repository/publications/economic-reports/state-of-the-airline-industry/ (accessed on 18-06-2021)

[6] https://www.iata.org/en/iata-repository/publications/economic-reports/airline-industry-economic-performance—april-2021—report/ (accessed on 18-06-2021)

[7] https://www.iata.org/en/iata-repository/publications/economic-reports/state-of-the-airline-industry/ (accessed on 18-06-2021)

demand change due to DOC increase would be -8.5%. Considering that the projected increase in demand for aviation is at 4% per annum [56], that would mean the offset due to growth in demand would completely negate the effects of an DOC rise. If one where to take a non realistic, instantaneous 100% pass on rate, it would cause a decrease in passenger demand by 17.2% which would be negated within 4 years of market growth. The aviation market, due to its inherent ties to national industries has been shown to handle much larger price fluctuations, [56] and this is without any regard to potential legislation supporting airliners switching to more environmentally friendly aircraft (as none have been proposed of yet). Thus a 15% DOC increase requirement is completely within the bearable range of airliners [45] yet give the head space to design an aircraft with maximum longevity with respect to emission regulations.

3.6. SWOT Analysis

Figure 3.7 displays the strengths, weaknesses, opportunities and threats from a financial perspective of developing a long range ATR aircraft using passive flow control. The strengths of the aircraft are that it is long range, which has high demand. Furthermore, the aerodynamic technologies, mainly riblets, allow fuel reduction and lower speed, so there are potentially less operating costs. As for weaknesses, the main one is that aircraft such as the A330 have limited demand; smaller aircraft such as the A320 have much higher sales. The riblets also bring weaknesses with them. Both the design and production costs will be higher as the technology is more complex. Integration of riblets could also increase maintenance cost as they need to be cleaned. Opportunities for the market as a whole are promising as aircraft demand is predicted to steadily increase in the future. New regulations can also be an opportunity. As stated before, future legislation is going in the direction of emmission regulations and large ATR reductions and this gives the low ATR aircraft an opportunity of being designed to excel in a future market. It is not uncommon of regulations coming with incentives to aide airliners transitioning. Finally, fuel prices will inevitably increase, which reduces the operating costs of efficient aircraft. As for threats, the main one is the oligopoly in the current market by Boeing and Airbus. It will be difficult to compete with them and a possibility could be selling the design to one of Boeing or Airbus. Another issue is extent of adoption of environmental legislation. Asia has a significant market share and countries like China are more lenient on imposing regulations. This makes it difficult to compete with a low ATR aircraft. Finally, the unknown future of the COVID pandemic aftermath could hinder the entire aviation industry, including this aircraft.

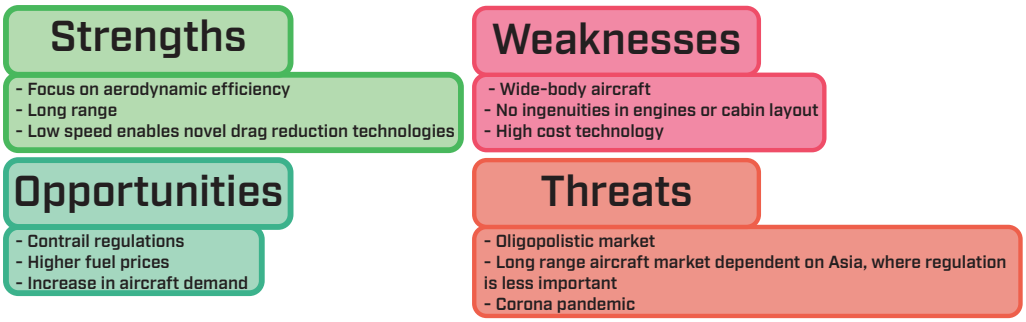

Figure 3.7: Market analysis SWOT table [38]

3.7. Stakeholders

The economic stakeholders can be divided into three categories: aircraft suppliers, aircraft users and regulatory bodies [38]. The relevant aircraft suppliers are the companies designing the ATR aircraft: TU Delft and Boeing & Airbus since they are the main aircraft suppliers. For them, design and manufacturing costs are vital as those costs are paid directly by them and is what limits their capabilities to produce a low ATR aircraft. Aircraft users consist of airliners that host flights which fly 8000 km ranges. For them, operating and aircraft costs are vital as it is what determines their profit margins as well as their return on investment. A 15% increase in DOC will be mainly effecting airliners as their margins would be taking a hit, thus it was important to come up with requirements that can be met by the stakeholders. Furthermore, the regulatory bodies are airports, governments and institutions, which are also located globally. The main institutions are the ICAO, FAA, CAA, EASA and JAA. They are largely impacted by the regulations regarding ATR reductions as the responbility of climate regulations are directed at them. Finally, is important to identify that another stakeholder to the low ATR aircraft are the consumers. Current consumer demands are directed into environmentally friendly (low greenhouse gas and noise emissions) yet affordable travel and thus the passed on increases of flying costs need to be justifiable for them to remain as consumers. [38]

4. Technical Risk Assessment

The risk chapter is divided into three sections. First, in Section 4.1 the general risk management procedure is presented. In Section 4.2 all the technical risks are presented and furthermore in Section 4.3 some design specific risks are presented.

4.1. General Risk Management Procedure

After a risk has been identified, it is scored based on likelihood and impact. For the total risk score then, the likelihood and impact are multiplied together, giving a value to the risk. If this value exceeds 7, as shown in Figure 4.1, a mitigation plan is outlined and a residual risk score is added. The whole risk procedure is depicted as a flow diagram in Figure 4.2. As there are so many risks, it is vital to keep a clear structure, hence the subdivisions.

Consequence	Likelihood				
	Rare (1)	Unlikely (2)	Possible (3)	Likely (4)	Almost Certain (5)
Catastrophic (5)	Moderate (5)	High (10)	Extreme (15)	Extreme (20)	Extreme (25)
Major (4)	Moderate (4)	High (8)	High (12)	Extreme (16)	Extreme (20)
Moderate (3)	Low (3)	Moderate (6)	High (9)	High (12)	Extreme (15)
Minor (2)	Low (2)	Moderate (4)	Moderate (6)	High (8)	High (10)
Negligible (1)	Low (1)	Low (2)	Low (3)	Moderate (4)	Moderate (5)

Figure 4.1: Risk matrix

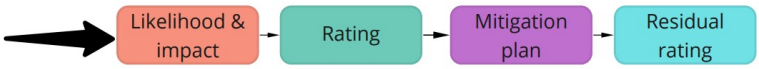

Figure 4.2: Risk mitigation flow diagram

4.2. Technical Risks

The technical risks are subdivided into the general design risks Table 4.1, the risks for each engineering department Table 4.2-Table 4.7 and finally miscellaneous Table 4.8.

Table 4.1: List of general design risks [39]

ID	Title	Likelihood	Impact	Rating	Mitigation Plan	Residual risk rating	
GD1	Key requirement not met	3	5	15	This is quite catastrophic as the design now does not meet the customer demand and makes the whole product worthless. The risk can be mitigated by keeping the key requirements into mind during each step of the design process. One of the ways this is done is by having parameter margins or budgets.	5	Likelihood can be reduced to 1, impact 5.
GD2	Requirement not met	3	4	12	Less disastrous than a key requirement not being met, but can still have major consequences. It can be mitigated the same way as missing a key requirement.	4	The likelihood is now 1.
GD3	Budget overshoot	3	3	9	It in itself is not a problem but can cause requirements to not be met. It is hard to mitigate but instant fixing should reduce the impact.	6	The impact is lowered to 2.
GD4	Time underestimation of a task	5	3	15	The impact can be reduced by having time margins. In the time planning, a small amount of time is left free in case for this. Furthermore, most of the group is open to working during the weekends or on national holidays to stay on top of work.	5	The impact can be reduced to 1.

Table 4.2: List of aerodynamics risks [39]

ID	Title	Likelihood	Impact	Rating	Mitigation Plan	Residual risk rating	
AR1*	Ice forming on the wing.	5	4	20	This may disturb the airflow around the wing and causes loss of lift. Mitigation can be done by heating the wing or by having a rubber membrane which can expand to break the ice.	4	The mitigation strategy reduces the likelihood to 2 and the seriousness to 2 as much less ice will be able to form.
AR2	Riblet dirt	3	2	6	This causes the aircraft to experience more drag. Therefor the aircraft flies less efficiently. This risk can be mitigated by cleaning the riblets before departure.	4	Likelihood will go down to 2 and the seriousness stays at 2.
AR3	CFD software problems	4	3	12	If the design is dependent on a CFD simulation then the development would experience large delays. For every iteration that has to happen this may increase. The use of proven software with a large user base for CFD is recommended in order to mitigate this risk. This way if problems occur there is a possibility to ask for help and resolve the problem relatively quickly.	6	The likelihood changes to 3 and the impact to 2.
AR4	Bottleneck in iteration due to overcomplexity of the design.	3	3	9	Calculations and simulations in aerodynamics can quickly become more complex. If multiple iterations are needed it will halt for too long at aerodynamics which can cause development delays. Mitigation can be done by resolving to simpler and proven software together with the use of analytical formulas.	4	The likelihood will go down to 2 and the impact will go down to 2 as well.

Table 4.3: List of structural risks [39]

ID	Title	Likelihood	Impact	Rating	Mitigation Plan	Residual risk rating	
SR1*	Fatigue	3	4	12	Fatigue can cause cracks and growth in already existing cracks. This can be mitigated by designing the parts which experiences cyclical loading with fatigue in mind and implementing a safe life or fail safe design philosophy. Depending on the part or subsystem.	6	The likelihood and the impact goes down to 2. As less parts will be able to fail due to fatigue and those who do have a redundancy due to the mitigation strategy.
SR2*	Pressure loss	2	5	10	When this occurs at high altitude passengers and crew might pass out with potentially catastrophic consequences. Oxygen masks can be installed for every passenger and pilot with enough supply to safely descent to a lower altitude.	4	The likelihood does not change however the impact drops to 2 due to the oxygen masks.
SR3*	Lightning	3	4	12	Lightning could always strike an airplane. This can cause a short circuit and could damage measuring equipment. Though it is a serious risk it can be mitigated fairly easily by ensuring that enough material is a electricity conducting metal. This way the aircraft structure acts like a cage of Faraday and protects everything within the structure.	6	This mitigation strategy does not reduce the likelihood. The impact however, is lowered to 2.
SR4*	High stress concentration due to load introduction	4	4	16	As load is introduced into the structure it creates stress concentrations. The structure could locally fail, induce cracks or deform the surrounding material with potential catastrophic consequences. In order to mitigate this risk proper reinforcement should be placed at points where large loads are introduced.	6	The likelihood of having these high concentrations drops down to 2 due to the reinforcements. The impact goes to three. With this strategy the amount of parts with high stress is reduced and the stress is less concentrated.
SR5*	Corrosion	5	4	20	Corrosion causes the structure to become weak and possibly even fail. This is a huge risk which almost every aircraft has to deal with. In order to deal with it proper alloys could be chosen that do not corrode easily. The aircraft should not have crevices or cavities where water can not flow out from. When the aircraft is not used it should be stored inside.	9	The likelihood will go to 3 and the impact to 3 as well with this strategy. This still is a rather high rating. Hence this should be monitored during the complete lifespan of the aircraft.
SR6*	Crack growth	4	3	12	When cracks exist they grow gradually. It is hard to avoid crack growth. However, it can be detected. To mitigate this risk frequent control for crack should be performed. Those parts who can not be checked as they are too hard to reach should be designed to handle cracks for the rest of the life-time.	3	Employing this strategy causes the likelihood to drop to 1. The impact however remains equally high at 3.
SR7*	Tyre puncture	3	3	9	Tyres are designed to withstand high loads and to not explode on impact. In case of a flat tyre, only deflation will occur [107]. Proper maintenance and inspection can also be applied to reduce deflation risk.	4	Using this strategy the impact drops to 2 and the likelihood as well.
SR8*	Undamped vibrations	3	4	12	There are a lot of vibrations induced on an aircraft. If certain parts have approximately the same eigenfrequencies as the vibrations they may fail. This risk can be mitigated by testing the eigenfrequency of every part and analysing them.	4	The likelihood can go down to one using this strategy properly. If it does occur the consequences can be high. Hence the impact stays on 4.

Table 4.4: List of flight performance risks [39]

ID	Title	Likelihood	Impact	Rating	Mitigation Plan	Residual risk rating	
FP1*	Obstacle clearance	3	4	12	At take-off and landing there might be some obstacles. The aircraft could fly into them causing a crash. To mitigate this risk the climb performance of the aircraft should be high enough such that it can avoid those obstacles at all times.	3	Likelihood can be reduced to 1, impact 3.
FP2	Rejected take-off	2	3	6	When a problem arises during take-off it can happen that the take-off is rejected. If the aircraft can not stop in time it could crash against something at the end of the runway. This risk can be mitigated by defining a clear and safe speed at which the aircraft has to take-off. The crew operating the aircraft should also be trained for this.	4	The impact of is now reduced to 2.
FP3*	Wind shear & Clear Air Turbulence	2	3	6	This happens when an aircraft is close to the airport (landing or take off) and there is a microburst present, which could make the aircraft crash. Best way of mitigation is to have the airport make constant observations and forecasts and train the pilot crew for the event. [19]	3	This mitigation plan lowers the likelihood to 1.
FP4*	Wake turbulence	2	3	6	Wake turbulence is caused by the vortexes of an aircraft, so that they are often present at airport. Mitigation is mainly the responsibility of air traffic control by having proper spacing between aircraft.	3	When air traffic control Employ its strategies the likelihood comes down to 1.

Table 4.5: List of materials risks [39]

ID	Title	Likelihood	Impact	Rating	Mitigation Plan	Residual risk rating	
MA1*	Non air or liquid tight joints	3	3	9	If certain joint are not air or liquid tight they could leak fuel or loss of cabin pressure at high altitudes could occur. Mitigation can be done by testing it before it leaves the factory. The tanks can be filled and the cabin can be pressurized to check that there are no leaks.	3	Performing these tests allows the likelihood to go down to 1. The impact however stays the same at 3.
MA2	Material imperfections	3	3	9	During manufacturing there is a possibility some imperfections arise in the material. These imperfections could make the part fail earlier than expected. This can be mitigated by the use of non-destructive testing methods and by adding redundancy to the parts.	2	The non-destructive testing of this strategy causes the likelihood to go down to 1. Adding redundancy causes the impact to move down to 2.
MA3*	Joint Weaknesses	2	4	8	Certain joint could become a weakness in the design and fail early. For example welding can cause the material to have locally weaker properties. This can be mitigated by avoiding welding and other joining techniques that causes weaknesses throughout the entire design.	4	The likelihood is moved down due to the strategy to 1. The strategy does not influence the impact.
MA4	Expensive new manufacturing	3	2	6	The manufacturing of riblets along the skin could cost more as this is a new manufacturing technique. This risk should be monitored and checked frequently.	6	The residual risk rating is assumed to stay the same.
MA5	No easy access to parts	3	2	6	When there is no easy access to certain parts they can not be replaced or examined. When such a part has to be replaced this could take a lot of time costing the airline company a lot of money. This risk can be mitigated by designing all parts which are difficult to access for safe life.	3	The likelihood of it happening is not altered employing this strategy. The impact however is brought down to 1.
MA6	Different thermal expansion of the riblets and the structure.	3	2	6	If the thermal expansion coefficient of the wing and the riblets differ to much the riblets may break and cause an increase in drag. This risk can be avoided by choosing the material of the two structures with a matching thermal expansion coefficient.	2	This strategy allows the likelihood to drop to 1. The impact stays the same at 2.
MA7	Too complex structures.	2	3	6	If certain structures are too complex they can not be manufactured with the current technology. This however can be mitigated by having frequent and good communications between the structures and the manufacturing departments.	2	The likelihood that a too complex structure is designed stays the same. However, by communicating these parts can be caught on early and a redesign can be quickly implemented. This causes the impact to drop to 1
MA8	Third party dependencies	3	2	6	Being dependent on third parties may cause delays, which is out of the design team field of influence. This can be mitigated by manufacturing in house as much as possible and by relying only on thrust worthy and proven partners.	4	This strategy lowers the likelihood to 2. The impact stays unaffected.
MA9	Laser pointing accuracy	2	3	6	The accuracy of the parts may not be high enough and can cause mismatches in the joints. In order to mitigate this the parts prone to such mismatches can be measured with lasers. If they do not meet the requirements they can be discarded.	3	The Likelihood is dropped to 1 using this strategy. The impact stays at 3.
MA10	Tool wear	3	3	9	After multiple usages tools can start to wear out. These worn out tools can cause parts to be less precise. Changing these tools frequently can mitigate this risk.	3	This mitigation cause the likelihood to drop to 1. It does not change the impact.
MA12*	Toxic hazards during production	2	4	8	During production workers might get in contact with toxic products from which they can get ill. This can be mitigated by having a safety manager who is responsible for the safety of the workers and the correct use of safety equipment.	4	The likelihood can go down to 1 when the safety measures are very strict. The impact will not move down and stays at 4.

Table 4.6: List of stability and control risks [39]

ID	Risk Title	Likelihood	Impact	Risk Rating	Mitigation Plan	Residual risk rating	
ST1*	Instability due to wrong loading	2	5	10	An unstable aircraft is an aircraft that cannot be flown. It is important that the loading allowance is specified in the flight manual and that sufficient safety margins are used.	5	The likelihood is changed to 1.
ST2*	Unstable eigenmotions	3	3	9	This is heavily dependent on which eigenmotions are unstable. Generally, they are all severely limiting except unstable spiral. The aircraft should be designed so that this is the only unstable motion and the characteristics of all the eigenmotions should be specified in the flight manual.	2	Likelihood can be reduced to 1, impact to 2.
ST3*	Too stable, no longer controllable	3	3	9	The more stable the less manoeuvrable. Meaning take- off & landing procedures and some turns could take too long. This is mitigated by adhering to CAT II landing and CS25 requirements.	3	Likelihood can be reduced to 1.
ST4*	Adverse yaw	3	4	12	This is caused by positive aileron deflection generating positive yaw, which causes the plane to roll in the opposite direction. As a consequence the aircraft turns in the opposite direction as well. The effect can be mitigated by keeping $C_{n_{\delta_{alpha}}}$ small, which is done by either differential deflections for roll controls or using Frise ailerons [70].	4	Likelihood can be reduced to 1
ST5*	Aileron reversal	3	4	12	This is caused by positively deflected aileron creating a too large twist on the wing, which decreases the local angle of attack. The effect can be mitigated by decreasing the wing sweep and aspect ratio [70]	4	Likelihood can be reduced to 1.

Table 4.7: List of propulsion risks [39]

ID	Title	Likelihood	Impact	Rating	Mitigation Plan	Residual risk rating	
PR1	Insufficient ATR reduction	3	3	9	This could happen if insufficient attention is paid during the design phase. This risk would cause the mission requirements to not be met and if ATR regulations are administered in the future, causes the plane to not be certified. It can be prevented by carefully studying ATR during the literature phase and then keeping it in mind during the design phases. For example, the bypass ratio should be kept limited and speed should be limited	6	This is done by reducing the likelihood from 3 to 2, the severity cannot be changed.
PR2*	Too low to the ground	5	2	10	If an engine hits the ground it could break or cause instability. This issue can be mitigated by checking the engine heights during the design phase. Note the height could be lower due to vibrations.	4	The likelihood can be reduced to 2, severity stays same.
PR3*	One engine inoperative	2	4	8	This causes a massive moment in lateral direction. If the aircraft meets CS-25 requirements it should still be able to land safely if this happens during cruise. Danger occurs as this happens at low speeds when the aerodynamic forces cannot produce enough counter moment. It is quite difficult to prevent this as there are various causes that need to be taken into account. One way of mitigation is to regularly and thoroughly inspect the engines and to design the engines such that they are easily inspected. Another way to mitigate this risk is to size the control surfaces accordingly to counteract the moment created.	3	The inspection strategy causes the likelihood to drop to 1. The impact can be reduced to 3 by the proper sizing of control surfaces.
PR4	Too much noise	2	2	4	This might get the aircraft banned from certain airport due to noise regulations, which would decrease sales. Noise levels can be inspected while testing the engines and it is possible to buy certified engines from a third party.	2	The likelihood is dropped to 1 and the impact stays at 2.
PR5*	Thermal expansion	3	3	9	Thermal expansion comes with great variety in magnitude. Some expansion will always be present with temperature fluctuation and in a rare case it will be catastrophic. This risk can be mitigated by taking expansion into account during the design and material selection or by again buying certified engines from a third party.	6	This is achieved by reducing the severity to 2, the probability stays the same.
PR6*	Blade detachment*	2	5	10	This could have severe consequences. The wing and or fuselage could get could get damaged. Wing damage could make the aircraft uncontrollable and thus set it on a crash course. Fuselage damage could severely injure the payload (which can be passengers). In order to mitigate this risk the aircraft should be designed such that the compressor blades do not hit any critical parts. It is also important that all the engine blades are designed in a way such that they are properly secured. Lastly, it is crucial that the blades are properly inspected during assembly and maintenance.	4	With this mitigation plan the severity is down to 4. As the aircraft can keep flying although there is still the possibility that a single passenger dies. The likelihood is also brought down to 1.
PR7*	Fuel compatibility	3	1	3	Fuel incompatibility could happen when the engines are not designed for a certain percentage of bio fuel or kerosene engines are supplied with hydrogen. Both instances can be mitigated by keeping fuel compatibility in mind during the design phase and specifying the fuel compatible sources to customers.	1	Keeping this mitigation in mind the likelihood is moved down to 1. The impact stays the same.
PR8*	Ice impact	4	3	12	This is caused by ice forming on the wing. The ice becomes too large, breaks off and enters the engine. Worst case is engine failure. This risk can be mitigated by ice prevention through heated wings.	2	The likelihood becomes 2, the severity 1.

Table 4.8: List of miscellaneous risks [39]

ID	Title	Likelihood	Impact	Rating	Mitigation Plan	Residual risk rating	
MS1*	Loss of hydraulics	3	5	15	Hydraulics are used for the empennage, nose wheel steering, secondary flight control and brakes. In all cases (except nose wheel steering) failure can be catastrophic and there can be multiple causes. It is therefore important to have backup systems in place and notify the pilots in the event of a failure. The pilots can then perform QRH or ECAM procedures [19].	6	Likelihood can be reduced to 2, impact to 3.
MS2*	Human error	3	5	15	There are an infinite amount of ways humans can make errors. For now they are separated into engineering, manufacturing, ground maintenance and aircrew errors. For engineering, human error is detected in verification and validation and the quality assurance department also checks the design. For manufacturing and ground maintenance, various inspections should be held. Finally, for aircrew, there should always be multiple pilots and these should be properly trained and certified. It is important to make everyone aware of the severest errors they can make so that plentiful effort is spent on prevention. Another possibility is to increase automation; less human work, less human error.	4	Likelihood can be reduced to 2, impact to 2.

MS3	Bad budget allocation	3	3	9	This could occur in the early design phase. It is important to check the allocated budget with other sources and see beforehand if it is reasonable.	4	Both likelihood and impact can be reduced to 2.
MS4	Cost (budget overshoot)	3	4	12	Budget overshoot could happen at anytime and could cause the project to no longer be able to meet the requirements. It is important to have margins and to have set target budgets during each phase of the design. This way a small overshoot can be taken care off before it snowballs and becomes too difficult to fix.	4	Both can be reduced to 2.
MS5*	Bird impact	4	1	4	Bird impact cannot be prevented. The severity is heavily depended on the impact location. It is therefore important that all exterior parts necessary to ensure a safe landing are impact proof.	4	Neither impact nor likelihood can be reduced.
MS6*	Inaccurate instruments	3	5	15	This is one reasons Turkish airlines flight 1951 crashed [110]. It can be prevented by often inspecting the instruments and by training the pilots so that they can cope with inaccurate instruments. It is also vital to have backup instruments.	6	Likelihood reduces to 2, impact 3.
MS7*	Short circuiting	3	3	9	Short circuits can range from not being able to use the entertainment system to explosions (flight TWA800). They can be prevented through proper insulation and part of the CS-25 requirements already take short circuitry into account [26].	6	Impact can be reduced to 2.
MS8*	Cabin fire	2	5	10	A fire in the cabin in mid flight could turn out catastrophic. There are multiple measures to be taken in order to mitigate this risk. Fire retardant materials can be used for the interior. There should be multiple fire extinguishers present in order to quickly extinguish small fires.	6	The likelihood of a fire ocurring stays at 2. The impact it has has dropped down to 3.
MS9	Flight crew incapacitation*	3	5	15	Sometimes people become incapable, even pilots. Therefore, there are always multiple pilots and each of them can fly the plane on their own. In case all pilots fail, a crew member or passenger could take over and follow air traffic control instructions.	6	Impact can be reduced to 2.

4.3. Design Specific Risks

The design specific risks can be subdivided into the wingpod risks 4.10, propfan risks 4.9 and finally tubular fuselage risks 4.11.

Table 4.9: List of propfan risks [39]

ID	Title	Likelihood	Impact	Rating	Mitigation Plan	Residual risk rating	
PF1	Higher noise	5	1	5	Propfans are louder but not to a significant extent. Therefore no specialized mitigation plan is made.	5	Nothing changes.
PF2	Prediction inaccuracy	3	4	12	Propfans are currently not the common convention and there are no commercial propfans. This makes it more difficult to find reference data and properly predict performance. This risk can be mitigated by keeping sufficient design margins.	6	Impact reduces to 2

Table 4.10: Wing podded engine risks[39]

ID	Title	Likelihood	Impact	Rating	Mitigation Plan	Residual risk rating	
WP1*	Low damp flutter	4	5	20	Wing flutter can cause instability which could inevitably tear the whole wing apart, crashing the plane. It is vital to perform structural analysis on the wing during the design phase such that flutter can be investigated early on. Furthermore, during flight tests small explosives can be detonated during flight to determine how the wing oscillates and see if it is a sufficiently damped system [65].	5	Likelihood can be reduced to 1, impact 5.
WP2*	Engine clearance	3	4	12	Engines hitting the ground can badly damage them, causing the aircraft to be grounded and out of service. Mitigation is done by taking engine height into account during the design phase, with one option being through increasing dihedral	4	The likelihood is now 1.
WP3	Large yaw moment with OEI	2	4	8	This can be reduced by increasing the vertical tail surface and control surfaces.	2	The impact is lowered to 2.
WP4*	Heat wear	3	3	9	Heat wear will increase maintenance as parts need to be replaced quicker. This can be mitigated by making the paint and metal sheets heat resistant	3	The impact can be reduced to 1.

Table 4.11: List of tubular fuselage risks [39]

ID	Title	Likelihood	Impact	Rating	Mitigation Plan	Residual risk rating	
TFS1	Larger longitudinal moments	4	3	12	The fuselage needs to be sized with the ability to withstand the longitudinal bending moments the fuselage might experience. This is done by a structural analysis.	4	Impact can be reduced to 1.
TFS2	Spatially less optimal	4	4	16	In case passenger and cargo capacity is not met with reasonable fuselage lengths, a double bubble fuselage can be implemented.	4	The impact is now 1.
TFS3	More windows required	4	3	12	It is not a problem, however it would mean more windows and more structural reinforcing will be required which will increase the weight of the fuselage.	6	The likelihood is lowered to 2.
TFS4	Longer electrical cables	4	4	16	This is not entirely a risk other than thicker cables will be needed which can increase weight.	4	The likelihood can be reduced to 1.
TFS5	Heavier	5	4	20	The aircraft needs to be built with the lightest possible materials and use most effective structural reinforcements.	5	The impact will be dropped to 1.
TFS6	Less lift	4	3	12	Aircraft aerodynamic systems need to be sized to make up for the lost lift due to the absence of a blended wing body.	3	The likelihood can be reduced to 1.
TFS7	Less marketable	5	4	20	The aircraft needs to be competitive in maintenance and operation costs and be profiting for the consumer while achieving ATR requirements.	5	The impact can be reduced to 1.

5. Functional Analysis

This chapter contains a functional analysis of the envisioned low-ATR, trans-pacific, 250-passenger aircraft employing passive flow control. The functional analysis of the aircraft is used as the basis from which to derive the requirements of the aircraft. The functional analysis will be done by means of two diagrams. These diagrams were constructed in the Baseline report [38]. The first diagram is the functional flow diagram, explained in Section 5.1. The second diagram is the functional breakdown structure, which is explained in Section 5.2.

5.1. Functional Flow Diagram

The functional flow diagram displayed in Figure A.1 visualises the logical order of functions the system shall fulfill within its operational environment. The operational life-cycle functionality of the aircraft is visualised and ordered. The functions are broken down in sub-functions and their order is annotated by the arrows.

5.2. Functional Breakdown Structure

The functional breakdown structure is presented in Figure A.2. The functional breakdown structure showcases the same functions as the functional flow diagram. However, the functional breakdown structure goes one level deeper and organises the functions to overarching branches resulting in and ”AND-tree”. Because the functional breakdown structure is one level deeper it is a usefull tool for generating requirements.

6. Requirements

During the design process of a large, complex system it is important to have clear constraints and guidelines on what to design for. For that reason a clear and verifiable set of requirements has to be set up. These requirements are a result of the mission statement, user requirements, stakeholder requirements and functionalities of the system. The requirements were set up in the baseline phase of this design project and the exact source of every requirement can be found in the Baseline Report [38].

As explained before in Section 3.4, the requirements regarding DOC and ATR were altered. Below in Table 6.1 and Table 6.2 the main requirements have been given. Any overlap between requirements has been removed, meaning some requirements will have multiple identifiers. Note that all the requirements given in the table are considered key requirements. Therefore only driver requirements are indicated in the table.

Table 6.1: User requirements

Identifier	Requirement	Type
MATRA-USER-PER-01	The maximum operating range at maximum payload shall be 8000 km.	
MATRA-USER-PER-02	The flight time associated with the maximum operating range specified in MATRA-USER-PER-01 shall not exceed 16 hours.	
MATRA-USER-PER-04, MATRA-STA-AL-01	The aircraft shall be designed to seat 250 passengers.	
MATRA-USER-PER-05	The aircraft shall be able to operate from existing airports.	
MATRA-USER-PER-06	The aircraft shall be able operate from runways of 2500 m length.	
MATRA-USER-PER-07	The aircraft shall be able operate in cross winds of 20 kts.	
MATRA-USER-PER-08, MATRA-STA-REG-01	The aircraft shall be able to operate in all-weather conditions specified in CS-25.	
MATRA-USER-PER-08, MATRA-STA-REG-01	The aircraft shall be able to perform CAT-II landings.	
MATRA-USER-PER-09, MATRA-STA-REG-01	The aircraft shall be able to perform diversions during CAT-II landing maneuvers.	
MATRA-USER-SAR-01, MATRA-STA-REG-02	The aircraft shall comply with the standard part 25 certification requirements.	
MATRA-USER-SAR-02	The passive flow control devices shall not require additional safety certification under CS-25.	
MATRA-USER-SUS-01	The aircraft shall employ laminar flow control to delay laminar-to-turbulent transition.	
MATRA-USER-SUS-02	The aircraft shall use riblets to reduce turbulent skin-friction drag.	
MATRA-USER-SUS-03	The aircraft shall use sustainable materials during manufacturing.	
MATRA-USER-SUS-04	The aircraft shall have a holistic end of life plan.	
MATRA-USER-BUD-01	The weight budget shall be finalised in the concept development phase.	
MATRA-USER-BUD-02	The drag budget shall be finalised in the concept development phase.	
MATRA-USER-COS-01	The development costs shall be less than 15 Billion € if pre-existing engines can be utilised.	
MATRA-USER-COS-02	The development cost shall be less than 20 Billion € if new engines must be developed.	
MATRA-USER-COS-03	The manufacturing cost per aircraft shall be less than 150 Million €.	Driver
MATRA-USER-COS-04	The aircraft's ATR footprint shall be minimised within a 15% DOC increase constraint compared to an A330-200 on the same flight.	Driver

Table 6.2: Stakeholder requirements

Identifier	Requirement	Type
MATRA-STA-TUD-01	The conceptual design phase shall be completed in 10 weeks time.	
MATRA-STA-TUD-02	The development costs shall not exceed 600,000 €, given a per capita salary of 150 €/hour.	
MATRA-STA-AL-02	The cabin layout shall provide sleeping coaches for crew and pilots.	
MATRA-STA-AL-03	The aircraft shall be competitively priced.	
MATRA-STA-AL-04	The aircraft shall have an operational lifetime of at least 35 years.	
MATRA-STA-AL-05	The aircraft shall be operable on short trans-pacific routes, such as Tokyo-Vancouver.	
MATRA-STA-AL-06	Pilot training costs for type rating shall be minimised, provided pilots have already attained such type rating for comparable aircraft such as the A330-200 or B777-200.	
MATRA-STA-AP-01	Costs resulting from additional ground services, besides those required for operating an Airbus A330-200, shall be minimised.	
MATRA-STA-RES-01	The aircraft shall have low emissions during ground operations.	
MATRA-STA-RES-02	The noise level experienced by residents living around the airport shall be equal or less than that of an Airbus A330-200.	
MATRA-STA-GP-01	The aircraft shall have a significantly lower environmental footprint compared to its competitors.	Driver
MATRA-STA-PAS-01	The airplane shall be comfortable and pleasant to be transported in.	
MATRA-STA-PAS-02	The relative increase in ticket price, compared to an Airbus A330-200 with the same cabin configuration, shall be minimised.	

7. Conceptual Design and Trade Off

In the baseline and midterm phase of the design project, a number of concepts were chosen and worked out in more detail, after which a trade-off was performed. The concepts that were analysed will be given in this chapter, as well as the trade-

off which resulted in the winning concept. In Section 7.1 the four analysed concepts will be given and in Section 7.2 a short summary of the trade-off will be given.

7.1. Concept Designs

During the selection of viable concepts, a large number of concepts were taken into consideration. The complete set of design options can be found in the baseline report [38]. After eliminating all the impossible and unfeasible options and the least favourable options, four concepts remained. These are given below.

- **Concept 1:** Wing-podded turbofan, tube-and-wing, low wing, as seen in Figure 7.1a
- **Concept 2:** Fuselage-mounted propfan, tube-and-wing, low wing, as seen in Figure 7.1b
- **Concept 3:** Fuselage-mounted BLI turbofan, blended wing-body, as seen in Figure 7.1c
- **Concept 4:** Fuselage-mounted BLI turbofan, tube-and-wing, low wing, as seen in Figure 7.1d

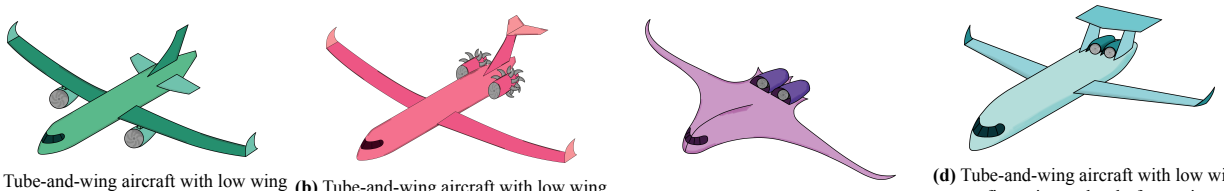

(a) Tube-and-wing aircraft with low wing configuration, and turbofan engines mounted beneath the wing

(b) Tube-and-wing aircraft with low wing configuration and fuselage-mounted propfan engines

(c) BWB aircraft with turbofan engines mounted on the fuselage

(d) Tube-and-wing aircraft with low wing configuration and turbofan engines mounted on the top aft portion of the fuselage

Figure 7.1: The four aircraft concepts that were considered

7.2. Trade-off Summary

In the trade-off, several trade-off criteria were used to perform the trade-off. This included the cost, development risk, operability, flight performance and propulsion performance of the concepts. In the trade-off it was found that concept 1 and concept 2 could be combined, to utilise the better propulsion performance of concept 2 while keeping the advantages of a more conventional aircraft configuration. This resulted in a new concept 2B which can be seen in Figure 7.2. The scores of concept 1 and concept 2B are almost equal, however 2B was chosen as it is believed that regulatory authorities, airlines and costumers will favor a lower climate impact over lower costs. The final trade-off outcome is given in Table 7.1. The complete explanation of the trade-off method and the scores per criterion can be found in the midterm report [39].

Table 7.1: Trade-off outcome

Criteria	Weight	Concept 1	Concept 2	Concept 3	Concept 4	Concept 2B
Cost	4/5	95.4	80.8	80.0	63.0	80.8
Development risk	3/5	95.0	88.0	38.0	83.0	89.0
Operability	3/5	100	86.7	46.7	80	93.3
Flight performance	5/5	82.2	74.2	58.4	68	82.7
Propulsion system	5/5	74.7	91.2	92.7	92.7	91.2
Total (%):		87.5	83.7	66.5	77.5	87.0

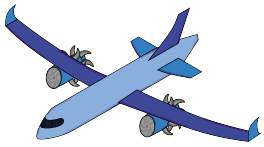

Figure 7.2: Tube-and-wing aircraft with low wing configuration, and propfan engines mounted beneath the wing

Part II
Aircraft Design

8. Aircraft Configuration and General Design

This section covers the general iterative design approach. Section 8.1 displays the Class II weight estimation, which returns a more accurate structural weight. The method is then used together with Class I to find a converged weight, explained in Section 8.2. Section 8.3, Section 8.4 and Section 8.5 cover the centre of gravity determination, aircraft configuration and landing gear design, respectively; which are easily acquired from the weight estimations. Finally, Section 8.6 covers the internal fuselage design.

8.1. Component Weight Estimation

In the Baseline report [38] the initial class I weight estimation was done. The class II weight estimation is presented in this section. The values shown are those of the final iteration. The class II method by Roskam [89] uses more thorough estimates based on statistics and the aircraft's configuration, dimensions and other relevant parameters. By iterating the class II and II weight estimations they converge to a final value for the operational empty weight. More information on the iteration process is presented in Section 8.2. A pie chart is provided in Figure 8.1 showing the relative size of each of the weight groups. Table 8.1 shows the weights of the major aircraft groups.

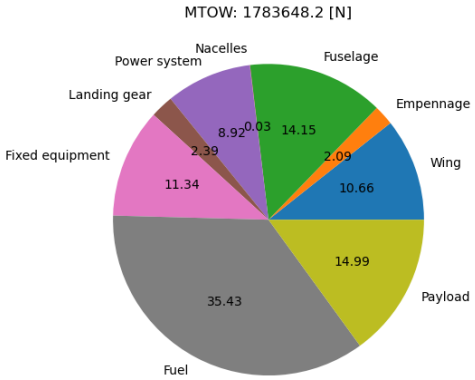

Figure 8.1: Component weight pie chart

Table 8.1: Weights of the major component groups

	Weight [N]
Wing group	190069
Empennage group	42118
Fuselage group	252411
Powerplant group	159124
Fixed equipment group	202260
OEW	889157

The powerplant group and the fixed equipment group are further broken down into their components. The pie charts for those groups can be found in Figure 8.2 and Figure 8.3. The values can be found in Table 8.2

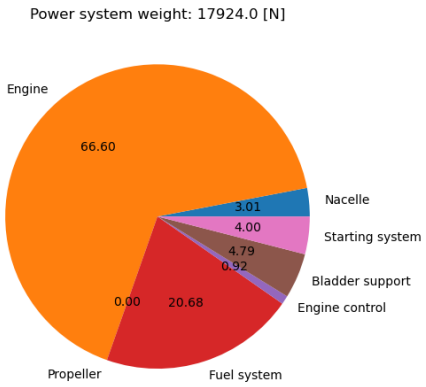

Figure 8.2: Power system weight pie chart

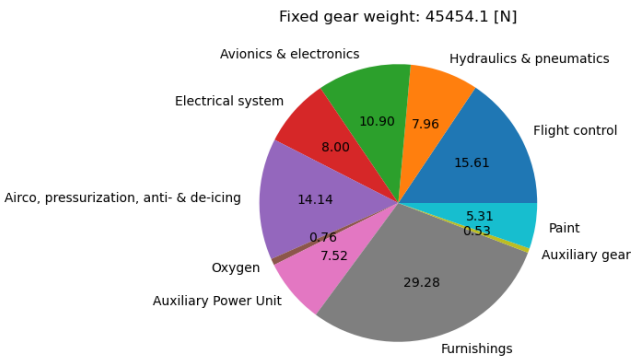

Figure 8.3: Power system weight pie chart

Table 8.2: Breakdown of the weights of the powerplant group and the fixed equipment group

Powerplant group	**Weight [N]**	**Fixed equipment group**	**Weight [N]**	**Fixed equipment group**	**Weight [N]**
Engine	106239	Flight control system	31582	Oxygen system	1531
Fuel system	20313	Hydraulic system	16099	Auxillary power unit	15204
Propulsion system	13448	Electrical system	16184	Furnishing	59224
Thrust reverser	19123	Avionics system	22047	Paint	10732
		Air conditioning system	28590	Auxillary gear	1062

The aircraft weight is arguably the most important set of parameters for aircraft design as most empirical relations are weight dependent. It is therefore vital to verify and validate the weight estimation models. For verification Tables 8.3, 8.4 and 8.5 show output data from the Roskam of similar aircraft and the absolute difference between the design aircraft and this reference material. Validation is not deemed necessary in this report as the Roskam is a commonly used method and has been validated numerous times.

Table 8.3 shows that only the fuselage weight is significantly off from the other aircraft. This is rather logical however, as the cruise altitude of the design aircraft is significantly lower than that of the reference. This means relatively less pressurization is required and thus, the structure can be lighter.

Table 8.3: Structural Class II weight verification

/GW	REF	**DC-9-30**		**MD-80**		**737-200**		**727-100**		**Ourania**	
	val WTO	value	diff %	value	diff %	value	diff %	value	diff	value	diff
Pwr Plt	0,0586	0,076	29,69	0,079	34,81	0,071	21,16	0,078	33,11	0,076	29,69
Fix Eqp	0,1134	0,0175	84,57	0,182	60,49	0,129	13,76	0,133	17,28	0,155	36,68
Empty W	0,41	0,538	31,22	0,564	37,56	0,521	27,07	0,552	34,63	0,544	32,68
Wing Grp	0,1128	0,106	6,03	0,111	1,60	0,092	18,44	0,111	1,60	0,105	6,91
Emp Grp	0,0276	0,026	5,80	0,024	13,04	0,024	13,04	0,026	5,80	0,025	9,42
Fus. Grp	0,0546	0,103	88,64	0,115	110,62	0,105	92,31	0,111	103,30	0,109	99,63
Nac. Grp	0,0152	0,013	14,47	0,015	1,32	0,012	21,05	0,024	57,89	0,016	5,26
Gear Grp	0,0279	0,039	39,78	0,038	36,20	0,038	36,20	0,045	61,29	0,04	43,37

Table 8.4 again shows the fuselage difference. Other than that, the design aircraft landing gear is a lot lighter than the reference data. This could be due to modern landing gear requiring less weight due to structural and material advancements but would have to be further investigated in a later stage.

Table 8.4: Continued total weight fraction absolute differences

	REF	737 – 200	%	727 – 100	%	747 – 100	%	A – 300 B2	
wing	0,275	0,340	23,71	0,351	27,47	0,408	48,46	0,414	50,57
empennage	0,067	0,087	29,31	0,082	21,05	0,056	16,89	0,056	17,27
fuselage	0,133	0,388	191,71	0,349	162,22	0,340	155,15	0,336	152,60
nacelle	0,037	0,045	20,31	0,076	105,91	0,047	27,80	0,066	78,08
landing gear	0,068	0,140	105,62	0,142	109,64	0,149	118,78	0,128	88,15

The final verification table, Table 8.5 shows that the design aircraft flight controls are a lot lighter while the auxiliary power unit APU is a lot heavier than the reference data.

Table 8.5: fixed equipment weight fraction absolute differences

	REF	737 – 200	%	727 – 100	%	747 – 100		A-300 B2	%
electrical system	0,090	0,072	19, 99	0,101	12,46	0,053	40,68	0,140	56,92
avionics & electronic	0,129	0,106	17,74	0,110	14,57	0,101	22,15	0,060	53,53
hydraulics	0,094	0,059	37,81	0,067	29,34	0,071	24,82	0,106	11,96
flight control	0,055	0,158	185,73	0,141	155,04	0,111	100,57	0,166	200,17
furnishings	0,318	0,446	40,50	0,482	51,76	0,591	85,96	0,375	18,22
auxiliary power	0,089	0,056	36,97	0,003	96,84	0,018	79,89	0,028	68,53

8.2. Iterations Between Class I and II Weight Estimations

After making a first estimate of the aircraft size and configuration in the midterm phase and setting up a class II weight estimation, the design is converged using iterations. These iterations will run between the class I and class II weight estimations. Between the two weight estimation methods, system-level design calculations are conducted as multiple systems depend on the aircraft weight. The iteration process will run until the aircraft OEW converges to a single value, for which the absolute difference between the class I and class II OEW is less than 1%.

First an iteration framework has to be set up. Since python scripts are used to perform all the computations, this framework involves the preparation of the different python files such that they can be used in a single main iteration file. Furthermore a database was used to store all the computed values. This also allowed scripts to pull the most recent data from this database. Next, an N2 chart of the iteration framework was made, which included all the scripts involved in the iterations and the inputs and outputs of each script. This N2 chart is provided below in Figure 8.4. When the iterations were first ran issues were encountered. The iterations were diverging and the stall speed was dropping rapidly. After several days of troubleshooting it was found that the new MTOW was not calculated correctly in the class I weight estimation script

and the loading diagram should not be ran every loop. After implementing the correct calculations the design started to converge. The iterations were started from the first class I weight estimation, which was already provided in the midterm report [39]. The OEW started at 915.000 N and soon converged to a new value of 829.000 N. The plot of the class I and class II OEWs per iteration loop is shown in Figure 8.5. In these iterations the input from the class II weight estimation was damped. This was done by only implementing 30% of the new OEW and 70% of the old OEW in the class I weight estimation.

After computing the new OEW and other system-level parameters of the aircraft, the mission profile was optimised. The mission profile is given in Figure 16.2. After optimising the mission profile the iterations were run one more time, as the cruise speed and altitude had changed. The final OEW was determined to be 889.000 N. In Figure 8.6 the convergence of the second iteration is given.

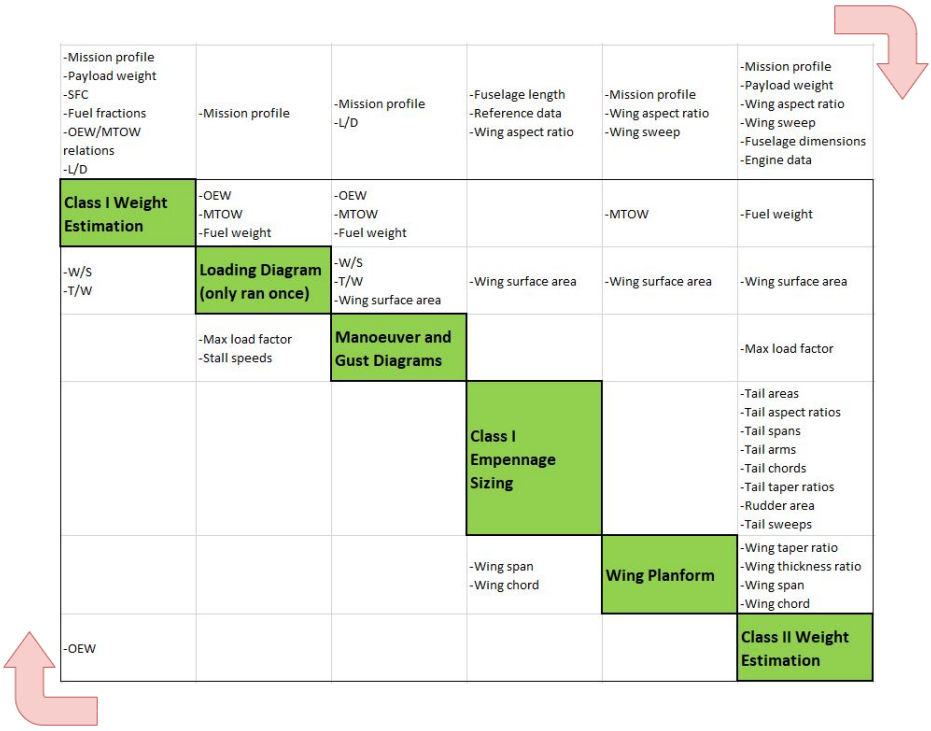

Figure 8.4: N2 chart of the iteration framework

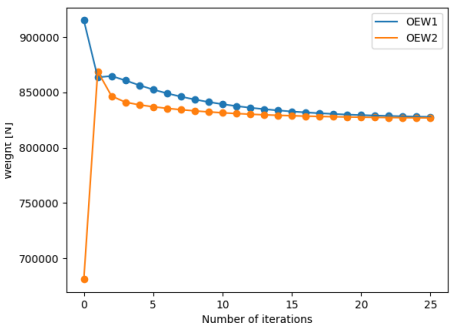

Figure 8.5: Initial class I-II iteration plot

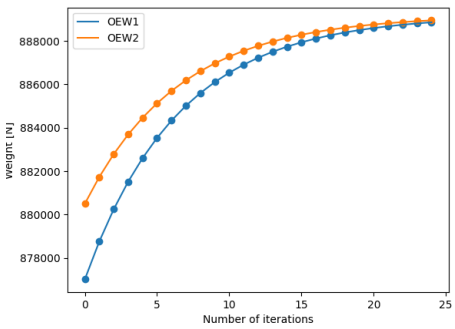

Figure 8.6: Second class I-II iteration plot

8.3. Centre of Gravity Determination

Now that the weights of the different components are known, the centre of gravity of the aircraft at operational empty weight can be determined. First, the center of gravity locations of each component are determined.This will be done in both x and z direction. Then, the center of gravity in x and z locations will be determined. The x location is measured along the aircraft length and is measured from the nose. The z location is measured along the height of the aircraft and is measured from the center of the fuselage. Table 8.6 shows the CG locations of the different aircraft components.

Table 8.6: Centre of gravity locations of the different aircraft components

Component	CG_x [m]	CG_x [% Fuselage]	CG_z [m]	Component	CG_x [m]	CG_x [% Fuselage]	CG_z [m]
Wing	28.1	48.2	-1.1	Hydraulic system	28.6	49.2	0.0
Horizontal tail	55.2	94.8	2.4	Electrical system	25.7	44.2	0.0
Vertical tail	55.1	94.6	7.0	Avionics system	2.0	3.4	0.0
Fuselage	23.3	40.0	0.0	Air conditioning system	23.3	40	0.0
Engine	25.7	44.2	-2.5	Oxygen system	22.2	38.1	0.0
Fuel system	25.7	44.2	-2.5	Auxiliary power unit	51.2	88.0	0.0
Propulsion system	25.7	44.2	-2.5	Furnishing	26.7	45.9	0.0
Thrust reverser	25.7	44.2	-2.5	Paint	28.6	49.2	0.0
Flight control system	41.8	71.9	0.0	Auxiliary gear	57.1	98.1	0.0

With the centre of gravity data from Table 8.6 and the weight data from Table 8.1 one can determine the centre of gravity location at operational empty weight. The centre of gravity is determined using Equation 8.1.

$$CG_{OEW} = \frac{\sum_i CG_i \cdot W_i}{\sum_i W_i} \tag{8.1}$$

The final values for $CG_{OEW,x}$ and $CG_{OEW,z}$ can be found in Table 8.7. To validate this result of $CG_{OEW,x}$ the data is compared tot the $CG_{OEW,x}$ of an Airbus A320-200. The CG at OEW for the A320-200 is taken from its weight and balance manual [2] and is expressed in %RC. A comparison between the two is given in Table 8.8. The MAC does not provide a good comparison of the two due to the sweep present on the A320-200. When looking at the chord one can find more similar values. The small difference is once again an effect of the sweep.

Table 8.7: OEW CG locations on the x and z axis

$CG_{OEW,x}$ [m]	25.29
$CG_{OEW,z}$ [m]	-0.49

Table 8.8: OEW CG location compared to A330-200

	Airbus A330-200	**Low-ATR concept**
$CG_{OEW,x}$ [%MAC]	-63	23.5
$CG_{OEW,x}$ [%RC]	28.1	22.7

The centre of gravity will still move due to the different loading conditions of the aircraft. An aircraft loading diagram will be constructed in Section 11.2 to assess the entire centre of gravity range of the aircraft.

8.4. Aircraft Configuration

The aircraft configuration three-view is provided in Figure 8.7. Figure 8.7 can be used as a reference to visualise the design choices made and can be referred to later on in the report.

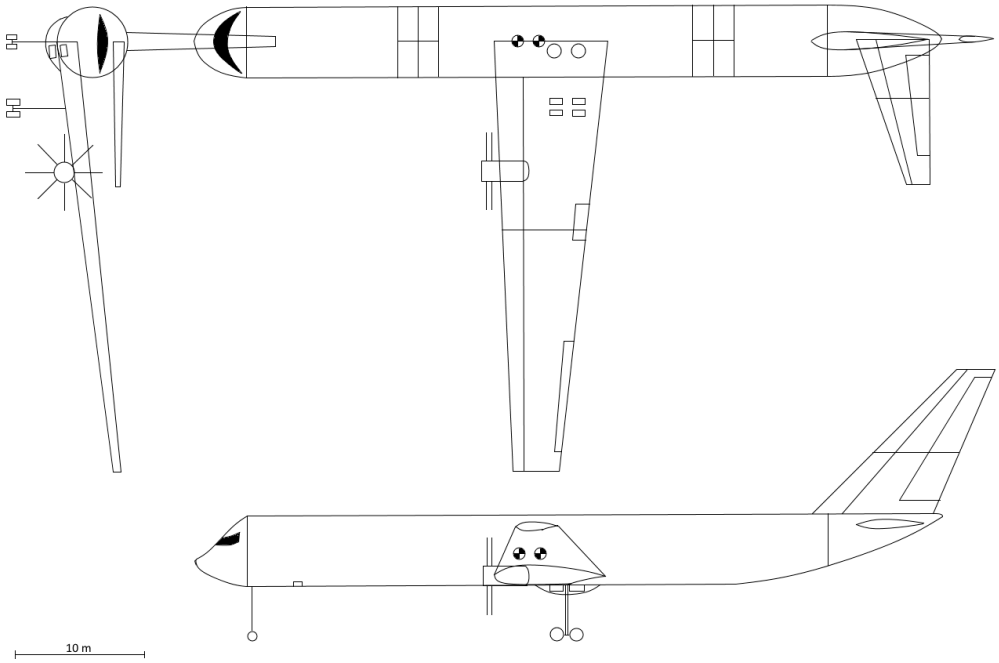

Figure 8.7: Aircraft top, side and front view

8.5. Landing Gear Design

For preliminary landing gear design, the Roskam method is once again be used [88]. It is found that 8 main wheels with 2 struts and 2 nose wheels with a single strut are required. The main wheel load is roughly 225 kN and the nose wheel load is 78 kN [39]. For the tyre selection an online manufacturers database is used [37]. These provide more modern tyres, which adhere to stricter regulations and have better performance than those from around the time of Roskam. The final selected tyres are displayed in Table 8.9.

Table 8.9: Tyre selection [37]

Wheel Type	Tyre Load (lbs)	Tyre Name	Tyre Size (in)	Rated Speed (mph)	Rated Inflation (psi)	Max braking Load (lbs)	Max Bottoming Load	Part Number	AR
P_{mw}	51900	Flight Leader	$49 \cdot 10.0 - 20$	235	195	77800	155700	491K29-3	0.767
P_{nw}	26500	Aircraft Rib	$36 \cdot 11$	201	235	39750	79500	461B-3219-TL	0.832

8.6. Aircraft Layout

In this section the aircraft layout is elaborated on. This includes the fuselage cross-section, the cabin layout and finally the baggage containers.

8.6.1. Fuselage Cross-Section

In this section the cross section of the aircraft is made which is based on the analysis performed in the midterm report [39]. It uses the methods available from Torenbeek [106], to determine the fuselage outer diameter and with it the internal cross-section.

As was determined in [39] the 250 passengers aboard the aircraft will have seven seats abreast in economy class with two aisles. With the design parameters seen in Table 8.11 the width of the cabin and width of the headroom could be determined. Furthermore with adding the height of the headroom and shoulder height, the bounding boxes for the cabin cross section could be determined. Also it was decided to have room for two LD3 cargo containers in the cargo area of the fuselage, which also provided more bounding boxes below the floor area. The final fuselage cross-section can be seen in Table 8.10.

8.6.2. Cabin Layout

In Section 8.6.1, the cabin cross-section was determined and with it the fuselage outer diameter. In this section the cabin layout is determined using methods from Torenbeek [106]. This discussion is a shorter version of the one presented in the Midterm report [39]. During the design of the aircraft a two class configuration was chosen and the number of business seats was based on reference airliners passenger distribution. This mean that there would be 8 business rows, with 5 seats abreast each. The remaining passengers are seated in the economy class, which accounts for the other 30 rows of seats. Making the distribution, 16% business class seats. Using the pitch of business seats, economy seats and accounting for lavatories, galleys and cross-aisles the length of the cabin can be determined. The design values can be retrieved in Table 8.11. Adding the standard lengths of the cockpit and tail the final fuselage length was determined to be 58.2 m.

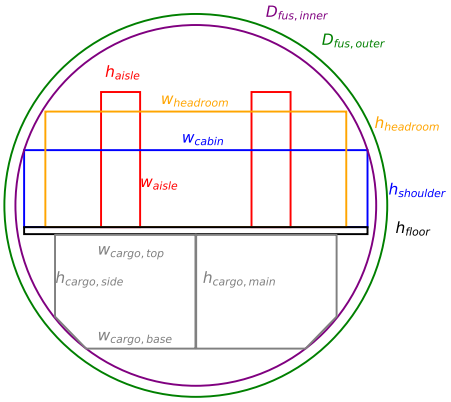

Table 8.10: Cabin cross-section for twin aisle configuration in economy class.

Parameter	Value	Unit	Parameter	Value	Unit
$n_{sa,e}$	7	-	n_{pax}	250	-
$n_{sa,b}$	5	-	$h_{shoulder}$	110	cm
n_{aisle}	2	-	$h_{headroom}$	165.1	cm
$w_{arm,e}$	5.5	cm	$w_{headroom}$	429.92	cm
$w_{arm,b}$	7	cm	h_{floor}	10	cm
$w_{seat,e}$	45.72	cm	$w_{cargo,base}$	200.66	cm
$w_{seat,b}$	63.5	cm	$w_{cargo,top}$	156.21	cm
w_{aisle}	55.8	cm	$h_{cargo,side}$	116.84	cm
h_{aisle}	193.04	cm	$h_{cargo,main}$	162.52	cm
$s_{clearance}$	2	cm	$s_{cargo,clearance}$	0.5	cm
$w_{cabin,e}$	490.64	cm	$D_{fus,inner}$	5.15	m
$w_{cabin,b}$	489.1	cm	$D_{fus,inner}$	5.47	m
p_{econ}	88.9	cm	$p_{lavatories}$	91.44	cm
p_{busi}	127	cm	$p_{galleys}$	76.2	cm
$n_{rows,busi}$	8	-	$p_{cross\ aisles}$	63.5	cm
$n_{rows,econ}$	30	-	$n_{lavatory\ rows}$	4	-
$n_{pax,busi}$	40	-	$n_{galley\ rows}$	4	-
$n_{pax,econ}$	210	-	$n_{cross\ aisles}$	3	-
$l_{pax,busi}$	10.16	m	l_{cabin}	45.44	m
$l_{pax,busi}$	26.67	m	$l_{cockpit}$	4	m
l_{pax}	36.83	m	l_{tail}	8.75	m
			$l_{fuselage}$	58.2	m

Table 8.11: Design table for the cabin cross-section and fuselage layout.

8.6.3. Baggage Containers

As determined by the fuselage cross-section in Section 8.6.1 the LD-3 container is used for cargo storage. According to Roskam[87] Equation 8.2 can be used to estimate the required baggage volume.

$$Vol_{\text{bag}} = \frac{m_{\text{bag}}}{\rho_{\text{bag}} \cdot \eta_{\text{bag}}} \tag{8.2}$$

with $\eta_{\text{bag}} = 0.85$ and $\rho_{\text{bag}} = 200\,\text{kg}\,\text{m}^{-3}$. The LD-3 container has a volume of $4.5\,\text{m}^3$ [1]. With the use of 8 containers each passenger will get a baggage allocation of 24 kg. Furthermore the passengers will be allowed 5 kg of hand baggage.

The containers will be split up into a front and rear cargo compartment. The front cargo compartment is placed at 30% of the fuselage length and the rear cargo compartment is placed at 80% of the fuselage length. The placement of the cargo containers can be seen in the aircraft three-view drawing in Figure 8.7.

8.7. Nose Design

The nose of the fuselage is to be designed for an optimal aerodynamic performance, in which drag is reduced. According to [34], for a strictly subsonic design, the main drag component comes from friction drag. Therefore the aim is to design for minimum wetted surface area. A short, blunt, smooth and elliptical shape is therefore chosen as the best performer for this subsonic regime [34]. An elliptical nose is obtained by rotating a half-ellipse around its major axis, and its 2D representation is given by Equation 8.3, where R is the length of the semi-minor axis and L the one of the semi-major axis.

With this shape chosen, in order to reduce friction drag the wetted surface area has to be minimized. The wetted area is given by Equation 8.4.

$$y = R\sqrt{1 - \frac{x^2}{L^2}} \tag{8.3}$$

$$S_{wet} = \pi L^2 + \frac{[\frac{\pi R^2}{\epsilon} \ln(\frac{1+\epsilon}{1-\epsilon})]}{2} \quad \text{where} \quad \epsilon = \frac{\sqrt{L^2 - R^2}}{L} \tag{8.4}$$

Plotting Equation 8.4 with respect to R and L leads to Figure 8.8, which can be used to minimise the wetted surface area of the nose. For this case, the maximum size of L is set to the fuselage diameter, and R maximum is limited to the fuselage radius.

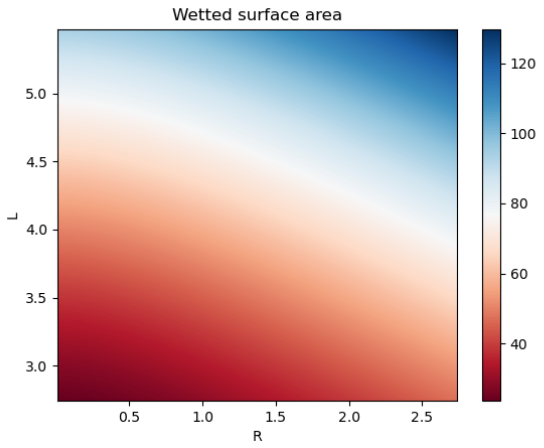

Figure 8.8: Nose wetted surface area with respect to R and L

It can be seen that the wetted area is minimised by reducing R and L, but these are constrained by the aircraft size. Bear in mind that the function of the nose is to enclose the cockpit, while minimising drag. Therefore, in order to use Figure 8.8, the space to be enclosed need to be sized. Once that is done, from Figure 8.8 it is known that both L and R should be minimised for minimum drag. This is to be done at a later stage of the design, when the cockpit is adequately sized according to its components.

9. Wing Design

This section contains the aerodynamic design of the main wing of the aircraft. Section 9.1 explains the selection procedure for the baseline airfoil of the wing, the NACA 633-418. Section 9.2 contains the lift computations of the wing, and Section 9.3 contains the procedure for an optimized wing planform. The wing design is finalised in Figure 9.10, where the high lift devices are sized. Finally, Section 9.5 includes recommendations for ATR reduction using airfoil optimization and miniature vortex generators.

[1] `https://www.searates.com/reference/ld3/` (last accessed on 17-06-2021)

9.1. Airfoil Selection

The choice of an airfoil is a critical part of the wing design. It does not only directly influence the lift and drag characteristics of the aircraft, but its stability and the structural performance of the wing. Therefore, the airfoil choice is a crucial decision as it interfaces with many other subsystems of the aircraft, and therefore should be considered carefully.

9.1.1. Selection Procedure

The tool chosen in order to perform the airfoil selection was XFLR5. This program uses a panel method for the aerodynamics calculations as explained in Section 9.1.3. Keeping the limitations of this method in mind, the process is started with a selection of the criteria to be accounted for in the airfoil choice. These criteria can be found in Table 9.1.

Table 9.1: Airfoil Selection Parameters

Airfoil Selection Parameters	
C_d at design C_l	Boundary layer transition point: X_{tr}
Moment coefficient: C_m	Maximum C_l
Stall characteristic	

Having this set of parameters, the next step is to calculate the design C_l. It is desired to have an airfoil with minimum drag coefficient and wide drag bucket around the design C_l. Equation 9.1 yields a design C_l of 0.46 for the chosen mission profile.

$$C_{L_{\text{des}}} = 1.1 \frac{1}{q} \left\{ \frac{1}{2} \left[\left(\frac{W}{S} \right)_{\text{start of cruise}} + \left(\frac{W}{S} \right)_{\text{end of cruise}} \right] \right\} \tag{9.1}$$

Having the selection criteria and the design C_l, the simulations to get airfoil data can be started. A selection of airfoils was made in order to design for laminar flow control (MATRA-USER-SUS-01). These airfoils were from the NACA 6 and 7 series and the NLF series by NASA since the geometries of these have been optimized to delay the onset of transition along the chord. In order to obtain a smooth lift loss, the airfoils are filtered by thickness in a first stage. All of the airfoils with a thickness to chord ratio (t/c) of less than 14% were discarded, as their stall characteristics are not suitable for a commercial airliner. The remaining airfoils are simulated using the conditions as shown in Table 9.2. The Mach number is chosen to be 0.0 as compressibility effects are not accurately modelled in XFLR5 (see Section 9.1.3). The simulation was run over an angle of attack range between $-5\,°$ and $30\,°$ angle of attack in increments of of $0.05\,°$. Each airfoil was simulated using the coordinates as obtained from the UIUC Airfoil Coordinates Database [1]. For a better readability of the results only the plots for the four best performing airfoils are shown.

Table 9.2: XFLR5 simulation conditions

Simulation Conditions	
Reynolds number	41.870.601
Mach number	0.0
Ncrit	9.0

[1] `https://m-selig.ae.illinois.edu/ads/coord_database.html` (last accessed on 18/06/2021)

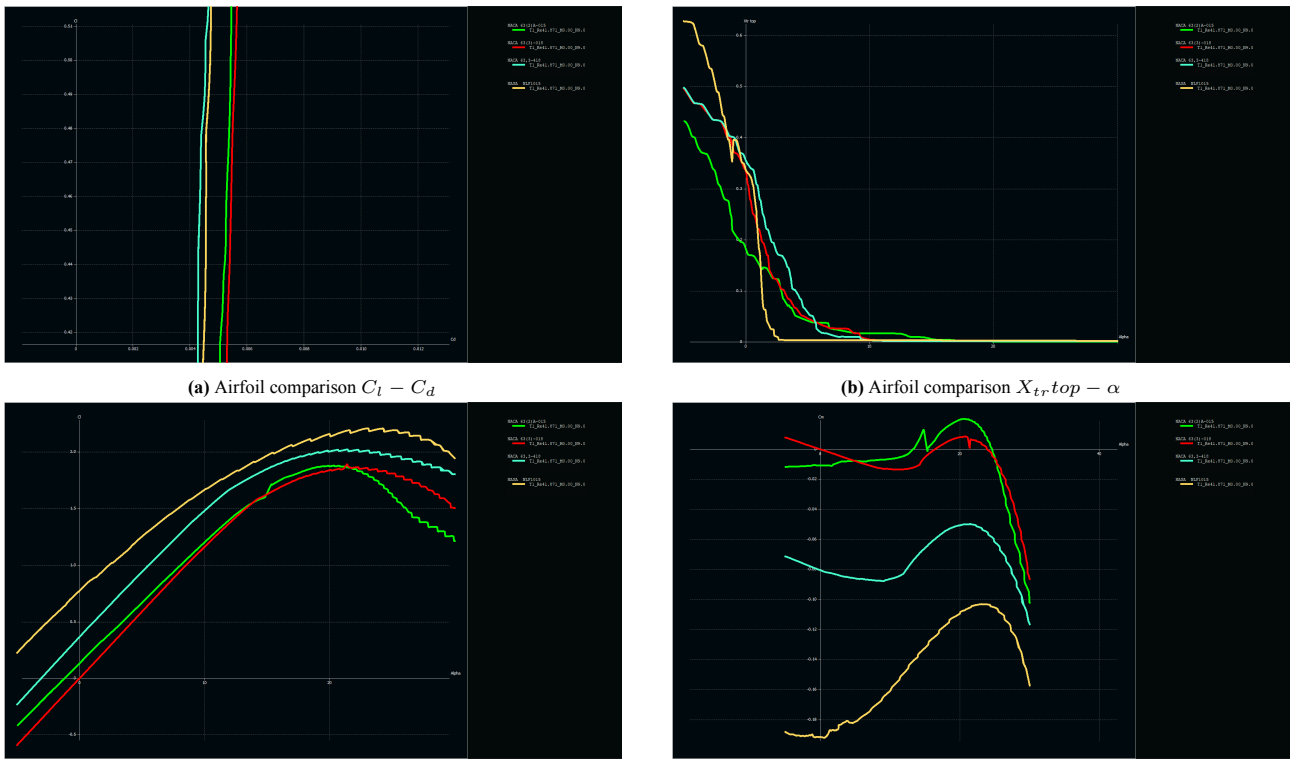

(a) Airfoil comparison $C_l - C_d$

(b) Airfoil comparison $X_{tr}top - \alpha$

(c) Airfoil comparison $C_l - \alpha$

(d) Airfoil comparison $C_m - \alpha$

Figure 9.1: Selection parameters comparison

Figure 9.1 shows how the four best performing airfoils compare with regards to the parameters described in Table 9.1. In Figure 9.1a the airfoils are compared in order to see which one has the lowest drag coefficient at the design C_l of 0.46. It can be seen that the NACA 633-418 has the lowest C_d at the design C_l, as well as the most delayed transition point. Furthermore, it also has a good C_l max, and an acceptable stability performance, which can be improved by sizing the empennage accordingly. The second best option is the NLF 1015, but the parameters in which it has a better performance are deemed less relevant. Finally, both the NACA 63(2)A-015 and the NACA 63(3)-018 are discarded as they have a worse overall performance.

After this first filter, the two best performing candidates are analyzed in a more refined simulation in order to confirm the previously discovered trend. As shown in Figure 9.2, the number of panels has been increased to 150, while maintaining the simulation Reynolds number and angle of attack range. Figure 9.4 shows the results of this simulation, and in this more refined analysis. The NACA 633-418 still outperforms the NLF 1015 in terms of drag and transition characteristics, which are considered the most important criteria (see requirement MATRA-SYS-10), as both Cl max (HLD) and Cm (empennage sizing) can be compensated.

In Figure 9.3 the pressure coefficient at an angle of attack of 2 ° of both airfoil candidates are shown as a function of the chord position. In Figure 9.3a it can be seen that the point of minimum pressure of the top part of the airfoil is located further aft for the NACA 633-418 than in the NLF 1015, shown in Figure 9.3b. This larger region of favorable pressure gradient means that the transition region of the NACA 633-418 airfoil will be located further aft, therefore having a larger laminar flow region over the wing than that of the NLF 1015, helping with requirement MATRA-SYS-10. Furthermore, the pressure recovery region has a smoother gradient in the case of NACA 633-418, which gives favorable stall characteristics. In both cases there are no sharp pressure changes over the airfoil.

One final thing to note is that the critical mach number of the NACA 633-418 is larger than that of the NLF 1015, giving more freedom in terms of the selection of the cruise speed. This value is found by plotting the minimum pressure coefficient at α = 0° corrected using the Prandtl-Glauert relation as a function of the Mach number. The intersection between this curve and the curve for the critical pressure coefficient as a function of Mach number determines the critical Mach number.

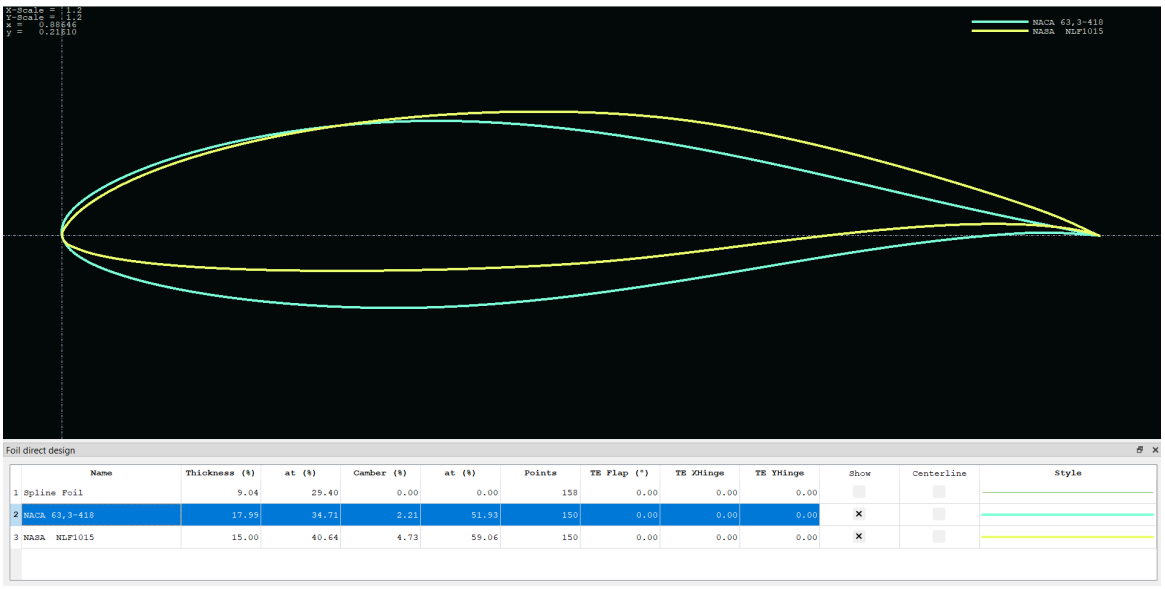

	Name	Thickness (%)	at (%)	Camber (%)	at (%)	Points	TE Flap (°)	TE XHinge	TE YHinge	Show	Centerline	Style
1	Spline Foil	9.04	29.40	0.00	0.00	158	0.00	0.00	0.00			
2	NACA 63,3-418	17.99	34.71	2.21	51.93	150	0.00	0.00	0.00	×		
3	NASA NLF1015	15.00	40.64	4.73	59.06	150	0.00	0.00	0.00	×		

Figure 9.2: NACA 633-418 and NLF 1015 shape comparison

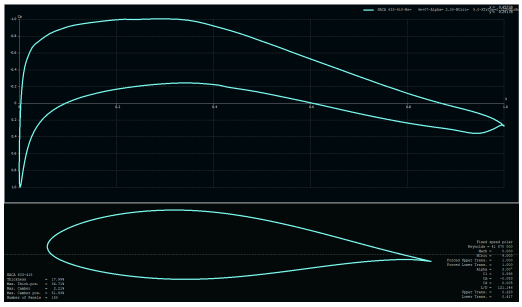

(a) NACA 633-418 pressure plot

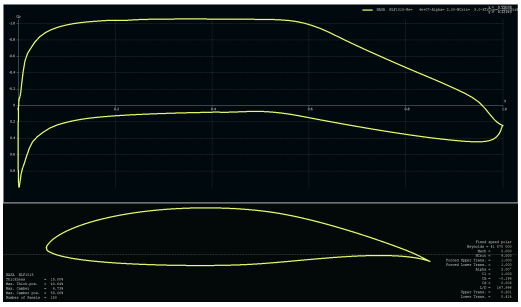

(b) NLF 1015 pressure plot

Figure 9.3: Pressure distribution at α=2°

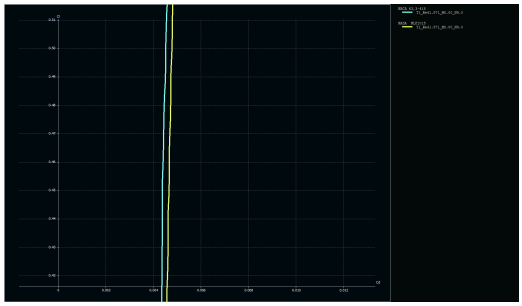

(a) Airfoil comparison $C_l - C_d$

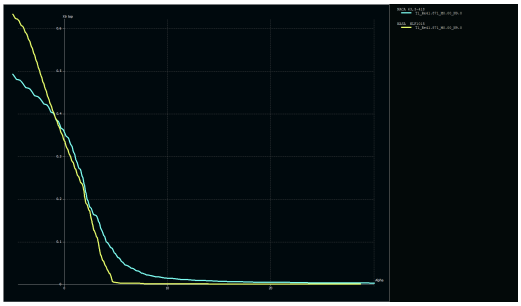

(b) Airfoil comparison $X_{tr}top - \alpha$

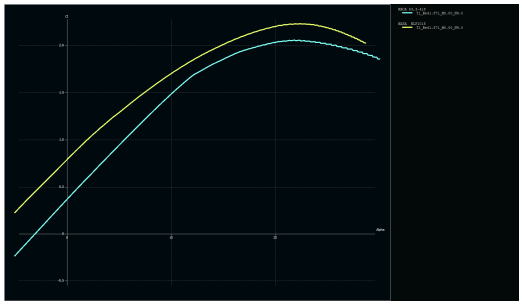

(c) Airfoil comparison $C_l - \alpha$

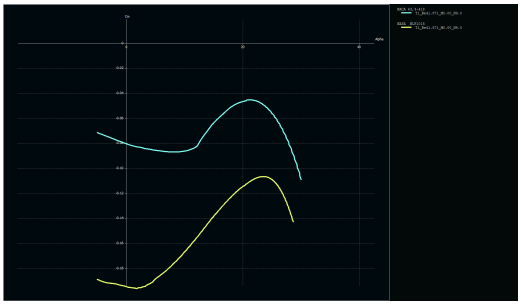

(d) Airfoil comparison $C_m - \alpha$

Figure 9.4: Comparison NACA 633-418 and NLF 1015

Taking into account all the aforementioned factors, the NACA 633-418 is chosen as the baseline airfoil for the envisioned

aircraft. It has the lowest C_d and the design C_l and has the most delayed transition point at approximately cruise angle of attack. This translates into a lower airfoil drag and better performance when designing for laminar flow. It was found that the NACA 633-418 also had the highest critical Mach number out of the final four airfoils. At a later stage, a sensitivity analysis is performed on the airfoil, shown in Section 9.5.1, in which the camber, the thickness to chord ratio, and the maximum thickness are changed in order to optimize the airfoil further for the characteristics found in Table 9.1. However, since wind tunnel experiments are currently not accessible, there is no way to validate the results obtained from this sensitivity analysis, and hence the aircraft will adopt the NACA 633-418 airfoil. Nevertheless, the sensitivity analysis provides insight into potential design modifications that can be made to current airfoils to improve their abilities to delay transition, whilst maintaining favourable stall characteristics.

9.1.2. Effect on ATR of Using a NLF Airfoil

Having chosen the NACA 633-418 for the wing of the aircraft, the ATR gain obtained from this choice should be quantified. In order to do so, first an airfoil is chosen to compare the NACA 633-418 with. It should be a supercritical airfoil, as that is the type of airfoil that reference aircraft, such as the A330-200 use, as current airliners fly in a transonic regime. Furthermore, it should be relatively similar to the NACA 633-418, as it has to be compared with it. Therefore, the NASA SC(2) 0414 is chosen, which is a common supercritical airfoil with the same deisgn C_l as the NACA 633-418 and a similar thickness (as the available supercritical airfoils found in [2] are thinner than 14% thickness to chord ratio). Next, the drag of the aircraft using both airfoils is calculated. This is the total drag of the aircraft without riblets, as the contribution to ATR reduction being calculated is of the NLF airfoil exclusively. In order to account for different airfoils, the drag is calculated using lifting-line theory and assuming elliptical distribution. This can be assumed as we have a large aspect ratio and a taper ratio of 0.4, so the actual distribution is close to elliptical, and this accuracy is enough for the current level of detail of the design. The results of this calculation are shown in Table 9.3, where the drag coefficient, drag, and ATR for the aircraft with both airfoils are shown.

Table 9.3: Drag and ATR comparison for NLF

Airfoil	C_D	Drag (N)	ATR µK
NACA 633-418	0.01434	89649.36	4.5762E-9
SC(2) 0414	0.01599	100019.87	5.0961E-9

From Table 9.3 it can be seen that the SC(2) 0414 has around 12% more drag, which is expected as the supercritical airfoil is not optimized for the airflow conditions being studied, for which friction drag is predominant. On the other hand, for a transonic regime in which wave drag becomes important, supercritical airfoils would perform better. From Figure 9.5b it can be seen that the position of minimum pressure is found very early along the chord, introducing turbulence and leading to a higher friction drag than in Figure 9.5a, explaining this higher drag. Having less aerodynamic efficiency, implies flying at a higher ATR, as can be seen from Table 9.3, which shows a 11.36% increase in ATR from using the SC(2) 0414 airfoil. This shows potential in the use of Natural Laminar Flow airfoil in commercial aviation, as thanks to the change in mission profile [78], this technology can be used and therefore lead to a further optimized design. Finally, note that the drag results shown in Table 9.3 are different from those in Chapter 12, and this is because a different approach is used for the calculation of the wing drag. While for the ATR calculations a more analytical approach is used, in which the different airfoil plays a role, while the approach Chapter 12 has a more statistical approach, and is the one used during the design and iterations.

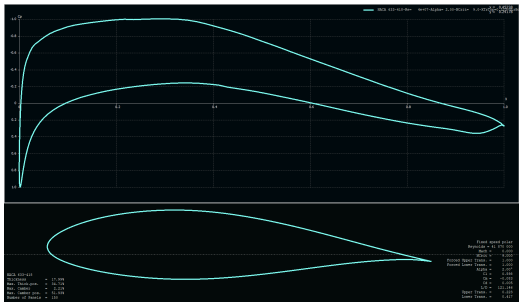

(a) NACA 633-418 pressure plot

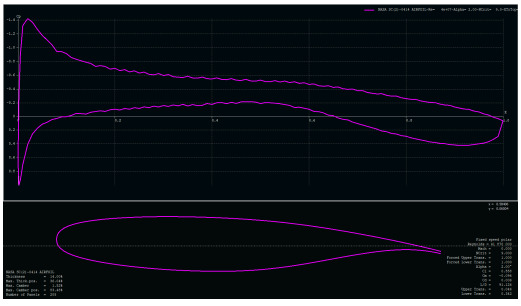

(b) SC(2) 0414 pressure plot

Figure 9.5: Comparison NACA 633-418 and SC(2) 0414

9.1.3. XFLR5 Validation

XFLR5 is a hybrid flow analysis tool that comprises of both a two- and three- dimensional solver. For two-dimensional airfoil analysis, XFLR5 uses the codebase from XFOIL, whereas for its three-dimensional solver, makes use of a vortex

[2] `https://m-selig.ae.illinois.edu/ads/coord_database.html` (last accessed on 28/06/2021)

lattice method (VLM), a lifting line method and a three-dimensional panel method [76]. Since experimental data for 3-D finite wings was not accessible, the three-dimensional models in XFLR5 could not be validated, and hence was concluded that they should not be used for any stage of the design. Performance parameters relating to the wing will be approximated using empirical formulas found in Raymer's aircraft design book [82]. The remainder of this validation section will be dedicated to the validation of the XFOIL two-dimensional analysis model.

XFOIL's viscous formulation makes use of a two-equation lagged integral boundary layer formulation to describe the boundary layer and wake. These equations are the compressible von Kármán integral momentum equation coupled with a kinetic energy shape parameter equation [30]. The choice to use integral equations over more accurate differential techniques was motivated by the fact that integral techniques are easier to solve and computationally less expensive. The transition point is estimated as a point rather than a region of finite length using spatial-amplification theory which builds from the e^n method. The method defines the point of transition to be the point where n, the amplitude of the most-amplified Tollmien-Schlichting (TS) wave reaches a user-specified value n_{crit}. For the case of a smooth wing in a wind-tunnel with moderate-to-low disturbances, n_{crit} has been set to 9 [69]. Full e^n methods track the amplification factors of each individual TS wave, however, the envelope method used by XFOIL only keeps track of the amplitude of the most amplified TS frequency. Although this is computationally less expensive, it has been shown to be less accurate than the full e^n method [76]. For this reason, the transition location will be used in a purely comparative manner between airfoils.

Previous research has already outlined some of the limitations of XFOIL, namely the over prediction of the point of flow separation, under prediction of c_d and over prediction of c_l values. The method used by XFOIL to compute drag is based on flat-plate boundary layer theory which sets the angle of attack of each panel to zero and sets the velocity normal to the plate at all points outside the boundary layer equal to the freestream velocity u_∞ [81]. These assumptions however do not hold for an airfoil, which have pressure distributions which vary in the direction normal to the airfoil surface η, causing a change in the velocity outside the boundary layer in the η direction. When applying these assumptions to an airfoil, it results in under predictions in the boundary layer momentum thickness which is the cause for the under prediction in c_d, and results in over predictions in the velocity at the edge of the boundary layer which is the cause for the over prediction in c_l. Ramanujam and Ozdemir investigated methods to improve the values of c_d and c_l by modifying the computation of the boundary layer momentum thickness to correct for the flat-plate assumptions used by XFOIL. By correcting the momentum thickness in the XFOIL codebase, they found significant improvements in XFOIL's ability to predict c_l, c_d within the linear lift regime [81] [80].

XFOIL was initially made as a design framework for airfoils at low Reynolds numbers less than 500,000. Since the Reynolds number of the envisioned aircraft at the time of validating the software was in the order of 40 million, it required a careful analysis into the feasibility of using XFOIL for the current application. There exists an extensive amount of wind tunnel data on airfoils at Reynolds numbers in the order of 3-9 million. To validate the feasibility of using XFLR5, simulations will be run on at Reynolds numbers of 9 million and compared with the lift and drag polars found in literature. Although 9 and 40 million may seem initially incomparable, since the Navier Stokes equations contain a factor $1/Re$, results gained from numerical simulations become asymptotically independent from Re for increasing Re. For this reason it is assumed that a validation based on comparisons at Reynolds number 9 million can still provide conclusions on the validity of XFLR5 at Reynolds number 40 million.

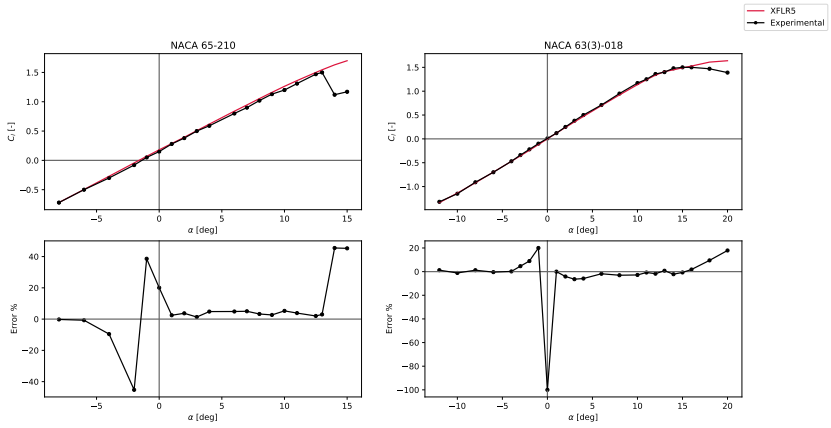

Figure 9.6: Comparison plots between experimental and numerical lift polar data for both NACA 63(3)-018 and NACA 65-210 airfoils at Re = 9 million. The bottom figures display the relative error between the numerical and experimental data

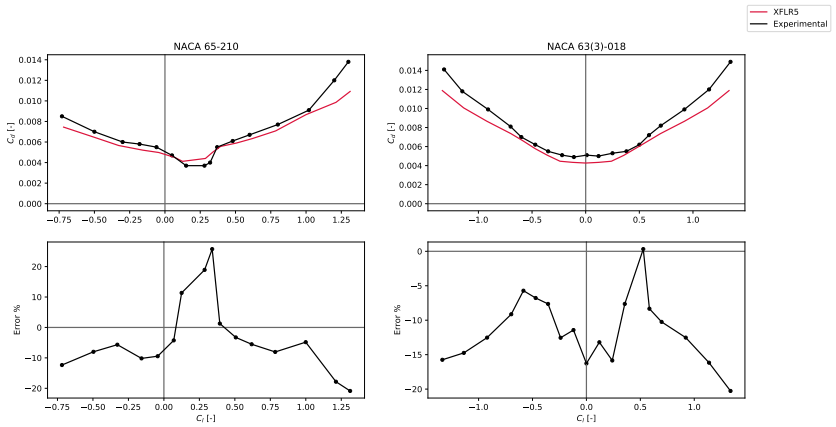

Figure 9.7: Comparison plots between experimental and numerical drag polar data for both NACA 63(3)-018 and NACA 65-210 airfoils at $Re = 9$ million. The bottom figures display the relative error between the numerical and experimental data

To determine the validity of XFLR5 on the specific series of airfoils that were being considered for the envisioned aircraft, the validation was run on 2 NACA 6-series airfoils: NACA 63(3)-018 and NACA 65-210. The experimental data for the NACA 63(3)-018 was found from a paper by Loftin and Bursnall [59] and the data for the NACA 65-210 was found in Anderson's Introduction to Flight book [6]. It should be mentioned that the experimental data was obtained from images, and so there will be inherent uncertainties from the collection of the data. Angle of attack values will have an uncertainty of ± 0.5, lift coefficient values will have an uncertainty of ± 0.05 and drag coefficient values will have an uncertainty of ± 0.0005. These were calculated as half the smallest scale division found on the axis.

From Figure 9.6, the relative errors within the linear regime for both airfoils are relatively small, with errors staying within $\pm 10\%$. There are some points for which errors are much higher, however, this is in part due to the small differences when the data values themselves are already small being exaggerated. The general over-estimation of the C_l values of XFLR5 relative to experimental data is as expected from the literature study into XFOIL's models [80]. Lastly for both airfoils, XFLR5 is not able to capture the stall behaviour of the airfoil. From Figure 9.7, the relative errors within the linear regime are likewise relatively small. The under-estimation of C_d values of XFLR5 relative to experimental data is also as expected from the paper by Ramanujam and Ozdemir [81]. The shape of the laminar drag bucket is somewhat accurately represented, however like with the lift polar, the relatively large errors are firstly due to the small differences being magnified on the small scale, and secondly the uncertainties in extracting the data from the papers, where multiple plots are typically superimposed for different Reynolds numbers. With this, the use of XFLR5 will be restricted to the laminar regime, since the software fails to capture the flow behaviour at stall, and hence does not hold any validity.

9.2. Wing Analysis

Having done a preliminary analysis on the airfoil selection, the wing aerodynamic properties can now be computed using the DATCOM method. The wing Oswald efficiency factor, lift curve, maximum lift coefficient, trim angle of attack and lift at zero angle of attack shall be computed and later iterated. These values play as crucial inputs for other subsystems on the aircraft and define the aerodynamic performance of the aircraft.

9.2.1. Lift Analysis

The lift analysis aims to realize the lift slope of the wing in the linear regime via the DATCOM method. It would also provide a value for the trim angle which is the angle of attack needed to fly at the design lift coefficient. The DATCOM method differentiates high and low aspect ratio wings and uses the airfoil geometric parameters as an input. To calculate the wing lift curve slope the following equation was used:

$$\frac{dC_L}{d\alpha} = C_{L\alpha} = \frac{(2\pi)A}{2 + \sqrt{4 + \left(\frac{AB}{\eta}\right)^2 \cdot \left(1 + \frac{\tan^2 \Lambda_{0.5C}}{(\beta)^2}\right)}} \tag{9.2}$$

Where β is the Prandtl-Glauret correction taking account the compressibility effects for flying at Mach numbers higher than 0.3, and Λ is the half-chord sweep. Then, using the DATCOM methods for a high aspect ratio wing, the maximum lift coefficient and trim angle of attack can be computed using the following equations:

$$C_{L\,\max} = \frac{C_{L\,\max}}{C_{l\,\max}} C_{l\,\max} + \Delta C_{L\,\max} \tag{9.3}$$

$$\alpha_s = \frac{C_{L\,\max}}{C_{L\alpha}} + \alpha_{0L} + \Delta\alpha_{C_{L\,\max}} \tag{9.4}$$

The $\frac{C_L}{C_L}$ and ΔC_{Lmax} term of the first equation and the $\Delta\alpha_{C_{Lmax}}$ term of the second equation are dependent on the sharpness parameter which is value dependent on the geometry of the leading edge of the airfoil. For the first equation, the

$\frac{C_L}{C_L}$ term provides a relationship between the incompressible lift of the wing and the airfoil and is found by cross correlating a chart to the leading edge angle of attack as well as sharpness parameter. The ΔC_{Lmax} in the first equation is a term accounting for the effect of mach numbers greater than 0.2 and is found by correlating another chart to the mach number and sharpness parameter of the airfoil. Finally the $\Delta\alpha_{C_{Lmax}}$ of the second equation is a term that accounts for non-linear vortices and is dependent on the leading edge angle of attack as well as the sharpness parameter. With this, it is found that the maximum clean wing lift coefficient to be 1.787 and trim angle to be 2.24 degrees. With the trim angle, design and maximum lift coefficient as well as the angle of attack at zero lift known, it is possible to find the lift coefficient of any angle of attack as long as it is in the linear region.

9.3. Wing Planform Optimization

This section will aim to introduce preliminary optimisation techniques for the aspect ratio by wingtips and the Torenbeek wing penalty function, and optimisation of the Oswald efficiency factor.

9.3.1. Winglet Versus Raked Wingtip Selection

Winglets and raked wingtips are aerodynamic lifting devices attached to the end of the wing which increase the effective wing aspect ratio. When dealing with finite wings, at the wingtips flow from the high pressure wing lower side curls over to the low pressure wing upper surface. This curl forms wingtip vortices which propagate downstream, generating a downwash velocity component. This downwash component reduces the effective angle of attack, and since lift is defined as being perpendicular to the effective freestream velocity vector, the lift vector is titled further backwards, introducing an additional horizontal drag component [74]. The addition of a raked wingtip or winglet devices work by reducing the strength of the wingtip vortices, reducing the downwash and consequently the induced drag.

Both raked wingtips and winglets work toward achieving a similar goal. However, it has been found that raked wingtips offer better induced drag reduction in cruise relative to a conventional winglet design [74]. Raked wintips do come with a penalty in increased span. This potentially raises issues in terms of operability when taxiing around airports, and increased bending moments due to the increased span. However, since airport regulations state a maximum wingspan limit of 80 m, and the envisioned aircraft's current iterated wingspan is 67.7 m, the small increase in span that the raked wingtips offer is not seen as a constraint. From literature it was found that raked wingtips can offer an increase in aspect ratio between 0.5 and 1.5. For the purpose of the aircraft design, it will be assumed that the raked wingtips will offer an increase in aspect ratio of 1. [74].

9.3.2. Oswald Efficiency

The Oswald efficiency factor is used to take into account the non-elliptical lift distribution on wings of general shape [6]. It is a factor which affects the aerodynamic efficiency of the aircraft which in turn determines the range and fuel burn. For this reason, having a higher fidelity model is crucial since this parameter appears frequently across other subsystems. The new estimation method in question is that of Nita and Scholz [72], and takes into account the wing-fuselage interaction, the parasitic drag from the class II drag estimation, the Mach number and the wing dihedral. The equation for the Oswald efficiency is as follows:

$$e = \frac{K_{e_M} \cdot K_{e_\Gamma}}{\frac{1}{e_{theo} \cdot K_{e_f}} + 0.38 \cdot C_{D,0} \pi A} \tag{9.5}$$

K_{e_M}, K_{e_Γ} and K_{e_f} represent penalties due to the Mach number, wing dihedral and fuselage-wing interaction respectively. These are defined as:

$$K_{e_M} = -0.001521 \left(\frac{M}{0.3} - 1\right)^1 0.82{+}1 \tag{9.6}$$

$$K_{e_\Gamma} = \left(\frac{1}{cos(\Gamma)}\right)^2 \tag{9.7}$$

$$K_{e_f} = 1 - 2\left(\frac{d_F}{b}\right)^2 \tag{9.8}$$

The parameter e_{theo} represents a theoretical Oswald efficiency based on the optimal taper ratio and quarter-chord sweep [72]. Since the envisioned aircraft will feature no quarter-chord sweep, the optimum taper ratio $\lambda_{opt} = 0.45$ [72]. This then yields a value of $e_{theo} = 0.9799$. The K penalty factors depend on the geometrical parameters and mission characteristic of the aircraft which have been subject to change during the iteration procedure. This is true of the Oswald efficiency factor itself. The final values for the K penalties and the final Oswald efficiency are presented in Table 9.4 below.

Table 9.4: Aircraft Oswald efficiency and K penalty factors for the take-off, landing and cruise phases with riblets

Flight condition	K_{e_M}	K_{e_Γ}	K_{e_F}	e
Take-off	1	1.01733	0.98693	0.69332
Landing	1	1.01733	0.98693	0.45043
Cruise	0.99573	1.01733	0.98693	0.86086

Nita and Scholz validated their method by comparing values obtained from the method to Oswald efficiency factors found from literature of aircraft of all categories [72]. They found that their method presented on average a deviation of 4% from

those reported, which gives confidence in using such a method for estimating the Oswald efficiency of the envisioned aircraft.

9.3.3. Aspect Ratio

The aspect ratio has currently been chosen as the upper limit set by Proesmans for the preliminary design of a low ATR aircraft [78]; an aspect ratio of 11. However, even in the preliminary design phase of the aircraft, it is worth exploring optimisation techniques. Torenbeek's book on advanced aircraft conceptual design offers a method which aims to minimize a certain objective function known as the wing penalty function (WPF) [105]:

$$F_{wp} = \Phi_1 A \sqrt{\frac{A}{\hat{C_L}}} + \frac{\Phi_2}{\hat{C_L}} + F_{prop}\left(\frac{C_{D,0}}{\hat{C_L}} + \frac{\hat{C_L}}{\pi A e}\right) \tag{9.9}$$

The WPF method takes into account three mutually independent weight contributions: the wing and tail structural weight, the engine weight required to balance the wing and horizontal tail drag, and the mission fuel weight to balance the wing and horizontal tail drag [105]. The variables Φ_1 and Φ_2 are dimensionless weight parameters which account for the wing and horizontal tail weight, and F_{prop} denotes the propulsion function which accounts for the engine weight and mission fuel weight contributions. The two selection variables for this optimization are the design lift coefficient $\hat{C_L}$ and the wing aspect ratio A. This allows for the plotting of contours of the WPF on a $\hat{C_L}$ - A design space.

Torenbeek identifies two main partial unconstrained optimisers, namely the optimum $\hat{C_L}$ for a given A ($\partial F_{wp}/\partial \hat{C_L} = 0$) and the optimum A for a given $\hat{C_L}$ ($\partial F_{wp}/\partial A = 0$).

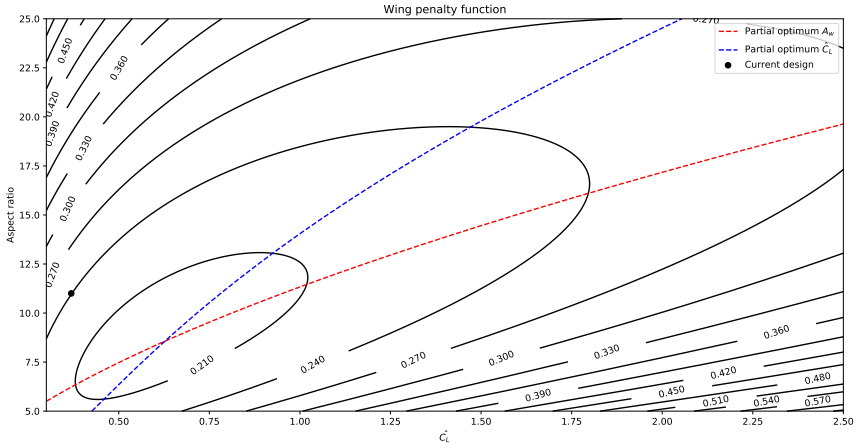

Figure 9.8: Wing penalty function contour plotted on the design lift coefficient - wing aspect ratio design space, along with the unconstrained partial optimiser for wing aspect ratio in red, and design lift coefficient in blue.

Figure 9.8 displays the contour plots, following the method of Torenbeek. The contours display the levels of the WPF, the dotted blue line represents the optimiser with respect to the design lift coefficient, and the dotted red line represents the optimiser with respect to the wing aspect ratio. These optimisers are known as unconstrained optimisers and their intersection point denotes the combination of wing aspect ratio and design lift coefficient that result in the minimum WPF. Since the design space is however unconstrained, the current global minima may be unfeasible due to practical and operation requirements. Hence, for further use of this method in the subsequent design phases following the DSE, the constraints will be identified, and a new constrained optimum will be computed. It needs to be mentioned that due to the lack of data or other papers which adopt this optimisation technique, the verification and validation procedures of this method have been limited. Hence, whilst this method poses an intriguing preliminary optimisation technique, results from this method will not be used in the current design.

9.4. High Lift Devices

In order to be able to comply with the landing and take-off requirements, high lift devices (HLDs) are needed in order to increase the C_L of the aircraft and generate the necessary lift. HLDs can be divided into leading edge and trailing edge devices. While trailing edge devices are used to directly increase the C_L by increasing the camber of the wing, leading edge devices help prevent separation and stall [75]. In this design, leading edge devices are discarded as the aim is to optimize the design for laminar flow, and these devices are seen as disturbances in the boundary layer, increasing the likelihood of an early transition.

The first step towards HLD sizing is to calculate the percentage of surface area available for mounting the flaps. This is chosen to be the region between the fuselage and the inboard ailerons, and between the inboard and outboard ailerons,

which is the part of the trailing edge with enough space to put them. This results in a flapped wing surface of 59.08% of the total wing area. Next, the $\Delta C_{l_{max}}$ of the type of flap chosen is calculated. This is dependent on the type of flap being used, and in order to choose one, the simplest (and therefore lightest) mechanism is the best option. Using Equation 9.10, the Fowler flap, single slotted flap and double slotted flap are checked in order to determine whether they generate enough $\Delta C_{L_{max}}$. Since the double slotted flap is the only HLD that provides the necessary lift coefficient, it is deemed the best option. In order to calculate the $\Delta C_{L_{max}}$ of the double slotted flap, its $\Delta C_{l_{max}}$ is needed. This is calculated as shown in Table 9.5. From Equation 9.11, $\frac{c'}{c}$ can be obtained, which needs $\frac{\Delta c}{c_f}$ to be obtained from Figure 9.9. In order to use Figure 9.9, the deflection angles of the flap are used, which for a double slotted flap are 20 ° at take-off, and 50 ° at landing. Furthermore, the chord length of the flap for a double slotted one is set as c_f = 0.375 c.

$$\Delta C_{L_{max}} = 0.9 \Delta C_{l_{max}} \frac{S_{wf}}{S} \cos(\Lambda_{hingeline}) \qquad (9.10)$$

$$\frac{c'}{c} = (\frac{c}{c_f} + \frac{\Delta c}{c_f})\frac{c_f}{c} \qquad (9.11)$$

Table 9.5: $\Delta C_{l_{max}}$ for each HLD type

High lift device	ΔCl_{max} when fully deployed
TE devices (flaps)	
Plain and split	0.9
slotted	1.3
fowler	$1.3c^1/c$
Double slotted	$1.6c'/c$
Triple slotted	$1.9c'/c$
LE Devices	
Fixed slot	0.2
Leading edge flap	0.3
Kruger flap	0.3
Slat	0.4

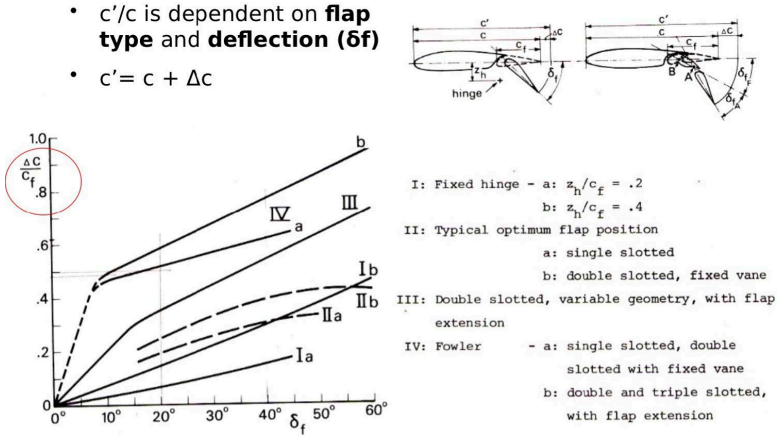

Figure 9.9: $\left(\frac{\Delta c}{c_f}\right)$ estimation

Figure 9.10: Data needed for HLD sizing [75]

Using Equation 9.10 and the values obtained from Equation 9.11 and Figure 9.10, the $\Delta C_{L_{max}}$ is obtained. This is added to the $C_{L_{max}}$ of the wing in clean configuration, giving the lift coefficient available. The final C_L obtained from the high lift devices is $C_{L_{TO}}$ = 2.75 and $C_{L_{Landing}}$ = 2.84. This allows us also to determine the stall speeds for take off and landing which are 50.4 and 39.9 ms^{-1}.

9.5. Future Research

Throughout the wing design stage, an effort was made into an initial airfoil optimisation by means of a sensitivity study. There were also further literature studies made into the use of miniature vortex generators (MVGs) for delaying transition and reducing the skin friction drag. Although at this current stage of the design it was not possible to validate the use of these, this section will delve into the findings of the optimisation of the airfoil and literature study on MVGs, and why they show promise for further improving the aerodynamic design.

9.5.1. Airfoil Optimization

As explained in Section 9.1.1, after the selection of an existing airfoil, an optimization of its shape is performed using XFLR5. This optimization is done in the form of a sensitivity analysis, analysing how the airfoil characteristics, such as C_l or C_d, change with variations in camber, thickness to chord ratio, and maximum thickness position. The analysis is done using XFLR5, with the same simulation conditions as in Table 9.2, except for the Mach number, which is set at 0.61 only for the X_{tr} calculations, such that XFLR5 computes a more accurate value by accounting for compressibility. The value of Mach 0.61 is set at the time of performing this analysis, however in the later stages of the design this will likely increase when the mission is optimized for decreasing DOC. Furthermore, the simulations for airfoil optimization were all refined with 200 panels. It is important to note that from Section 9.1.3, XFLR5 simulations lose validity outside of the linear regime and therefore, if the optimization procedure is to be used in future work, it should be properly validated with experimental data.

First, Figure 9.12 shows the analysis of the airfoil with a change in the maximum thickness position. First of all, note that that there is a jump in characteristics between the original NACA 633-418 (in white) and the modified versions of the airfoil. This is due to the nature of the shape modification in XFLR5, for which a change in the maximum thickness position results also in a (small) change in camber, as seen in Figure 9.11, where the geometrical properties of each airfoil are shown so its correspondence with each graph in Figure 9.12 can be found.

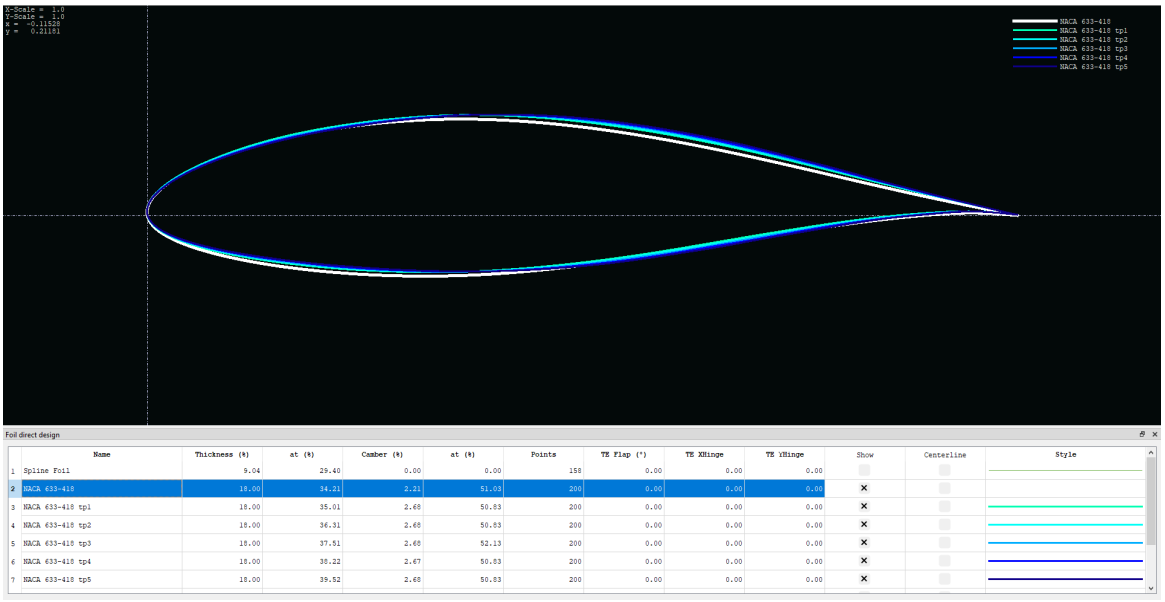

	Name	Thickness (%)	at (%)	Camber (%)	at (%)	Points	TE Flap (°)	TE XHinge	TE YHinge	Show	Centerline	Style
1	Spline Foil	9.04	29.40	0.00	0.00	158	0.00	0.00	0.00			
2	NACA 633-418	18.00	34.21	2.21	51.03	200	0.00	0.00	0.00	×		
3	NACA 633-418 tp1	18.00	35.01	2.68	50.83	200	0.00	0.00	0.00	×		
4	NACA 633-418 tp2	18.00	36.31	2.68	50.83	200	0.00	0.00	0.00	×		
5	NACA 633-418 tp3	18.00	37.51	2.68	52.13	200	0.00	0.00	0.00	×		
6	NACA 633-418 tp4	18.00	38.22	2.67	50.83	200	0.00	0.00	0.00	×		
7	NACA 633-418 tp5	18.00	39.52	2.68	50.83	200	0.00	0.00	0.00	×		

Figure 9.11: Shape of NACA 633-418 and modified airfoils for a change in maximum thickness position

From Figure 9.12b it can be seen that this is the main point of improvement of a shift in the maximum thickness position. For small angles of attack and small shifts in the position, the transition point is improved at the cost of reducing C_l max and increasing c_d. Furthermore, the fact that there is also a small change in camber also gives a higher $C_{l_{\alpha=0}}$. The fact that a more aft better transition point is obtained, is because moving the maximum thickness position aft leads to a more aft minimum pressure position, delaying transition. This can be seen in Figure 9.13, where it can be found that for the NACA 633-418 and a modified version with the maximum thickness position 2.10% more aft (both at $\alpha = 1\,°$), the modified airfoil has its minimum pressure more aft than the original. Note that for larger changes in the maximum thickness position, the transition point starts to be moved forward for a smaller α, while for smaller changes, the transition point starts to be more forward only at larger angles of attack.

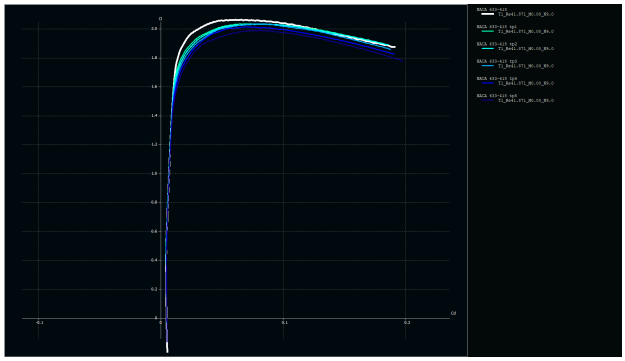

(a) Airfoil comparison $C_l - C_d$

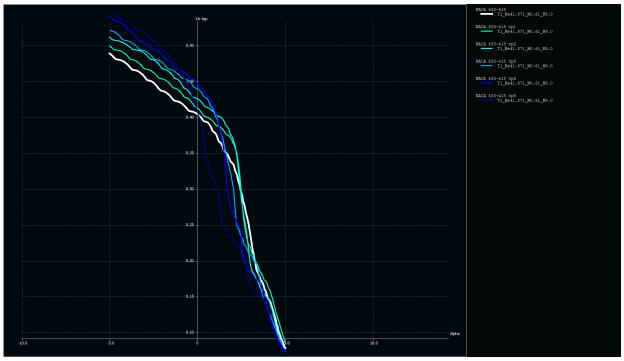

(b) Airfoil comparison $X_{tr}top - \alpha$

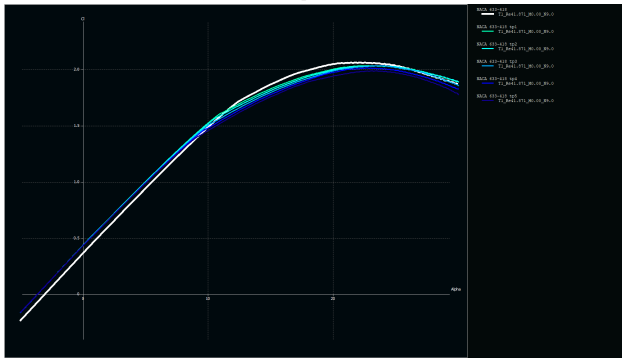

(c) Airfoil comparison $C_l - \alpha$

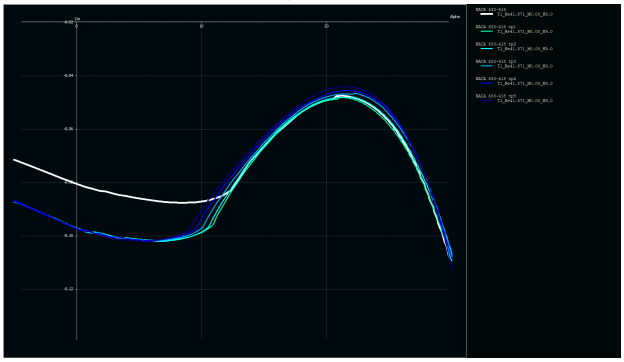

(d) Airfoil comparison $C_m - \alpha$

Figure 9.12: Analysis of NACA 633-418 and modified airfoils for a change in maximum thickness position

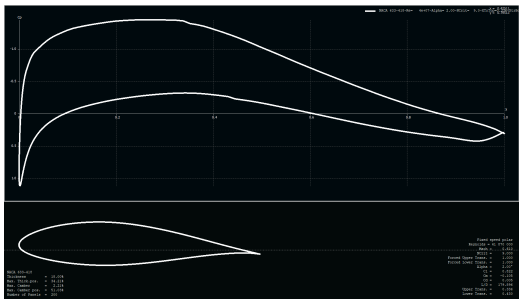

(a) NACA 633-418 pressure plot

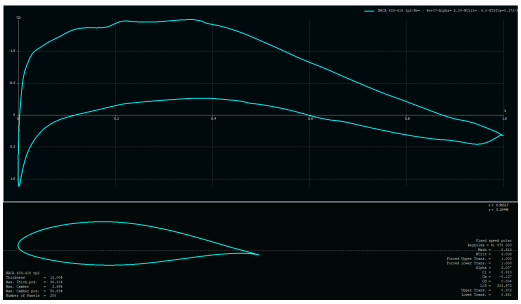

(b) Modified NACA 633-418 pressure plot (2.10% more aft maximum thickness position)

Figure 9.13: Pressure plot comparison of the NACA 633-418 and its modification in maximum thickness position

Onto the sensitivity due to changes in camber, the geometries are shown in Figure 9.14, and the results from the analysis in Figure 9.16. A change in camber is more promising, as it results in higher C_l max, better transition, and a wider drag bucket, which can be beneficial since this corresponds to a greater proportion of the boundary layer being laminar. The overall increase in C_l is the main reason for choosing a more cambered airfoil, but it also leads to a more negative C_m. In terms of transition, increasing camber gives a better transition performance, as it leads to a more aft position of the minimum pressure point (Figure 9.15). The more gradual change in pressure helps to maintain laminar flow by delaying the minimum pressure point. Note that from Figure 9.15 it can also be seen that the modified airfoil experiences a steeper pressure recovery, which can cause a larger separation and therefore more pressure drag and a worse stall behaviour.

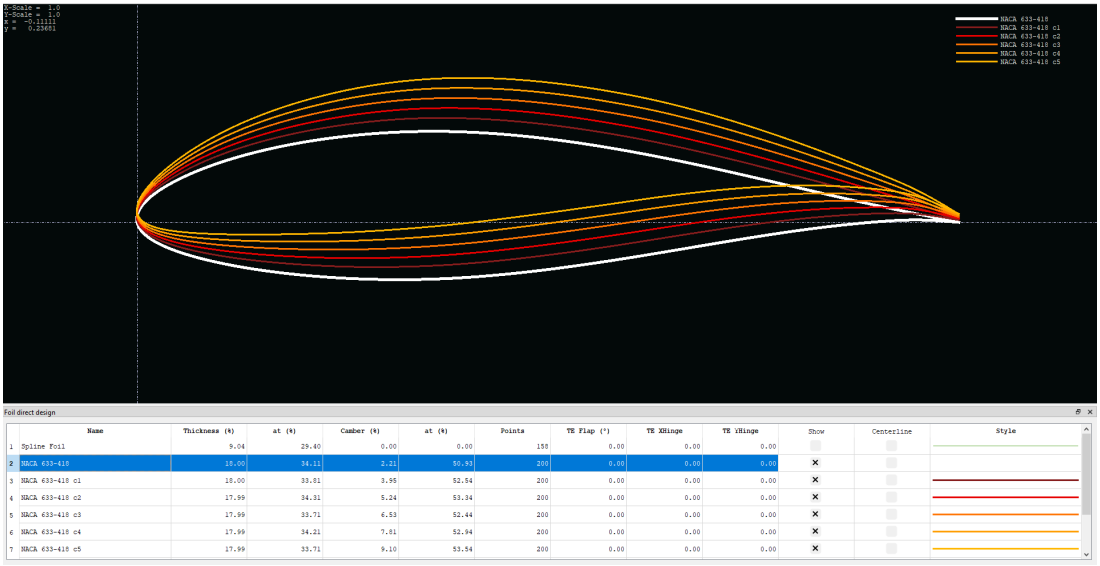

	Name	Thickness (%)	at (%)	Camber (%)	at (%)	Points	TE Flap (°)	TE XHinge	TE YHinge	Show	Centerline	Style
1	Spline Foil	9.04	29.40	0.00	0.00	158	0.00	0.00	0.00			
2	NACA 633-418	18.00	34.11	2.21	50.93	200	0.00	0.00	0.00	✕		
3	NACA 633-418 c1	18.00	33.81	3.95	52.54	200	0.00	0.00	0.00	✕		
4	NACA 633-418 c2	17.99	34.31	5.24	53.34	200	0.00	0.00	0.00	✕		
5	NACA 633-418 c3	17.99	33.71	6.53	52.44	200	0.00	0.00	0.00	✕		
6	NACA 633-418 c4	17.99	34.21	7.81	52.94	200	0.00	0.00	0.00	✕		
7	NACA 633-418 c5	17.99	33.71	9.10	53.54	200	0.00	0.00	0.00	✕		

Figure 9.14: Shape of NACA 633-418 and modified airfoils for a change in maximum thickness position

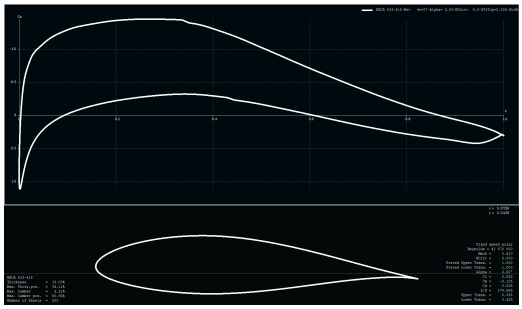

(a) NACA 633-418 pressure plot

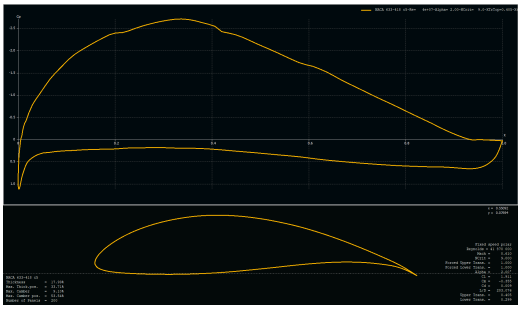

(b) Modified NACA 633-418 pressure plot (2.61% more camber)

Figure 9.15: Pressure plot comparison of the NACA 633-418 and its modification in camber

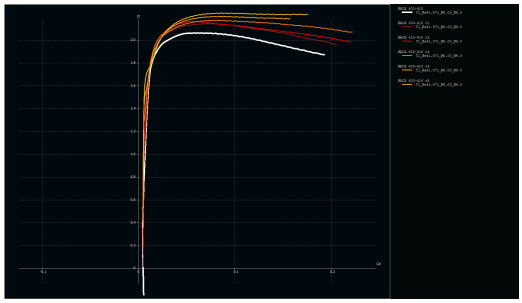

(a) Airfoil comparison $C_l - C_d$

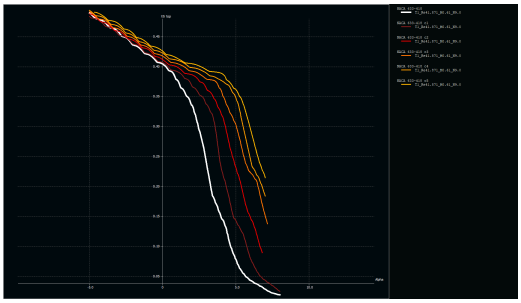

(b) Airfoil comparison $X_{tr}top - \alpha$

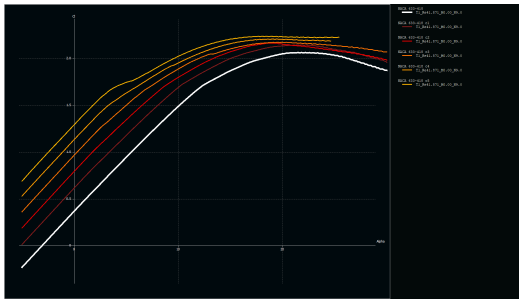

(c) Airfoil comparison $C_l - \alpha$

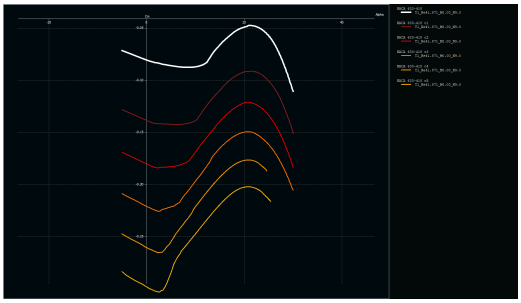

(d) Airfoil comparison $C_m - \alpha$

Figure 9.16: Analysis of NACA 633-418 and modified airfoils for a change in camber

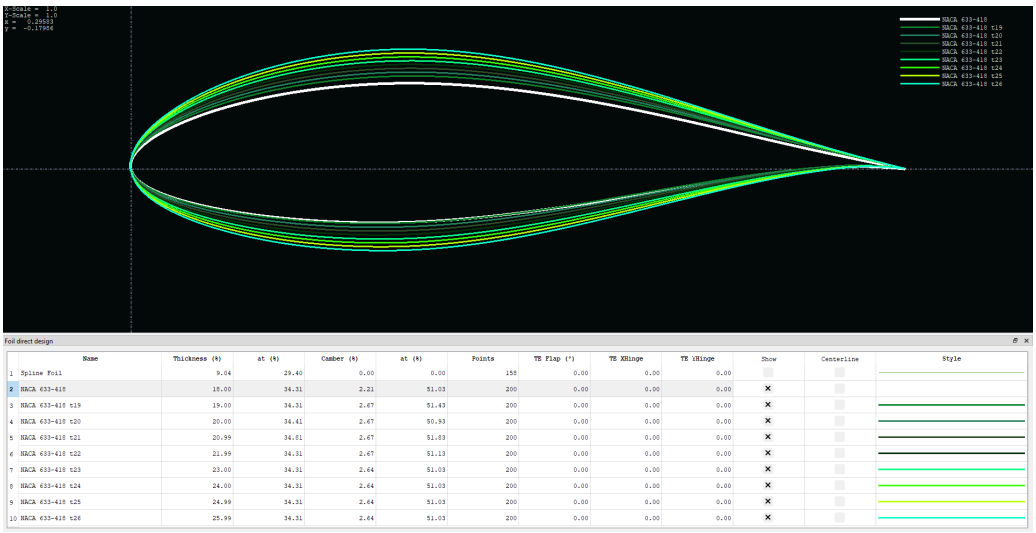

	Name	Thickness (%)	at (%)	Camber (%)	at (%)	Points	TE Flap (°)	TE XHinge	TE YHinge	Show	Centerline	Style
1	Spline Foil	9.04	29.40	0.00	0.00	158	0.00	0.00	0.00			
2	NACA 633-418	18.00	34.31	2.21	51.03	200	0.00	0.00	0.00	✕		
3	NACA 633-418 t19	19.00	34.31	2.67	51.43	200	0.00	0.00	0.00	✕		
4	NACA 633-418 t20	20.00	34.41	2.67	50.93	200	0.00	0.00	0.00	✕		
5	NACA 633-418 t21	20.99	34.81	2.67	51.83	200	0.00	0.00	0.00	✕		
6	NACA 633-418 t22	21.99	34.31	2.67	51.13	200	0.00	0.00	0.00	✕		
7	NACA 633-418 t23	23.00	34.31	2.64	51.03	200	0.00	0.00	0.00	✕		
8	NACA 633-418 t24	24.00	34.31	2.64	51.03	200	0.00	0.00	0.00	✕		
9	NACA 633-418 t25	24.99	34.31	2.64	51.03	200	0.00	0.00	0.00	✕		
10	NACA 633-418 t26	25.99	34.31	2.64	51.03	200	0.00	0.00	0.00	✕		

Figure 9.17: Shape of NACA 633-418 and modified airfoils for a change in thickness to chord ratio

The final parameter that was analyzed in order to optimize the airfoil is the thickness to chord ratio of the airfoil. The geometrical parameters from the studied airfoils are shown in Figure 9.17. Again note that XFLR5 introduces a small increase in camber when changing the thickness, and that is why in Figure 9.18 there is a jump in results between the original airfoil and the modified ones.

Figure 9.18 shows the results from the simulation of airfoils with a change in thickness. The main advantage of the modified airfoils is a small increase in C_l, potentially due to the camber increase introduced by XFLR5. However, there is a decrease in the maximum C_l and an increase in drag in the cruise flight region, as well as a decrease in C_m. The behaviour of the transition point is very dependant on the angle of attack, ranging from worse to similar transition characteristics for low angles of attack, but better transition at high angles of attack. Looking at Figure 9.19 this trend is explained. The NACA 633-418 is plotted together with a modified version of it that has a 26% thickness to chord ratio. Comparing Figure 9.19a and Figure 9.19c it can be seen that the minimum pressure point is further aft for the NACA 633-418, leading to it having better transition characteristics as seen in Figure 9.18b. However, this is reversed for higher angles of attack, for which the thicker airfoil provides a smoother pressure gradient, and therefore reaching its minimum pressure point later than the NACA 633-418, and delaying transition. As the transition improvement happens only at higher angles of attack, increasing thickness is deemed not a promising improvement for the current project. Moreover, the pressure recovery is steeper for the airfoil with modified thickness, leading to higher pressure drag. Furthermore, thicker airfoils would increase the wetted surface area, increasing skin friction, and would affect the structure and stability characteristics.

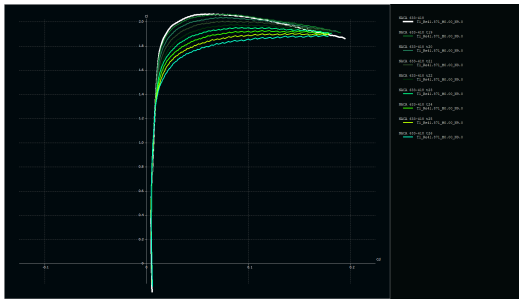

(a) Airfoil comparison $C_l - C_d$

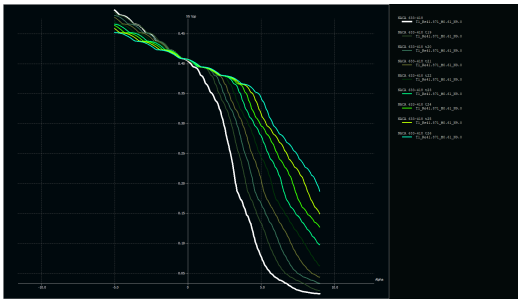

(b) Airfoil comparison $X_{tr}top - \alpha$

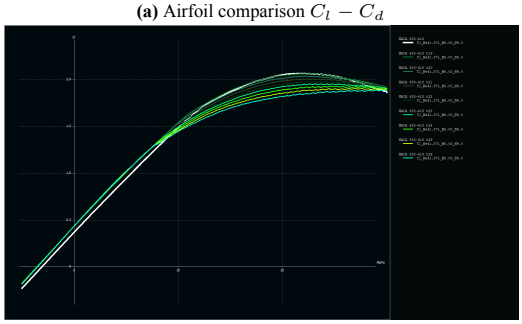

(c) Airfoil comparison $C_l - \alpha$

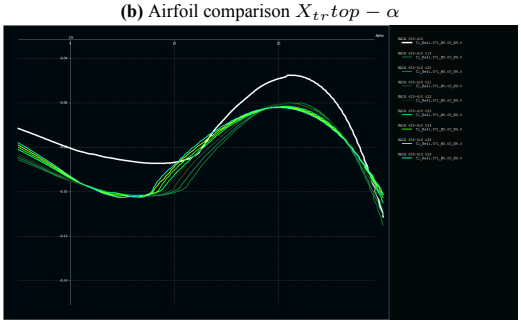

(d) Airfoil comparison $C_m - \alpha$

Figure 9.18: Analysis of NACA 633-418 and modified airfoils for a change in thickness to chord ratio

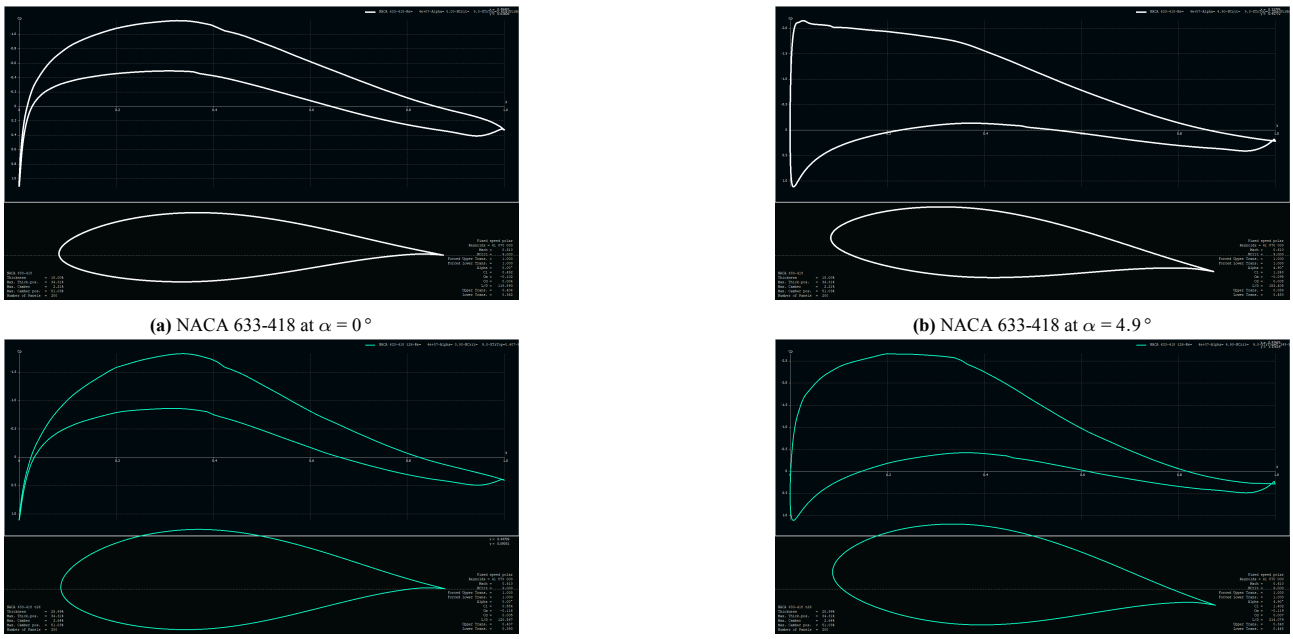

(a) NACA 633-418 at $\alpha = 0°$

(b) NACA 633-418 at $\alpha = 4.9°$

(c) Modified NACA 633-418 at $\alpha = 0°$

(d) Modified NACA 633-418 at $\alpha = 4.9°$

Figure 9.19: Pressure plots of NACA 633-418 and modified airfoils for a change in thickness to chord ratio

In conclusion, increasing camber shows the highest potential for an airfoil optimization, increasing the overall C_l and delaying transition. Shifting the maximum thickness position more aft also shows potential. Increasing thickness does not give improvements until higher angles of attack are reached, which is not the case for the current α at cruise. Therefore adjusting camber and the position of maximum thickness show the greatest potential for a more optimized airfoil, and should be tested experimentally in order to validate these results, and be able to use these airfoils on actual designs.

The next step is to quantify how much ATR reduction can be obtained from airfoil optimization. In Figure 9.20 the $C_l - Cd$ graphs are shown around design and cruise C_l. The modified airfoils are colored, while the white graph belongs to the baseline NACA 633-418. Even though optimizing the drag of the airfoil shows potential, as the airfoil drag at the design C_l is reduced by around 3%, as shown in Figure 9.20a, for this design the airfoil optimization does not give any gains. This is because, after finalising the design, the cruise C_l found (around 0.1) is lower than the design C_l (0.46), and therefore as shown in Figure 9.20, the drag of the NACA 633-418 gives lower drag. This is explained as depending on the angle of attack the pressure distribution varies, and while at some angles of attack the minimum pressure position on the optimized airfoil is found more aft and therefore have a later transition and less drag, for others it may be the other way around. However, the fact that for the current design problem no performance gains are found, does not take away the fact that there is a drag reduction around the design C_l, and therefore this can be a point for study in future research and design work.

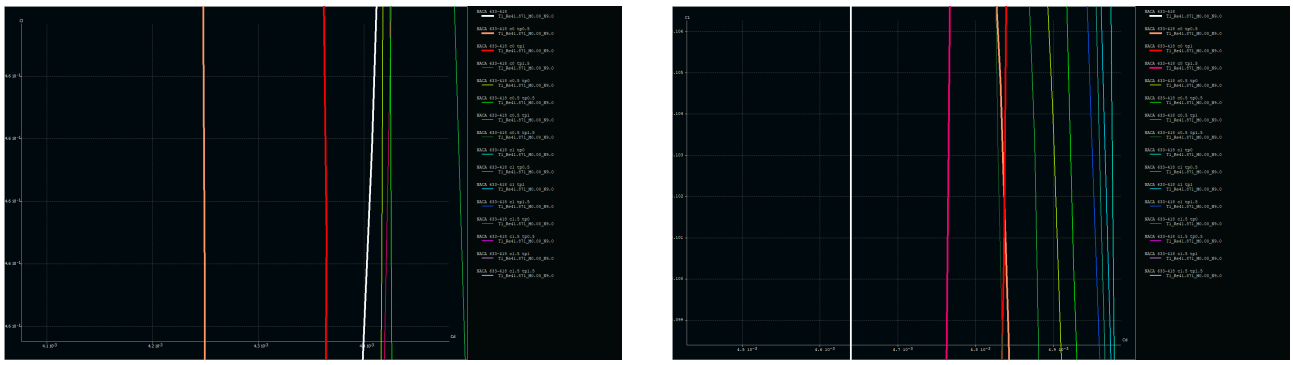

(a) $C_l - Cd$ for airfoil optimization around design C_l

(b) $C_l - Cd$ for airfoil optimization around cruise C_l

Figure 9.20: Drag comparison of the NACA 633-418 and its modification in camber

The ATR performance of the aircraft was computed for both the baseline NACA 633-418 and a modified version with the maximum thickness position 1.5% more aft, which is the closest to the baseline airfoil in Figure 9.20b. An ATR increase of 1.13% is found for the modified version of the airfoil, as expected from the drag increase. Even though this does not

show any ATR gains, it is still useful, as in the end it is a measure of the sensibility of the ATR to changes on the airfoil. It can be seen that the ATR and the airfoil geometry have a close relationship, in which a change on the airfoil that leads to increased drag, directly affects the environmental impact of the aircraft. In Section 16.3 a further analysis the ATR performance of the aircraft is found.

Table 9.6: Drag and ATR comparison for airfoil optimization

Airfoil	CD	Drag (N)	ATR (μK)
NACA 633-418	0.01434	89649.36	4.5762E-9
Modified NACA 633-418	0.01450	90686.41	4.6281E-9

9.5.2. Miniature Vortex Generators

Vortex generators are aerodynamic devices placed on surfaces within a flow, which generate vorticity within the boundary layer, mixing the low energy boundary layer flow with high energy freestream flow. By increasing the energy within the boundary layer, it has sufficient energy to travel through regions of adverse pressure gradients, delaying flow separation. Miniature vortex generators (MVGs) differ from the classical notion of vortex generators in that they are much smaller in absolute height, typically reaching a maximum height of half the boundary layer thickness δ^*. Another major defining difference is that vortex generators are used to delay separation whilst MVGs have been shown to delay transition. MVGs work by creating a streaky boundary layer with alternating low and high speed streaks in the spanwise direction [32]. By carefully choosing the spacing and size of elements, Tollmien-Schlichting waves can be attenuated, increasing boundary layer stability and delaying transition. Experiments conducted by Fransson et al. showed an increase in the proportion of laminar-to-turbulent flow in the near flow-field aft of the MVG array relative to a flat plate not using MVGs [32]. In the case of no MVGs a clear early transitional process was also shown in the energy spectrum, where harmonics rapidly appeared at multiples of the fundamental frequency until eventually developing into a broad energy spectrum once the flow had completely transitioned. This differed from the case with MVGs where the energy spectrum displayed only a single low-frequency mode at the first harmonic which decays until vanishing downstream. However, another study showed that further downstream, there is an exponential recovery of the modulated laminar base flow, generating instability and triggering transition. This same study looked into the performance benefits of installing a second array of MVGs further downstream of the first array, and found a prolonged streamwise extent of laminar flow, greater than just a single array. MVGs therefore show a great promise as a means of passive flow control since although the mechanism itself used by the MVGs will generate drag, the drag penalty is deemed reasonable when compared to the reduction in skin friction drag by having a more predominant laminar boundary layer. Current experiments have been limited to Re up to 450000, and therefore there exists questions as to whether the performance benefits seen in literature can be scaled to the much higher Reynolds numbers the aircraft wing will experience in cruise. Therefore, it would be beneficial to conduct wind-tunnel experiments on flat-plates using no MVGs, a single and a double MVG array, at Re in the order of 40 million to verify the applicability of them for future design iterations of the aircraft.

10. Propulsion System Design

This chapter reports on the implementation of a whole-engine model for an unducted propfan configuration, based on the Variable Bypass Ratio Model of of E. Schwartz Dallara [27]. Said model consists of a classical turbofan core cycle analysis based on energy relationships and an open-rotor performance estimation method based on momentum, blade element and vortex theory. This model is capable of estimating the TSFC, the available installed thrust T_{inst} and other engine performance metrics under any flight condition (Ma, h) and throttle setting, as well as sizing the engine for its critical design operating condition. Before addressing the model itself, a brief note on sustainable aviation fuels, based on the extensive literature study conducted in Section 12.3 of the foregoing Midterm Report [39], shall be provided. Hereafter, the propfan engine model inputs and workings shall be presented, following which the engine is sized for its design operating condition (to be established in Section 16.5) and finally "tested" under off-design conditions. Next, a turbofan model employing the same engine core model, however, with different input parameters and a separate bypass flow analysis approach is developed to model the A330-200's CF6-80E1A3 engines. This chapter is concluded with an extensive section on model verification and a sensitivity study, thus constituting a solid base for the ATR and DOC analysis performed in Chapter 16.

10.1. Sustainable Aviation Fuels

Synthetic kerosenes provide a short-term, easy-to-implement solution to reduce the environmental impact of aviation. Composition-wise, these fuels are almost free of aromatics, sulfur and bound nitrogen. Whereas CO_2 emissions are basically indifferent with respect to conventional Jet-A-1 fuel, particulate emissions such as soot are reduced by up to a factor 20, also reducing the likelihood of contrail formation and resultant cloud nucleation. Moreover, their heating value is typically slightly higher compared to fossil-based kerosene (44.3 MJ kg^{-1} for FTK compared to 43 MJ kg^{-1} for coventional Jet-A-1), enabling a higher thrust per unit mass of emitted climate agents. Based on a trade-off involving the 5 currently

ASTM-certified synthetic aviation fuels (FTK/BTL, SIP, HEFA, ATJ-SPK and ATJ-SKA) conducted towards the Midterm Report [39], Fischer Tropsch kerosene was chosen for use on the envisioned low-ATR aircraft. This was motivated by the large commercial scale at which it is being produced (examples of involved companies include Shell, Sasol and Solena), unlike its competitors. Current regulations limit its use to 50% blends with Jet-A-1, however, in the near future it is imaginable to blend it with 8% aromatics in order to meet the ASTM D7566 standard. The most optimistic studies anticipate a price equivalency with Jet-A-1 as early as 2030, and a market share of 73.4% by 2050. Considering that fuel accounts for up to 30% of airline's DOC, this factor is expected to be a cornerstone for both the environmental and cost effectiveness of the low-ATR airliner proposed in this report.

10.2. Propfan Engine Model Inputs

Table 10.1-Table 10.3 contain the input parameters to the propfan engine model devised in this chapter. Whereas most parameters are invariant inputs, some are first guessed (such as the rotor diameter D_{fan} and specific fan power $(\frac{P}{\dot{m}})_{fan}$) and subsequently iterated until the model has converged to a coherent engine design (see HSection 10.3.4). The meaning of each parameter can be looked up in the nomenclature section at the beginning of this report.

Table 10.1: Technology par.

Parameter	Value	Parameter	Value
$\pi_{ch}\pi_f$ (OPR)	30	e_{tl}	0.915
π_{df}	1	e_{th}	0.905
π_{db}	1	$\eta_{gearbox}$	0.98
π_{dc}	0.995	η_b	0.995
π_b	1	η_{ml}	0.985
π_{nf}	1	η_{mh}	0.997
π_{nc}	0.995	η_{inst}	0.96
e_f	0.9	β	0
e_{ch}	0.91	δ_1	0.03
η_{nozzle}	0.98	δ_2	0.02

Table 10.2: Physical par.

Parameter	Value
h_{fuel} $(\frac{\text{J}}{\text{kg K}})$	$44.3 \cdot 10^6$
R_c $(\frac{\text{J}}{\text{K mol}})$	287
R_t $(\frac{\text{J}}{\text{K mol}})$	287
C_{pc} $(\frac{\text{J}}{\text{kg}})$	1000
C_{pt} $(\frac{\text{J}}{\text{kg}})$	1150
γ_c	1.4
γ_t	1.33

Table 10.3: Design par.

Parameter	Value	Parameter	Value
α	30	$\Omega_{1_{max}}$	240
pi_f	1.16	$\Omega_{2_{max}}$	240
pi_{ch}	25.97	ϵ_1	0.023
T_{T4} (K)	1700	ϵ_2	0.025
B	10	η_1	0.9
D_{fan} (m)	4	η_2	0.9
ξ	0.25	$(\frac{P}{\dot{m}})_{fan}$ $(\frac{Ws}{kg})$	1000

Overall, the engine parameters displayed in the above tables are based on 2010 technology levels [27]. Note that the fuel heating value of 44.3 MJ kg^{-1} corresponds to the Fischer Tropsch synthetic kerosene introduced in Section 10.1. For the purpose of this model, the heating value is the only parameter by which the effect of the synthetic fuel compared to conventional Jet-A-1 can be quantified. At this point, the insights gained from Chapter 16 shall be anticipated to give context to the most important engine parameters, namely the BPR, TET (T_{T4}) and OPR ($\pi_{ch}\pi_f$). According to P. Proesmans [78], a high OPR and TET typically reduces the TSFC, however, it enhances the production of thermal NO_X. A large BPR enables further TSFC reductions, although it requires a high OPR and TET to drive the large fan and typically promotes contrail formation. Hence, a subtle balance between minimising fuel burn (and thus CO_2, H_2O, soot and SO_4 emission) and secondary forcing effects ought to be found. In this work, it is found that for the analysed propfan model an above-average TET of 1700 K, combined with a below-average OPR of 30 and a very large BPR of 30 results in the lowest ATR footprint. Ideally, one would strive to reduce the TET too, however, this high value is inalienable for driving the fan, whilst having the lowest impact on ATR of the aforementioned parameters. A coolant air mixer to be discussed as part of the following section prevents that the high-pressure turbine blades exceed their melting temperature.

10.3. Propfan Engine Model Workings

This section contains a detailed description of the model employed for assessing the open rotor engines' performance. A traditional turbofan cycle analysis quite literally lies at the heart of this model (i.e., to model the core), whereas the unducted bypass flow analysis is conducted via by a dedicated counter-rotating, open-rotor model. The core and bypass flow models are treated in Section 10.3.1 and Section 10.3.3, respectively, to be then evaluated under design (Section 10.3.4) and off-design (Section 10.3.5) conditions.

Figure 10.1 provides a comprehensive overview of the engine architecture employed in this chapter, which, in combination with the input parameters listed in Table 10.1-Table 10.3, may be considered representative for today's state-of-the-art. It should be noted that the station numbering is in accordance with the ARP 755A standard [1]. Note that the below cycle diagram is applicable to the present propfan architecture and the turbofan model devised in Section 10.4 alike. However, in case of the low-ATR aircraft (i.e., concerning the propfan engines) no bleed air is extracted ($\beta = 0$), whereas the CF6-80E1A3 engine extracts 1.5% of the total compressed airflow. Conversely, the propfan engines employ a gearbox with an efficiency of 0.98 to limit the rotor disk loading and blade tip speed, whichever is more limiting, whereas the CF6-80E1A3 does not have such a gearbox ($\eta_{gearbox} = 1$).

[1] `https://onlinelibrary.wiley.com/doi/pdf/10.1002/9780470774533.app1#:~:text=Reference%201%2C%20ARP%20755A%2C%20is,when%20data%20passed%20between%20companies` (last accessed on 21/06/2021)

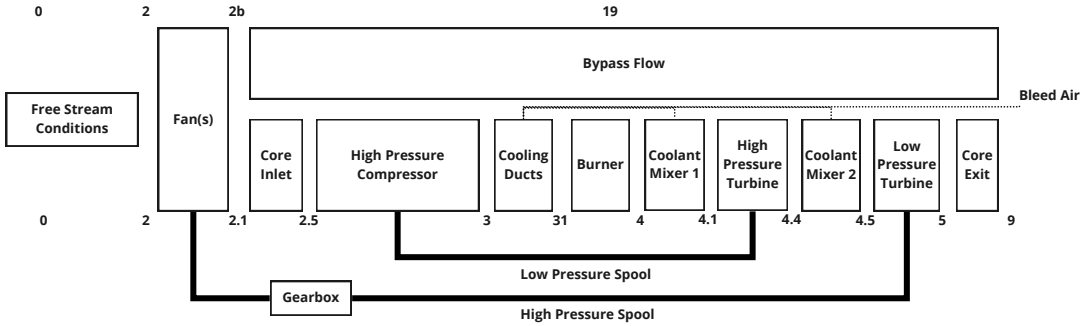

Figure 10.1: Engine architecture used for propfan design

10.3.1. Engine Core Flow Analysis

Before delving into the precise workings of this turbofan core model, it is deemed beneficial to introduce the reader to the assumptions lying at its heart.

Assumptions

- The flow is one-dimensional and steady at each axial station.
- The flow behaves like a perfect gas with constant but different molecular weights and specific heats up- and downstream of the burner.
- Diffusers and nozzles are adiabatic.
- Component polytropic efficiencies are constant throughout the operational envelope.
- Installation losses are modeled as thrust penalties.

Analysis

In this section, the engine core is analysed by means of a cycle analysis. The engine architecture is modelled with respect to the diagram shown in Figure 10.1. The basis of this cycle analysis comprises of calculating the total pressures and temperatures at each station.

To calculate the stagnation temperature and pressure upstream of the fan, at station 0, based on the ambient temperature T_0, ambient pressure P_0 and free stream mach number M_0, Equation 10.2 and Equation 10.1 are used [64], where τ_r and π_r represent the temperature and pressure ratios at station 0, respectively, and γ_c is the ratio of specific heats of air, taken to be 1.4 [64]. The total temperature T_{T0} and total pressure P_{T0} can then be calculated from the ambient conditions.

$$\tau_r = \frac{T_{T0}}{T_0} = 1 + \frac{\gamma_c - 1}{2} {M_0}^2 \qquad (10.1) \qquad\qquad \pi_r = \frac{P_{T0}}{P_0} = \tau_r^{\frac{\gamma_c}{\gamma_c - 1}} \qquad (10.2)$$

The first stage which the air must pass through are the propfan rotors located before the engine core. The fan pressure ratio π_f denotes the increase in total pressure over the fans. In Aircraft Design for Reduced Climate Impact by E. Schwartz Dallara [27], Figure A.3 relates the fan polytropic efficiency e_f to the fan pressure ratio π_f. In [27], a fan polytropic efficiency of 0.9 is assumed, which corresponds to a fan pressure ratio of 1.155. The pressure and temperature, before and after the fan are then calculated using Equation 10.3 and Equation 10.4 respectively. Where T_{T2} and P_{T2} are the total temperature and pressure before the fan, which due to the fan being surrounded by freestream air, equal T_{T0} and P_{T0}.

$$\pi_f = \frac{P_{T21}}{P_{T2}} \qquad (10.3) \qquad\qquad \tau_f = \frac{T_{T21}}{T_{T2}} = \pi_f^{\frac{\gamma_c - 1}{\gamma_c e_f}} \qquad (10.4)$$

After the air has passed through the fans, it will either bypass the engine core or move through it. The ratio of these two mass flows is dictated by the bypass ratio α. The mass flow of the bypass flow $\dot{m}_{2b}$ is calculated using Equation 10.6, and the mass flow of the core $\dot{m}_{2c}$ is calculated using Equation 10.7. In these equations, $\dot{m}_0$ is the total mass flow going through the engine. For reasons specified in Section 10.2, a bypass ratio of 30 was selected. This engine cycle calculation is part of a rubber engine sizing process, therefore the initial $\dot{m}_0$ is not important, as the engines will be scaled up or down depending on the required thrust. For an initially assumed rotor diameter D_{rotor}, the overall mass flow is computed via Equation 10.5.

$$\dot{m}_0 = \rho \cdot \frac{\pi {D_{rotor}}^2}{4} \cdot V_0 \qquad (10.5) \qquad\qquad \dot{m}_{2b} = \frac{\alpha}{\alpha + 1} \dot{m}_0 \qquad (10.6) \qquad\qquad \dot{m}_{2c} = \frac{1}{\alpha + 1} \dot{m}_0 \qquad (10.7)$$

The air going into the engine core will pass through a diffuser, which is assumed to be adiabatic [27]. This means the air will adiabatically expand, decreasing the total pressure and increasing the temperature, which can be seen in Equation 10.8 and Equation 10.9 [64]. The pressure drop or increase is quantified by the core diffuser pressure ratio π_{dc}, which is taken to be 0.995 [27].

$$\pi_{dc} = \frac{P_{T25}}{P_{T21}} \quad (10.8) \qquad \tau_{dc} = \frac{T_{T25}}{T_{T21}} = (\pi_{dc})^{\frac{1-\gamma_c}{\gamma_c}} \quad (10.9)$$

After the core inlet, the core mass flow passes through the high pressure compressor. The key characteristic of this stage is the compression ratio. Increasing the compression ratio will decrease the fuel consumption and generally improve the efficiency of the engine, however, it also has its downsides (see Section 10.2). The compressor pressure ratio multiplied by the fan pressure ratio (also referred to as the OPR) was taken equal to 30. From this value, the compressor pressure ratio π_{ch} was calculated. The total pressure and temperature at station 3 can be calculated using Equation 10.10 and Equation 10.11, where e_{ch} is the polytropic efficiency of the compressor taken to be 0.91 [27]. The power required by the high pressure compressor is needed to design the high pressure turbine, which it is driven by via the high-pressure spool seen in Figure 10.1. The required power can be calculated using Equation 10.12 [64], where $\dot{m}_3$ is the mass flow through the compressor, equal to $\dot{m}_{2c}$, and C_{pc} is the specific heat of the gas, taken to be $1000\,\mathrm{J\,kg^{-1}\,K^{-1}}$ before the fuel is added.

$$\pi_{ch} = \frac{P_{T3}}{P_{T2.5}} \quad (10.10) \qquad \tau_{ch} = \frac{T_{T3}}{T_{T2.5}} = \pi_{ch}^{\frac{\gamma_c - 1}{\gamma_c e_{ch}}} \quad (10.11) \qquad P_{HPC} = \dot{m}_3 \cdot C_{pc} \cdot (T_{T3} - T_{T25}) \quad (10.12)$$

After the compressor the cooling ducts remove air from the flow, to be used later to cool the high pressure turbine, low pressure turbine (no bleed air is extracted for this design). Therefore, at the inlet of the burner (stage 3.1) the mass flow is reduced because air has been removed for cooling. The bleed air fraction β, and cooling fractions δ_1 and δ_2, are taken to be 0, 0.03 and 0.02, respectively [27]. It is assumed that in going from stage 3 to 3.1, no pressure or temperature losses occur.

$$\dot{m}_{3.1} = (1 - \beta - \delta_1 - \delta_2)\,\dot{m}_3 \quad (10.13)$$

Over the burner the temperature will evidently increase, a design parameter which will dictate the amount of energy which can be added to the flow is the turbine inlet temperature. If this temperature increases by too much, the turbine blades will melt. The allowed turbine inlet temperature has steadily grown over the years, and it is expected that current turbine inlet temperatures T_{T4} can reach up to 1700 K. Via Equation 10.14, the amount of fuel needed per second is calculated, where C_{pt} is the specific heat of the gas with the fuel mixed in and h_{fuel} is the FT synthetic kerosene's heating value, equal to $44.3\,\mathrm{MJ\,kg^{-1}}$[64]. Equation 10.15 calculates the fuel to air ratio and Equation 10.16 calculates the new mass flow, corrected for the added fuel. Finally, Equation 10.17 allows to calculate the pressure after the burner, assuming a value for π_b of 0.995 [27].

$$\dot{m_{fuel}} = \frac{\dot{m_{3.1}} \cdot C_{pt} \cdot (T_{T4} - T_{T3.1})}{h_{fuel} \cdot \eta_b} \quad (10.14) \qquad f = \frac{\dot{m_{fuel}}}{\dot{m_{3.1}}} \quad (10.15)$$

$$\dot{m}_4 = (1 + f)\dot{m}_{3.1} \quad (10.16) \qquad \pi_b = \frac{P_{T4}}{P_{T3.1}} \quad (10.17)$$

In the coolant mixer cool air from the compressor is mixed with hot air from the combustion chamber such that the turbine inlet temperature remains within the operating limits. The actual pressure and temperature change is not modelled in this cycle, and thus remains constant. The mass flow is corrected by adding the first coolant air back into the total mass flow.

The high-pressure turbine directly powers the high-pressure compressor through the high-pressure spool. For this reason, the power from the high-pressure turbine must be equal to the power required by the high-pressure compressor, accounting for the spool efficiency η_{mh}. The change in temperature over the turbine required to achieve this power is calculated in Equation 10.18 and the corresponding pressure change over the turbine via Equation 10.19. In Equation 10.18, η_{mech} represents the mechanical efficiency of the spool taken to be 0.99 [64], γ_t is the ratio of specific heats for the gas with fuel mixed into it, taken equal to 1.33 [64] and in Equation 10.19, e_{th} is the polytropic efficiency of the high-pressure turbine taken to be 0.905 [27].

$$\tau_{th} = \frac{T_{T4.4}}{T_{T4.1}} = \frac{P_{HPC}}{\eta_{mech}\dot{m_{4.1}}c_{pt}} \quad (10.18) \qquad \pi_{th} = \frac{P_{T4.4}}{P_{T4.1}} = \tau_{th}^{\frac{\gamma_t}{(\gamma_t - 1)e_{th}}} \quad (10.19)$$

After the high-pressure turbine there is another coolant mixer which operates identically to mixer 1. The low-pressure turbine employs a similar strategy as the high-pressure turbine, apart from the fact that the low-pressure turbine will need to produce enough power to drive the propfan rotors at the from via the low-pressure spool passing through a gearbox. However, the fan power required is only calculated in Section 10.3.2, therefore a starting value is taken, and iterated until convergence is achieved. The equation for calculating the temperature ratio and pressure ratio over the turbine can be seen in Equation 10.20 and Equation 10.21. In these equations, η_{gearbox} is the gearbox efficiency, assumed to be equal to 0.98 [64].

$$\tau_{tl} = \frac{T_{T5}}{T_{T4.5}} = \frac{P_{fan}}{\dot{m_{4.5}}c_{pt}\eta_{mech}\eta gearbox} \quad (10.20) \qquad \pi_{tl} = \frac{P_{T5}}{P_{T4.5}} = \tau_{tl}^{\frac{\gamma_t}{(\gamma_t - 1)e_{tl}}} \quad (10.21)$$

Finally, the core exit accelerates the air out of the nozzle, which is assumed to be adiabatic. This means that the temperature and pressure are again related by an adiabatic expansion or compression process. They can be calculated via Equation 10.22 and Equation 10.23.

$$\pi_{nc} = \frac{P_{T9}}{P_{T5}} \quad (10.22) \qquad \tau_{dc} = \frac{T_{T9}}{T_{T5}} = (\pi_{nc})^{\frac{1-\gamma_t}{\gamma_t}} \quad (10.23)$$

For this cycle computation, the nozzle is assumed to be a perfect De Laval nozzle or convergent-divergent duct. An important criterion is whether the nozzle is choked or not,indicating whether the flow is supersonic in the throat of the nozzle. To establish this, a critical pressure ratio is calculated for which the nozzle becomes choked. The critical pressure ratio is calculated in Equation 10.24, where η_{nozzle} is the efficiency of the nozzle, taken to be 0.98 [64].

$$\pi_{crit} = \left(1 - \frac{\gamma_t - 1}{\eta_{nozzle}}\right)^{\frac{-\gamma_t}{\gamma_t - 1}} \quad (10.24)$$

Option 1: If $\frac{P_{T5}}{P_0} >= \pi_{\text{crit}}$, the nozzle is choked. In this case, Equation 10.25 calculates the static temperature at the nozzle exit, Equation 10.26 the static temperature at the nozzle, Equation 10.27 the velocity at the nozzle exit and Equation 10.28 the effective area of the nozzle throat [96]. Finally, the thrust is calculated via Equation 10.29.

$$P_9 = \frac{P_{T5}}{\pi_{crit}} \quad (10.25) \quad T_9 = T_{T5} \cdot \frac{2}{\gamma_t + 1} \quad (10.26) \quad V_9 = \sqrt{\gamma_t R_t T_9} \quad (10.27) \quad A_9 = \dot{m}_9 \frac{R_t \cdot T_9}{P_9 \cdot V_9} \quad (10.28)$$

$$T_{core} = \dot{m}_9(V_9 - V_0) + A_9 \cdot (P_9 - P_0) \quad (10.29)$$

Option 2: If $\frac{P_{T5}}{P_0} < \pi_{\text{crit}}$, the nozzle is not choked. This condition requires different formulas. First of all, it is assumed that the pressure of the nozzle is equal to the ambient static pressure in Equation 10.30. Subsequently, the static temperature is calculated in Equation 10.31. The exit velocity of the nozzle is calculated in Equation 10.32. Finally, the thrust is calculated using Equation 10.33.

$$P_9 = P_0 \quad (10.30) \quad T_9 = T_{T5} \cdot (1 - \eta_{nozzle}(1 - \frac{P_0}{P_{T5}})^{\frac{\gamma_t - 1}{\gamma_t}}) \quad (10.31) \quad V_9 = \sqrt{2 c_{pt} \eta_{nozzle}(1 - \frac{P_0}{P_{T5}})^{\frac{\gamma_t - 1}{\gamma_t}}} \quad (10.32)$$

$$T_{core} = \dot{m}_9(V_9 - V_0) \quad (10.33)$$

10.3.2. Engine Bypass Flow Analysis

This section elaborates on the chosen open rotor, counter-rotating model based on classical momentum, blade element and vortex theory [27]. Said model accounts for losses associated with swirl, tip effects and viscous blade drag. A counter-rotating configuration is chosen to minimise swirl losses, which can be as high as 25% of the overall engine efficiency for single-rotor propfan engines [27], and because of the inherent cancellation of reaction torques, imposing lower torsional stiffness requirements on the wing box designed in Section 15.5. First and foremost, the assumptions on which this stand-alone method is based shall be presented.

Assumptions

- The principle of superposition may be applied to the induced velocities of counter-rotating rotors (Lock's assumption) [27].
  - The induced velocity fields of the two rotors may be considered independently and eventually added [27].
    - The tangential velocity induced behind either rotor equals twice the tangential velocity within the corresponding rotor disk [27].
    - No tangential velocity is induced ahead of either rotor [27].
  - The interference velocity field produced by either rotor affects the rotor itself as if the other rotor was not present [27].
  - The time average of the combined velocity field of the two rotors, which varies with time, may be employed for performance analysis [27].
- The density at each rotor disk is constant, but not necessarily equal to its free stream value [27].
- The synthesis of momentum, blade element and vortex theory, which is developed for low disk loadings, suffices for a preliminary performance estimation of highly loaded propfan rotors [27].
- The propeller efficiency η has a constant value along each blade [31].
- The propeller efficiency is constant under all flight conditions due to the employed propeller pitching mechanism.
- The front and rear rotor have the same number and type of blades.

Analysis

The dimensionless axial and tangential velocities (i.e., interference factors) induced by each rotor ($i : 1 \hat{=}$ front rotor, $2 \hat{=}$ rear rotor) in its own rotational plane at a distance r from the rotational axis are denoted as $a_i(r) = \frac{u_{a,i}}{V_0}$ and $a'_i(r) = \frac{u_{t,i}}{\Omega_1 r}$, respectively. Furthermore, each rotor induces an axial and tangential velocity on the other rotor, denoted as $a_j(i, r)$ and $a'_j(i, r)$, respectively, as can be inferred from Equation 10.34. Henceforth, the argument r shall be omitted for visual clarity, though keep in mind that all a's are a function of radial position.

$$i = 1 \begin{cases} a_i' = a_1' \\ a_j' = 0 \end{cases} \quad , \quad i = 2 \begin{cases} a_i' = a_2' \\ a_j' = -2a_1' \end{cases} \tag{10.34}$$

W.F. Durand derives explicit expressions for a_i and a_i' from general momentum theory, as shown in Equation 10.36 and Equation 10.37 [31]. In these equations, x is the dimensionless radial coordinate, which depends on the free stream velocity V_0 and the rotational velocity Ω_i of rotor i, and η is the propeller efficiency. As mentioned in the foregoing list of assumptions, the present open rotor design shall employ a variable pitch mechanism to ensure a high performance throughout the rather comparatively vast operational altitude and Mach number envelope for a propeller aircraft.

$$x = \frac{\Omega_i r}{V_0} \tag{10.35}$$

$$a = \frac{x^2\eta(1-\eta)}{1+x^2\eta^2} \tag{10.36}$$

$$a' = \frac{1-\eta}{1+x^2\eta^2} \tag{10.37}$$

The Prandtl loss function κ_i of rotor i defined in Equation 10.38 quantifies the momentum loss due to radial swirl near the blade tips, which is a function of the flow angle in this radial position $\phi_{i,r=R}$ (Equation 10.39).

$$\kappa_i = \frac{2}{\pi}\cos^{-1}\left(\exp\left[\frac{-B\left(1-\frac{r}{R}\right)}{2\sin\phi_{i,r=R}}\right]\right) \tag{10.38}$$

$$\tan\phi_i = \frac{V_0(1+a)}{\Omega r\,(1-a')} \tag{10.39}$$

The circulation Γ_i at rotor i was derived from [27] and is expressed by Equation 10.40.

$$\Gamma_i = \frac{4\pi {V_0}^2 a_i(1+a_1+a_2)}{B\Omega_1(\frac{\Omega_i}{\Omega_1} - a_i' - a_j')} \tag{10.40}$$

The net resultant force of the counter-rotating propeller configuration is resolved into an axial thrust contribution and a tangential torque contribution. The thrust per unit radius F' and torque per unit radius Q' produced by rotor i are expressed by Equation 10.41 and Equation 10.42, respectively. The quantity ϵ_i represents the rotor drag-to-lift-ratio.

$$F_i' = 4\pi r\rho V_0^2 a_i\,(1+a_1+a_2)\,\kappa_i - B\epsilon_i\rho\Gamma_i V_0\,(1+a_1+a_2) \tag{10.41}$$

$$Q_i' = B\rho\Gamma_i V_0 r\,(1+a_1+a_2) + B\epsilon_i\rho\Gamma_i\Omega_1 r^2\left(\frac{\Omega_i}{\Omega_1} - a_i' - a_j'\right) \tag{10.42}$$

Finally, the specific thrust and specific power of the entire open rotor configuration is obtained by integrating the foregoing expressions in radial direction, namely from the radius of the engine core nacelle ξR (ξ is the so-called hub-to-tip-ratio) to the blade radius R.

$$\frac{F_{dual}}{\dot{m}_{dual}} = \frac{\int_{\xi R}^{R}\left(\frac{F_1'+F_2'}{\rho}\right)dr}{\int_{\xi R}^{R} 2\pi r V_0\,(1+a_1+a_2)\,dr} \tag{10.43}$$

$$\frac{P_{dual}}{\dot{m}_{dual}} = \frac{\int_{\xi R}^{R}\left(\frac{\Omega_1 Q_1'+\Omega_2 Q_2'}{\rho}\right)dr}{\int_{\xi R}^{R} 2\pi r V_0\,(1+a_1+a_2)\,dr} \tag{10.44}$$

10.3.3. Core and Bypass Synthesis

This section synthesises the insights gained from the foregoing separate analyses of the core and bypass flow to arrive at whole-engine performance parameters such as the installed thrust, power, TSFC and propulsive efficiency.

With reference to the comment on "rubber engine sizing" made in Section 10.3.1, the overall mass flow $\dot{m}_0$ first ought to be updated based on the installed design thrust $T_{instdesign}$:

$$\dot{m}_0 = \frac{F}{\frac{F}{\dot{m}_0}} \tag{10.45}$$

$$F = T_{instdesign}\eta_{inst} \tag{10.46}$$

$$\frac{F}{\frac{F}{\dot{m}_0}} = \frac{F_{dual}}{\dot{m}_{dual}}\frac{\alpha}{\alpha+1} + \frac{T_{core}}{\dot{m}_0} \tag{10.47}$$

F is the uninstalled ("engines only") thrust and η_{inst} a penalty factor on the available thrust due to engine installation effects (scrubbing drag, for example, which is quantified in Section 16.2.4). The overall uninstalled-thrust-to-mass-flow-ratio $\frac{F}{\dot{m}_0}$ is expressed by Equation 10.47. With this updated mass flow, computing the mass flows through the core and the open rotor configuration via Equation 10.7 and Equation 10.6 is trivial. The power consumed by the fan may be updated via Equation 10.48. Finally, the $TSFC$ and $PSFC$ may be obtained via

$$P_{fan} = \frac{P_{dual}}{\dot{m}_{dual}}\dot{m}_{2b} \tag{10.48}$$

$$TSFC = \frac{\dot{m}_f}{T_{inst}} \tag{10.49}$$

$$PSFC = \frac{\dot{m}_f}{P_{fan}} \tag{10.50}$$

To complete the spectrum of engine performance parameters, the propulsive efficiency η_{prop} and the overall efficiency η_0 may be distinguished. The propulsive efficiency describes the ratio of useful thrust power to the input shaft power (see Equation 10.51), and is in turn a function of the fan polytropic efficiency; a measure for the entropy rise during fan compression. The flow velocity V_{19} behind the fan stages can be obtained via Equation 10.52. The overall efficiency, as the name suggests, denotes the ratio of useful thrust power to the "power content" of the fuel.

$$\eta_{\text{prop}} \approx \frac{2V_0}{V_0 + V_{19}} e_f \quad (10.51) \qquad V_{19} = \sqrt{\frac{2P_{T2}(\pi_f - 1)}{\rho} + {V_0}^2} \quad (10.52) \qquad \eta_0 = \frac{T_{inst} V_0}{\dot{m}_f h_{fuel}} \quad (10.53)$$

10.3.4. Design Point Operation - Engine Sizing

This section outlines how the engine is physically sized to comply with the thrust requirement imposed by the critical design operating condition. Based on the thrust-to-weight ratio read off the iterated loading diagrams (Section 8.2), a take-off thrust of 517.14 kN ought to be designed for. Additionally, a note on parameter iteration and design convergence shall be made.

Physical Engine Sizing

The engine is sized by performing the foregoing cycle analysis at a single design operating condition. According to the loading diagrams devised in the Midterm Report [39], the minimum climb rate requirement following take-off determines the installed thrust required from the engines, and thereby the engine dimensions. By the end of this section, the initially guessed parameters D_{fan} and $(\frac{P}{\dot{m}})_{fan}$ from Table 10.3 can be corrected.

The corrected fan diameter D_{fan} is straightforwardly obtained from the corrected overall mass flow $\dot{m}_0$, which in turn permits computing the fan area A_{fan} and core diameter D_{core}.

$$D_{fan} = \sqrt{\frac{4\dot{m}_0}{\pi \rho V_0}} \quad (10.54) \qquad A_{fan} = \frac{\pi D_{fan}^2}{4}(1 - \xi^2) \quad (10.55) \qquad D_{core} = \xi D_{fan} \quad (10.56)$$

As done for the Midterm Report [39], the overall engine length can be computed from Equation 10.57, where L_{ref} is a reference length equaling 121.2 inches (3.08 m) and T_{ref} a reference thrust equaling 25000 pounds (121.21 kN), taken from E. Schwartz Dallara's sizing procedure [27].

$$L_{\text{eng}} = L_{\text{ref}} \left(\frac{T_{\text{sls}}}{T_{\text{ref}}} \right)^{0.337} \quad (10.57) \qquad FR \approx \frac{L_{\text{eng}} + D_{\text{core}}}{0.9 \cdot D_{\text{core}}} \quad (10.58) \qquad S_{\text{wet,eng}} = \pi D_{core} L_{\text{eng}} \quad (10.59)$$

Now that the fan diameter and the engine length are known, two further engine performance properties can be estimated: the nacelle parasitic drag and the overall engine weight. The nacelle parasitic drag includes both skin friction and pressure drag, where the former is a function of the wetted surface area (Equation 10.59), the proportion of laminar-to-turbulent boundary layer and the flight Reynolds number, and the latter mainly depends on the fineness-ratio defined in Equation 10.58. From Equation 10.62, the overall single nacelle parasitic drag can be estimated, where q is the dynamic pressure (Equation 10.60), k the nacelle form factor (Equation 10.61), c_f the skin friction drag coefficient ($c_f = 0.00229$ following the application of riblets) and $S_{\text{wet,eng}}$ has been computed via Equation 10.59.

$$q = \frac{\rho (M_{\text{cr}} \sqrt{\gamma R T_{\text{cr}}})^2}{2} \quad (10.60) \qquad k \approx 1.0706 + 2.0306 e^{-0.5228 FR} + 17.9547 e^{-2.3116 FR} \quad (10.61) \qquad D_{\text{p,eng}} = q k c_{\text{f}} S_{\text{wet,eng}} \quad (10.62)$$

The overall single engine weight is constituted by the partial component weights defined in Equation 10.63-Equation 10.65, where the reference shaft power P_{ref} = 5000 horsepower = 3.73 MW, the reference engine dry weight W_{ref} = 10000 pounds = 44.48 kN and the reference fan diameter D_{ref} = 8 feet = 2.44 m [27]. N_{rot} denotes the number of rotors, equaling two for the counter-rotating configuration considered in this work. Finally, GR = $\Omega_{\text{fan}}/\Omega_{\text{LPT}}$ is the so-called gear ratio, being the ratio of fan-to-low-pressure turbine rotational velocity. The obtained engine dry weight can then be fed back into the Class II weight estimation for a more accurate estimate of the OEW and MTOW.

$$W_{\text{pf,core}} = 0.098 T_{\text{instdesign}} \quad (10.63) \qquad W_{\text{pf,fan}} = 0.059 N_{\text{rot}} \left(\frac{P_{\text{design}}}{P_{\text{ref}}} \right)^{0.3} \left(\frac{D_{\text{fan}}}{D_{\text{ref}}} \right)^{1.836} W_{\text{ref}} \quad (10.64)$$

$$W_{\text{pf,gearbox}} = 0.021 \frac{P_{\text{inst}}}{P_{\text{ref}}} \frac{D_{\text{fan}}}{D_{\text{ref}}} \sqrt{\frac{GR}{8}} W_{\text{ref}} \quad (10.65) \qquad W_{\text{pf,dry}} = W_{\text{pf,core}} + W_{\text{pf,fan}} + W_{\text{pf,gearbox}} \quad (10.66)$$

Design Convergence

Two output parameters which concomitantly serve as outputs and inputs to the model during the very first iteration are the fan radius R_{fan} and the fan-power-to-fan-mass-flow ratio $\frac{P_{fan}}{\dot{m}_{fan}}$. The former is required to compute the overall engine mass flow $\dot{m}_0$ for a given altitude and Mach number, whereas the latter determines the power required by the low-pressure turbine to drive the dual-rotor fan. Based on the updated engine thrust and fan power which is computed in line with Section 10.3.3, these quantities are corrected and fed back into the model. This iterative convergence process is visualised in Figure 10.2, where after approximately 5 iterations the the engine design may be considered as converged. The final value of $D_{fan} = 2R_{fan}$ is provided in Table 10.10.

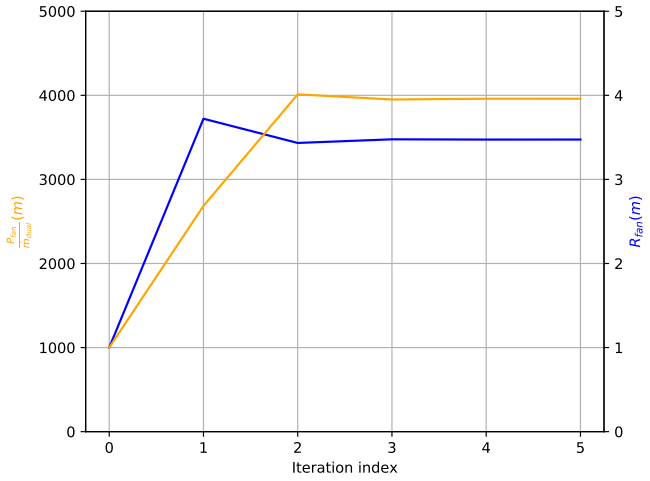

Figure 10.2: Convergence of engine design

10.3.5. Off-Design Operation - Engine Performance Computation

In order to assess the engine's performance under off-design operating conditions, considerable model restructuring is required. Within the scope of this work, "off-design operation" implies operation under a different altitude, Mach number and/or throttle setting compared to the foregoing design point analysis. As will be shown in Chapter 16, the design point corresponds to a cruise altitude of 5000 m and a Mach number of 0.82. However, the engine had to be over-sized for this condition to comply with the aforementioned take-off thrust requirement, and to allow sufficient performance margin to climb/accelerate in response to changing weather conditions and/or air traffic control instructions.

Assumptions

The forthcoming off-design cycle analysis warrants the following additional assumptions:

- Turbine and compressor isentropic efficiencies equal their design point values.
- T_{T4} must not exceed its design point value.
- The fan disk loading $\frac{P_{fan}}{A_{fan}}$ must not exceed its design point value.

Analysis

The fan diameter D_{fan}, the design fuel mass flow $\dot{m}_{fuel_{design}}$ and the design fan disk loading $(\frac{P_{fan}}{A_{fan}})_{design}$ are the invariant input parameters fed forward from the design-point cycle analysis. Similar to the foregoing section, the fan-power-to-fan-mass-flow-ratio $\frac{P_{fan}}{\dot{m}_{fan}}$ is iteratively updated from the initial design-point value to the off-design value, however, this time one update is sufficient seeing that the fan diameter D_{fan} is now fixed.

The second and third assumption in the above list raise the need for a simple engine control system limiting the maximum thrust. In a real engine, other design variables such as the high-pressure spool rotational velocity, burner entry temperature and burner pressure would also need to be actively controlled. However, for the purpose of this work, the following approach was deemed sufficient.

The Mach number Ma and the altitude h primarily determine the overall mass flow through the engine, based on which the total temperatures and pressures at the various core stations ahead of the combustor can be found in accordance with Section 10.3.1. Assuming the throttle setting to be linearly proportional to the fuel mass flow $\dot{m}_{fuel}$, the high-pressure turbine entry temperature T_{T4} can be derived by rearranging Equation 10.14. If for a given combination of Ma, h and throttle setting the high-pressure turbine inlet temperature turns out to exceed the design limit of T_{T4} =1700 K, $\dot{m}_{fuel}$ is regulated to comply with said limit.

To model the fan thrust variation as a function of throttle setting, based on [95] a linear relationship between the dual-rotor rotational speed Ω and the fuel mass flow $\dot{m}_{fuel}$ is assumed. With reference to the third assumption made in this section, the rotor disk loading must not exceed the design point loading $(\frac{P_{fan}}{A_{fan}})_{design}$ for any combination of altitude and Mach number. Unlike outlined in the previous paragraph, where the required $\dot{m}_{fuel}$ to comply with $T_{T4_{design}}$ could be explicitly computed, the rotational speed Ω must be stepwise reduced and the updated disk loading recomputed until said condition is met.

To conclude this section, the uninstalled thrust variation (not incorporating any thrust losses due to engine installation effects) with altitude h, Mach number Ma and throttle setting is displayed in Figure 10.3a, Figure 10.3b and Figure 10.3c, respectively. All three plots consider a hypothetical sizing condition of $T_{\text{req}} = 300$ kN at Ma =0.24 and $h = 0$ m, which corresponded to the sizing condition during the initial design phase. As expected from literature [93], the uninstalled thrust

of both the engine core and dual fan reduces with increasing altitude (less so for the turbojet core than for the propeller contribution, as would be expected), whereas the core thrust is approximately invariant with Mach number and drops of heavily for the dual fan. The latter is the result of the aforementioned limit imposed on the rotor disk loading, which for a constant altitude, scales directly with Mach number. The thrust variation with throttle setting is approximately linear in accordance with [95], at least in the upper throttle range. Finally, the concomitant installed thrust variation with Mach number and altitude is considered in Figure 10.3d, where it is noteworthy that the altitude effect on the dual fan thrust is balanced by the higher allowed rotor speed due to the lower ambient air density, resulting in the same black graph as in Figure 10.3b. In summary, the propfan engine model devised in this chapter behaves as expected with all three mission parameters.

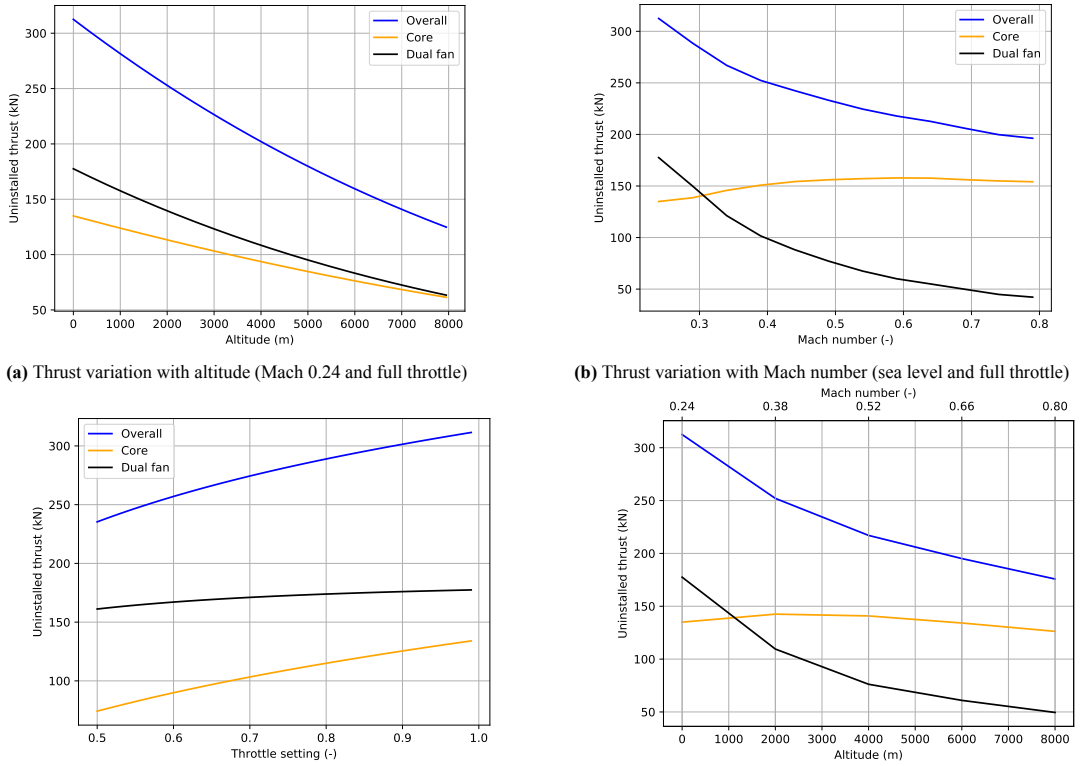

(a) Thrust variation with altitude (Mach 0.24 and full throttle)

(b) Thrust variation with Mach number (sea level and full throttle)

(c) Thrust variation with throttle setting (Mach 0.24 at sea level)

(d) Thrust variation with altitude and Mach number (full throttle)

Figure 10.3: Thrust variation with various mission parameters

10.4. CF6-80E1A3 Turbofan Model

In order to compare the propfan engines' performance under varying operating conditions to the CF6-80E1 engines of the A330-200 reference aircraft, an analogous model ought to be developed. As will be seen in Section 16.3.3, this will come in particularly handy to compare the precise ATR and DOC performance of the two competing aircraft on the mission profiles output by the SUAVE software.

10.4.1. Turbofan Model Inputs

This section contains the technical data of the General Electric CF6-80E1 series turbofan engines mounted on the A330-200. The certification date of these engines dates back to July 1999, hence the technology corresponding to the data in Table 10.4 and Table 10.6 is about 10 years behind that of the propfan engines (see Section 10.2). Unlike the foregoing propfan engine model, the CF6-80E1 engines run on fossil-based Jet-A-1, explaining the lower heating value of 43 MJ kg^{-1}.

Table 10.4: Technology par.

Parameter	Value	Parameter	Value
$\pi_{ch}\pi_f$ (OPR)	32.6	e_{tl}	0.93
π_{db}	0.98	e_{th}	0.93
π_{dc}	0.98	η_b	0.99
π_b	0.95	η_{ml}	0.985
π_{nf}	0.99	η_{mh}	0.997
π_{nc}	1	η_{inst}	0.96
π_{nb}	0.98	η_{mech}	0.99
e_f	0.93	β	0.015
e_{ch}	0.91	δ_1	0.02
η_{nozzle}	0.98	δ_2	0.02
$\eta_{gearbox}$	1		

Table 10.5: Physical par.

Parameter	Value
h_{fuel} ($\frac{\text{J}}{\text{kg K}}$)	$43 \cdot 10^6$
R_c ($\frac{\text{J}}{\text{K mol}}$)	287
R_t ($\frac{\text{J}}{\text{K mol}}$)	287
C_{pc} ($\frac{\text{J}}{\text{kg}}$)	1000
C_{pt} ($\frac{\text{J}}{\text{kg}}$)	1150
γ_c	1.4
γ_t	1.33

Table 10.6: Design par.

Parameter	Value	Parameter	Value
α	5.3	pi_{ch}	20.375
pi_f	1.6	T_{T4} (K)	1500

10.4.2. Turbofan Model Workings

In the following, the workings of the CF6-80E1 turbofan model shall briefly be outlined. The reason for which resources are being allocated to developing this model is threefold: first of all, in literature only values for the TSFC at take-off and cruise can be found, but if the Airbus A330-200 is flying at a different altitude or Mach number, it would be difficult to estimate the engines' performance. Secondly, performance values differ significantly between different sources, based on the conditions under which/the accuracy with which they were measured. Finally, comparing two models based on similar assumptions and comparing their relative performance is more reliable than computing engine parameters for the low-ATR aircraft and employing reference value from literature for the Airbus A330-200. Due to the above reasons it was decided to devise a dedicated turbofan model, whose core works identically as the core model of the propfan engine described in Section 10.3.1, except that now the engine dimensions are known (D_{fan}). The fan diameter is found to be 2.44 m [49], and forms the basis for calculating the mass flow which passes through the engine. The parameters used to perform the cycle calculation on the CF6-80E1 engine were listed in Table 10.4-Table 10.6, and are coordinated with the inputs to the A330-200 SUAVE model in Table 16.5. The overall mass flow is calculated using Equation 10.67.

$$\dot{m}_0 = \rho \cdot V \cdot \frac{\pi}{4} \cdot D_{fan}^2 \tag{10.67}$$

The mass flow through the bypass duct can be calculated via Equation 10.6. Station 2b in Figure 10.1 denotes the pressure behind the fan, which in the case of the CF6-80E1 is taken equal to 1.6. This is the value taken from the GasTurb 13™ engine design software, and is confirmed by [66] for twin-spool turbofan. The total temperature and pressure at station 2b are calculated analogous to Section 10.3.1, Equation 10.3 and Equation 10.4. The bypass flow first has to pass through a diffuser, which is assumed to be adiabatic, where it will experience a pressure loss and temperature change. The total pressure drop and total temperature loss over the diffuser, with a pressure ratio of 0.99, can be calculated via Equation 10.8 and Equation 10.9 by exchanging the π_{dc} for π_{db}.

As for the core calculation, this cycle computation assumes a perfect De Laval nozzle. Again, the nozzle can be choked or not, and to judge this a critical pressure ratio is calculated for which the transition between these two scenarios occurs (see Equation 10.68). In said equation, $\eta_{\text{nozzle, byp}}$ is the efficiency of the bypass nozzle, taken to be 0.98 [64] as for the core nozzle. γ_c is the ratio of specific heats for a gas prior to mixing with fuel.

$$\pi_{crit,byp} = \left(1 - \frac{\gamma_c - 1}{\eta_{nozzle,byp}}\right)^{\frac{-\gamma_c}{\gamma_c - 1}} \tag{10.68}$$

Option 1: If $\frac{P_{T2b}}{P_0} >= \pi_{\text{crit,byp}}$, the bypass nozzle is choked. In this case, Equation 10.69 calculates the static pressure at the nozzle exit, Equation 10.70 the static temperature at the nozzle, Equation 10.71 the velocity at the nozzle exit, and Equation 10.72 defines the effective area of the nozzle throat [96]. Finally, the thrust is calculated in Equation 10.70.

$$P_{19} = \frac{P_{T2b}}{\pi_{crit,byp}} \tag{10.69}$$

$$T_{19} = T_{T2b} \cdot \frac{2}{\gamma_c + 1} \tag{10.70}$$

$$V_{19} = \sqrt{\gamma_c R_c T_{19}} \tag{10.71}$$

$$A_19 = \dot{m_{19}} \frac{R_c \cdot T_{19}}{P_{19} \cdot V_{19}} \tag{10.72}$$

$$T_{byp} = \dot{m_{19}}(V_{19} - V_0) + A_{19} \cdot (P_{19} - P_0) \tag{10.73}$$

Option 2: If $\frac{P_{T2b}}{P_0} < \pi_{\text{crit,byp}}$, the bypass nozzle is not choked. This condition requires different formulae. First of all, it is assumed that the pressure of the nozzle is equal to the ambient static pressure in Equation 10.74. Subsequently, the static temperature is calculated in Equation 10.75. The exit velocity of the nozzle is calculated in Equation 10.76. Finally, the thrust is calculated using Equation 10.77.

$$P_{19} = P_0 \tag{10.74}$$

$$T_{19} = T_{T2b} \cdot (1 - \eta_{nozzle,byp}(1 - \frac{P_0}{P_{T2b}})^{\frac{\gamma_c - 1}{\gamma_c}}) \tag{10.75}$$

$$V_{19} = \sqrt{2 c_{pc} \eta_{nozzle,byp}(1 - \frac{P_0}{P_{T2b}})^{\frac{\gamma_c - 1}{\gamma_c}}} \tag{10.76}$$

$$T_{byp} = \dot{m_{19}}(V_{19} - V_0) \tag{10.77}$$

10.4.3. Turbofan Model Performance

In this section a close look is taken at the CF6-80E1 engine model towards its off-design performance. Also the differences with the propfan engine model at off-design will be made.

In Figure 10.4a the uninstalled thrust of the CF6-80E1 turbofan is considered. One can see that the overall thrust will decrease with altitude. This is due to the lower density of the air at a higher altitude, which in term decreases the mass flow through the engine. Therefore it decreases the thrust. What can also be seen is that the engine fan decreases its thrust almost parallel to the overall engine, while the core produces a more constant value of the thrust. This can be the do with the bypass ratio of the engine, as more air is flowing past the fan, it will be impacted more by the shift in mass flow. Furthermore, most of the core is only there to provide the power that the fan requires to produce thrust. That is why initially the core thrust increases, while the fan thrust is decreasing, the fan does no longer require as much power to be driven, leaving more energy in the core flow, and producing ever so slightly more thrust than at sea level conditions. This effect is overruled when the engine lose more of its mass flow at even higher altitudes.

In Figure 10.4b the uninstalled thrust of the CF6-80E1 is provided as a function of the inlet Mach number of the turbofan engine, at a fixed altitude of 5000 m. The overall engine produces more thrust when the inlet mach number increases. Again similar to the previous discussion this can be attributed to the change in mass flow, increasing the flow velocity increases the amount of air entering the engine, and thus the thrust. This behaviour is different to the propfan engine as it had a decreasing thrust with increasing mach number, because the propfan blades were limited by the amount of force per unit area they could handle. The turbofan has no such limitation and this allows it to increase its thrust with increasing mach number.

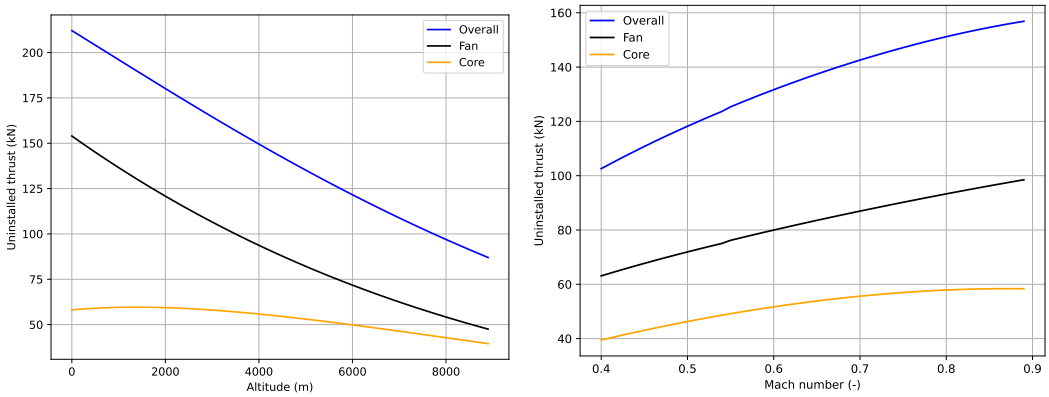

(a) Uninstalled thrust variation of the CF6-80E1 engine model, with altitude for a constant Mach number of 0.63.

(b) Uninstalled thrust variation of the CF6-80E1 engine model, with Mach number for a constant altitude of 5000 m

Figure 10.4: Performance graphs of the CF6-80E1 engine model.

10.5. Verification and Validation of the Propfan Engine Model

This section implements a holistic verification strategy for both the propfan and turbofan engine model devised in this chapter. This strategy is based on two instances of external, well-validated software: the Gasturb 13^{TM} engine design and cycle analysis software, as well as the SUAVE mission design tool based on [99], and modified and kindly provided by A. Dorsey [29].

10.5.1. Validation with GasTurb 13^{TM}

In this subsection, both engine models are verified using the aeroengine design software GasTurb 13^{TM}. In GasTurb 13^{TM}, a twin-spool turbofan engine is selected and its input parameters are subsequently modified. To validate the engine script, a conventional, ducted bypass configuration (turbofan) is used. This is to ensure that the engine core is fully functional before implementing the dual rotor configuration, which is more complex and less established, and thus more prone to errors.

Firstly, the engine core model is verified by feeding equal parameters into GasTurb 13^{TM} and the engine script. The input parameters are listed in Table 10.7. Other parameters such as the inlet pressure ratio or nozzle efficiency were deemed to have a negligible effect on the final outcome of the cycle analysis, and were therefore taken equal to the input parameters chosen in Section 10.2 for both GasTurb 13^{TM} and the propfan engine script. However, as will become clear in the following discussion, this assumption proved to be invalid, as these parameters turned out to have large effect on the computed temperature and pressures ratios. Therefore, a second attempt was made to obtain a better fit, as represented by Table 10.8, Figure 10.6 and Figure 10.5.

In Table 10.8, a number of outputs from GasTurb 13^{TM} and the engine script are provided. Firstly, there are the total temperatures and pressures, for which one must look at Figure 10.5 and Figure 10.6, respectively. In Figure 10.5, the total

temperature in K is given. One can see that there are small discrepancies at stations 3, 44, 45 and 5. Station 3 is located at the combustor entrance, where the total temperature difference of about 60 K is entirely due to the pressure difference suggested by Figure 10.6, the cause of which shall be explained in the following. At station 44 the temperature of the model is 20 K higher than the one predicted by GasTurb 13^{TM}. This is due to the total temperature ratio τ_{th} across the turbine (see Table 10.8), which only displays a 0.65% relative difference between the two models, though still amounts to a 7 K absolute temperature difference. Moreover, the specific heat of the gas mixture leaving the combustion chamber is taken equal to 1150 J kg^{-1} K [96], which is believed to be more accurate than the constant cold- and hot-air specific heat assumed by GasTurb 13[13]. After setting this parameter equal in both models, a better match was obtained. With the specific heat parameter adjusted, the total temperatures at station 45 and 5 were also corrected.

In Figure 10.6 the total pressures at each station are provided. One can again observe that the post-compressor stations 3, 44, 45, 5 and 9 are not matching to the same degree of accuracy as the pre-compressor stations. The total pressure at station 3 is overestimated by the present core model, which was related to a pressure loss over the inlet that was not accounted for. This resulted in an OPR for verification purposes computed by GasTurb 13^{TM} to be 49.3 instead of 50, as input to the model. Correcting this deficiency also rectified the temperature at station 3, as these are linked through adiabatic relations. Also the pressure loss over the combustor initially displayed some discrepancy, which was again related to different model input parameters. Finally, the pressure ratio over the turbine is directly linked to the total temperature ratio, which was corrected as discussed previously, resulting in a near-perfect model match at stations 44, 45, 5 and 9. All in all, these corrections resulted in an excellent match of the specific fuel consumption, uninstalled thrust and fuel-to-air-ratio, as confirmed by Table 10.8.

Table 10.7: Input parameters used

Inputs	Value	Units
T_{req}	200	kN
M_0	0.8	-
h_0	1000	m
BPR	10	-
T_{T4}	1700	K
OPR	50	-
$\dot{m}_0$	2550	kg s^{-1}

Table 10.8: Output parameters

Output	GasTurb 13[13]	Model	Update Model	Units
Total Pressure	See Figure 10.6			Pa
Total Temperature	See Figure 10.5			K
τ_{th}	0.616	0.612	0.612	-
τ_{tl}	0.863	0.860	0.860	-
sfc	22.4	17.3	19.1	g kN^{-1} s^{-1}
T	186.18	218.9	185.9	kN
f	0.0181	0.0173	0.016	-

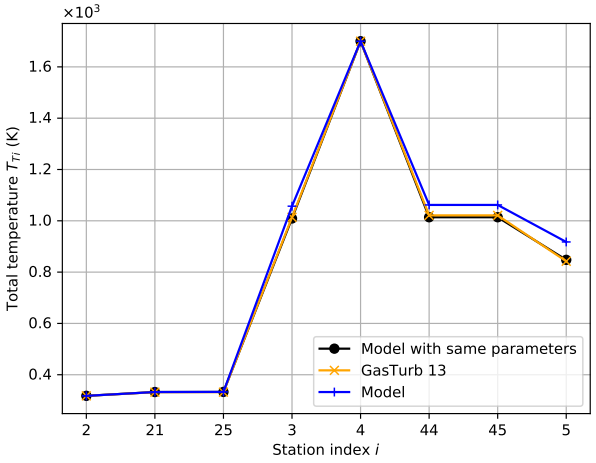

Figure 10.5: Verification of engine core total temperatures with Gasturb 13^{TM}

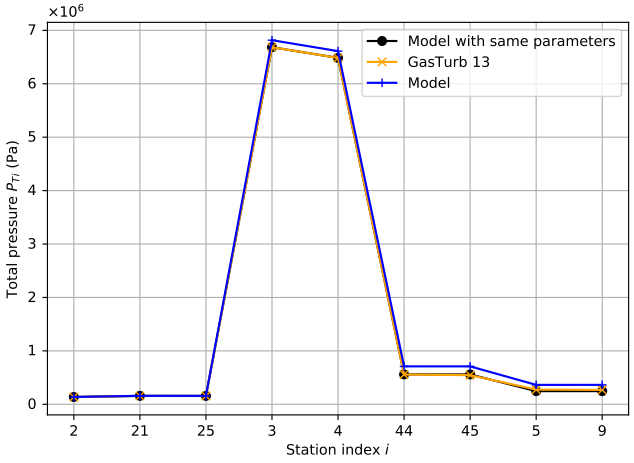

Figure 10.6: Verification of engine core total pressures with Gasturb 13^{TM}

From the data provided above, the model devised in Section 10.3.1 may be considered a verified.

After the core and regular bypass script (and therewith the CF6-80E1A3 turbofan model) has been verified, the regular fan is replaced by the counter-rotating, open-rotor configuration. All other parameters remain invariant following this integration step. In Table 10.9, the mass flow, bypass and core thrust, total thrust and thrust-specific fuel consumption obtained from GasTurb 13^{TM}, the turbofan model and finally the whole-propfan engine model are summarised. The difference in mass flow stems from the mass flow no longer being an input to the propfan model. Instead, the required fan diameter is calculated and the corresponding mass flow is obtained from the flight velocity, ambient density and rotor disk area. The modelled bypass thrust is less than that predicted by the turbofan model, which is due to the propfan not having a nozzle accelerating the bypass flow before being expelled. The core thrust is fairly constant, although it increases slightly due to the higher core mass flow, which could be a result of neglecting the radial nacelle thickness. Finally, the TSFC reduces to 18.3 g kN^{-1} s^{-1}, which is due to the higher propulsive efficiency and reduced bypass losses of the propfan, which can also be understood from the $\frac{T_{core}}{\dot{m}_0}$ and $\frac{T_{bypass}}{\dot{m}_0}$ parameters. In essence, a higher specific thrust indicates a more efficient conversion of mass flow into usable thrust.

Table 10.9: Validation data GasTurb verus turbofan model versus propfan model.

Parameter	Gasturb 13^{TM}	Turbofan Model	Propfan Model	Unit
$\dot{m}_0$	2449	2450	2478	$\mathrm{kg\,s^{-1}}$
T_{bypass}	98	99.1	91.3	kN
T_{core}	87.9	86.8	94.7	kN
T_{tot}	186	185.9	186	kN
TSFC	22.4	19.1	18.3	$\mathrm{g\,kN^{-1}\,s^{-1}}$
$\frac{T_{\text{core}}}{\dot{m}_0}$	-	34.05	38.2	$\mathrm{kN\,s\,kg^{-1}}$
$\frac{T_{\text{bypass}}}{\dot{m}_0}$	-	38.86	40.55	$\mathrm{kN\,s\,kg^{-1}}$

10.6. Final Propulsion System Design

This section presents the converged open rotor engine design that has emerged from the foregoing propfan model, within the grand scheme of the aircraft design iteration loop. In Section 16.5, an optimal cruise altitude of 5000 m and a Mach number of 0.63 are identified. However, in order to meet the critical take-off thrust criterion (517.14 kN), the engines actually needed to be oversized for cruise, i.e., provide a higher thrust than the cruise drag of 82.34 kN, taking into account the thrust lapse with altitude and Mach number quantified in Section 10.3.5. Table 10.10 contains the converged propfan design data: a very high BPR of 30 facilitates an excellent TSFC of 11.76 $\mathrm{g\,kN^{-1}\,s}$ at Mach 0.63 and 5000 m altitude. The large rotor diameter of 5.3 m enables meeting the stringent take-off thrust requirement per engine, and approximately corresponds to that of an Airbus A400M [2]. Naturally, for a BPR of 30, the core diameter turns out to be rather small, and the total engine length of 3.79 m is also shorter than the CF6-80E1 nacelle length (4.23 m, as indicated in Table 16.5). In terms of dry weight, the current propfan engine design is about 22.95% heavier than the CF6-80E1A3 engine, and the rotor disk loading of $2.62 \cdot 10^6$ $\mathrm{W\,m^{-2}}$ is very high despite the large diameter. The latter characteristic warrants effective noise reduction measures, examples of which shall be proposed in Section 10.9. Finally, the overall engine efficiency of 38.75% is in excellent agreement with Figure 4.7 in [27], and in excess of what competing turbofan engines can deliver.

Table 10.10: Converged propfan design data

Design parameter	**BPR**	D_{fan} **(m)**	D_{core} **(m)**	L_{tot}	$S_{wet_{tot}}$	$W_{dry_{tot}}$
Value	30	5.30	1.33	3.79	15.78	5334.43
Design parameter	$W_{dry_{core}}$ **(kg)**	$W_{dry_{fan}}$ **(kg)**	$W_{dry_{gearbox}}$ **(kg)**	$\frac{P_{fan}}{A_{fan}}$ $(\frac{W}{m^2})$	**TSFC** $(\frac{g}{kNs})$	η_{tot} **(%)**
Value	1449.01	3282.72	602.68	$2.62 \cdot 10^6$	11.76	38.75

The following two figures display the final propfan engine design, including the (short) pylon structure attaching the engines to the wing. For reasons related to ground clearance and to reduce the pylon weight, it is desirable that the engine be mounted as close as possible to the wing, possibly necessitating the application of heat shielding material on the lower wing surface in proximity to the hot core flow.

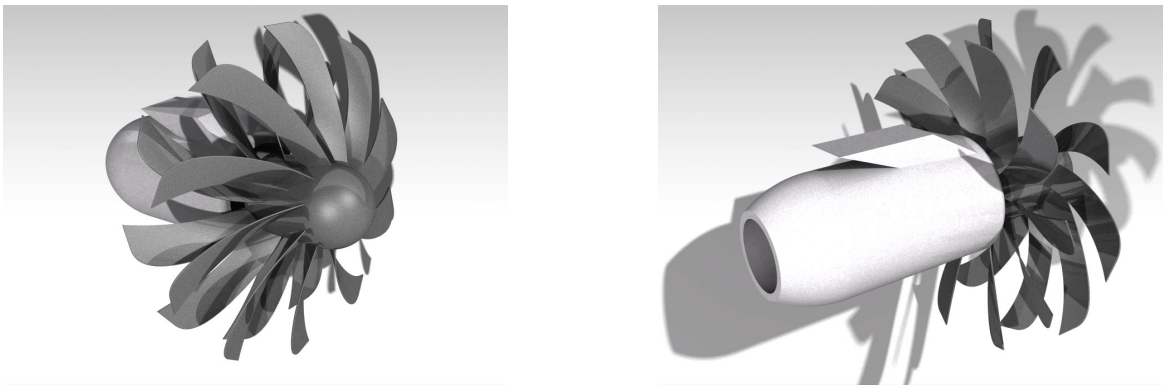

(a) Propfan engine front view

(b) Propfan engine rear view

Figure 10.7: CATIA V5 model of converged propfan design including pylon, propfan blades are only representative of the number of blades and the diameter.

[2] `https://www.airbus.com/defence/a400m.html` (last accessed on (22/06/2021)

10.7. Propulsion System Parameter Analysis for Low-ATR Design

In this section, three output parameters of the propulsion system script, which are vital input parameters to the ATR script devised in Chapter 16, are explored. This will be of help in interpreting the graphs in said chapter, and elucidates on why a propfan configuration was chosen in the first place. Section 16.5.

In Figure 10.8, the performance behaviour of the propulsion model is plotted as a function of altitude and Mach number. It can be observed that for Mach numbers lower than 0.7 the propfan is operating at a very low TSFC (roughly 11 to 13 $\mathrm{g\,kN^{-1}\,s^{-1}}$), whereas from Mach 0.7 onwards the TSFC rapidly increases as the maximum permissible disk loading limits the fans' rotational velocity and the blades suffer from compressibility losses. The TSFC does not vary significantly with altitude, although the slope of the line separating high TSFC values from low TSFC values is inclined such that operation at higher altitudes permits a lower TSFC in the higher Mach number regime. This is due to the lower density at higher altitudes, resulting in a lower mass flow, requiring less fuel to heat up the core flow to its design turbine inlet temperature. As a result, the fuel burn decreases more than the thrust would decrease, resulting in an overall lower TSFC.

In Figure 10.9 and Figure 10.10, the total temperature and pressure at the compressor exit face are provided in K and Pa as a function of altitude and Mach number. Unsurprisingly, both exhibit the same behaviour, namely that a high altitude and low Mach number results in lower values of the total temperature and total pressure (recall that station 3 is located in front of the burner). Higher altitudes lower the temperature of the incoming air, and thus the total temperature, whereas flight at high Mach numbers increases the absolute pressure, and therewith the total temperature. The latter relation is captured by Equation 10.1 and Equation 10.2.

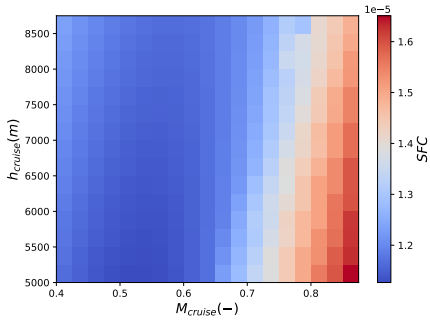

Figure 10.8: TSFC ($\mathrm{g\,kN^{-1}\,s^{-1}}$) variation with altitude and Mach number

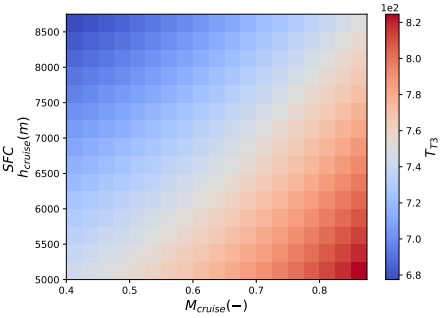

Figure 10.9: Total temperature at compressor outlet (K) variation with altitude and Mach number

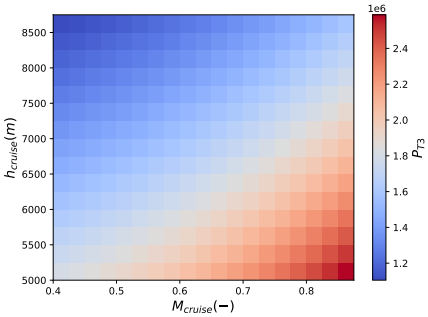

Figure 10.10: Total pressure at compressor outlet (Pa) variation with altitude and Mach number

10.8. Sensitivity of Propfan Engine Design

In this section, the sensitivity of the converged propfan engine design presented in Section 10.6 to a range of model input parameters is investigated.

In Table 10.11, the sensitivity of different propulsion system design parameters for an incremental change in input parameters is systematically studied. The parameters in the first column represent the input parameters which have been incremented by 1% to obtain the sensitivity of the model parameters denoted in the top row.
From the data contained in Table 10.11, insights can be gained on the evolution of the engine design for a change in technology parameters. Currently, the fan diameter of the propfan is rather large and it would be interesting to investigate which parameters drive the fan size in particular. The following parameters have a fan diameter-reducing effect: M_{cr}, T_{T4}, B, η_{ch}, η_{th} and η_{tl}. As the cruise Mach number is a variable dependent on the mission profile, it is not something which will be decreasing the engine size in the future. Increasing T_{T4} increases the specific thrust of the bypass and core flow, the required total mass flow, and it decreases the engine dry weight and the diameter of the core. Surprisingly, in this case increasing T_{T4} does raise the TSFC, however, this only applies to when the engine performs at its maximum thrust; at any other throttle setting, TSFC will decrease for an increased T_{T4}. An underrated variable to increase which positively effects all parameters considered during the sensitivity study is the blade number. Currently 10 blades are considered for the propfan and it is unlikely that more than 12 blades could be tolerated on the rotor. Finally increasing the efficiency of the compressor and turbines is very beneficial for the entire engine, as increasing it will have a beneficial contribution to all parameters, and during the design of the engine carefull consideration should paid towards increasing these efficiencies.

As a summary the input parameter which induces the largest change in each of the output parameters is highlighted. Green color indicates the largest change which has a positive effect on the engine performance, for example a lower weight. The color red indicates that this input parameter has the largest negative impact on the engine performance, for example an increase in weight. In this case positive and negative does not denote the sign of the change, but whether it is beneficial or detrimental to the engine performance. One can see that the fan diameter is positively impacted by the turbine inlet

temperature, and negatively by the required thrust. For the specific thrust of the rotor the turbine inlet temperature again has the largest positive contribution, while the mach number which is flown at, reduces the specific thrust, as the maximum blade loading is limited for the propfan. For the core increasing the bypass ratio decreases the specific thrust the most, as increasing the bypass ratio increases the fan diameter, and therefore increases the power required to the fan, which reduces the thrust of the core as the thrust balance is shifted more towards the bypass flow. The specific fuel consumption is mostly influenced by the fuel fuel heating value, in a positive way. In Section 10.1 a discussion is made on sustainable aviation fuels and their positive effect on the aircraft emissions, which apparently also carry over into the lowering of the specific fuel consumption, as burning 1 kg of sustainable aviation fuel generates more heat that standard aviation fuel. Finally the engine dry weight is most negatively impacted by the required thrust, as a larger thrust requirement crudely translates to a larger engine. The compressor efficiency is most beneficial for reducing the engine weight, as less pressure is lost, and the effective overall pressure ratio is increased.

Table 10.11: Sensitivity analysis of the Propfan design parameters

Parameters	D_{fan} (m)	$\frac{T_{rotor}}{\dot{m}_0}$ ($\frac{Ns}{kg}$)	$\frac{T_{core}}{\dot{m}_0}$ ($\frac{Ns}{kg}$)	SFC ($\frac{kg}{s}$)	$W_{engine_{dry}}$ (kg)
$\frac{d}{dM_{cr}}$	-1.28E-03	-7.42E-03	-4.76E-03	6.13E-03	3.32E-03
$\frac{d}{dh_{cr}}$	2.20E-03	1.63E-03	7.39E-03	-5.61E-04	3.20E-03
$\frac{d}{dT_{T4}}$	-6.59E-03	1.30E-02	1.36E-01	5.12E-03	-1.23E-02
$\frac{d}{d\Omega}$	1.22E-03	-2.45E-03	-5.53E-02	2.44E-03	4.42E-03
$\frac{d}{dQ}$	3.56E-03	-7.17E-03	-9.63E-02	-2.49E-03	6.70E-03
$\frac{d}{dT_{req}}$	4.62E-03	6.83E-04	-1.59E-02	-6.83E-04	1.20E-02
$\frac{d}{dB}$	-4.62E-04	9.23E-04	1.55E-03	-9.24E-04	-1.20E-03
$\frac{d}{d\eta_{prop}}$	1.49E-03	-2.98E-03	-3.69E-02	3.88E-03	2.78E-03
$\frac{d}{dh_{fuel}}$	1.50E-04	-3.00E-04	-3.60E-03	-9.70E-03	2.81E-04
$\frac{d}{dOPR}$	2.78E-04	-5.56E-04	-6.68E-03	-1.94E-03	5.20E-04
$\frac{d}{d\eta_{ch}}$	-2.97E-03	5.92E-03	6.64E-02	-7.07E-04	-5.56E-03
$\frac{d}{d\eta_{th}}$	-1.50E-03	2.99E-03	3.46E-02	-3.00E-03	-2.80E-03
$\frac{d}{d\eta_{tl}}$	-2.24E-03	4.46E-03	5.08E-02	-4.48E-03	-4.18E-03

10.9. Recommendations for Detailed Propulsion System Design Phase

This section summarises the deficiencies of the foregoing propfan engine model and proposes recommendations as to which aspects ought to be investigated during the detailed design phase. First and foremost, no suitable open rotor noise model for the scope of this exercise was found in literature. A noise assessment based on literature is postponed to Section 23.3.1. Nonetheless, a number of concrete noise mitigation strategies for open rotor design have been made public and shall now be addressed. Furthermore, a discussion is made on the risks of the propfan design, concerning its size but also more general about the risks pertaining to propfans which turbofans do not have.

Multiple authors suggest that a low-thickness (blade noise scales with air volume displaced), high-camber (lower rotor loss and hence weaker tip vortices, though preferably different for both rotors to prevent excitation and resultant amplification of the same acoustic frequencies), high aspect ratio (lower blade interaction noise) and cropping the rear rotor blades to prevent interaction with the front rotor's tip vortices are effective noise reducing measures [43]. Furthermore, increasing rotor axial spacing dissipates the front rotor vortex strength before interacting with the rear rotor, reducing interaction noise. Finally, geared and variable pitch rotors permit reducing rotor tip speeds (reduced compressibility losses) and limiting the disk power loading (reducing loading noise contribution) whilst maintaining high efficiencies under both takeoff and cruise conditions. Another important aspect concerns the wing-engine interaction depending on the propfan engines' position; seeing that the engines are of puller-type, the propeller wake impinges on the aft-located portion of the wing, locally increasing the wing's lift coefficient, but causing an additional scrubbing drag contribution addressed in Section 16.2.4. This configuration is also beneficial from an aeroacoustics point of view, as the propfan rotors ingest free stream air, as opposed to the turbulent boundary layer downstream of the trailing edge in a pusher configuration. A downside of front-mounted engines relates to the poor performance of any NLF airfoils in turbulent wakes, however, this may be partially remedied by the application of riblets to reduce the turbulent skin friction drag [39].

Propfan Uncertainties

The design of the low-ATR aircraft is quite conventional in the sense that it has a low-wing configuration, a conventional tail plane and a tubular fuselage, which are all concepts that have been designed many times, and are proven to work. Introducing new technologies into the design ultimately comes at a risk and the propfan is also one of those risks. In the quest for minimising ATR two counter rotating propfans were considered as the optimal solution to obtain the maximum ATR reduction compared to an A330-200. This required to divide the required take-off thrust over two engines, which has resulted in a large fan diameter of 5.3 m as can be seen from Section 10.6. This fan diameter is larger than any known propfan which has ever been designed. With these large, highly swept, high aspect ratio blades, aeroelasticity

could become an issue. A bigger issue is that during this design phase, there are not enough resources to investigate the aeroelasticity of the propfan blades accurately, and therefore literature should be consulted, which is difficult since this engine would be larger than any known propfan ever designed. The engines which have similar propeller diameters are the Airbus A400M TP400 engine, it also has a fan diameter of 5.33 m [49] which due to its highly swept blades can be considered a single rotor propfan. Another example is the Tupolev-95 engine the Kuznetsov NK-12, which has a propeller diameter of 6.2 m[49]. This engine is a counter rotating propeller engine, with 4 blades per rotor. However, its blades are not swept at all, and the blades do not resemble those of a propfan, however it has a similar speed range and even larger propeller diameter. We are confident that the propfan which has been proposed can be designed and built in real life, due to much newer material technologies since the design of other propfans, further optimisation of the rotor spacing and the two aforementioned examples.
In the case where the propfan can not be produced, two options are presented. Firstly a conversion from two engines, to four engines is looked into, to reduce the fan diameter. If this is done a fan diameter of around 4 m per propfan is obtained. At the expense of increasing the total weight due to engines from 10.8 tons, to 14.7 tons. Also this increase in engine number would decrease the amount of natural laminar flow which can exist on the wing in the sphere of influence of the propfans. However, it could be looked into to convert from a tractor to pusher configuration and what its effect is on the laminar flow on the wing.
The other option is converting to two turbofan engines, which was also a concept during the midterm phase of the DSE [39]. Choosing a turbofan engine, would be beneficial in terms of cost, laminar flow over the wing, and the possibility of covering the engine nacelles with riblets, worse in terms of specific fuel consumption, and also much worse in terms of ATR, as the high compression ratio required for the engines will increase the NO_X production which is a major factor in the ATR production.
A carefull trade-off shall be made in the event the propfan can not be designed.

10.10. Propfan-Wing Interference

This section investigates the potential adverse effects of a wing-podded propfan on the wing's aerodynamic performance. Firstly, induced flutter shall be analysed, and secondly a brief study on interference drag is performed. Figure 10.11a shows that disk flutter stability can be achieved for speeds lower than Mach 0.65 with the right choice of blade type and incidence angle. Regarding the former, E. Schwartz Dallara suggests a United Technologies single-rotation, high-speed propeller design [27]. The latter is being taken care of by the aforementioned variable-pitch rotor design. Unfortunately, high-frequency phenomena are difficult to predict with steady linear aerolastic models, requiring more sophisticated FEM or CFD methods for detailed analysis. Theoretically, a propfan could also act as a damper for the combined wing-engine system but this has not been experimentally proven yet [102]. Figure 10.11 suggests that by installing a propfan, the interference drag coefficient increases from 0.002 to roughly 0.0028 below Mach 0.7. The present aircraft's cruise Mach number falls within this range, meaning that the interference drag impact is rather minor and is not expected to pose major design challenges [51]. One might expect that the propfan propellers causes whirl flutter, however, this is likely not the case since each engine has two sets of counter-rotating rotors.

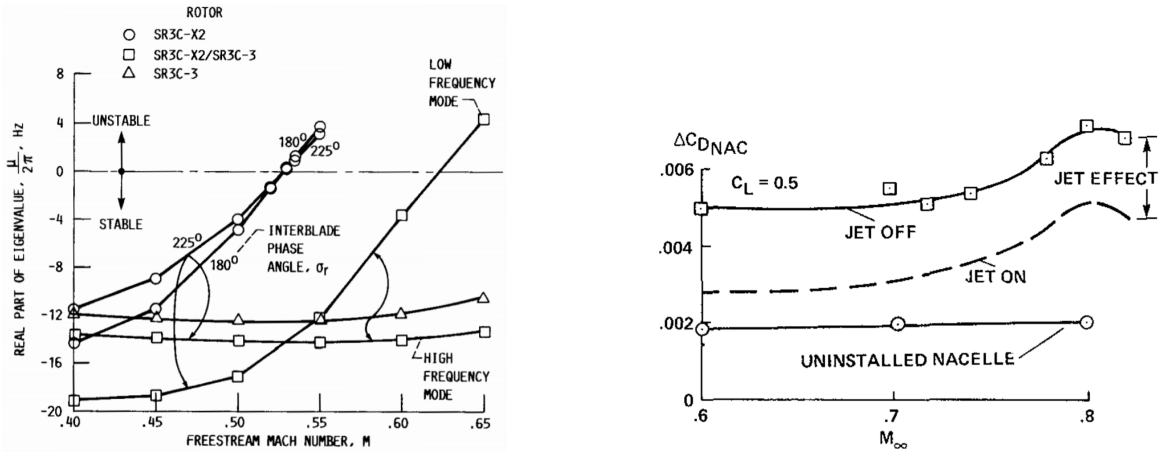

(a) Propfan flutter stability [51]

(b) Propfan interference drag [102]

Figure 10.11: Further notes on characteristics of wing-podded propfans

11. Empennage Design

The design of the empennage has been done in two parts. First a preliminary sizing has been done, after which a more accurate sizing has been done. In Section 11.1 the Class I sizing of the empennage is given.

11.1. Preliminary Empennage Sizing

The preliminary sizing of the empennage is done to get a first estimate of the size of the empennage and the rudder and elevators. This data is also used in the iterations between the Class I and Class II sizing of the aircraft. The preliminary sizing of the empennage is based on a Class I method described in Roskam [86]. This method uses reference aircraft to compute relevant parameters. The reference aircraft used for this design are based on similar size, mission and empennage configuration. Below in Table 11.1 the chosen reference aircraft are given, along with their fuselage length, tail arms and tail volumes. Note that the volumes are dimensionless

Table 11.1: Reference aircraft for tail sizing with their relevant data obtained from literature [50]

Aircraft	$l_{\mathbf{f}}$ (m)	$x_{\mathbf{h}}$ (m)	$x_{\mathbf{v}}$ (m)	$V_{\mathbf{h}}$	$V_{\mathbf{v}}$
A330-200	57.8	26.2	25.2	0.96	0.06
A321-200	44.5	16.2	15.2	0.96	0.08
A300-600R	53.3	25.6	24.9	1.06	0.10
A310-300	45.1	22.5	20.2	1.12	0.09
A340-200	58.2	26.5	25.5	0.73	0.06
B757-300	54.0	19.9	19.0	0.96	0.09

Aircraft	$l_{\mathbf{f}}$ (m)	$x_{\mathbf{h}}$ (m)	$x_{\mathbf{v}}$ (m)	$V_{\mathbf{h}}$	$V_{\mathbf{v}}$
B767-200ER	47.2	20.3	19.8	0.80	0.07
B767-300ER	53.7	23.7	23.2	0.93	0.08
DC8-73	55.7	24.9	25.7	0.66	0.05
IL-86	56.1	25.3	24.9	0.94	0.09
IL-96-300	51.2	24.3	23.6	0.74	0.07
Tu-204-200	46.7	21.3	21.8	0.96	0.10

In order to find the tail arms for the preliminary empennage sizing, linear regression was performed on the fuselage length - tail arm relation. Furthermore the tail volumes were computed by computing the average value of the reference aircraft tail volumes. After computing the tail arms and volumes, the tail areas could be computed using Equation 11.1 and Equation 11.2.

$$S_{\mathrm{h}} = \frac{\bar{V}_{\mathrm{h}} S \bar{c}}{x_{\mathrm{h}}} \tag{11.1}$$

$$S_{\mathrm{v}} = \frac{\bar{V}_{\mathrm{v}} S b}{x_{\mathrm{v}}} \tag{11.2}$$

The preliminary rudder and aileron areas could be computed using area fractions, which were computed from reference aircraft (averages).

Before the iterations started, an empennage configuration was chosen. This was done following the guidelines stated in Roskam [86]. In the book a range of values is given and from that range suitable values were chosen for the mission. As the designed aircraft will fly relatively low and slow, a low sweep and low aspect ratio was chosen for both tail wings. For the other parameters conventional values were chosen. In Table 11.2 the range of parameters is given and in Table 11.3 the chosen parameters are given.

Table 11.2: Tail planform parameter ranges for a jet transport aircraft [86]

Parameter	Horizontal tail	Vertical tail
Dihedral angle Γ (°)	0 - +11	90
Incidence angle i (°)	Variable	0
Aspect ratio AR	3.4 - 6.1	0.7 - 2.0
Sweep angle $\Lambda_{c/4}$ (°)	18 - 37	33 - 53
Taper ratio λ	0.27 - 0.62	0.26 - 0.73

Table 11.3: Tail planform parameters

Parameter	Horizontal tail	Vertical tail
Dihedral angle Γ (°)	0	90
Incidence angle i (°)	0	0
Aspect ratio AR	6.1	1.8
Sweep angle $\Lambda_{c/4}$ (°)	18	33
Taper ratio λ	0.32	0.32
Airfoil	NACA 0012	NACA 0015

11.2. Aircraft Loading Diagram

In Section 8.3 the centre of gravity at operational empty weight is determined. In this section the centre of gravity range of the aircraft will be determined. An aircraft loading diagram will be constructed giving all possible loading options of the aircraft.

11.2.1. Cargo Loading

All passengers are allocated 24 kg of baggage. This cargo is placed in the front and rear cargo compartments placed at 30% and 80% of the cabin as defined in Section 8.6.3. Thus, the loading of the cargo can be analysed for front to back and back to front loading. The CG extrusion for cargo loading can be found at the bottom of Figure 11.1.

11.2.2. Passenger Loading

The layout of the cabin is defined in Section 8.6.2. From this one can extract all the seat locations along the x axis. With the business class having a 2-1-2 configuration and the economy class having a 2-3-2 configuration one can determine the center of gravity of different loading situations. The window-aisle-middle rule is used for loading. Meaning that first, the window seats will be filled, then the aisle seats and lastly the remaining middle seats. For determining the CG limit for passenger loading both front to back and back to front loading options are assessed. Each passenger has a mass of 80 kg and has 5 kg of hand baggage allocated. This results in the two curves for passenger loading in Figure 11.1.

11.2.3. Fuel Loading

Lastly, the fuel is added to the loading diagram. The fuel weight is determined in by the mission profile in Section 16.2. The fuel weight is placed at 40% of the MAC of the main wing and consequently moves with the wing positioning.

11.2.4. Aircraft Loading Diagram

The loading diagram can be plotted for different wing positions and as such the CG range of different wing positions can be determined. Figure 11.1 shows the aircraft loading diagram for the final wing positioning of xLEMAC at 41.4% of the fuselage. Furthermore, Figure 11.2 shows the CG range of different wing positions. This diagram is used in combination with the scissor plot from Figure 11.4 to determine the final wing positioning and the final horizontal tail surface area. Section 11.3

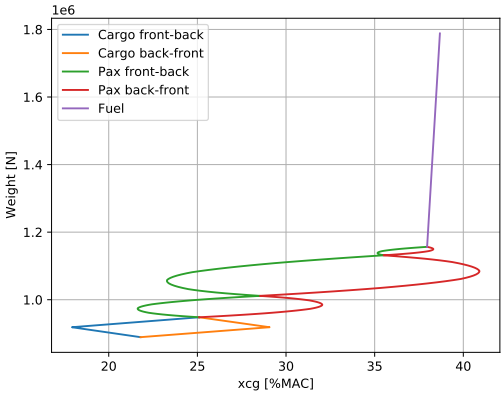

Figure 11.1: Aircraft loading diagram showing the aircraft CG range under different loading scenarios

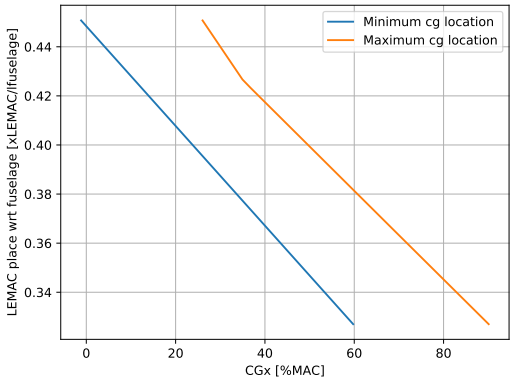

Figure 11.2: Wing placement diagram showcasing how the CG range changes with wing placement

The final CG range can be found in Table 11.4. The CG range is compared with that of an Airbus A330-200, with the data taken from its weight and balance manual [2]. Due to the sweep that is present on the A330-200 and not on the low-ATR concept the CG range in terms of the MAC is not a good comparison. When looking at the CG range in terms of the RC however, one can see that very similar CG locations arise and that the CG range is also very similar. This CG range is used to place the wing and size the horizontal tail surface in the next sections.

Table 11.4: Aircraft centre of gravity range compared to that of a Airbus A330

	Most forward CGx (%MAC)	Most rear CGx (%MAC)	Most forward CGx (%RC)	Most rear CGx (%RC)
Low-ATR concept	16.92	41.91	20	38
Airbus A330-200	-77	-47	17	41

11.3. Sizing for Static Stability and Control

11.3.1. Stability

The stability of the aircraft can be assessed by the method of Torenbeek [106]. Geometric definitions, forces and moments relevant for the stability analysis can be found in Figure 11.3.

In order to be stable the aircraft center of gravity must be in front of the neutral point. The neutral point is defined as the point trough which the resultant change in lift acts due to a change in angle of attack. Consequently, a increase in angle of attack will lead to a change of moment around the neutral point of 0. Thus, Equation 11.3 holds.

$$\Delta M_{\text{np}} = \Delta L_{\text{A-h}}(\bar{x}_{\text{np}} - \bar{x}_{\text{ac}}) - \Delta L_{\text{h}}(\bar{x}_{\text{h}} - \bar{x}_{\text{np}}) = 0 \tag{11.3}$$

By making the substitutions of Equation 11.4 and Equation 11.5 one gets Equation 11.6.

$$\Delta L_{\text{A-h}} = C_{L_{\alpha_{\text{A-h}}}} \Delta\alpha \frac{1}{2}\rho V^2 S \tag{11.4}$$

$$\Delta L_{\text{h}} = C_{L_{\alpha_{\text{h}}}} (\Delta\alpha - \Delta\epsilon) \frac{1}{2}\rho V_{\text{h}}^2 S_{\text{h}} \tag{11.5}$$

$$\bar{x}_{\text{np}} = \bar{x}_{\text{ac}} + \frac{C_{L_{\alpha_{\text{h}}}}}{C_{L_{\alpha_{\text{A-h}}}}} \left(1 - \frac{d\epsilon}{d\alpha}\right) \frac{S_{\text{h}} l_{\text{h}}}{S\bar{c}} \left(\frac{V_{\text{h}}}{V}\right)^2 \tag{11.6}$$

By adding in a safety factor, $SM = \bar{x}_{\text{np}} - \bar{x}_{\text{cg}}$ we reach Equation 11.7 which is the final equation that has to be satisfied. The free variables are x_{cg} and $\frac{S_{\text{h}}}{S}$. The other parameters are estimated using Torenbeek[106] methods. The values for the parameters can be found in Table 11.5. The stability equation with and without a safety margin is plotted on Figure 11.4.

$$\bar{x}_{cg} = \bar{x}_{ac} + \frac{C_{L_{\alpha_h}}}{C_{L_{\alpha_{A\text{-}h}}}} \left(1 - \frac{d\epsilon}{d\alpha}\right) \frac{S_h l_h}{S\bar{c}} \left(\frac{V_h}{V}\right)^2 - SM \tag{11.7}$$

11.3.2. Controllability

Stability of an aircraft comes at the cost of controllability. To ensure that the aircraft can still be controlled the moment equation of the aircraft must be satisfied for trim condition. Figure 11.3 gives the geometric definitions, forces and moments. Taking the moment equation around the aerodynamic center and setting the moment equal to zero gives Equation 11.8

$$M = M_{ac} + W\left(x_{cg} - x_{a\,c}\right) - L_h l_h = 0 \tag{11.8}$$

Substituting $W = L_{A\text{-}h}$ and making the equation dimensionless gives Equation 11.9

$$\bar{x}_{cg} = \bar{x}_{ac} - \frac{C_{m_{a\,c}}}{C_{L_{A\text{-}h}}} + \frac{C_{L_h}}{C_{L_{A\text{-}h}}} \frac{S_h l_h}{S\bar{c}} \left(\frac{V_h}{V}\right)^2 \tag{11.9}$$

The free variables are x_{cg} and $\frac{S_h}{S}$. The other parameters are estimated using Torenbeek[106] methods and can be found in Table 11.5. The controllability line is plotted on Figure 11.4.

11.3.3. Scissor plot

In Figure 11.4 one can see the scissor plot of the aircraft. The scissor plot is used to size the horizontal tail surface and to determine the wing position. By overlapping Figure 11.2 with Figure 11.4 one can determine the optimal wing positioning for minimising tail surface. A few iterations are done and the final results are plotted. The xLEMAC is placed at 41.4% of the fuselage and the required tail surface fraction $\frac{S_h}{S}$ is 0.21 . Figure 11.4 shows that with this surface fraction and the centre of gravity range defined in Section 8.3 the stability and control requirements are met. The final horizontal tail parameters are presented in Table 11.6.

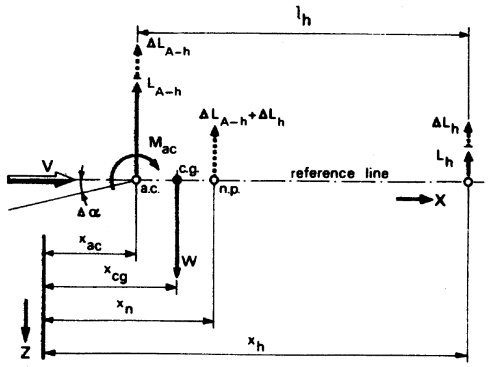

Figure 11.3: Geometric definitions, forces and moments for the longitudinal stability and control analysis of an aircraft [106]

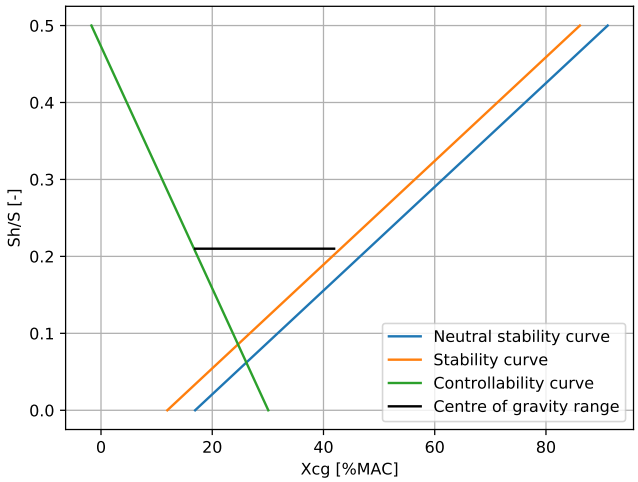

Figure 11.4: Scissor plot of the aircraft

Table 11.5: Aircraft parameters required for stability and control analysis

Parameter	Value	Parameter	Value
x_{ac}	0.169	$C_{m_{ac}}$	-0.410
$C_{L_{\alpha_h}}$	4.87	C_{L_h}	-0.640
$C_{L_{\alpha_{A\text{-}h}}}$	6.48	$C_{L_{ah}}$	3.12
$\frac{d\epsilon}{d\alpha}$	0.363	l_h	28.0
$\frac{V_h}{V}$	0.85	$\bar{c}$	6.53

Table 11.6: Horizontal tail planform parameters

Parameter	Value	Parameter	Value
S_h [m^2]	87.4	$C_{t,h}$ [m]	1.84
b_h [m]	23.1	λ_h	0.320
Ar_h	6.10	$\Lambda_{qc,h}$ [rad]	0.248
$C_{r,h}$ [m]	5.74		

11.4. Vertical Tail Sizing for One Engine Inoperative

For a configuration with wing mounted engines, the vertical tail size is limited by the one engine inoperative scenario [106]. The rudder will have to be able to deal with the moment generated by the thrust difference. Torenbeek [106] provides a fast sizing method for OEI in Figure 11.5. Another figure is available for propeller aircraft. Given that the low-ATR aircraft concept will use propfans, both options for sizing might seem viable. However, the sizing for jet aircraft is a bit more

conservative and hence it was chosen as the best option.The design point can be found on the figure. The final vertical tail parameters are found in Table 11.7.

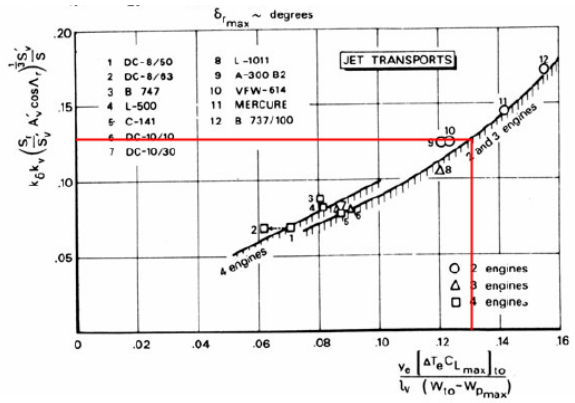

Figure 11.5: A quick sizing method for the vertical tailplane for the one engine inoperative scenario [106]

Table 11.7: Vertical tail planform parameters

Parameter	Value	Parameter	Value
S_v [m^2]	68.7	$C_{t,v}$ [m]	3.00
b_v [m]	11.1	λ_v	0.320
Ar_v	1.80	$\Lambda_{qc,v}$ [rad]	0.576
$C_{r,v}$ [m]	9.36		

11.5. Empennage Spin Characteristics

If the aircraft is in a sideslipping, high angle of attack flight there is a high chance of getting into a spin. This spin could become uncontrollable if a large portion of the vertical tail is shielded by the horizontal tail. As indicated in MATRA-SSYS-SAC-07c, no more than 2/3 of the rudder area shall be shielded by the horizontal stabiliser in the event of an aggravated spin with 45 ° angle of attack. In Figure 11.6 the portion of the rudder that is shielded in such an event is shown. It was calculated that the shielded rudder area is about 11.4 m^2. The total rudder area is 20.3 m^2, thus 56 % of the rudder is shielded. This means the spin characteristics of this empennage are sufficient.

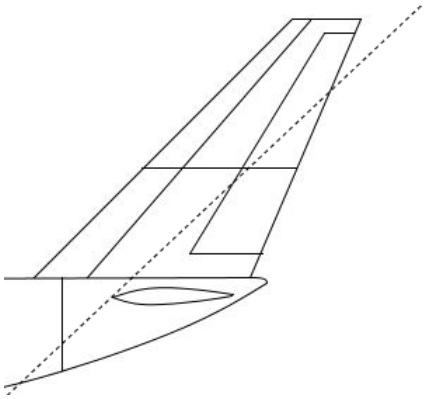

Figure 11.6: Shielded portion of the rudder during a spin

11.6. Control Surface Sizing

The control surfaces of the aircraft are placed and sized by using reference data. In Table 11.8 one can find the parameters related to the control surface sizing and placement. The reference aircraft are the Boeing 737-200, 747-200B and 767-200 with the data coming from Roskam [86]. The airlerons are split into a inside and a outside aileron. The inside is for use in cruise, The control surfaces are visualised on the aircraft three-view in Figure 8.7.

The hinge moment created by the ailerons during deflection is of importance for the design of the wingbox of the main wing. As such the maximum hinge moment coefficient has to be determined. The hinge moment is defined in Equation 11.10. The hinge moment coefficient can be expressed in terms dependent on the angle of attack and the aileron deflection. The equation for the hinge moment coefficient can be found in Equation 11.11. The first term is equal to 0 for symmetrical airfoils, for unsymmetrical airfoils no data could be found and thus a value of 0 was assumed. The second and third terms are determined via Roskam[90]. In Figure 11.7 and Figure 11.8 one can find the values for the hinge moment coefficients for different angle of attacks and aileron deflections. These hinge moments will be taken into account in the design of the wing box in Chapter 15.

Table 11.8: Aircraft control surface parameters compared to reference aircraft [86]

Parameter	737-200	747-200B	767-200	Low-ATR concept
S_e/S_h	0.27	0.24	0.23	0.24
S_r/S_v	0.24	0.3	0.35	0.25
S_a/S	0.024	0.040	0.041	0.040
Elevator/chord fraction	0.30/0.32	0.29	0.3/0.25	0.33
Rudder/chord fraction	0.25/0.22	0.30	0.33/0.36	0.36
Inside aileron/chord fraction	none	0.17/0.25	0.23/0.20	0.15
Outside aileron/chord fraction	0.23/0.30	0.11/0.17	0.16/0.15	0.15
Elevator halfspan fraction	unknown	unknown	unknown	0.10/0.79
Rudder span fraction	unknown	unknown	unknown	0.10/0.74
Inside aileron halfspan fraction	none	0.38/0.44	0.31/0.40	0.38/0.46
Outside aileron halfspan fraction	0.74/0.94	0.70/0.95	0.76/0.98	0.7/0.95

$$H_a = \frac{1}{2} C_{H_a} \rho V^2 S_a \bar{c}_a \qquad (11.10)$$

$$C_H = C_{H_0} + \frac{dC_H}{d\alpha}\alpha + \frac{dC_H}{d\delta}\delta \qquad (11.11)$$

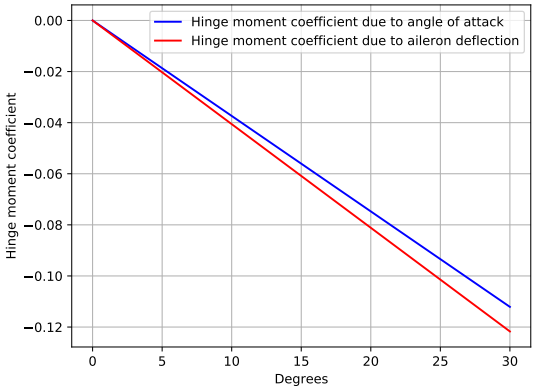

Figure 11.7: Inside aileron hinge moment coefficient due to angle of attack and aileron deflection

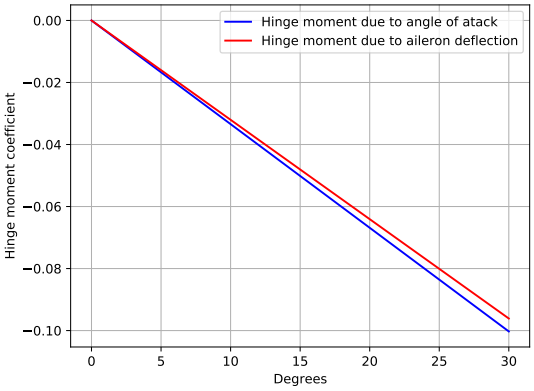

Figure 11.8: Outside aileron hinge moment coefficient due to angle of attack and aileron deflection

11.7. Aircraft Moments of Inertia

To analyse the dynamic stability of the aircraft, the moments of inertia of the aircraft will have to be determined. As a proper determination of the MOI's of the aircraft is not viable at the conceptual design phase, a method from Roskam [89] based on statistics is used. The moments of inertia are analysed at takeoff, cruise and landing conditions. Table 11.9 gives the aircraft's moments of inertia. The MOI's will be used in Section 11.8 where a range of 5% around the determined MOI's is analysed.

Table 11.9: Aircraft moments of inertia around the centre of gravity

MOI	Takeoff	Cruise	Landing
Ixx [10^3 kg m^2]	12832	10433	8034
Iyy [10^3kg m^2]	23945	20877	17808
Izz [10^3 kg m^2]	45468	38877	32285

11.8. Dynamic Stability Analysis

The dynamic stability of an aircraft is crucial to its functioning. If an aircraft is dynamically unstable, it is difficult to control and the consequences can be disastrous. A fine example of the dangers of dynamic instability is the Japan Airlines Flight 123 crash. The Boeing 747 involved in the crash lost all hydraulics and its vertical stabiliser. As a result of the missing vertical stabiliser, the plane got into an unstable dutch roll mode, ultimately leading to the plane crashing into a ridge about 30 minutes after the mechanical failures.

As the low-ATR aircraft has a configuration that is not highly conventional, it is important to conduct a dynamic stability analysis. In this stage of the design a class 2 dynamic stability analysis will be performed. This analysis will be based on the method outlined in Roskam part 7, chapter 3 [91]. In a later design phase this analysis must be complemented by a class 3 dynamic stability analysis. At the end of this section a ride comfort analysis will be given as well.

11.8.1. Analysis Method and Regulations

A more detailed explanation of the analysis method is given in Roskam part 7 [90]. There are a couple of dynamic modes which will be analysed, which are the phugoid motion, short period motion, spiral motion and the dutch roll motion. In Roskam's method, the natural frequency (ω_n) and damping ratios (ζ) of those modes are estimated, using estimations of relevant stability derivatives. For the spiral motion the estimation shows whether or not the motion is stable and if it is not, it gives the time to double the amplitude (T_2).

Firstly, the stability derivatives must be estimated. This is done using an estimation method based on empirical data. This estimation method is given in Roskam part 6, chapter 10 [90]. The derivatives that were estimated are: $C_{l_\beta}, C_{n_r}, C_{n_\beta}$ and C_{l_r}. A number of assumptions were made in the calculations of those derivatives: firstly the horizontal tail contribution to C_{l_β} was neglected due to the small magnitude of $\frac{S_h b_h}{Sb}$. Secondly the sideslip downwash gradient was assumed to be 0. Furthermore, for all calculations the stability margin was assumed to be 5%, as this is the least allowable stability margin. This represents the least favourable COG or AC position. Using a script written in python the derivatives could be calculated for different flight conditions. Empirical values were taken from figures given in Roskam part 7.

As the CS25 regulations do not provide a numerical requirement on the dynamic modes of the aircraft, Roskam has provided military regulations in Roskam part 7, Appendix B. In the method it is mentioned that these can be used to do a preliminary analysis of the dynamic stability of an aircraft. Below in Table 11.10 the applicable regulations are given. Note that category B includes climb, cruise, loiter and descent and category C includes take-off, approach and landing.

Table 11.10: Military requirements on dynamic modes [8]

Motion	Category	ω_n (rad/sec)	ζ(-)	T_2 (s)
Phugoid	B	N.A.	min. 0.04	N.A.
	C	N.A.	min. 0.04	N.A.
Short period	B	0.3 - 2.0	N.A.	N.A.
	C	0.35 - 1.3	N.A.	N.A.
Spiral	B	N.A.	N.A.	min. 20
	C	N.A.	N.A.	min. 12
Dutch roll	B	min. 0.4	min. 0.08	N.A.
	C	min. 0.4	min. 0.08	N.A.

The analysis is done for a couple of flight conditions. These include take-off, landing, high cruise and low cruise. Low cruise includes loitering and leg patterns. High cruise is the flight condition for which the aircraft is designed (0.63 mach and 5 km). During the take-off the aircraft is assumed to fly at $1.3V_{\text{stall}}$, at sea level, flaps at take-off deflection and the landing gear extended. For landing the same configuration is used, except for the flap deflection being at the landing deflection. Note that the landing stall speed is lower than the take-off stall speed, so the speed is not equal to the take-off speed. In the low cruise flight condition the aircraft is assumed to fly at an altitude of 1 km, at a speed of 100 m/s in clean configuration.

11.8.2. Dynamic Stability Results

After calculating the stability derivatives, the estimation method could be used to calculate the natural frequencies and damping ratios of the dynamic modes. Below in Table 11.11 the results of the estimation method have been given for each flight condition.

As can be seen in the table, all dynamic modes adhere to the regulations, except for the phugoid motion during low cruise. The damping ratio is too low, meaning the damping of this motion is slow. However, as CS25 does not have numerical requirements for the phugoid motion and the period of this motion is large (estimated to be around 45 s) this value is considered acceptable. Furthermore, when computing the stability characteristics with the original 5 ° of dihedral, it was found that the spiral mode was unstable and the time to double amplitude was too low. Therefore the dihedral angle was increased to 7.5 °.

As MATRA-USER-PER-07 mentions that the aicraft should be able to operate in cross winds of 20 kts, it is checked whether this is the case. In Roskam part 7 it is mentioned that for lateral stability the aircraft should be stable in sideslip conditions (thus cross wind). For this C_{n_β} should have a positive value and C_{l_β} should have a negative value, which is the case in every flight condition for the low-ATR aircraft. Furthermore the stability derivatives are very comparable to operational airliners, which comply with the requirement as well.

Table 11.11: Dynamic stability analysis results

Motion	Flight condition	ω_n (rad/sec)	ζ(-)	T_2 (s)
Phugoid	Take-off	0.21	0.05	N.A.
	Landing	0.27	0.12	N.A.
	Low cruise	0.14	0.02	N.A.
	High cruise	0.07	0.06	N.A.
Short period	Take-off	0.44	1.24	N.A.
	Landing	0.56	1.16	N.A.
	Low cruise	0.65	1.25	N.A.
	High cruise	0.99	1.30	N.A.
Spiral	Take-off	N.A.	N.A.	16.2
	Landing	N.A.	N.A.	13.7
	Low cruise	STABLE	STABLE	STABLE
	High cruise	STABLE	STABLE	STABLE
Dutch roll	Take-off	0.51	0.33	N.A.
	Landing	0.48	0.40	N.A.
	Low cruise	0.75	0.24	N.A.
	High cruise	1.32	0.19	N.A.

11.8.3. Verification and Validation of Python Script

As the stability derivatives are computed using a python script and errors could be made, the code has to be verified and validated. The script for the phugoid and short period motion was validated using a Laplace transform computation of the natural frequencies and damping ratios of a Boeing 747 [55]. Using data from Roskam part 6, chapter 11 [90] a class 2 estimation of the Boeing 747 was performed with the script and compared to the data from the paper. In the python script the same flight conditions as in the paper were used and geometrical data from Roskam part 6 was used. In Table 11.12 the computed values are given. Note that the subscript ”p” is used for the phugoid motion and ”sp” for the short period motion.

Table 11.12: Validation of the phugoid and short period motion scripts

	$\omega_{n,p}$ (rad/sec)	ζ_p (-)	$\omega_{n,sp}$ (rad/sec)	ζ_{sp} (-)
Validation data	0.073	0.037	1.260	0.466
Python script	0.068	0.044	1.338	0.553

As shown in the table, the computed values are quite close to the values computed using a Laplace transform method. The differences in the values are most likely caused by the difference in the two methods. Moreover, the Roskam method is a class 2 estimation. In roskam part 7, chapter 3, the indication is given that class 3 methods should be used in later stages of the design, but class 2 is an excellent method to reach a sufficient level of confidence regarding the dynamic stability of a design [91].

Validation of the computations of the other 2 modes turned out to be difficult. Validation data was difficult to find, as well as detailed geometrical data needed for the analysis method. Validation of the script was done by comparing the sign and magnitude of computed derivatives to those of a Boeing 747 under the same flight conditions. Discrepancies in the values were present due to the different configurations of the airplanes. In Table 11.13 the computed derivatives and those of the Boeing 747 have been given.

Table 11.13: Validation of the lateral stability derivatives

	C_{l_β}(-	C_{n_r} (-)	C_{n_β} (-)	C_{l_r} (-)
Boeing 747 data [90]	-0.160	-0.280	0.160	0.130
Python script	-0.218	-0.194	0.160	0.155

The values were computed for both aircraft flying at the same flight conditions, which is at 7 km at a speed of 205 m/s. The computed values are the right sign and in the right order of magnitude for this flying condition. A direct comparison cannot be made due to the lack of accurate available data. However the confidence is high that this code is validated and is working correctly.

Verification of the code has been done using hand calculations and the Roskam book. Intermediate values were computed by hand and then compared to the computations of the script. No errors in the calculations were encountered.

11.8.4. Sensitivity Analysis of Moments of Inertia to Stability

The moments of inertia of the aircraft are computed using a fairly simplified method given by Roskam, therefore a sensitivity analysis is done. The moments of inertia have a considerable impact on the dynamic stability of the low-ATR aircraft. For this stability analysis a 5% increase or decrease was imposed on the moments of inertia of the aircraft. This resulted in the dynamic mode properties indicated in Table 11.14. A range of values have been given, first the value corresponding to an MMOI decrease has been given, then the value corresponding to an MMOI increase has been given.

Table 11.14: Moments of inertia sensitivity analysis

Motion	Flight condition	ω_n (rad/sec)	ζ(-)	T_2 (s)
Phugoid	Take-off	0.212-0.212	0.047-0.047	N.A.
	Landing	0.267-0.267	0.118-0.118	N.A.
	Low cruise	0.139-0.139	0.018-0.018	N.A.
	High cruise	0.069-0.069	0.056-0.056	N.A.
Short period	Take-off	0.456-0.0.433	1.237-1.247	N.A.
	Landing	0.573-545	1.151-0.164	N.A.
	Low cruise	0.666-0.634	1.248-1.255	N.A.
	High cruise	1.015-0.966	1.300-1.307	N.A.
Spiral	Take-off	N.A.	N.A.	15.38-17.00
	Landing	N.A.	N.A.	13.01-14.38
	Low cruise	STABLE	STABLE	STABLE
	High cruise	STABLE	STABLE	STABLE
Dutch roll	Take-off	0.520-0.495	0.333-0.323	N.A.
	Landing	0.497-0.473	0.401-0.392	N.A.
	Low cruise	0.771-0.733	0.241-0.235	N.A.
	High cruise	1.353-1.287	0.192-0.188	N.A.

From the table it becomes apparent that the aircraft is still sufficiently stable when taking uncertainty in the MMOI calculation into account. The military requirements are met and the differences in the dynamic mode properties are small.

11.8.5. Ride Comfort Analysis

As the low-ATR aircraft will be transporting passengers, it is important it has a sufficient level of ride comfort. Therefore a ride comfort analysis is performed. The analysis is done according to the method described in Roskam part 7, chapter 4. This method uses a gust/turbulence probability and computed stability derivatives to provide a ride comfort rating. Data on passenger satisfaction has been compared to these ride comfort ratings, which results in a rating to passenger satisfaction relation [91].

The computed ride comfort ratings for the low-ATR aircraft were in the range of 2.0 - 2.03, using the least favourable gust and turbulence probabilities. As indicated in Roskam part 7, the passenger satisfaction has to be at least 80%, which is achieved at a ride comfort rating of at most 4. The passenger satisfaction of the low-ATR aircraft is around 95%.

12. Class II Drag Estimation

In the previous Midterm Report [39], a preliminary estimation of the parasitic drag $C_{D,0}$ of the complete aircraft was made based on a statistical approximation of the equivalent skin-friction coefficient of the aircraft and the ratio of the wetted surface area to the reference area. Having now conducted sub-system level design and analysis, a more accurate estimation of the parasitic drag of the aircraft can be made using a higher fidelity component build up method. A defining feature of this aircraft will be its use of riblets to reduce the turbulent skin-friction drag, hence this reduction will also be accounted for in the model. Therefore, this chapter will begin with a description of the component build up method and a computation of the complete drag breakdown of the aircraft. Following this, the theory behind riblets and the modifications to account for them will be discussed. A new drag breakdown which utilizes riblets will be presented, along with the relative performance gains of using riblets.

12.1. Component Build Up Method

Being able to accurately estimate the amount of drag an aircraft experiences is important not only for the aerodynamic department, but also for the propulsion department as well as flight performance. With the total drag at cruise, this sets a lower limit on the amount of thrust the engines must produce at cruise, as well as provides the aerodynamic efficiency of the aircraft and thereby the range of the aircraft by the Breguet range equation. In the previous Midterm Report [39], the following estimation for the parasitic drag was used:

$$C_{D,0} = C_{f,e}\frac{S_{wet}}{S_{ref}} \tag{12.1}$$

This estimation method is crude in that it does not account for pressure drag due to viscous separation, nor does it account for the boundary layer interaction between components. This was the motivation behind looking for a higher fidelity estimation method, namely the component build up method. This method estimates the drag contribution of each major aircraft component and sums them together. The estimation model is as follows:

$$C_{D,0} = \frac{1}{S_{ref}} \sum_{c} C_{f,e_c} \times FF_c \times IF_c \times S_{wet_c} + \sum C_{D,misc} \tag{12.2}$$

$$C_{f,e} = C_{f,lam} \times f + C_{f,turb} \times (1-f) = \frac{1.329}{\sqrt{Re_{sub}}} \times f + \frac{0.455}{(\log_{10} Re_{sub})^{2.58}(1+0.144M_{\infty}^2)^{0.65}} \times (1-f) \tag{12.3}$$

The term FF, denotes the form factor component, a factor that estimates the pressure drag due to viscous separation as a result of the shape of a component. It is calculated using the methods provided by Raymer [82]. IF denotes the interference factor. This is a measure of the the effect that each component has on the drag experienced by other components. This IF is the result of the interaction between boundary layers at the connection of two components. As airflow travels around a component, it is accelerated to a velocity higher than the freestream V_{∞}. Therefore, this flow has a higher dynamic pressure, and components immersed in the this flow will experience greater drag. The interaction itself of the boundary layer also contributes to an increase in drag since the boundary layer at the point of interaction thickens. S_{wet} denotes the wetted surface area of an individual component. The term $C_{f,e}$ denotes the equivalent skin-friction drag coefficient of a component. Boundary layers consist of three main regions: laminar, transition and turbulent. For the purposes of this analysis, the transitional region which is in reality of finite length will be treated as a point. The amount of skin-friction drag felt in a boundary layer depends on the velocity profile $\partial u/\partial y$ of the boundary layer. Turbulent boundary layers have a much fuller velocity profile and hence a higher skin-friction drag. This effect is captured in Equation 12.3, where f is used to denote the fraction of laminar flow over the component. The final summation term of Equation 12.2 takes into account the fuselage upsweep drag, the fuselage base drag, drag due to flap deployment, and wave drag. Note, the wave drag for this aircraft is set to zero since in Section 9.1 it was found that the free stream Mach number is less than the critical Mach number of the airfoil.

12.2. Influence of the Propfan Wake on Skin Friction Drag

Although the method found in Raymer presents a comprehensive high fidelity yet still empirical drag estimation, it does not offer a way to quantify the increase in skin-friction drag caused by the presence of the wing-mounted propfan engine. Within the wake of the open-rotor, the flow is at a higher velocity than the freestream, and the increase in drag that components in the wake experience is called scrubbing drag. Research by Dorsey and Uranga into the modelling and performance analysis of open rotor engines, presented a method to model the increase in dynamic pressure and thereby the increase in drag within the rotor wake [29]. The nacelle and part of the wing will experience a new dynamic pressure, q_{scrub}. The new skin-friction drag of the nacelle can be computed as follows:

$$q_{scrub} = \frac{1}{2}\rho(V_{\infty} + \Delta V)^2 \tag{12.4}$$

$$C_{D,0nacelle} = \frac{1}{S_{ref}} \times FF \times C_f \times S_{wet} \times \Delta q \tag{12.5}$$

With $\Delta q = \frac{q_{scrub}}{q_{\infty}}$. When computing the increase in drag of the wing due to scrubbing, first the region which will be effected by this increase in flow velocity needs to be identified. For the in-house drag model, this area known as the scrubbed scrubbed area A_{scrub} was assumed to equal the product of the wing chord length at the point where the propfan is placed and the diameter of the rotor blade. The increase in skin-friction drag of the wing can be computed using once more the adjustments presented by Dorsey and Uranga [29]:

$$\Delta C_{D,0wing} = \frac{1}{S_{ref}} \left((\Delta q - 1) \times A_{scrub} \times C_f\right) \times 1.3 \tag{12.6}$$

12.3. Drag Breakdown without Riblets

To carry out the component breakdown method as discussed in Section 12.1, closed-form equations for the form factor, wetted surface area and the interference factor estimations will be taken from Raymer's book on aircraft design [82]. Although estimations on the fraction of laminar to turbulent flow can also be taken from Raymer, it is worth a small discussion. No detailed care will be taken into the horizontal and vertical tails in this analysis and their f values will be taken as 0.35 as given in Raymer. Since the propulsion system is a puller propfan, the entire region in the wake of the propfan will be turbulent and therefore f will be taken as 0 for the nacelles. For the fuselage, f has also been taken from the book of Raymer as 0.2. Whilst in Raymer, the wing is given a value of 10%, it is felt that this is quite low considering the NLF airfoil technology and low sweep the envisioned wing is adopting. With a low sweep angle, cross-flow instabilities are attenuated thereby maintaining boundary layer stability and delaying transition [97]. The choice of an NLF airfoil was also motivated by this requirement to employ laminar flow control to delay transition. With these two, it has already been shown experimentally that the boundary layer of the wing can remain up to 60% laminar [1]. However, since the accelerated

[1] `https://blogs.nasa.gov/armstrong/2011/02/11/post_1296777084480/` (last accessed on 18/06/2021)

flow from the propfan over the scrubbed wing area will be fully turbulent, an average of 40% was taken. For calculations of the induced drag coefficient, the lift coefficient was found by assuming the weight is equal to the lift.

Table 12.1: Complete drag breakdown of the aircraft in landing, take-off and cruise conditions.

Drag component	Landing	Take-off	Cruise
Skin friction	0.0116045	0.01153337	0.00962569
$C_{D,misc}$	0.0756462	0.01966421	0.00087775
Total $C_{D,0}$	0.09379451	0.0335374	0.0112912
$C_{D,i}$	0.21941073	0.26288142	0.00257469
$C_{D,Tot}$	0.31320524	0.29641882	0.01386589
L/D	5.89112729	8.44622761	19.91238447

Table 12.1 shows the complete drag breakdown of the aircraft due to skin-friction, miscellaneous drag components, and induced drag. These values will act as the base value, and will be compared in Section 12.5 with the drag when riblets are applied to quantify the performance gain in using riblets.

12.4. Riblet Technology

Riblets are micro-groves aligned in the streamwise direction that have been shown to reduce the turbulent skin-friction drag at full scale conditions up to 5% [103]. The physical mechanism behind riblets reducing turbulent skin friction drag has been researched extensively, and there exists a general consensus as to the flow phenomena that occurs over small riblets. Streamwise vortices near a wall induce lateral flow fluctuations in the viscous sublayer. Small riblets have been shown to dampen these lateral fluctuations by lifting the vortices upwards away from the wall, thereby reducing the turbulent stresses on the wall and the coefficient of skin-friction [68]. The amount of drag reduction achievable depends on the geometry and spacing of the riblets.

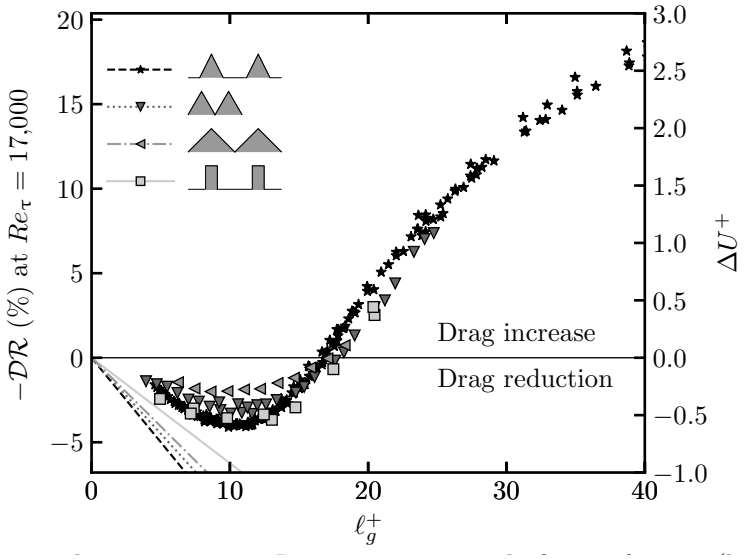

Figure 12.1: On the left axis, the drag reduction at $Re_\tau = 17000$, and on the right axis the velocity shift relative to a smooth wall of four varieties of riblet configurations [60]

Figure 12.1 displays both the velocity shift relative to a smooth wall ΔU^+ and the drag reduction due to riblets as a function of the viscous-scaled square root of the groove cross-sectional area, $l_g^+ \equiv \sqrt{A_g}/\delta_v$ [67]. The drag reduction due to riblets was quantified by Spalart and McLean [103] as:

$$DR \approx -\Delta U^+ \sqrt{2C_{f,s}} \qquad (12.7) \qquad C_{f,s} = (2log_{10}Re_x - 0.65)^{-2.3} \qquad (12.8)$$

The region in which small riblets reduce drag is known as the viscous regime, within which increasing l_g^+ increases the drag reduction linearly until an optimum value of 11. Further increasing l_g^+ causes a degradation of the viscous regime and ultimately drag increase [67]. One reason for this degradation is that increasing l_g^+ beyond this optimum gives rise to Kelvin-Helmholtz instabilities, increasing the Reynolds stresses locally and therefore the skin-friction drag [33].

What is clearly identified from Equation 12.8 is the relationship between the amount of drag reduction and the local Reynolds number. Since $C_{f,s}$ depends inversely with Re_x, to increase the performance benefits of the riblets it would be preferable to decrease the local Reynolds number. This can be done in one of two ways: flying at a higher altitude to increase the kinematic viscosity, or by flying at a slower Mach number.

12.5. Drag Breakdown with Riblets

The exercise presented in Section 12.1 can now be repeated with the inclusion of riblets. Equation 12.7 represents the percentage change in the turbulent skin-friction drag, and hence Equation 12.3 must be changed accordingly. Ideally, one would want to place riblets in all parts where the boundary layer is deemed to be turbulent on the wing, nacelles, tail and fuselage. However, due to restrictions imposed by maintenance, connection joints, and other factors, it is not possible to completely cover the turbulent wetted area with riblets. It was therefore estimated that with these limitations, 70% coverage of the wetted turbulent surface area with riblets would be feasible. Therefore, for the computation of the equivalent coefficient of skin-friction, there now exist three regimes: laminar boundary layer, turbulent boundary layer without riblets, and turbulent boundary layer with riblets. The model was updated with this new computation for the skin-friction drag:

$$C_{f,e} = C_{f,lam} \times f + \left(C_{f,turb} \times \left(1 - \frac{DR}{100} \right) \times 0.7 + C_{f,turb} \times 0.3 \right) \times (1 - f) \tag{12.9}$$

For the new drag computation, a value for U^+ of -1 was chosen.

Table 12.2: Complete drag breakdown of the aircraft in landing, takeoff and cruise conditions, and the reduction in drag relative to the no-riblet configuration

Drag component	Landing	% Reduction	Take-off	% Reduction	Cruise	% Reduction
Skin friction	0.01109671	-4.37580249	0.01102943	-4.369408074	0.00922949	-4.116068562
$C_{D,misc}$	0.0756462	-	0.01966421	-	0.00087775	-
Total $C_{D,0}$	0.09324863	-0.581995684	0.03299566	-1.615330944	0.01086529	-3.772052572
$C_{D,i}$	0.21871656	-0.31637924	0.26161305	-0.4824875033	0.00256251	-0.4730666605
$C_{D,Tot}$	0.31196518	-0.3959256876	0.29460871	-0.6106596066	0.0134278	-3.159479846
L/D	5.91454445	+0.3974987952	8.4981221	+0.6144102716	20.56204035	+3.262571999

Table 12.2 presents the complete drag breakdown for take-off, landing and cruise conditions. It also shows the reduction in drag per component relative to the results of the aircraft not adopting riblets in Table 12.1. What is clear from this analysis is that in each flight stage, the use of riblets results in a reduction in not only the skin-friction drag, but also the total aircraft drag, and consequently an increase in aerodynamic efficiency. Riblets bring the most performance gain in the cruise phase since the proportion to of skin-friction relative to the total parasitic drag $C_{D,0}$ is higher without the presence of flap drag. A value of 5% skin-friction drag reduction in cruise gives confidence in our model to estimate drag since it aligns with what has been estimated already in literature [67]. Since the cruise phase is also the flight phase the aircraft will spend the majority of its service time, a total drag reduction of approximately 4.5 % is extremely promising and will further promote reductions in ATR.

13. System Characteristics

An aircraft has several main systems. Each system has its own function and needs to be sized to the needs of the mission. In this chapter these systems will be defined and explained. In Section 13.1 the electrical system of the aircraft will be explained, in Section 13.2 the fuel system will be explained, in Section 13.3 the hydraulic system will be explained, in Section 13.4 the air conditioning system will be explained and finally in Section 13.5 the data handling and communication systems will be explained.

13.1. Electrical System

The electrical system of an aircraft is crucial for its functioning. The aircraft is full of components that need electric power. The hydraulic motors, fuel pumps, onboard computers, lighting, etc. all need electricity to function. Therefore it is important to size the electrical system accordingly and create a general layout of the electrical system. The sizing of the electrical system is done based on reference data of a DC10, given in Roskam part 4 [88]. It is sized according to MTOW. As the DC10 is a bit older than the low-ATR aircraft, a higher estimation of components like entertainment is made. Furthermore a distinction is made between essential and non-essential load requirements. The redundancy systems on the aircraft have to be sized for the essential load requirements, so the aircraft can at all times be provided with electrical power. In Table 13.1 the required electrical power for the different flight stages are given. Note that the 150 kW required by the electrical taxiing system (see Section 23.3), which is powered by fuel cells, has been added to the non-essential ground operations power budget.

Table 13.1: Required electrical power per flight stage

Flight stage	Non-essential power (kW)	Essential power (kW)
Ground loading	40 + 150 for ETS	11
Take-off and climb	82	25
Cruise	80	18

As can be seen in the table, the batteries and APU have to be sized for 25 kW as this is the highest essential required power. In case only one battery or only the APU is available, the plane should still get the required power. Furthermore in Figure 13.3 a flow diagram of the electrical system has been given. This layout is based on conventional electrical system layouts used on existing airliners

13.2. Fuel System

The fuel system of an aircraft is another crucial one. During flight this system should always supply the engines with fuel at the right flow conditions. Furthermore, the weight distribution of an aircraft is a crucial parameter in the stability of an aircraft. Since the fuel weight is a large chunk of the total weight, pumping around fuel through the different tanks is an ongoing process during flight. This means failure of one of the system components can have a significant impact on the performance of an aircraft. To account for failure, redundancy is installed in the system. Every fuel tank has two fuel pumps, so failure of a pump will not affect the system. Additionally, suction valves have been installed on the wing fuel tanks. These allow the engines to be fed fuel using gravity, in case all fuel pumps fail. Vent tanks have been fitted to allow for expansion of the fuel and spill pipes have been installed to prevent fuel spills during refueling.

The fuel system layout of the low-ATR aircraft has been based on examples given in Roskam part 4 [88]. Note that the wing fuel tanks might be divided up in several tanks in the detailed design phase of this aircraft. The fuel distribution of the tanks has been based on reference aircraft and the required fuel capacity of the aircraft. The layout is shown in Figure 13.2.

13.3. Hydraulic System

The aircraft has parts that need to move in flight. most of them are moved with the help of hydraulics. It is important that when the hydraulics would fail the plane would still be controllable. Therefore two independent hydraulics systems are implemented. If one would fail the other takes over and the aircraft would still be controllable. A schematic diagram of the hydraulic system can be seen in Figure 13.1. There are two different pumps each running on a different system. The engine driven pump is the one that will be used in flight. The electrical pump will only be used if engine failure would occur or other unforeseen failures occur.

13.4. Air Conditioning System

As the low-ATR aircraft will obviously be transporting passengers, a proper air conditioning system is crucial. This system should provide fresh air to the passengers, as well as cabin pressurisation and temperature control. The system should provide about 0.57 m^3 of cabin air per minute per passenger [88], which for the low-ATR aircraft would equal about 143 m^3 of cabin air per minute in total. For the layout of the air conditioning system a conventional system is chosen. This means the incoming air comes from the engine bleed system. It is then directed into a pack where it is cooled and later mixed with the recirculation air in the mixing unit. A diagram of the layout is given in Figure 13.4.

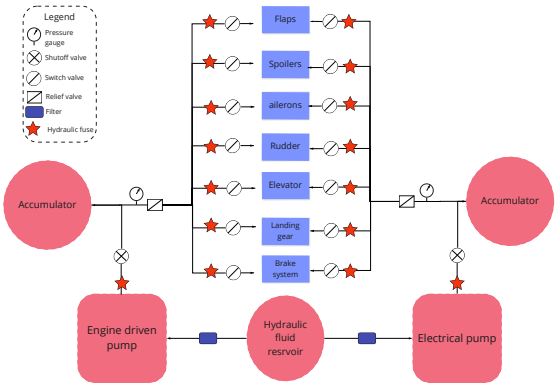

Figure 13.1: Hydraulics diagram

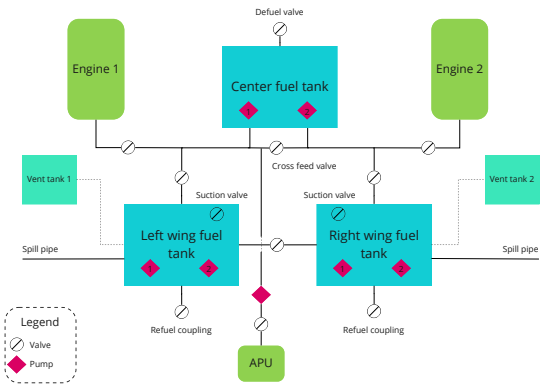

Figure 13.2: Fuel system layout

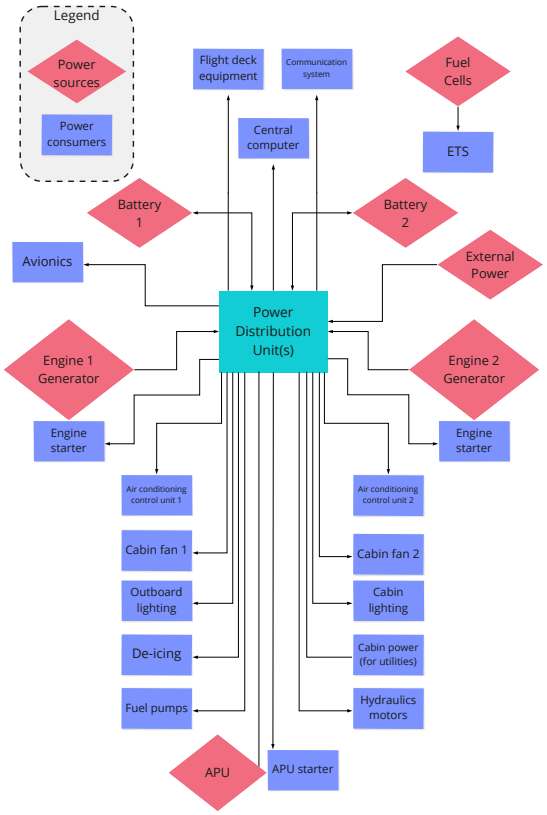

Figure 13.3: Electrical block diagram

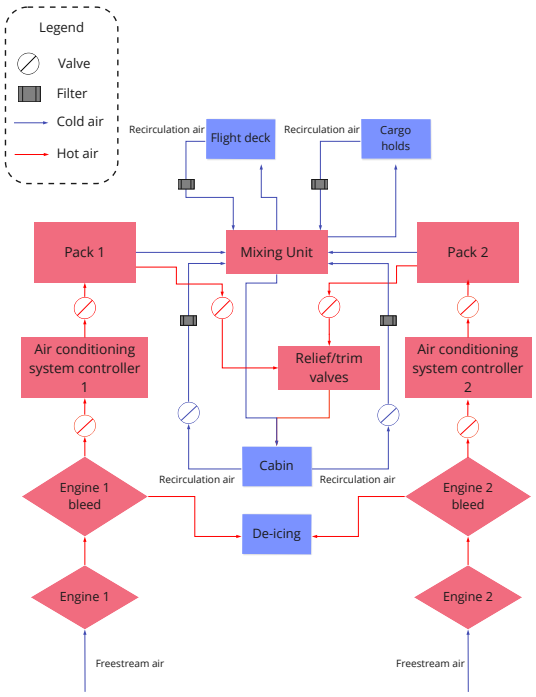

Figure 13.4: A schematic drawing of the airconditioning system.

13.5. Data Handling and Communication Systems

In modern aircraft a large number of data is processed during operations. Onboard computers process data at an extremely high rate. In order to ensure proper functioning of the aircraft as a whole, the data handling system of the aircraft should be designed well. The interface between software and hardware has to be established well. Data is collected by sensors, which is then processed by onboard computers after which the usable data is provided to the pilots. Furthermore automated systems are also used, which need to get the proper data. The pilots and these systems then respond to incoming data and give inputs to the system. Those inputs then need to be processed as well. An example is the autopilot system which receives processed sensor data from the onboard computer and feeds back inputs into the onboard computer. That data is then processed and fed into for example the flight control computer, which then provides an input to the control surface actuators. A general layout of the data handling system is given in Figure 13.5

Next to the data handling system of an aircraft, communication is also essential. Being closely linked to the data handling and hardware/software system of an aircraft, the communication system involves all communication interfaces. These include the communication between the pilots and the ATC, but also the communication between onboard computers and sensors or actuators. Furthermore a communication link between the system and the environment is also present. In Figure 13.6 the communication flow of the aircraft is provided.

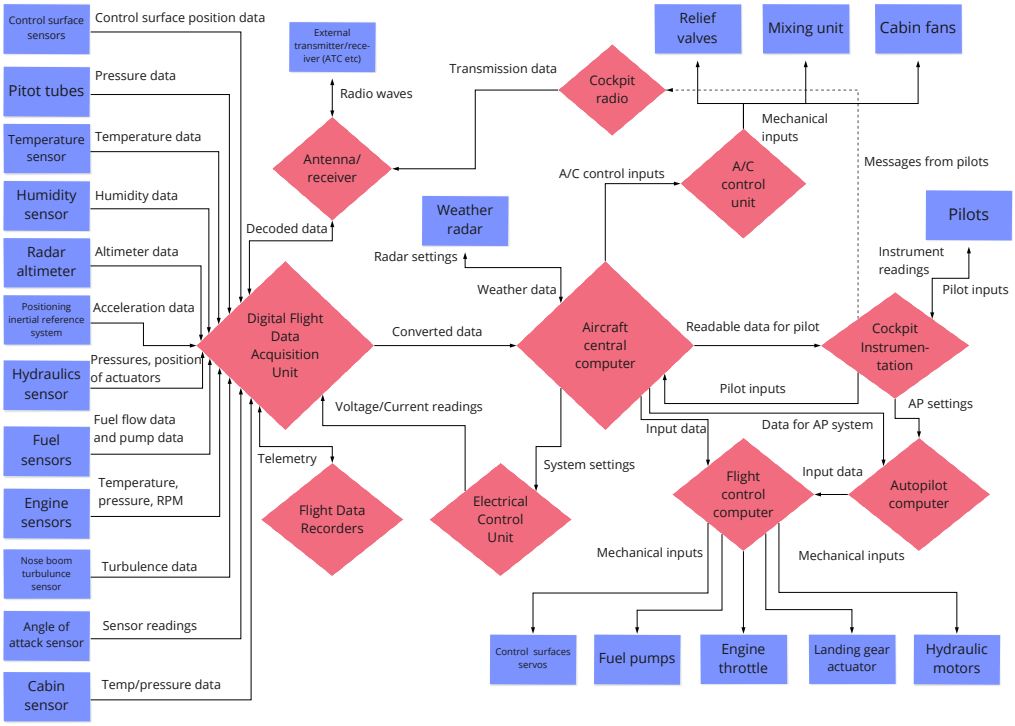

Figure 13.5: Hardware, software and data handling diagram

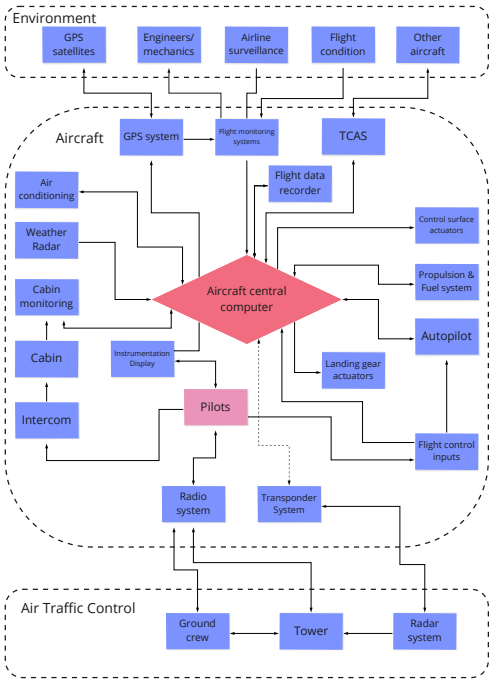

Figure 13.6: Communication flow diagram

14. Material Selection

In this chapter a material selection will be made for all the subsystems in the aircraft. This material selection can then be used in the future to proceed with the design. In Section 14.1 The selection philosophy of the materials will be explained. In Section 14.2 a material for the wing and the empennage will be chosen (which, was later revised in Section 15.5.2). Next in Section 14.3 the fuselage material will be chosen followed by The landing gear and engine material in Section 14.4 and

Section 14.5 respectively. In Section 14.6the materials of the cabin interior are discussed. In Section 14.7 the sustainability of the materials will be researched. Finally in Section 14.8 some concluding remarks and recommendations are given.

14.1. Selection Philosophy

In order to select a single material for a structure some constraints and criteria for which to optimise must be determined. First, to cut down the vast list of materials, some constraints will be set. According to the cost analysis [39] the materials used can not be more expensive than 500 EUR/kg (divide the total material cost by the total structural weight). Next to this a material must be tough enough especially as basis of primary structures in aircraft. Therefore the rule of thumb suggest no material should have a K_{1c} of less than 15 $MPam^{1/2}$. In order to sort out a lot of very light and very weak and elastic materials some extra constraints will be set based on engineering experience. Materials of primary airframe structures should not have lower values than these described below. The yield stress should not be lower than 75 MPa, The tensile and compressive stress should not be lower than 50 MPa. The E-modulus must be higher than 10 GPa and the shear modulus must be higher than 5 GPa. Although it is possible to coat and protect most materials from water it is still important that they can at least handle limited usage of fresh and salt water. If that coating would get damaged then the consequences will not be to severe if it is spotted on time. The materials should also be able to handle limited usage of lubricating oil and kerosene. The materials used should not be more flammable than 'slow-burning' as this would pose a great danger for passengers and the aircraft itself. The fuselage shall also be resistant against electricity to handle lightning strikes. The main component materials shall also not be on the EU critical materials list. Furthermore, the material shall have a SIN list indicator lower than 0.3, meaning the main component materials will not be toxic. All these constraints can be put in in the CES edupack software [57]. This gives a much shorter list of materials that can be used. The aerospace materials database will be used in the software for the material choice. There will be some additional constraints depending on which subsystem is designed for. These will be explained in their subsequent paragraphs.

The next step is to select the most suitable material for each subsystem. Therefore certain criteria will be determined, given weights and a trade-off will be done for each subsystem. In general, weight is a very important parameter for which the material should be chosen. However, this will not be included in the trade-off as a separate criterion. Instead, it will be included in multiple criteria where a certain mechanical property will be divided by the density. The strength criteria is used as it is one of the most important features of primary structures to not yield. This will be measured using the ratio $\frac{\sqrt{\sigma_y}}{\rho}$. The same will also be used for tensile, compressive and shear stress. Stiffness is the following criterion which will be used. For stiffness the ratio of $\frac{\sqrt{E}}{\rho}$ will be used to score this criterion. aeroelasticity will in some structures be of great importance, which can be countered by choosing a material with a high natural frequency this can be compared using the ratio $\sqrt{\frac{E}{\rho}}$. The next criteria is crack growth. This can be compared using the ratio $\frac{K_{1c}}{\sigma_y}$. When materials have high values of this ratio they will yield before they fracture. This is a desirable property; when cracks do not get spotted in time the structure will deform, which can often be clearly seen, before it will completely fracture. Comparable to this, fracture toughness will also be looked at separately in some cases. This is defined by the parameter K_{1c}. Fatigue is a failure mode which should always be carefully considered in moving structures. Due to vibrations, pressurisation and changing loads the structures will experience fatigue and the structure should be able to handle this. A useful parameter to measure the resistance of a material is the σ_e. Next to these criteria there are some additional criteria to be assessed for certain subsystems. The cost per unit mass will also be a trade-off criterion. Furthermore, sustainability and corrosion will also be looked at. Sustainability will be measured by the CO_2 footprint of the primary production. Corrosion will get a score of 1 till 4 based on the CES Edupack database.

In the following subsections a separate trade-off will be made for each subsystem as different subsystems require different weights and criteria. The basis for mechanical property requirements of each subsystem are derived from Figure 14.1. The trade-off is quantitative and based on the properties off the material. These values can not just be summed up to a final score as their magnitude is completely different and not comparable. Therefor the entries will be normalised. Then these will be multiplied with the weight of the criteria and these will be summed to get to the final score. The material with the highest score will be chosen for that subsystem. Which criteria that will be used for each subsystem is explained in their corresponding sections and are based on [104]. Figure 14.1b is used as a small sanity check. Furthermore, the whether a selected material is actually used for it's assigned purpose will also be analyzed by going through the CES Edupack database.

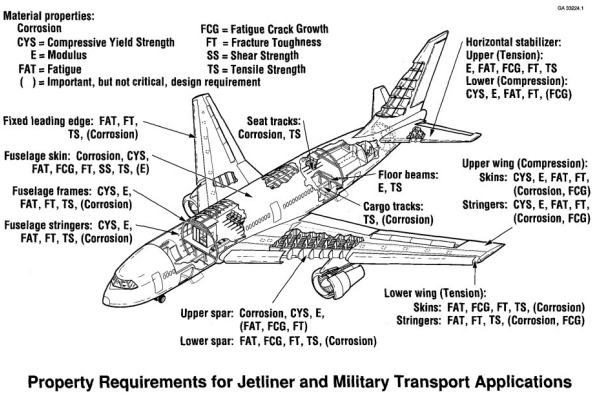

(a) material requirements [104]

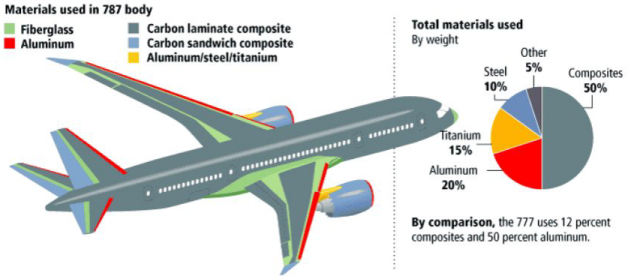

(b) Boeing 787 materials [1]

Figure 14.1: Material design process

14.2. Wing and Empennage Material Trade-Off

For the wing and empennage the criterion of fatigue will be looked at this is given a weight of 5 as the wing experience a great amount of vibrations and different loading cases. Then crack growth will be looked at. This is given a weight of 4. Next aeroelasticity is taken into account with a weight of 5. As the wing will highly likely encounter some aeroelastic problems due to the high aspect ratio. Then tensile and compressive stress are two separate criteria for the trade-off both with a weight of 2. The criterion of stiffness then gets a weight of 3 and corrosion will get a weight of 1. Finally the cost and sustainability of the material will also be considered for the wing and they both get a weight of 3. All of the criteria described above are used in the trade-off for the material of the wing and the empennage. The materials used for this trade-off were chosen with the constraints and extra materials have been excluded as the trade-off would become too large. The exclusion of the extra materials was done based on their the criteria. If the material scored really bad on a certain criteria it was eliminated. This left eight materials to be analysed. These materials can be seen in Table 14.1. The composites Epoxy/HS carbon fiber, UD prepeg, UD lay-up and Epoxy/aramid fiber, UD prepreg, UD lay-up are taken at 90% uni directional as a mitigation for load perturbations.

Table 14.1: Trade-off wing material [57]

Possible materials	Al(6061)-25%SiC(p) MMC powder	Al(AMC217-xa, T351)-17%SiC(p) MMC	Al(8089)-20%SiC(p) MMC powder	Aluminum, 2024, T3	Aluminum, 8019, rapid solidification
score	0.921	1.150	0.988	2.171	0.838
Possible materials	Aluminum, 7249, T76511	Al(AMC217-xa, T4)-17% SiC(p) MMC powder	Aluminum, 2090, T83	Epoxy/HS carbon fiber, UD prepeg, UD lay-up	Epoxy/aramid fiber, UD prepreg, UD lay-up
score	0.952	1.171	1.243	2.174	1.899

The final score of the trade-off can be observed in Table 14.1, which shows that Epoxy/HS carbon fiber, UD prepeg, UD lay-up attains the highest score, barely defeating Aluminum, 2024, T3. The Edupack database also states that this composite is commonly used in lightweight aerospace structures [57]. This material choice was revised in a later iteration, see Section 15.5.2.

Potential of Aluminium Composites

According to CES Edupack AMc's are currently not broadly used in Aerospace applications and they also did not win the trade-off. However, they do have tremendous potential by infusing the material with nano particles, called aluminum matrix nano-composite (AMNC). The main advantage of this material is that it has a high E-modulus while being produced with laser additive manufacturing (which allows for complex geometry and this in turn saves both weight and produced waste). AMNC has a yield strength of a 1000 Mpa, a Young's modulus of 20 GPa and thermal stability up to 400 °C; a comparison with other materials is shown in Figure 14.2 [58].

[1] `https://aviation.stackexchange.com/questions/35441/why-are-the-leading-edges-on-the-boeing-787-made-from-aluminum` (last accessed on 11/06/2021)

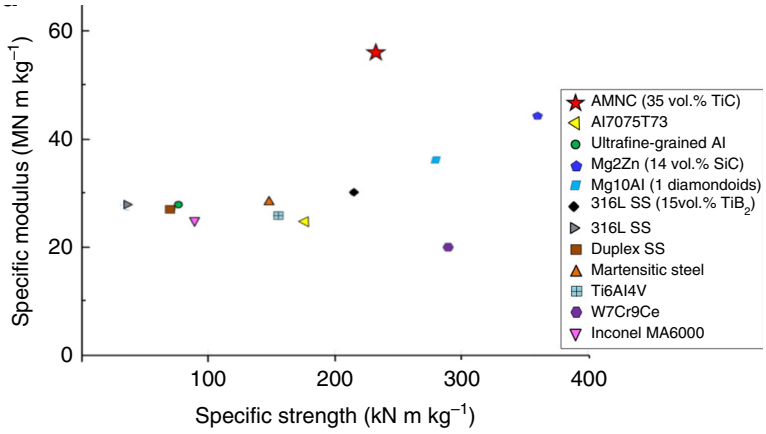

Figure 14.2: AMNC (35% TiC) compared to other aerospace materials [58]

14.3. Fuselage Material Trade-Off

The fuselage crack growth will be looked at with a weight of 4. Next, compressive and shear strength will be evaluated separately, both with a weight of 2. Then the stiffness will be given a weight of 2. Next fatigue will be given a weight of 5 as the fuselage must pressurise every flight and causes different loading and can result in fatigue. The cost and sustainability of the material will also be considered for the wing and they both get a weight of 3. The material of the fuselage must also pass the leak-before-break criterion (LBBC) as the fuselage is a pressure vessel. This is satisfied if Equation 14.1 is met. For this the pressure difference of cruising altitude and 6,000 ft will be used as this is most comfortable for passengers.

$$p \leq \frac{1}{Y^2 \pi R} \left(\frac{K_{1c}^2}{\sigma_y} \right) \tag{14.1}$$

The materials that are included in the trade-off are the same as the wing and empennage group as the constraints are very similar and the composites are again set at 90% unidirectional.

Table 14.2: Trade-off Fuselage material.

Possible materials	Al(6061)-25%SiC(p) MMC powder	Al(AMC217-xa, T351)-17%SiC(p) MMC	Al(8089)-20%SiC(p) MMC powder	Aluminum, 2024, T3	Aluminum, 8019, rapid solidification
LBBC	FALSE	FALSE	TRUE	FALSE	TRUE
score	0.895	1.115	0.948	1.276	0.804
Possible materials	Aluminum, 7249, T76511	Al(AMC217-xa, T4)-17% SiC(p) MMC powder	Aluminum, 2090, T83	Epoxy/HS carbon fiber, UD prepeg, UD lay-up	Epoxy/aramid fiber, UD prepreg, UD lay-up
LBBC	FALSE	TRUE	TRUE	TRUE	TRUE
score	0.868	1.139	1.021	2.074	1.542

The outcome of the trade-off can be seen in Table 14.2. It is clear that the material with the highest score also passes the LBBC and the material that will be used for the fuselage is again Epoxy/HS carbon fiber, UD prepeg, UD lay-up. It wins due to largely the same reasons as why it won for the wing and empennage. Note that the composite has an electrical resistivity of $1.82 * 10^5 muOm.cm$, which is five orders higher than that of metals. Therefore, the addiction on small thin metal rods as lightning rods could be considered to create a Faraday cage around the structure. Furthermore, the material is also self-extinguishing [57].

14.4. Landing Gear Material Trade-Off

For the landing gear there are some additional constraints on the material. This is a consequence of the high loads the landing gear must be able to endure. The E-modulus and yield stress must be higher than 150 GPa and 1000 MPa respectively. The fracture toughness must be higher than 30 MPam$^{1/2}$. These extra constraints are set as the impact of landing on landing gears can get rather high. Next to these constraints the landing gear material will be chosen with a trade-off as well. For this trade-off fatigue will be the first criterion with a weight of 5. Next crack growth with a weight of 4. Then stiffness and compressive stress both with a weight of 3. Sustainability, cost and corrosion will also be included with a weight of 3. In the trade-off only the material that can be seen in Table 14.3 will be looked at as only these materials passed all the constraints set for the landing gear.

Table 14.3: Trade-off Landing gear material [57]

Possible materials	Stainless steel, martensitic, FV535,	Stainless steel, martensitic, ASTM	Nickel-Co-Cr alloy, AEREX 350, cold worked,	Cobalt-base-superalloy, multiphase, MP35N,
score	1.851	1.553	2.882	2.702

The final scores of the trade-off are displayed in Table 14.3. There it can be seen that the material Nickel-Co-Cr alloy, AEREX 350, cold worked, aged get the highest score and will be used for the landing gear. While this material is currently not used for landing gear design, it is expected to be used for more aerospace applications in the future [113].

14.5. Engine Material Trade-Off

For the engine there will also be some additional constraints. Namely the high temperature E-modulus must be greater than 80 GPa. The high temperature strength must be atleast 500 MPa. The fracture toughness must be higher than 30 $MPam^{1/2}$. The high creep resistance must be smaller than 1E-4 $year^{-1}$. The corrosion and oxidation Resistance must be smaller than 10 µm $year^{-1}$. All of these constraints only leaves 4 materials to be chosen from. These four materials can be found in Table 14.4. Now these materials will be judged on following criteria. First the high temperature strength, which is given a weight of 3. Then on fracture toughness which has a weight of 3. Next the thermal expansion is given a weight of 5. Followed by the cost and sustainability, which will both get a weight of 3. Lastly the stiffness and the fatigue will be given the weights of 2 and 3 respectively.

Table 14.4: Trade-off engine material [57]

Possible materials	Titanium, near-alpha alloy, Ti-8Al-1Mo-1V,	Low alloy steel, Hy-Tuf, quenched & tempered	Intermediate alloy, Fe-9Ni-4Co-0.30C steel,	Maraging steel, 300, maraged at 482°C
score	1.870	2.048	2.072	1.944

The final result of this trade-off can be seen in Table 14.4. There it is clear that Intermediate alloy, Fe-9Ni-4Co-0.30C steel, quenched & tempered will be chosen. This is a steel alloy which is indeed often used in aircraft jet engines [57]. Table 14.5 shows some of the major properties of all the winning materials. These properties are also implemented in the structural design and subsequent sections.

Table 14.5: Material property chart [57]

	engine	wing	fuselage	landing gear
material property table	Intermediate alloy, Fe-9Ni-4Co-0.30C steel, quenched & tempered	Epoxy/HS carbon fiber, UD prepeg, UD lay-up	Epoxy/HS carbon fiber, UD prepeg, UD lay-up	Nickel-Co-Cr alloy, AEREX 350, cold worked, aged
density (kg/m^3)	7750	2600	2600	8620
price (EUR/kg)	26.3	70.7	70.7	41
yield stress (MPa)	1330 [H]	1950	1950	1360
Young's modulus (GPa)	202 [H]	141.5	141.5	216
fracture toughness (MPa.m^0.5)	125	66.85	66.85	75.5
primary C02 production (kg/kg)	3.37	48.2	48.2	24.6
fatigue stress 10^7 cycles (MPa)	675	1185	1185	519
compressive strength (MPa)	1510	1550	1550	1360
tensile strength (MPa)	1340	1960	1960	1360
shrear strength (MPa)	1340	1955	1955	1360
thermal expansion (µstrain/°C)	12.2	-0.14	-0.14	13.5

14.6. Cabin Materials

While the materials of the cabin, such as the wall panels, the seats, or the floor, may not have a critical structural function, their choice is important as it has an impact on things like the weight of the aircraft, the fire resistance, the environmental impact, or the passenger satisfaction. Sustainability is the focus for this part of the material selection, together with strict requirements such as the fire resistance. The possibilities for the cabin material choice are therefore recycled plastics for the less structurally demanding parts, and eco-composites.

Starting with plastics, they can be used for drawer doors or floor coating, but if a wrong management of plastic waste is done, it has serious environmental consequences. All plastics in an aircraft can be recycled (not re-used) [2], but they have to be carefully treated beforehand, and not contain impurities like paint, that could damage the future product where this plastic would be used. Furthermore, when possible, thermoplastics should be used, as they can be melted after having shaped them. Thermosets on the other hand, cannot be melted after curing due to the formation of cross-links between its polymer chains. During a detailed design phase, the components of each plastic part should be carefully documented, as it is crucial to know its composition for it to be recycled.

On the other hand, eco-composites show promise for their future implementation in future applications. Eco-composites use vegetable fibers in combination with a bio-based resin, that are less toxic than the standard carbon fibers. Furthermore, a fire-retardant is applied to the fibers so they are suitable for cabin usage. Promising results are being obtained with flax fibers, being researched for aircraft [3] and motor-sport [4] applications, such as seat shells or wall panels. This type of composites should be ready to operate in 5-10 years, and therefore they are to be used on the low-ATR aircraft [12].

[2] `https://www.aircraftinteriorsinternational.com/features/recycling-aircraft-interiors.html` (last accessed on 29/06/2021)

[3] `https://www.magoda.com/aerospace/new-sustainable-composite-material-for-aircraft-cabin-interiors/` (last accessed on 29/06/2021)

[4] `https://www.mclaren.com/racing/team/natural-fibre-sustainable-composite-racing-seat/` (last accessed on 29/06/2021)

14.7. Material Sustainability

The choice of material has great impact on the sustainability of the aircraft. The acquisition of the raw materials on itself has already a great influence and has been taken into account for the material trade-off. Next to this the forming of the materials can have a large impact on the emissions as some materials require a lot of energy to form and others such as composites needs to be put in an autoclave, which also requires a rather large amount of energy. These emissions from manufacturing a part out of a raw material is hard to quantify at this stage as it is not clear exactly which methods will be used. However, an attempt will be made by assuming the most common techniques for aircraft. Lastly, the end of life capabilities of the material will be looked at. The best case scenario for a material is reusability or recyclability. This way materials can be given new purpose and less raw material is needed. The worst case scenario is when a material can only be thrown away in a landfill and no energy or raw material can be obtained from it.

Table 14.6: Emissions regarding the use of the selected materials.

Materials	**Epoxy/HS carbon fiber, UD prepeg, UD lay-up**	**l NickelCoCr alloy,AEREX 350, cold worked, aged**	**Fe-9Ni-4Co-0.30C steel**	**Aluminium 7075 T6**
Raw material CO_2 footprint (kg/kg)	45.8	23.4	3.21	12.5
Manufacturing CO_2 footprint (kg/kg)	1.67	1.52	0.782	1.57
End of life strategy (+ CO_2) (kg/kg)	Downcycle	Recyclable (+4.55)	Recyclable (+0.77)	Recyclable (+2.48)
Total CO_2 footprint (kg/kg)	47.5	29.5	4.76	16.6

In Table 14.6 a summary is given of the CO_2 emissions of the materials used. These values were obtained using the CES edupack environment [5]. The aluminium alloy was added as a reference material as this material is the most used material for aircraft until recently. For the carbon fibre composite an autoclave molding manufacturing method is assumed, for the nickel alloy extrusion is assumed, for the steel alloy casting and for the aluminium alloy extrusion is also assumed. These are the most used manufacturing techniques for these materials with their purposes. It should be noted that recycling is better than downcycling, however, an additional CO_2 emission is given when the material is recycled. The carbon fiber composite has the most CO_2 emissions and can not be recycled. This material will also have the most contribution to the aircraft as it is used in the wings, empennage and the fuselage. This might not seem a very sustainable material. Yet the great benefits in weight saving due to its superior properties justifies the increase in emissions. As savings in weight causes the aircraft to be smaller and have less drag which means it has less required thrust therefore the engines use less fuel. When the aircraft flies 20 years these fuel savings have greater impact than the increase in material production emissions. It should also be noted that the footprint is given as the amount of mass of CO_2 that is released per kg of material. As there is less mass needed for the same structures with the carbon fibre composite a relatively less CO_2 will be emitted as well.

The metal alloys, which will be used, are all recyclable. This eases the end of life strategy and decreases their impact on the environment. The parts containing these metal alloys can be dismantled and the alloys themselves can then be send to a recycling company where it will be recycled. The carbon fibre composite can not be recycled, however, it can be downcycled. It is possible to give another purpose to the carbon fibre material so it does not have to be immediately discarded. This can only be done a few times as the material degrades every time. At the end of the life of the carbon fibre when it can not be downcycled anymore, it will be burned in order to get the remaining energy out of it.

14.7.1. Aircraft production C02 comparison

Figure 14.3 shows the CO2 production during the manufacturing phase (primary & secondary production and minus recycling) of the ATR aircraft, the A330-200 and the A350-900; from which the material composition was roughly acquired from various sources [4] [11] [57]. The A330 mass fraction is not publicly known and is therefore assumed to be the same as the A300 [89]. Overall, the ATR aircraft has a 30% lower CO2 production than an A330 and a 49% than an A350. Per kilogram of aircraft weight the ATR aircraft produces 28-, the A330 30 and the A350 35 kg of CO2. The riblet manufacturing CO2 production is 459 kg per ATR aircraft, which is based on the coating thickness, riblet area and reference urethane material [17] [57]. This confirms that the material trade-off succeeded in increasing aircraft sustainability. As a small note this calculation also returned an estimate of the riblet weight: 42 kg. This weight is negligible compared to the aircraft total structural weight and is therefore not included in subsequent calculations.

[5] `https://www.ansys.com/products/materials/granta-edupack` last visited 19/06/2021

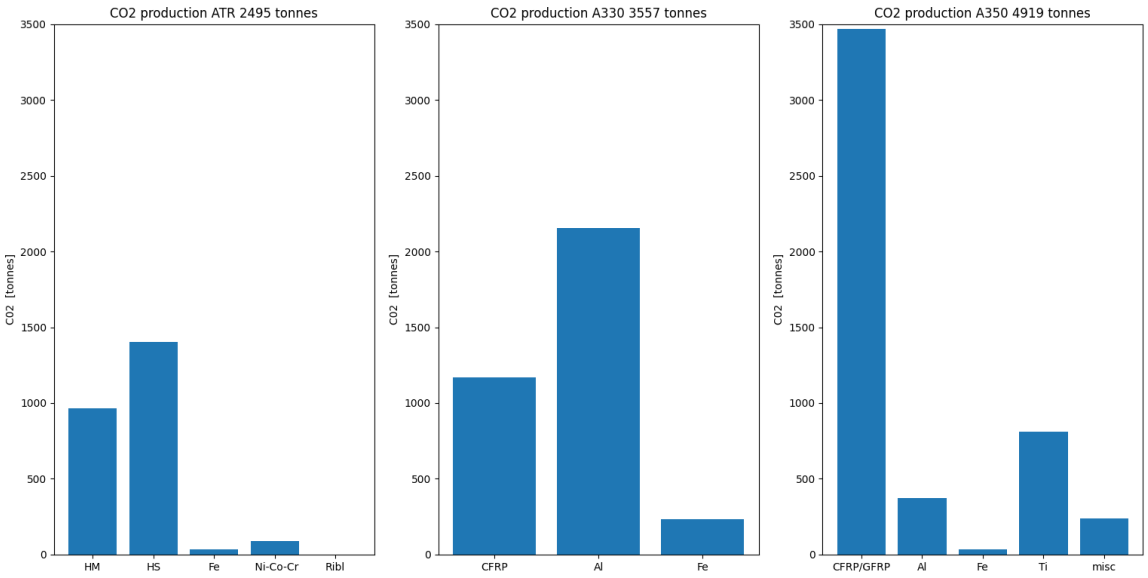

Figure 14.3: Manufacturing CO_2

A small note can be made about an aircraft riblet with paint comparison. Aircraft are roughly repainted every four years meaning the ATR aircraft will receive eight paintjobs during the 35 years of operation. Assuming riblets are reapplied during these jobs, the total riblet production emission is 3672kg. Furthermore, the riblet weight seems to be in the right order of magnitude as paint weights a few hundred kg for a Boeing 777 but is also 0.1mm thick [6].

Table 14.7 shows that the optimized end of life strategy (minimal CO_2 emission) in more detail for both the ATR aircraft and an A330-200; materials and component weight fractions are kept the same as in Figure 14.3. The ATR aircraft will dispose less CO_2 during disposal but significantly less material can be used for recycling.

Table 14.7: Disposal and End of Life emissions [57]

	ATR-AC		**A330-200**	
Disposal				
Component	**EoL option**	**CO_2 (kg)**	**EoL option**	**CO_2 (kg)**
wing	Landfill	270	Recycle	1700
fuselage	Landfill	360	Recycle	1400
empennage	Landfill	53	Landfill	68
engine	Recycle	530	Recycle	660
landing gear	Recycle	210	Recycle	530
Recycling				
Component	**EoL option**	**CO_2 (kg)**	**EoL option**	**CO_2 (kg)**
wing	Landfill	0	Recycle	-370
fuselage	Landfill	0	Recycle	-300
empennage	Landfill	0	Landfill	0
engine	Recycle	-280	Recycle	-35
landing gear	Recycle	-860	Recycle	-28
net total (tonnes)		-108.6		-725.5

14.8. Miscellaneous Materials and Recommendations

While Figure 14.1b is not an academic source, it did provide the inspiration to further investigate the use of sandwich structures in the vertical tail and the use of more impact resistant materials for leading edges on the wing and horizontal tail, nose cone and control surfaces. Sandwich structures can provide similar strength properties compared to laminates at a cost of less flexibility [73]. This means they could be used in areas that can be rigid such as the vertical tail or the yehudi.

A common problem with composites is that they are not very impact resistant due to their an-isotropic nature. Normally the impact vulnerable areas, leading edges on the wing and horizontal tail, nose cone and control surfaces, are made from an isotropic material such as aluminium (see Figure 14.1b) or with an additionally reinforced composite such as

[6] https://www.boeing.com/commercial/aeromagazine/aero_05/textonly/fo01txt.html (accessed on 29-6-21)

GLARE. The problem with aluminium is that is significantly heavier than composites and the problem with GLARE is that it is expensive and difficult to design with. A promising solution would be the use of a metal composite on the inside of the skin, see Figure 14.4a, which is said to be cheaper than composite while still being relatively light and able to make the surface impact resistant. Furthermore, the patent for this technology expires in 2028, which would make it easier to copy the material and manufacturing [5]. Figure 14.4b shows a microscopic image of the incorporated riblet technology. If technology similar to Microtau or from Microtau is used, the riblets will be a coating made from urethane-acrylate photopolymer, which is UV curable (optimally under low energy). These specific riblets will adhere to the United States Airforce Programmed Depot Maintenance (PDM) requirements and the MIL-PRF-85285 durability specification [16]. Another option is to use surface film, such as the BASF AeroSHARK technology. This technology is claimed to be especially durable and able to be applied on older aircraft as well [14].

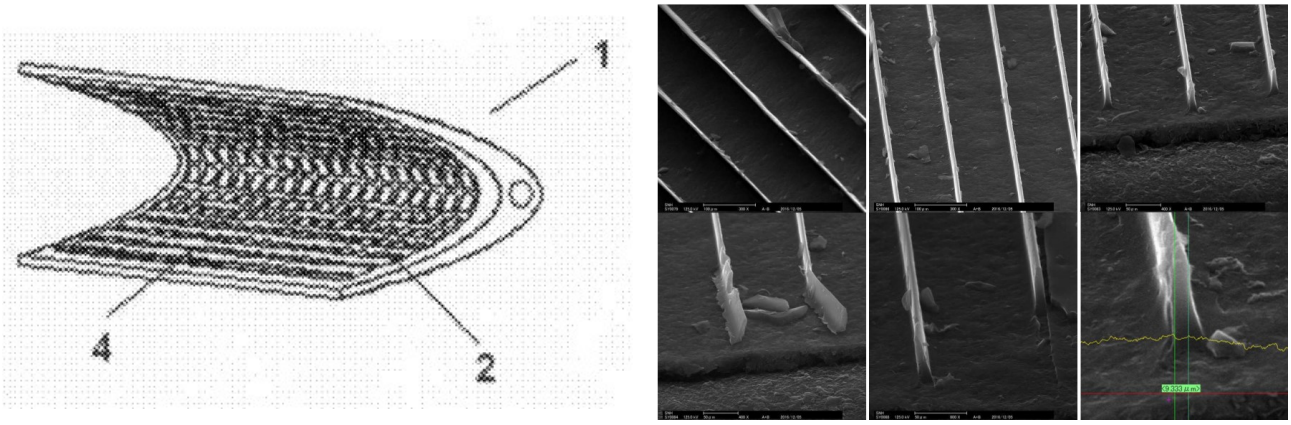

(a) Leading edge composite matrix [5]

(b) riblet technology [16]

Figure 14.4: Advanced aerospace technologies

15. Structural Analysis

At this point the shape of the wing is determined together with the airfoil. Now it is time to look at the wing as a load bearing structure and analyse the loading, stresses and aeroelasticity of the wing. In Section 15.1 The loading diagrams of the wing will be calculated. These loading diagrams will then be used in Section 15.3 to calculate the bending and shear stresses of the wing. Finally in Section 15.4 the aeroelasticity will be researched a bit more in depth.

15.1. Loading Diagram

The wing experiences a lot of different loads. These loads should all be carefully identified and calculated in order to be able to calculate stresses from these. For these calculations it will be assumed that all the forces act on the same line along the span. all the distributed loads acting over the surface of the wing will be assumed on being distributed load along the half-chord line. These two assumptions causes the wing box to have a different internal torque. The lift force is a distributed load, which is assumed to have an elliptical distribution. The drag is assumed to be an uniform distributed force . The weight is a distributed force based on the class II weight estimation and the distribution is determined based on the squares of the chords. The weight and trust of the engines are point forces acting where the engine is placed. The z-axis runs along the span, The y-axis is directed upwards and the x-axis is directed to the tail of the aircraft. This can all be seen in Figure 15.1 where the FBD is given.

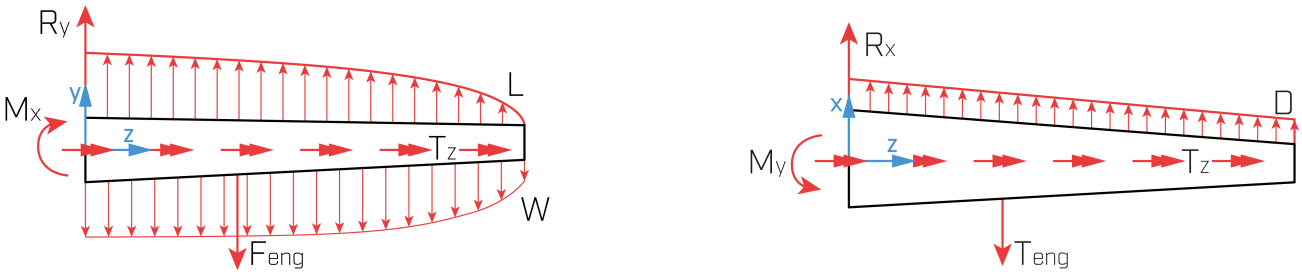

(a) Front view of the FBD of the wing.

(b) Top view of the FBD of the wing.

Figure 15.1: Free body diagram of the wing in front (a) and top (b) views

From these FBD's the internal loading diagrams can be constructed. First the internal shear is calculated along the span. For

this the distributed loads are integrated in function of the span wise location. Next the internal moment can be calculated. For the moments around the x- and y-axis the shear forces are integrated along the span. The moment around the z-axis is called the torsion and is calculated from the moment coefficient of the wing.

The internal loading diagrams should be verified in order to make sure the model is correctly calculated. This is done by calculating the reaction forces of each force or distributed force separately and comparing them to the script.

The reaction forces of the distributed loads however, give a slightly different magnitude than the total load present. This can be explained due to the integration that is used for the calculation of the shear force. As a numerical integration is used it gives a small discretisation error which is to be expected. For 1000 steps used the reaction force based on the shear load distribution is off with approximately 1.5 %. This is a very reasonable percentage for the loading diagrams. Then the magnitude and signs of the reaction forces where checked and found to be corresponding to the FBD. Next to this the distribution function along the span was checked. It could be seen that a point force gave a straight internal shear function and a linear internal moments function. The uniform distributed forces then gave linear internal shear diagrams and quadratic internal moments diagrams as is expected.

15.2. Moments of Inertia

In order to calculate the moment of inertia of the wing box certain assumption will have to be made. First of all the thin walled assumption was used this causes the moment of inertia to be lower than the actual moment of inertia. The stringers are added with to the moment of inertia calculations assuming that they are point areas. This also reduces the moment of inertia slightly. Next to this the shape of the wing box does not follow the shape of the airfoil exactly. Instead it is assumed that the wing box starts at 15% of the chord and ends at 75% and another spar is assumed to be in at the center of the wing box. Important to note is that the wing box is assumed to be symmetrical over the x-axis. Hence the product moment of inertia is equal to zero. This script has been verified by increasing input parameters and checking if the outcome changes as expected. Figure 15.2 is a digitisation of the preliminary wing box cross section.

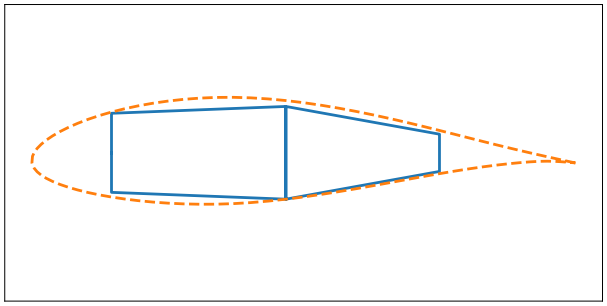

Figure 15.2: Wing box cross section

The verification of the moment of inertia script was done by taking a square wing box, assuming no taper of the wing and then by calculating the moment of inertia by hand and comparing this to the script. The calculations where an exact match with the script.

15.3. Stresses

In this chapter the internal stresses and the buckling stress constraint will be determined.

15.3.1. Normal Stress

The normal stress is calculated using Equation 15.1. This equation is already simplified with the assumption that the product moment of inertia is equal to zero. In order to verify the normal stresses the maximum stresses were also calculated by hand at the root and then compared by the script. These were identical to each other as is expected. Now it is desired to perform some kind of validation in order to check that the right model was used to calculate the moments of inertia, the loading and the stress calculations. Unfortunately due to the time and resource constraint it is not possible to perform a test and to analyse the measurements of these tests. It should however be considered if this work would be continued.

$$\sigma_z(y,x) = -\frac{M_x}{I_{xx}}y + \frac{M_y}{I_{yy}}x \tag{15.1}$$

15.3.2. Shear Stress

Equation 15.2 displays the main Equation to compute the shear flows within each panel. For shear flow calculations it is assumed that the stringer area can be smeared out, increasing the skin thickness. Furthermore, it is assumed that the rate of twist is constant per location along the wing span, meaning that this property has the same value for each cell in a

multi-cell wingbox. Setting the internal and external torque equal and setting the rates of twist in each cell equal creates a linear system which is solved for the internal shear flow q_i for each cell i. The model was verified by unit testing and system tested with by hand calculations.

$$q_{ij} = \frac{S_y I_{xy}}{I_{xx} Iyy - I_{xy}^2} \int_0^s txds - \frac{S_y I_{yy}}{I_{xx} I_{yy} - I_{xy}^2} \int_0^s tyds + q_i \tag{15.2}$$

Shear Centre

One of the most important parameters for aeroelasticity is the shear centre (or flexural centre or elastic axis). It has located on the y-axis (y-axis points upwards, x-axis left) due to the vertical symmetry. In order compute the horizontal position, the shear flows are calculated for a unit load is applied. Dividing the internal torque generated by the shear flows with the unit load returns yields the moment arm, which returns the position of the shear centre. In turn, this position is also used to calculate the polar radius of gyration [1], static moment, displacement of centre of gravity and mass moment of inertia about the elastic axis.

15.3.3. Buckling Stress

The critical buckling stress must also be calculated. It is assumed that Euler column buckling can be used describe the buckling. For the plate and stringer boundary conditions it is assumed that the these elements have large aspect ratios (higher than 3); so that the buckling coefficient is constant per aspect ratio for each type of support. During system testing, it was found that the stiffener pitch and cross sectional area play a much larger role in increasing the panel buckling stress than the sheet thickness, which matches with literature results. Furthermore, the ATR aircraft buckling model was able to similar results to those found in literature buckling examples, shown in Table 15.1. Note that for this example all inputs were changed to match the reference.

Table 15.1: Buckling model verification

Stiffener	**Model**	**Reference literature**
buckling stress (MPa)	296	296
Reinforced panel	**Model**	**Reference literature**
panel crippling stress (MPa)	25.31	26.1
effective sheet width (cm)	47.89	48.4
panel buckling stress (Mpa)	274	275

These stresses must be calculated dependent on the number of stringers and the skin thickness, as these are the main parameters of the wing that can be altered. These parameters must then be chosen in order to have the lightest possible configuration while still meeting the yield stress and buckling constraints.

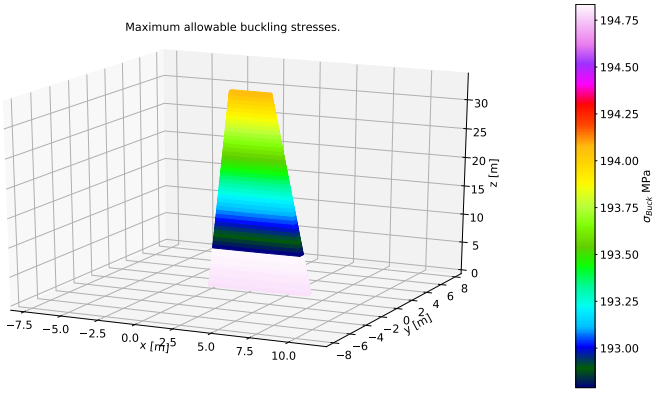

Figure 15.3: Buckling stress constraint

15.4. Aeroelasticity

One of the major ways to reduce ATR is by increasing the aspect ratio. Preliminary literature study found that aeroelasticity can be design constraining for these configurations [52]; therefore aeroelasticity is thoroughly analyzed. Figure 15.4 shows all of the primary results obtained from the aeroelasticity analysis. For the divergence speed, both infinite and finite (which delivers accurate results according to literature) wing are computed to estimate the infinite wing assumption accuracy as the infinite wing assumption is used for the aileron reversal and flutter speeds [65]. The flow is assumed steady and the

[1] http://old.staff.neu.edu.tr/ rresatoglu/shapebuilder.pdf accessed on 23-06-2021

airfoil uncambered with quasi steady angle of attack. It is required that all of the unstable regions should be at least 15% from the flight envelope. The most left diagram has the most constraining speed, which is designed to fit the requirement at 0m altitude by increasing the wing box thickness. Note that infinite wing has a 90% higher value than finite but doing this calculation in reverse for the other speeds still does not impose constraints. The aileron reversal speeds impose no constraints on the design nor does the flutter speed. The flutter was speed computed using the Pine's model and both Pine's conditions, see Equation 15.3and Equation 15.4,were used as verification as these need to be positive, which is the case. Finally, the reduced frequency was also computed to assess the steady flow assumption. The highest value is encountered at cruise speed 0.000242 and this means that the model can be considered steady to quasi-steady, which is acceptable. Another note on the flutter is that damping terms were neglected and these terms usually increase the flutter speed by 30% [48].

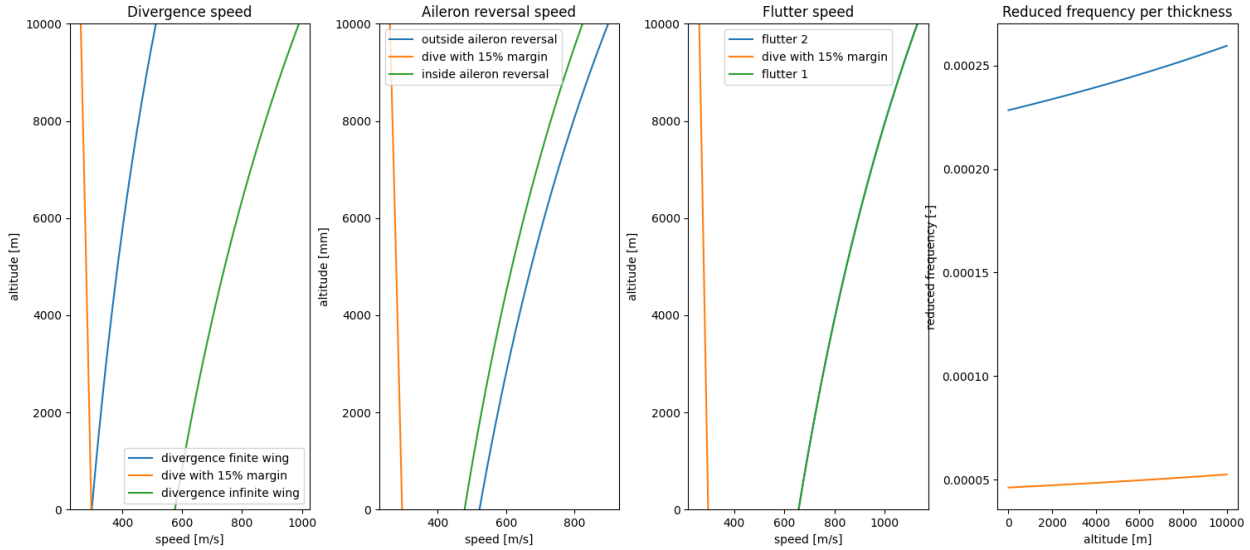

Figure 15.4: Aerolastic analysis

$$x_\theta \left[x_\theta + 2e - 2e \left(\frac{w_h}{w_\theta} \right)^2 \left(1 + 2e \frac{x_\theta}{r_\theta^2} \right) \right] > 0 \qquad (15.3)$$

$$x_\theta + 2e + \left(\frac{w_h}{w_\theta} \right)^2 \left(x_\theta - 2e + 4e \frac{x_\theta^2}{r_\theta^2} \right) > 0 \qquad (15.4)$$

15.5. Wing Box Design

Now that all important Stresses are calculated the design of the wing box can be finalised. It should be noted that the outer shape of the wing box is set due to the aerodynamic constraints on the wing planform. These parameters are discussed in Chapter 9. Now the wing box is designed such that it can bear all stresses and can resist aeroelasticity with the goal to be as light as possible. The variables for this design are the skin thickness, the number of stringers, the stringer area. The amount of stringers and the skin thickness may variate throughout the span of the wing. To know which parameter has to be increased and which can be lowered to save weight it is important to look at the different stresses separately. and based on that increase the right parameters. As the stringer area is very hard to determine at this stage and within the time constraint given a stringer with an area of 180 mm^2 is chosen.

Now the right loading cases must first be chosen in order to design the wing box for. These must include all different loading cases which can occur during flight. So first stationary conditions are added for when the plane sits on the tarmac in rest with full fuel thanks and no aerodynamic forces. Then the take-off condition is added. with aerodynamic forces at low speeds, low altitude, full fuel tank and full thrust. Followed by the cruise condition where the full thrust, empty fuel tanks, maximum load factor and aerodynamic forces are added. Finally the landing condition is added. Here empty fuel tanks are assumed, aerodynamic forces at low speeds and full thrust are added. These are the most extreme loading cases and define the maximum stress that will occur during its lifetime.

Then a random combination is added of the design parameters and for this the moment of inertia is calculated using the method described in Section 15.2. From this the stresses are then calculated as explained in Section 15.3 for each loading case. Then the maximum and the minimum stresses are stored separately. Then the stresses are first multiplied with a safety factor of 1.5 and then checked with the constraints at hand. These constraints are the yield stress,which is dependent on the material chosen inChapter 14, the buckling stress, which is defined in Section 15.3.3 and the aeroelasticity constraints

set in Section 15.4. If the wing box would fail the most efficient thing to do is add stringers. If the wing box would not meet the aeroelasticity constraint the skin thickness should be increased. This contributes more to the resistance of aeroelasticity as it improves the torsional moment greatly. Adding stringers would more improve the moment of inertia which has a more minor contribution to the aeroelasticity. The First design will be discussed in Section 15.5.1 and an iteration on that design will be performed in Section 15.5.2

15.5.1. Initial Design

Following this trial and error approach the final wing box design was achieved. Due to the high aspect ratio aeroelasticity became a extremely limiting factor. In order to be able to resist flutter the wing box made of the carbon fibre composite chosen in Chapter 14 a skin thickness of at least 8mm is needed. An additional of 40 stringers at the top and bottom plate of the wing box is also place from the root until 1/10 of the span in order to be able to cope with the buckling constraint. The yield stress is than also met with a very large margin. In Figure 15.5a the maximum Mohr's stresses can be observed it is important that these are not higher than the yield stress of the material. Next to this the compressive stress, which can be seen in Figure 15.5b should not be higher than the constraint stress set in Figure 15.3.

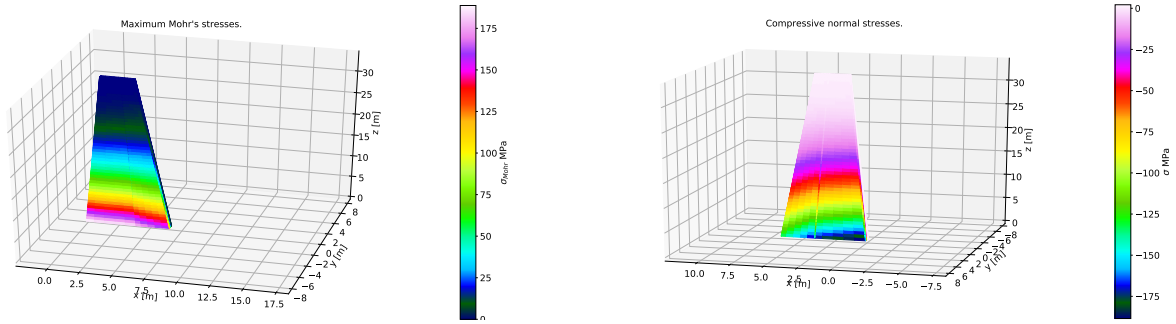

(a) Maximum Mohr's stresses **(b)**

Both of these conditions are met with a big margin. This large margin for stresses can be explained by the aeroelasticity constraint.

15.5.2. Iterated Design

It should be noted that the parameters of the wing box are mainly determined by the constraint around aeroelasticity. This also determines the weight of the wing. As there is a lot of margin on the stress constraints it would be beneficial to look at a material which has better properties in resisting aeroelasticity. The material properties that impact aeroelasticity the most are the E-modulus and the shear modulus. Thus a material with higher values of these two properties was searched for and Cyanate ester/HM carbon fiber, UD prepreg, QI lay-up was found to be the best fit. While Cyanate esters are currently not the industry standard, they are expected to increase in use with a predicted market growth between 2020-2024 of 11% [2]. Following the same design approach as before the parameters of the wing box are set. The thickness is 4.2 mm along the entire span, this is determined by the aeroelasticity. The final design is then set on a wing box with a skin thickness of 4.2 mm and only 45 stringers from the root chord untill 1/10 of the span at the top and bottom of the wingbox.

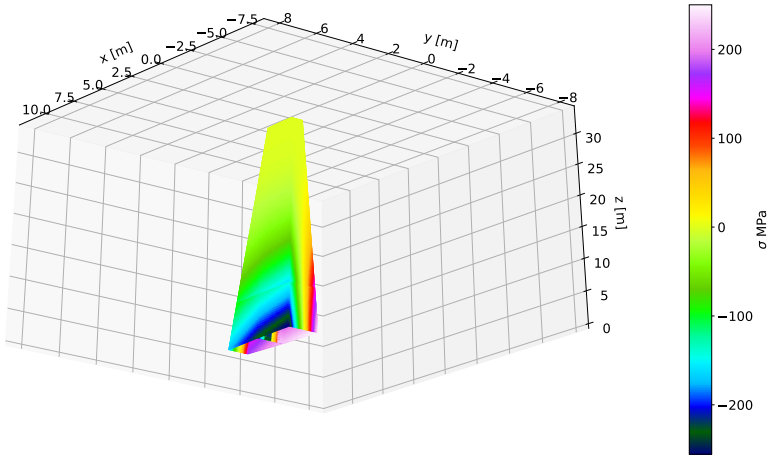

Figure 15.6: Maximum stresses occurring in iterated wing box design.

[2] https://www.businesswire.com/news/home/20200915005956/en/Cyanate-Ester-Resin-Market-Insights-on-the-Crisis-and-the-Roadmap-to-Recovery-from-COVID-19-Pandemic-Technavio accessed on 24-6-2021

15.6. Propfan Blade Aeroelasticity

One of the concerns raised after preliminary designing is the propfan engine size and therefore further literature study was required. Figure 15.7a shows a flutter speed of 202 m s^{-1}, which was a for a counter rotating blades CBR propfan with a 3.701 m and 8 blades per rotor. This research however, used a blade optimized for single rotor flutter, no CBR and the results were not validated. This research did show however, that counter rotating blades are more prone to flutter than single rotating. Figure 15.7b shows the stability for a single rotor with 2.743 m diameter and a maximum rotation of 7484 rpm but this research neglected Coriolis forces and blade interference. The ATR aircraft has CBR with 10 blades per rotor, a diameter of 5.3 m, a required thrust of 259 kN, an rpm of 2200 and a minimum flutter speed requirement of 308 m s^{-1}. According to the research, this would mean that the current propfan configuration is highly unstable. There is however, already an example of an 8 blade CBR propfan with a massive diameter of 4.5 m and a maximum thrust of 119 kN at a 1000 rpm in the Progress D-27 engine [3]. While this example is already more promising than the research, it is the only commercial CBR propfan and still no where close to the required performance. An engine that does meet the requirements is the NK-62M propfan [4], which has a 285.2 kN thrust, specific fuel consumption of 8.0 g kN^{-1} s^{-1} at take off and 13 g kN^{-1} s^{-1} at cruise and a 4815 kg weight (Note that the SFC is 0.49 g kN^{-1} s^{-1} lower at take off, the SFC at cruise is 0.2 higher and the engine weight 601 kg lighter than the ATR propfan) while being CBR. While the engine has been succefully tested, it has never been used on a commercial aircraft.8

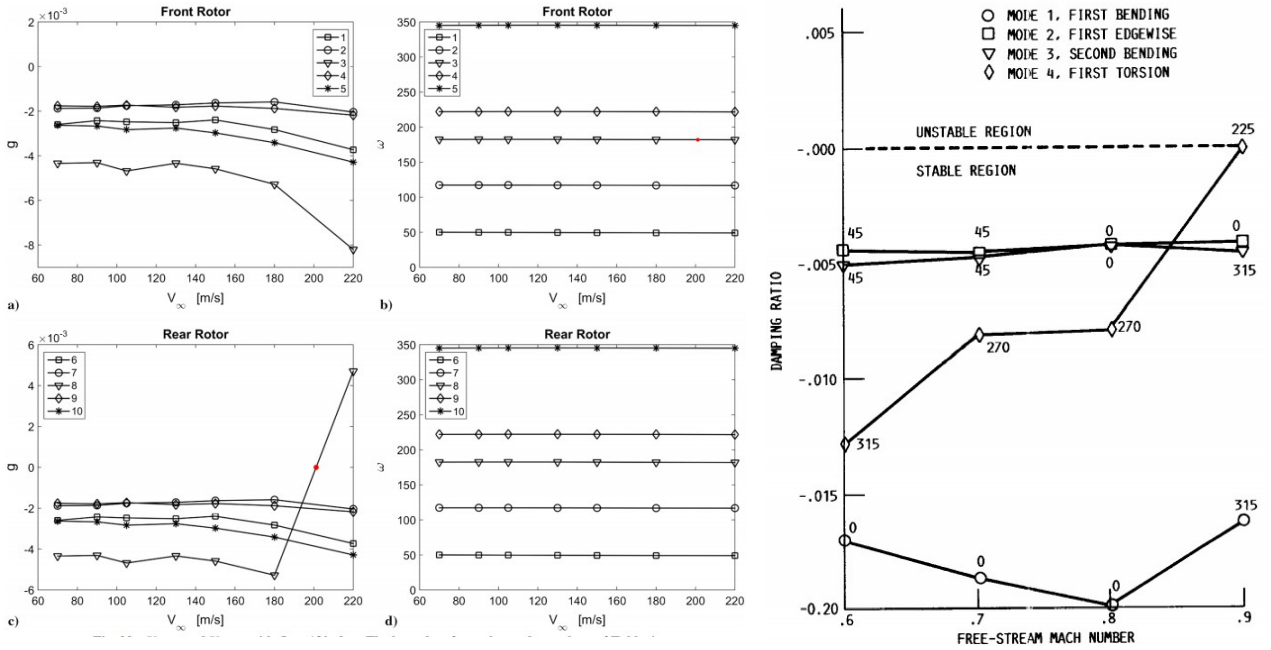

(a) Counter rotating blades flutter [77]

(b) SR7L stability analysis

Figure 15.7: Reference literature propfan flutter characteristics [77]

Overall, the propfan development will be a major challenge, requiring significant design time and cost. One advantage the ATR aircraft has is that technology has significantly progressed; all other propfan designs are more than thirty years old. More flutter resistant materials such as Cyanate esters (which have a 1.6 times better flutter resistance than the epoxy carbon fibre composites that are used in the research blades) [57] could and will be used for the blades and improved FEM allows for better design optimization. If the design is still not feasible, either the engine has to become single rotor, the diameter has to decrease or the rpm need to be lowered.

15.7. Conclusion and Recommendation

It was clear that during the material selection not enough attention was paid to the aeroelasticity constrain. Therefor a iteration was needed on the wing box design which could have been avoided. Next to this There will probably be weight penalties on the wing due to its thickness which is needed for resisting aeroelasticity. This should be investigated later on. Next to this the fatigue of the wing structure should be investigated as the flight regime is currently at 5 km a lot more turbulence is expected. Therefor more cyclic loading will appear and this may pose some problems on the wing structure. As a final note, weight penalty from creating cut-outs and holes and adding webs should be considered.

[3] https://ivchenko-progress.com/?portfolio=d-27&lang=en accessed on 24-6-2021

[4] http://engine.aviaport.ru/issues/115/pics/pg20.pdf accessed on 25-6-2021

16. Performance Analysis

This chapter analyses the aircraft performance, mainly covering the analysis of the aircraft and its performance in order to minimise ATR whilst having a maximum DOC increase of 15% with respect to the Airbus A330-200, by coming up with the optimum mission profile, i.e. cruise altitude and cruise mach number. First, the mission analysis and optimisation logic will be described in Section 16.1. Then, SUAVE will be introduced and the low-ATR aircraft and the A330 will be modeled and analysed over defined mission profiles in Section 16.2. Subsequently, the ATR performance evaluation and the DOC performance will be discussed in Section 16.3 and Section 16.4, after which a design point is found in Section 16.5 by synthesising the ATR and DOC performance. Additionally, the relative ATR versus DOC per technology is evaluated in Section 16.6, followed by a sensitivity analysis regarding ATR and DOC in Section 16.7. Finally, in Section 16.8 recommendations are given regarding the flight performance part of the design

16.1. Mission Analysis and Optimisation Logic

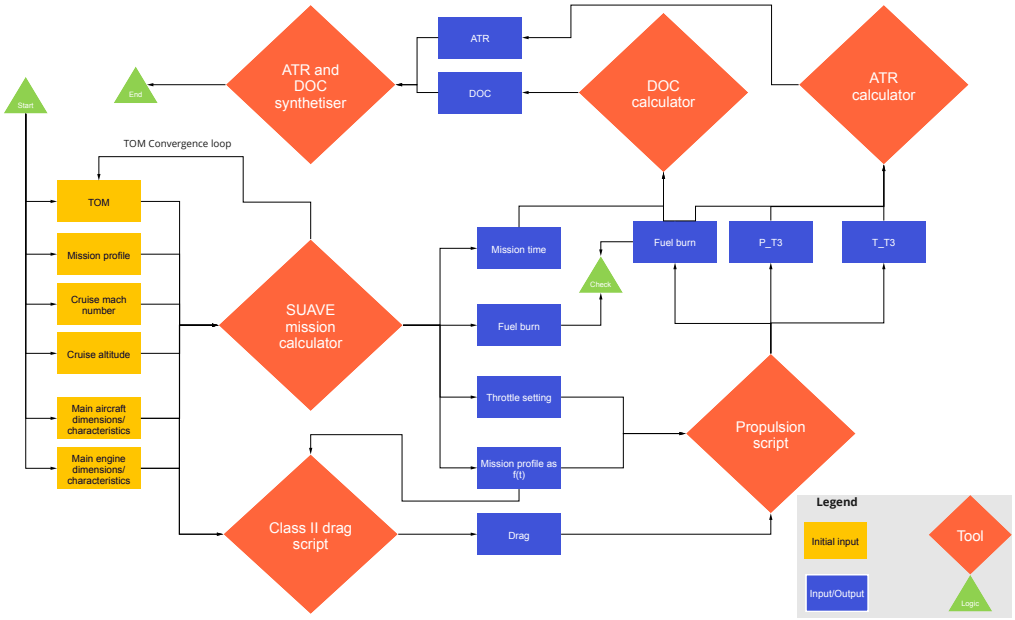

Figure 16.1: Mission optimisation logic

The mission is analysed using the open-source python-based conceptual level aircraft design tool Stanford University Aerospace Vehicle Environment (SUAVE) [111][1]. This tool can be used in the conceptual design phase for both conventional and unconventional aircraft configurations, including methods for the analysis of its aerodynamics characteristics, flight dynamics, flight performance, propulsion performance and weights. It is decided to limit the use the SUAVE tool to only model the aircraft's mission in order to get an insight in the general aircraft performance characteristics over its mission profile and to compare the results with the models created by the team. Furthermore, different outputs are used as input by other tools in order to optimise the mission profile. The SUAVE tool has been modified to make it more flexible regarding changes in aircraft and engine characteristics, as well as allowing for different cruise altitude and cruise mach number in order to be able to look for an optimal mission profile. It should be noted that both the low-ATR aircraft and the Airbus A330-200 will modeled in SUAVE

The optimisation flow has been visualised in Figure 16.1, where the different inputs and outputs for the models described in this chapter are linked are shown in order to clarify the steps to be taken to arrive at the optimum mission profile regarding the ATR objective and DOC constraint. Note that the propulsion, class II drag and DOC scripts are discussed in Chapter 10, Chapter 12 and Chapter 22, respectively, while the ATR calculator and the ATR and DOC synthesis will be discussed later in this chapter.

16.2. Flight Profile Modeling with SUAVE

This section covers the modeling of the low-ATR aircraft and the Airbus A330-200 over a low-ATR and a reference mission profile in SUAVE. The methods used have been described, including their assumptions and limitations. The results have been discussed and compared to the in-house drag and propulsion models. Finally a sensitivity study has been performed, after which verification and validation of the different components of the model have been carried out.

[1] `https://github.com/suavecode/SUAVE` (last accessed on 08/06/2021)

16.2.1. Method

The general SUAVE mission solving will be elaborated on in next subsection, followed by a discussion on the modifications made to the original SUAVE code in order to model the propfan and the riblets. The ultimate goal is to compare the project aircraft with the Airbus A330-200, hence the A330-200 is modeled on its own reference mission and the proposed low-ATR mission as well.

16.2.2. Mission Modeling in SUAVE

Mission definition

A mission in SUAVE is evaluated by solving the equations of motion, by means of iterating until the residuals of the problem are zero [99]. In order to do that, a mission should be precisely defined. The aircraft mission is to fly 8000 kilometers within 16 hours. Within this mission, there is accounted for a 200 nautical mile diversion and 30 minutes loitering at 1500 feet. Different mission segments have been set-up and the segments composing the proposed low-ATR mission can be found in Table 16.1.

SUAVE offers different possibilities to define the climb and descent segments. It is decided to make use of the constant True Air Speed (TAS)- constant Rate of Climb (ROC) and constant TAS - constant Rate of Descent (ROD) for the different climb and descent segments, respectively. As the SUAVE tool should be iteration proof, i.e. allowing for varying cruise altitude and cruise mach number, a simplified but feasible mission profile has to be set up. In order to get a feasible approximation of the climb and descent segments, typical values for an A330-200 mission profile have been taken [1][2] [3]. As indicated in these references a typical mission of an A330, as for every other commercial aircraft, consists of constant Indicated Air Speed (IAS) climb segments, until the cross-over point where after a constant mach climb is performed. SUAVE does not allow for constant IAS, hence it is decided to convert the typical IAS to TAS that the aircraft will attain within that altitude segment. The TAS in the final climb segment and the first descent segment was reduced as in the cruise conditions iterations it became apparent that the mach number in these two segments exceeded the cruise mach number. Furthermore, as a low ATR mission profile typically results in relatively low mach numbers, no constant mach segment are used besides the cruise segment, where the aircraft flies at the cruise altitude and cruise mach number. In order to allow for iterations of the cruise conditions, it is decided to have only one climb and descent segment between 1000 ft and the cruise altitude. The maximum achievable cruise altitude and the maximum ROC is related to the aircraft's excess power and weight, hence a conservative value for the ROC for this final climb segment has been taken, resulting in underestimating the aircraft climb performance at lower altitudes but making sure the climb segment is feasible when reaching possibly high cruise altitudes. Furthermore, as low-ATR mission profiles typically result in significantly lower cruise altitudes and the vast majority of the mission is the cruise segment, this assumption is not expected to give significant loss of accuracy. Finally it should be noted that this mission is not optimised for either ATR or fuel burn, as the goal of the modeling is to compare the aircraft regarding DOC and ATR, and the most significant part of the flight is the cruise phase.

Table 16.1: Low-ATR mission definition for SUAVE

Segment	Start altitude (ft)	IAS (kts)	TAS (kts)	ROC (ft/min)	ROD (ft/min)	Configuration	Remark
Climb 1	0	145	145	2000	-	Take-off	
Climb 2	1000	175	185	2000	-	Cruise	
Climb 3	5000	290	310	2500	-	Cruise	
Climb 4	10000	290	310	1500	-	Cruise	
Cruise regular	h_{cruise}	-	-	-	-	Cruise	Fly at M_{cr}
Descent 1	h_{cruise}	290	340	-	2500	Cruise	
Descent 2	10000	230	260	-	1600	Cruise	
Descent 3	3000	190	195	-	1600	Landing	
Descent 4	1500	140	142	-	1200	Landing	
Climb div. 1	0	145	145	2000	-	Take-off	
Climb div. 2	1000	175	185	2000	-	Cruise	
Climb div. 3	5000	290	310	2500	-	Cruise	
Climb div.4	10000	290	310	1500	-	Cruise	
Cruise div.	h_{cruise}	-	-	-	-	Cruise	Fly at M_{cr}
Descent div. 1	h_{cruise}	290	340	-	2500	Cruise	
Descent div. 2	10000	230	260	-	1600	Cruise	
Descent div. 3	3000	190	195	-	1600	Landing	
Loiter	1500	220	225	-	-	Cruise	30 minutes @ 1500 ft
Descent div. 4	1500	140	142	-	1200	Landing	

[2] `https://www.skybrary.aero/index.php/A332` (last accessed on 16/06/2021)

[3] `https://contentzone.eurocontrol.int/aircraftperformance/details.aspx?ICAO=A332&NameFilter=airbus` (last accessed on 16/06/2021)

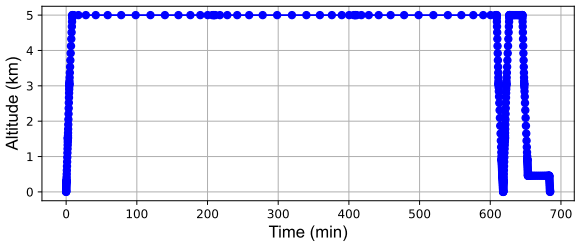

(a) Altitude variation over time of the low-ATR mission profile

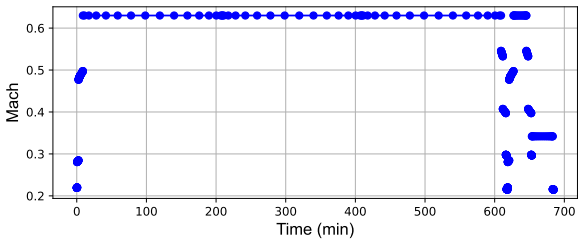

(b) Mach variation over time of the low-ATR mission profile

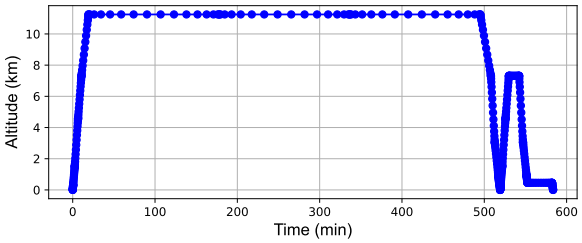

(c) Altitude variation over time of the reference mission profile

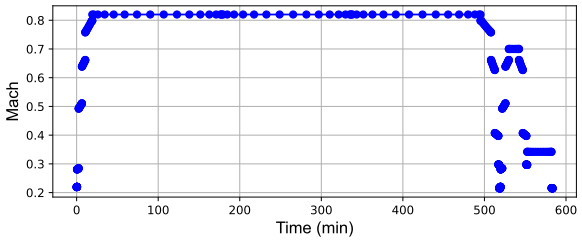

(d) Mach variation over time of the reference mission profile

Figure 16.2: Visualisation of the low-ATR and reference mission profiles as defined inTable 16.1 and Table 16.3, respectively

Table 16.2: Mission time and range

Mission	Regular mission time (min)	Total mission time (min)	Regular range (km)	Total range (km)
Low-ATR	618.27	684.62	7421	8000
Reference	519.29	583.57	7421	8000
Difference(%)	19.1	17.3	0.0	0.0

Table 16.3: Reference mission definition (A330-200) for SUAVE

Segment	Start altitude (ft)	IAS (kts)	TAS (kts)	ROC (ft/min)	ROD (ft/min)	Configuration	Remark
Climb 1	0	145	145	2000	-	Take-off	
Climb 2	1000	175	185	2000	-	Cruise	
Climb 3	5000	290	320	2500	-	Cruise	
Climb 4	15000	290	400	2200	-	Cruise	
Climb 5	24000	-	458	1500	-	Cruise	Approximation for MACH climb at $M = 0.8$
Cruise regular	37000	-	470	-	-	Cruise	Fly at $M_{cr} = 0.82$
Descent 1	37000	-	458	-	1000	Cruise	Approximation for MACH descent at $M = 0.8$
Descent 2	24000	290	400	-	3000	Cruise	
Descent 3	10000	230	260	-	1600	Cruise	
Descent 3	3000	190	195	-	1600	Landing	
Descent 4	1500	140	142	-	1200	Landing	
Climb div. 1	0	145	145	2000	-	Take-off	
Climb div. 2	1000	175	185	2000	-	Cruise	
Climb div. 3	5000	290	320	2500	-	Cruise	
Climb div. 4	15000	290	400	2200	-	Cruise	
Cruise div.	24000	-	496	-	-	Cruise	Fly at $M = 0.7$
Descent div. 1	24000	290	400	-	3000	Cruise	
Descent div. 2	10000	230	260	-	1600	Cruise	
Descent div. 3	3000	190	195	-	1600	Landing	
Loiter	1500	220	225	-	-	Cruise	30 minutes @ 1500 ft
Descent div. 4	1500	140	142	-	1200	Landing	

As mentioned before, the A330-200 is used as reference regarding ATR and DOC and will also be modeled in SUAVE. To be able to see where the low-ATR aircraft stands with respect to the A330-200, the A330-200 will be modeled on both the low-ATR mission profile as shown in Table 16.1 and its own reference mission, which is defined in Table 16.3. The reference mission's cruise altitude and Mach number have been taken to be 37000 ft and 0.82, respectively, as proposed by [54]. This mission is built-up in a similar fashion compared to the low-ATR mission, except some changes and additions to the climb and descent segments to account for the fact that the aircraft will fly at a higher cruise altitude, therefore also opting to incorporate the constant mach and descent segments. However, it is decided to model these segments with a single TAS that does not exceed the constant Mach number, in order to simplify the calculation that ensures that the diversion distance and total flight distance are exactly 200 nm and 8000 km, respectively. Furthermore, it is assumed that the diversion has a cruise segment at FL240 at a Mach number of 0.7.

The results of a comparison of the mission times and ranges are shown in Table 16.2, in which a distinction is made between the total mission, i.e. the mission including diversion and loitering, and the regular mission, which is just the mission to the opted destination airport. The flight time for the regular mission is approximately 19%, while the difference in cruise mach number is 24.4%. The main contributor to this relatively smaller increase in mission time is the fact at lower altitudes a Mach number results in a higher TAS compared to the same Mach number at a higher altitude. The mission times in Table 16.2 show compliance with the maximum flight time requirement (MATRA-USER-PER-02).

Mission input

Before SUAVE is able to evaluate the defined mission, the main aircraft and engine dimensions, including some aircraft and engine performance characteristics have to be defined[99]. The final input parameters for the project aircraft and the A330-200 can be found in Table 16.4[4] and Table 16.5. Note that the propulsion modeling in SUAVE is further discussed in Section 16.2.3. The main weight input for the SUAVE mission calculator is the Take-Off Mass (TOM).The first option to model a certain mission in SUAVE is to assume the TOM to be the equal to the MTOM, hence assuming maximum fuel on board whilst the mission requires potentially less fuel. Because weight means more fuel burn, this redundant fuel weight should preferably be eliminated as burning more fuel than required is undesired from both a low fuel burn and a low-ATR perspective. In practice, an aircraft will indeed only take the amount of fuel on-board that is required for its mission, plus some extra that is required by regulations. To solve this, one desires to include only the required fuel weight in the TOM. However, the problem here is that the fuel burn and therefore the required fuel burn is an output of SUAVE. This problem of fuel redundancy is thereby solved by creating a TOM convergence tool that runs the SUAVE codes several times until the fuel weight that is used in the input TOM is within a 0.1 kg margin with respect to the output fuel weight by SUAVE. Note that the TOM is the sum of the OEM, payload (and cargo) weight and the fuel weight.

To return to the extra fuel required by regulations, an aircraft generally has to take the fuel board to fulfil its regular mission (trip fuel), plus the fuel to divert (alternate fuel) and to loiter for 30 minutes at 1500 feet (final reserve fuel). On top of that, a certain contingency margin is required to account for additional en-route fuel consumption caused by wind, re-routing or other maneuvers imposed by Air Traffic Control (ATC). Typically this contingency margin is 5% of the planned trip fuel, while nowadays it is sometimes allowed to use 3%. The trip fuel, alternate fuel and final reserve fuel are all incorporated in the mission, as these segments are included in the mission definitions shown in Table 16.1 and Table 16.3. It is decided to not include a contingency margin as the goal of the SUAVE modeling is to compare aircraft performance and fuel burn, and a contingency margin will amplify the actual differences. Note that the payload and cargo weight as shown in Table 16.4 for the A330-200 is assumed to be the same as for the low-ATR aircraft in order to see the differences between the aircraft on a mission with the same range and payload. This assumption is substantiated as an A330-200 in a three-class configuration can accommodate approximately 250 passengers as well.

Table 16.4: Main aircraft input for SUAVE

Parameter	Unit	Low-ATR Aircraft	Airbus A330
MTOM	kg	182,280	230,000
OEM	kg	90,638	120,200
Payload & Cargo weight	kg	27,250	27,250
Fuselage length	m	58.19	57.77
Fuselage diameter	m	5.47	5.64
Wing area	m^2	416.4	363.1
Wing aspect ratio	–	11	9.26
Wing quarter chord sweep	deg	0	29.7
Wing MAC	m	6.53	7.26
HTP area	m^2	87.44	72.9
HTP aspect ratio	–	6.1	5.0
HTP quarter chord sweep	deg	14.21	29.0
VTP area	m^2	85.13	47.65
VTP aspect ratio	–	1.8	1.87
VTP quarter chord sweep	deg	33	45.0

Table 16.5: Main engine input for SUAVE [10]

Parameter	Unit	Low-ATR Aircraft	Airbus A330
Number of engines	–	2	2
BPR	–	30	5.3
Engine length	m	3.78	4.27
Nacelle diameter	m	1.33	2.90
Fan diameter	m^2	5.30	2.44
Inlet nozzle polytropic efficiency	–	1	0.98
Inlet nozzle pressure ratio	–	1	0.98
LPC polytropic efficiency	–	1	0.91
LPC pressure ratio	–	1	1.4
HPC polytropic efficiency	–	0.91	0.91
HPC pressure ratio	–	25.97	14.55
Combustor efficiency	–	0.995	0.99
Turbine inlet temperature	K	1700	1500
Combustor pressure ratio	–	1	0.95
Turbine mechanical efficiency	–	0.98	0.99
HPT polytropic efficiency	–	0.905	0.93
LPT polytropic efficiency	–	0.915	0.93
Core nozzle polytropic efficiency	–	1	0.95
Core nozzle pressure ratio	–	1	0.99
Fan nozzle polytropic efficiency	–	1	0.95
Fan nozzle pressure ratio	–	1	0.99
Fan polytropic efficiency	–	0.9	0.93
Fan pressure ratio	–	1.155	1.6
Take-off thrust	kN	517	640
Total design thrust	kN	82.3	640
Design altitude	m	5000	0
Design mach number	–	0.63	0.22(TO)

[4] `https://booksite.elsevier.com/9780340741528/appendices/data-a/table-1/table.htm` (last accessed on 20/06/2021)

Limitations
The limitations of the SUAVE as used are the following:

- Although SUAVE has some functions to optimise climb and descent segments, it is decided not to use these as these did not guarantee convergence of the mission and increased the computational time significantly. However, as the most time is spent in cruise and the A330 mission profile has been used as reference, no significant loss of accuracy is expected for this stage of the design.

16.2.3. Propulsion Modeling in SUAVE

The computation of the propulsion performance is essential to the analysis of the over-all aircraft performance. Propulsion system modeling is achieved in SUAVE by setting up a so called 'energy network'. This subsection concerns the methods and main input used to model the turbofan and propfan in SUAVE, plus the limitations coming with the chosen propulsion models. Before discussing both models, the reader should be pointed towards the important principle of thrust drag bookkeeping, i.e. what does one account to engine efficiency and what to aircraft drag. This is defined for both engine types in their respective description.

Turbofan Modeling in SUAVE
The default turbofan network has been used to model the CF6 turbofan engine of the A330-200 in SUAVE, and is used as the baseline for the propfan modeling for the low-ATR aircraft as will be further elaborated on later in this subsection. The propulsive cycle of the engine is modeled by this turbofan network using one dimensional flow equations, via isotropic relations, first-order physics and set stage efficiencies [29]. For a more detailed discussion on this physics based model approach the reader is referred to Reference [99], where these 1D flow equations that are solved across the different engine components (inlet, fan, compressor(s), combustor and turbine(s), outlets) can be found as well. The main engine input parameters for the CF6-80E1A3 turbofan engine of the A330-200 can be found in Table 16.5 [5], including the different pressure ratios and polytropic efficiencies used in the analysis. The BPR, design thrust and design conditions have to be specified as well in order to for SUAVE to be able to calculate the performance of the engine. The engines lengths are used in SUAVE's own weight methods, which are not used for the mission evaluation, and for the computation of the engine's contribution to the aircraft's drag. The aircraft performance such as thrust and thrust specific fuel consumption can now be evaluated over the mission profile. As small remark on the thrust drag bookkeeping, for turbofans it is convention to call the outside of the nacelle aircraft drag, and the losses inside the nacelle are considered part of the engine efficiency or TSFC, and hence is defined this way in SUAVE as well. It is interesting to note that SUAVE can only handle, with fixed efficiencies and pressure ratios, a combination of fan pressure ratio and BPR that results in a physical engine, that is one where the work balance means the stagnation pressure coming from the core is greater than or equal to the freestream static pressure [29].

Propfan Modeling in SUAVE
As the low-ATR aircraft is equipped with propfans, and SUAVE does not have a propfan model in its available energy networks yet, it is decided to model the open-rotor engine in SUAVE as proposed by Dorsey [29]. Dorsey models the propfan with the same structure as the turbofan. The propfan engine parameters can be found in Table 16.5, which have either been computed or decided on in Chapter 10 or will be now be explained. The following changes have been made to the turbofan model in order to model the designed propfan of the low-ATR aircraft:

- The fan inlet efficiencies and pressure ratios have been set to 1, as an open-rotor design does not have an inlet nor outlet.
- The propfan uses the same core as the turbofan, except that it does not have a low pressure compressor, hence its polytropic efficiency and pressure ratio have been left at unity.
- The propfan has a gearbox in order to reduce the tip speed of the propfan blades. The efficiency of this gearbox is incorporated in the turbine mechanical efficiency and can be interpreted as a constant heat loss.

Note that in Chapter 10 it was decided to use a core nozzle polytropic efficiency and nozzle pressure ratio equal to 1. Furthermore,it should be noted that the fan polytropic efficiency incorporates the efficiency of the two counter-rotating fans.

Dorsey decided that besides the core, which is the same as for the turbofan, only the gearbox and the fan efficiency count towards the propulsive efficiency. This results accounting the external nacelle drag and wing scrubbing drag due to the wash of the propfans, as will be further discussed in Section 16.2.4, to the aircraft drag.
Limitations
The advantage of the chosen propulsion models is that it is completely physics based. However, the chosen propulsion models have the following limitations [29]:

- Efficiencies do not change with throttle settings, while in reality this is the case due to difference core temperatures amongst others.

[5] `https://booksite.elsevier.com/9780340741528/appendices/data-a/table-1/table.htm` (last accessed on 20/06/2021)

- Dorsey [29] swept over a large number of possible turbofan and propfan designs in order to compare them. Dorsey wanted to cover the general trend of propfans instead of modelling them in detail, hence resulting in according to him a conservative open-rotor model.

16.2.4. Aerodynamic Modeling in SUAVE

It is crucial to compute the aerodynamics of the aircraft in order to evaluate the aircraft performance. SUAVE offers different methods to predict the aerodynamics. It is decided to use the default Fidelity Zero methods, which uses a vortex lattice for the prediction of lift and correlations for the prediction of drag. These methods are described in more detail in [99]. This section concerns the modifications made to the aerodynamic models in SUAVE in order to model the propfan and the riblets, plus the limitations of the chosen aerodynamics models.

Modifications due to Propfan

As mentioned in Section 16.2.3, it is really important to define the boundaries between propulsive efficiency and aircraft drag [29]. It is decided to account the external nacelle drag and the scrubbing drag to aircraft drag. Scrubbing drag is the drag caused by the wash of the propfans, by means of an increase in dynamic pressure resulting in a higher dynamic pressure seen by the nacelle and a part of the wing resulting in higher drag. This scrubbing drag effect has been included using the same methods as described in Section 12.2 [29].

Application of Riblets

Specific to the aerodynamics of the low-ATR aircraft are the application of the riblets to reduce turbulent skin friction drag. The riblet technology has been discussed in Section 12.4 and the application of the riblets in the in-house Class II drag breakdown in Section 12.5. To be able to compare the results of SUAVE with the Class-II drag method, the riblets should be modeled in SUAVE as well. In the Low fidelity methods SUAVE uses scripts to compute the skin friction coefficient of a compressible mixed flat plate and a compressible turbulent flat plate. These models have been modified in order to take into account the skin-friction drag reduction by the riblets within the turbulent boundary layer over the aircraft components. This reduction is computed in the same way as performed in Section 12.5 by using Equation 12.9, with the riblet reduction only applied to 70% of the turbulent wetted surface area, only differing by the fact that SUAVE requires to specify the the transition location over both the upper and lower side of the flat plate approximations. These proportions depicted by f have been listed in Table 16.6. The values for the low-ATR aircraft are the same as decided on in Table 12.1 and mainly taken from Raymer [82], assuming the same proportion for the upper and lower side of the flat plate as no literature has been found to substantiate a difference. Note that one would expect to have laminar to turbulent transition point more aft on the lower side of a wing than on the upper side, but this is thus neglected. The A330-200 is modeled with same proportions, except for the wing where the proportion proposed by Raymer is used [82] and the nacelle for the turbofan of an A330-200 is assumed to have a later transition point than the nacelle of the propfan as it is not affected by the open-rotor's wake.

Table 16.6: Proportion of laminar flow over aircraft components

Component	Low-ATR Aircraft		A330-200	
	f upper	f lower	f upper	f lower
Fuselage	0.20	0.20	0.20	0.20
Wing	0.40	0.40	0.10	0.10
Horizontal tail	0.35	0.35	0.35	0.35
Vertical tail	0.35	0.35	0.35	0.35
Nacelle	0	0	0.1	0.1

Limitations

The chosen aerodynamic models have the following limitations:

- The wing is modeled as a trapezoid, while modern transport aircraft such as the A330 have a slightly advanced geometry using yehudi for instance.
- The Low-Fidelity method does not allow to specify a certain airfoil, hence the aerodynamics of the wing is not an one-on-one approximation of the chosen airfoil but a general approximation.
- The used lower-fidelity parasite drag models do not account for boundary layer interaction and other more advanced phenomena.
- The laminar-to-turbulent transition point is assumed to be the same for both the upper and lower part of the flat-plate models. One would expect the transition to occur more aft for the lower plate, resulting in less area the riblets are assumed to be effective. This assumption eventually will result in over-estimating the skin-friction drag reduction by the riblets.
- High lift performance is estimated by SUAVE without inputting crucial parameters such as the maximum lift coefficient as designed for in Chapter 9, resulting in no one-to-one modelling of the designed high lift devices.

16.2.5. Results

General Results

In order to visualise the capabilities of the low-ATR aircraft a payload diagram has been constructed, as shown in Figure 16.3a. As comparison and as means of verification and validation, this diagram of the Airbus A33-200 has been constructed and can be found in Figure 16.3b. The design payload corresponding to 250 passengers and the design range of 8000 kilometer has been visualised by a star and a vertical line, respectively. From this payload range diagram it is clear that the range and payload requirements, i.e. MATRA-USER-PER-01 and MATRA-USER-PER-04, are met. It should be noted that the maximum zero-fuel mass and the maximum fuel mass has been estimated using the same fractions with respect to MTOM compared to the Airbus A330-200. The maximum payload the aircraft is assumed to be 32 700 kilogram, corresponding to 300 passengers.

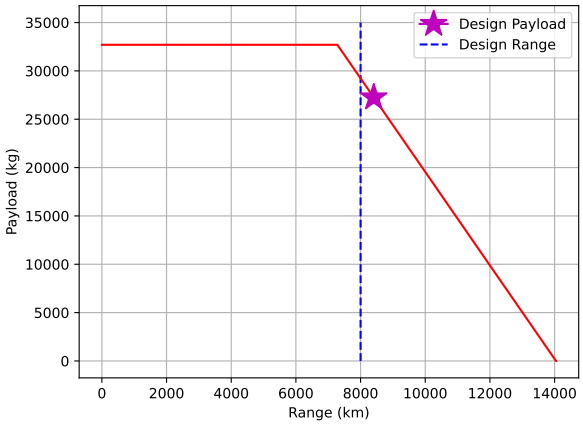

(a) Low-ATR aircraft

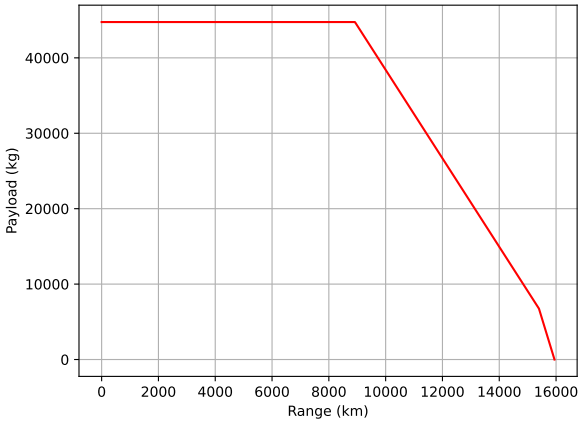

(b) Airbus A330-200

Figure 16.3: Payload-range diagram for the low-ATR aircraft and the A330-200

The required fuel for the different aircraft have been computed for the relevant mission profiles, which can be found in Table 16.7. This verifies MATRA-SSYS-AFP-12, as the aircraft is able to perform its design mission including diversion and loitering as defined in Table 16.1. The evolution of the aircraft mass and fuel mass for the low-ATR aircraft over the low-ATR mission profile starting at its MTOM is visualised in Figure 16.6. It should be noted that the required fuel for the low-ATR aircraft is significantly lower compared to the A330, mainly due to the better aerodynamic and propulsive efficiency. However, the low ATR-aircraft benefits from a approximately 50 tonnes lower MTOM compared to the A330-200 as well. To make a more fair comparison, the effect of an increased TOM of the low-ATR aircraft has been evaluated in Section 16.2.6.

Table 16.7: Results of SUAVE mission modelling on the mission defined in Table 16.1 and Table 16.3

		Mission at MTOM		Mission at converged TOM		
Aircraft	**Mission**	**TOM (kg)**	**Fuel burn (kg)**	**TOM (kg)**	**Fuel burn (kg)**	**Time (min)**
A330-200	Low-ATR	230,000	62,150	205,286	57,836	684.62
A330-200	Reference	230,000	62,279	202,588	55,137	583.57
Low-ATR Aircraft	Low ATR	182,280	43,860	159,477	41,589	684.62

The evolution of main aircraft parameters of the low-ATR aircraft over the low-ATR mission profile are presented in Figure 16.4-Figure 16.11. These results will be interpreted in the following subsections.

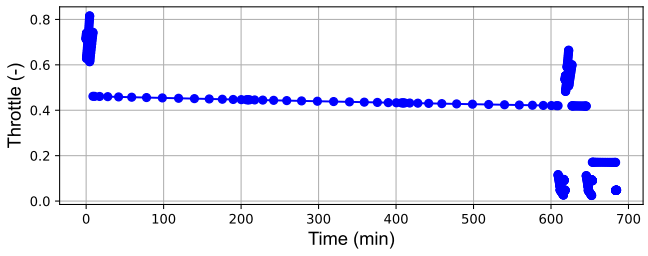

Figure 16.4: Throttle variation over the mission profile

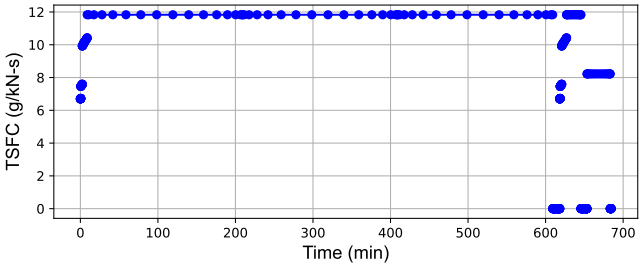

Figure 16.5: TSFC variation over the mission profile

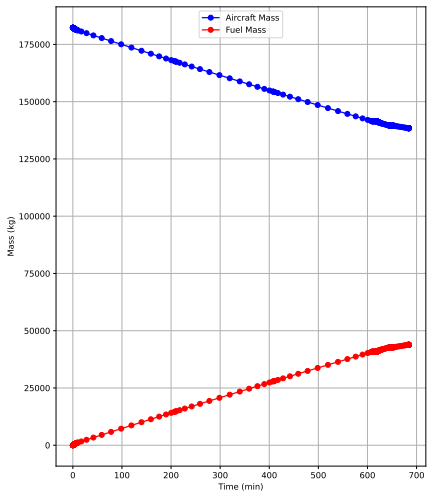

Figure 16.6: Aircraft mass and burnt fuel mass variation over the mission profile

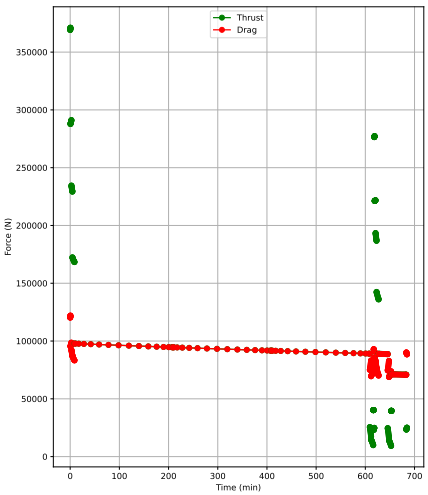

Figure 16.7: Thrust versus drag variation over the mission profile

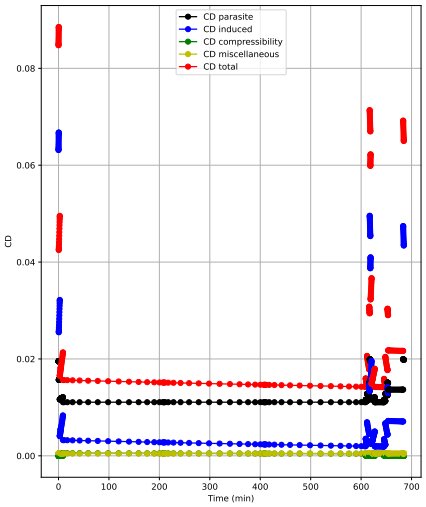

Figure 16.8: Drag breakdown over the mission profile

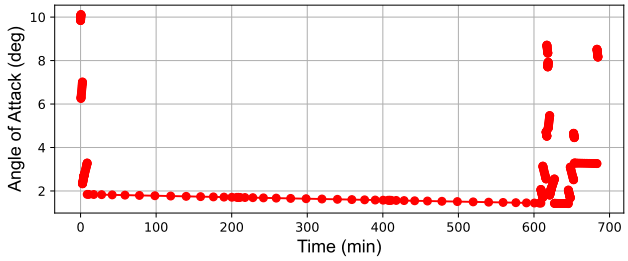

Figure 16.9: Angle of attack variation over the mission profile

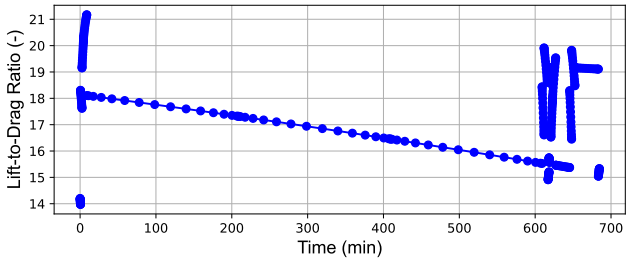

Figure 16.10: Lift-to-drag ratio variation over the mission profile

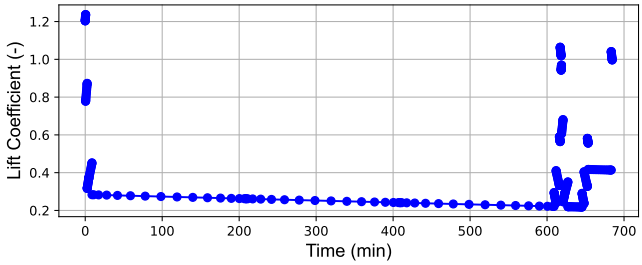

Figure 16.11: Lift coefficient variation over the mission profile

Aerodynamic Results

Before the graphs regarding the aerodynamic characteristics will be interpreted, it is interesting to look at the effect of the riblets. The low-ATR aircraft has been modeled with and without riblets on the low-ATR mission profile starting with its MTOM. The results can be found in Table 16.8. The same has been performed for the A330-200 in Table 16.11 in Section 16.2.9, where a smaller reduction in both total and parasite drag has been observed, and therefore a smaller reduction in fuel burn as well. Note that the parasite drag consists of form drag and skin friction drag and that the riblets reduce skin friction drag in turbulent boundary layers. The main reason for the more significant effect of the riblets is that the low-ATR aircraft has a relatively large wetted surface area due to its relatively large wings, increasing the proportion of skin friction drag of the total drag. Furthermore, the low-ATR aircraft has a higher Oswald efficiency factor and aspect ratio, resulting in a smaller reduced induced drag. This is all substantiated by the drag breakdown over the mission profile in Figure 16.8, where one can observe that in cruise the parasite drag is the main contributor to the total drag. Finally, discussed as limitation in Section 16.2.3, is that the assumption that the bottom plate has the same portion of turbulent flow as the top plate results in over-estimating the wetted surface area of the riblets. However, the introduction of the 70% coverage makes the analysis already more conservative.

Figure 16.8 also shows that the induced drag is the main contributor in the flight phases where high lift coefficients are obtained, as can be seen by looking at the lift coefficient variation of the mission profile in Figure 16.11. The angle of attack variation over the mission profile is visualised in Figure 16.9, which has an identical shape as Figure 16.11 as the angle of attack and lift coefficient follow a linear relationship in this angle of attack regime.

Table 16.8: Effect of riblets for low-ATR aircraft

Aircraft	Riblets	TOM (kg)	Fuel burn (kg)	Total drag coefficient at start of cruise (-)	Parasite drag coefficient at start of cruise (-)
Low-ATR aircraft	No	182,280	45,251	0.016162	0.0115632
Low-ATR aircraft	Yes	182,280	43,860	0.0156445	0.011075
Difference (%)	-	0.00	3.10	3.20	4.22

Table 16.9: Drag prediction comparison between SUAVE and in-house Class-II drag model

Model	Total drag coefficient @ start cruise	Total drag reduction due to riblets @ start cruise
SUAVE	0.0156	3.200
In-house class II drag	0.0134	3.159
Difference (%)	16.4	1.3

The total drag coefficient and the drag reduction due to the riblets at the beginning of cruise computed by SUAVE have been compared to the values obtained in the Class-II drag estimation in Chapter 12. The results in Table 16.9 show both models predict a similar trend regarding the drag reduction by the riblets. However, it shows that the total drag coefficient calculation is more conservative. This is most probably caused by the limitations in the SUAVE model as discussed by Section 16.2.4. As no airfoil can be selected in SUAVE the advantages of the NLF are not included in the SUAVE model. Furthermore, slightly different drag calculation methods have been used. This discrepancy in drag coefficient also results in an approximately 10% lower Lift-to-Drag ratio in cruise in Figure 16.10 compared to the Class-II drag model in Chapter 12. The Lift-to-Drag ratio in cruise reduces over time as the lift coefficient reduces more significantly than the drag coefficient. The lift coefficient in cruise reduces as a smaller lift coefficient is required as the aircraft gets lighter. It should be noted that this is not an optimal cruise strategy regarding fuel burn, but the mission is optimised with respect to ATR for a single cruise altitude and Mach number.

Propulsion Results

Figure 16.7 shows the the thrust and drag variation over the aircraft's mission profile. It satisfactorily confirms that horizontal equilibrium in cruise with the required thrust in cruise reducing over time as the induced drag decreases due to decreasing aircraft weight because of fuel burn. Furthermore, it shows that thrust is larger or smaller than the drag in phases where acceleration or deceleration is desired, respectively. The throttle setting corresponding to the thrust is presented in Figure 16.4, confirming the conclusion drawn in Chapter 10 regarding the fact that the aircraft is over-designed in cruise to meet the take-off requirement. Finally, the TSFC plotted in Figure 16.5 shows that the TSFC in cruise computed by SUAVE is almost identical to the TSFC computed by the in-house propfan model in Chapter 10, i.e. 11.8 versus 11.76 g/kN-s.

16.2.6. Sensitivity Analysis

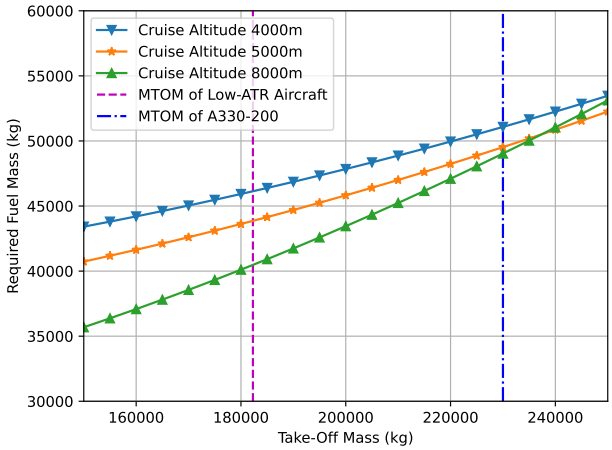

Figure 16.12: Required fuel sensitivity to input take-off mass and cruise altitude for the low-ATR mission profile as defined in Table 16.1

At this stage of the design, there is still some uncertainty in the aircraft parameters. In order to investigate the sensitivity of the mission calculator to the main SUAVE input, a sensitivity study regarding TOM and cruise altitude has been performed while keeping the cruise Mach number 0.63, as shown in Figure 16.12. It can be observed that flying higher generally means lower fuel burn as expected, except after a certain TOM where it cost more fuel to get to the cruise altitude than one would benefit from the reduced fuel burn flying at that altitude. This graph can also be used to see how much fuel the low-ATR requires if it would take-off with the MTOM of the A330-200. The low-ATR aircraft would require 49.5 tonnes of fuel, while the A330-200 would need 62.2 tonnes, i.e. 20% lower. It should be noted that generally such an increase in MTOM would require to resize the aircraft and the engine resulting in more drag and more fuel required. This has not been considered in this analysis.

16.2.7. Verification and Validation: SUAVE Mission Modeling

Verification and Validation of the SUAVE software

Reference [99] presents a verification and validation study of the SUAVE software. The low-fidelity methods and the mission solving that is used for the low-ATR aircraft and A330-200 have been verified and validated using three conventional designs. For example, the Boeing 737-800 has been modeled with SUAVE over its nominal mission profile , resulting the main mission parameters predicted by SUAVE well within a 10% margin compared to values predicted by three other tools, as can be seen in Table 16.10 [99].

Verification

The first step is to check that SUAVE is properly installed. This is done by modeling the Boeing 737 as described in Reference [99]. The results in Table 16.10 show that the SUAVE has been installed correctly, with minor discrepancies seen in the most right column most likely caused by minor differences in input.

Table 16.10: Validation data of SUAVE used as means of verification of installed SUAVE

Parameter	Unit	SUAVE [99]	SUAVE discrepancies w.r.t. validation models (%) [99]	Installed SUAVE	Difference (%)
Fuel burn	lb	39,400	4	39,265	0.3
L/D (beginning of cruise)	–	16.5	6	16.65	0.9
Cruise C_L	–	0.58	3	0.595	2.6
Cruise thrust per engine	lb	5000	3	5060	1.2
Cruise SFC	lb/lbf-hr	0.63	3	0.63	0.0

As the objective is to vary cruise altitude and Mach number, these have been varied in order to see if the models responds as it should, i.e. increasing cruise Mach number should result in an increase in fuel burn, while flying higher if feasible should reduce the fuel burn for long range missions. After this was ascertained, the in-house made TOM convergence tool that has been explained in Section 16.2 is to be verified. This is done by running the convergence tool with a convergence residual of 0.1 kg to obtain a certain fuel weight. Then the sum of this fuel weight and the OEM and payload weight is plugged in as TOM in the SUAVE with the convergence tool turned off. By obtaining the same fuel weight as was used in the input, the TOM convergence has been verified. This can be checked by looking at the difference between the TOM and the burnt fuel for the mission of converged TOM in Table 16.11, which is equal to the sum of the OEM and the payload weight (147,450 kg) as defined in Table 16.4.

The most dangerous pitfall that comes with the use of SUAVE, besides verifying and validating the modifications made to SUAVE, is to make sure that the correct input are used. There are many input parameters for the aircraft and the mission. Especially the fact that two aircraft are modeled over potentially two mission profiles, plus having one version that does and one that does not include the riblets, makes room for potential errors, hence results are always double checked en double modeled.

16.2.8. Verification and Validation: SUAVE Payload-Range Diagram

The general payload-range diagram function of SUAVE has been validated in Reference [99] by computing the diagram for an Embraer aircraft. This modeling has been repeated with the installed SUAVE resulting in identical results. However, in order to verify the correct implementation and usage of the tool, the payload-range diagram of the Airbus A330-200 has been constructed, with additional data obtained from Reference [1], and is visualised in Figure 16.3b. The results have been compared with a given payload-range diagram in Reference [1] resulting in minimal differences, resulting in the implemented SUAVE payload-range diagram to be verified, and giving another proof of the validity of the tool itself. [1]

16.2.9. Verification and Validation: Riblet Model

A tool to calculate the reduction in skin friction coefficient due to riblets, by means of a flat plat approximation, was provided to the team. This tool was also used in the in-house Class-II drag estimation in Chapter 12 and is assumed to be verified and validated. Care was taken with the implementation into SUAVE, and to verify this, the A330-200 has been modeled on its reference mission with and without riblets. The results can be found in Table 16.11. The reduction in parasite drag and total drag coefficient is in line with the expectations of what riblets can achieve as was more discussed more in depth in Chapter 12, i.e. approximately 4-5 % reduction in parasite drag and a 2% reduction in total drag coefficient. From Table 16.11 shows that the drag calculation behaves as expected, in the sense that aircraft weight does not have an effect on parasite drag, but that the proportion of parasite drag of the total drag reduces for increasing weight due the increased induced drag.

Table 16.11: Verification riblets

			Mission at MTOM				Mission at converged TOM				
Aircraft	Mission	Riblets	TOM (kg)	Fuel burn (kg)	C_D total @ start cruise	C_D parasite @ start cruise	TOM (kg)	Fuel burn (kg)	C_D total @ start cruise	C_D parasite @ start cruise	Time (min)
A330-200	Reference	No	230,000	62,279	0.03050538	0.011670	202,588	55,137	0.026524	0.011670	583.57
A330-200	Reference	Yes	230,000	61,161	0.029963	0.011164	201,111	53661	0.0257623	0.011164	583.57
Reduction w.r.t. no riblets(%)		-		1.80	1.78	4.34	0.73	2.68	2.87	4.34	-

16.2.10. Verification and Validation: Propfan model

Verification

The propfan engine is modeled in SUAVE using Dorsey's method[29]. Dorsey provided a part of his code, which have been modified to be implemented for the low-ATR aircraft. To verify the propfan modelling in SUAVE, it is decided to use the 150 passengers 4000 nautical mile design range aircraft Dorsey described in his paper [29]. However, as not all parameters were given, some aircraft parameters and the whole mission profile had to be approximated, resulting in significant discrepancies between the results. As all engine input parameters were provided, the engine model itself could be verified as the SFC at the start of cruise as can be seen in Table 16.12 is very close to the TSFC computed by Dorsey.While the SFC is computed very accurately, the fuel burn is off significantly, caused by the thrust over the mission profile being off due to the differences in aircraft and mission input.

Table 16.12: Propfan model verification [29]

Parameter	Unit	Dorsey [29]	SUAVE	Differences (%)
SFC @ start cruise	lb/ lbf-hr	0.555	0.559	0.72
Fuel burn	lb	14,921	17,328	16.13

Validation

In order to validate the used propfan model, the TSFC calculated by SUAVE is compared to the value computed by the in Section 10.5. In this respective section the TSFC of the propfan at 5000 meters was computed to be 11.76 g/kNs, while SUAVE computed a cruise TSFC of 11.8 g/kNs as can be seen in Figure 16.5 , resulting in the propfan of SUAVE to be assumed validated.

16.3. ATR Performance

This section summarises and extends the ATR model devised in the foregoing Midterm Report [39], to now permit computing the ATR footprint of the novel aircraft designed in this report on its optimised mission profile. Firstly, the various inputs to this model shall be presented, including both aircraft (sub-)system/mission parameters, as well as model-specific coefficients. Subsequently, the model itself shall be summarised, and finally leveraged to investigate the relative ATR gain compared to an Airbus A330-200 which this aircraft is expected to achieve.

16.3.1. ATR Model Inputs

Table 16.13 contains the inputs fed into this model, which stem from two principle sources: firstly, the propfan engine model, yielding the TSFC and total high-pressure compressor outlet temperature $T_{T3}(t)$ and pressure $P_{T3}(t)$, and secondly, the SUAVE mission design tool kindly provided by A. Dorsey, which yields the mission profile in terms of Mach number $Ma(t)$, altitude $h(t)$ and throttle setting as functions of mission time.

Due to the inherent workings of the ATR model, the aforementioned parameters must be converted into time-averaged/total quantities. For each SUAVE mission segment i of length t_i, the altitude h_i, Mach number Ma_i and throttle setting $t\%_\mathrm{i}$ are fed into the propfan engine model, which in turn outputs the corresponding $TSFC_\mathrm{i}$, T_{insti}, $T_{T3\mathrm{i}}$ and $P_{T3\mathrm{i}}$. Considering the varying time spans pertaining to different mission segments, the time averages (h_tavg, $T_{T3\mathrm{tavg}}$ and $P_{T3\mathrm{tavg}}$) ought to be taken. The total mission fuel mass $m_{fuel\mathrm{tot}}$ is computed rather intuitively by summing up the fuel mass per mission segment $m_{fuel\mathrm{i}} = TSFC_\mathrm{i} \cdot T_{insti} \cdot t_\mathrm{i}$ over all segments.

Table 16.13: Input parameters from other models

Parameter	h_tavg	$m_{fuel\mathrm{tot}}$	$T_{T3\mathrm{tavg}}$	$P_{T3\mathrm{tavg}}$
Source	SUAVE	Engine Model	Engine Model	Engine Model

Table 16.14-Table 16.16 summarise the model-specific input parameters, which are constituted by the physical properties of the greenhouse agents under consideration. Finally, Figure 16.13 visualises the variations in radiative forcing factors of three greenhouse agents (O_{3S}, CH_4 and O^{3L} are depletion products of NO_X) with altitude.

Table 16.14: Properties of various combustion species [78] [21]

Specie i	**CO_2**	**CH_4**	**O_3**	**H_2O**	**SO_4**	**Soot**	**AIC**
λ_i	0.73	0.86	1.00	0.83	0.66	0.51	0.43
Eff_i	1.00	1.18	1.37	1.14	0.90	0.70	0.59
$(\frac{RF_\mathrm{ref}}{E_\mathrm{ref}}{}_\mathrm{i})$	-	-	$1.01 \cdot 10^{-11}$	$7.43 \cdot 10^{-15}$	$-1 \cdot 10^{-10}$	$5 \cdot 10^{-10}$	$2.21 \cdot 10^{-12}$
EI_i $(\frac{\mathrm{kg}}{\mathrm{kg}})$ [78]	3.16	See text (total NO_X)		1.26	$4 \cdot 10^{-5}$	$2 \cdot 10^{-4}$	NA
A_i $(\frac{\mathrm{W}}{\mathrm{m}^2\ \mathrm{kg}_{NO_X}})$	-	$-5.16 \cdot 10^{-13}$	$-1.21 \cdot 10^{-13}$ (O_{3L})	-	-	-	-

Table 16.15: Coefficients of impulse response function $G_{\chi_{CO_2}}$ [78]

i	1	2	3	4	5
α_i ($\frac{ppbv}{Tg(CO_2)}$)	0.067	0.1135	0.152	0.097	0.041
τ_i (years)	∞	313.8	79.8	18.8	1.7

Table 16.16: Coefficients of G_{CO_2} [28]

j	1	2	3
α_{cj}	0.259	0.338	0.186
τ_{cj} (years)	172.9	18.51	1.186

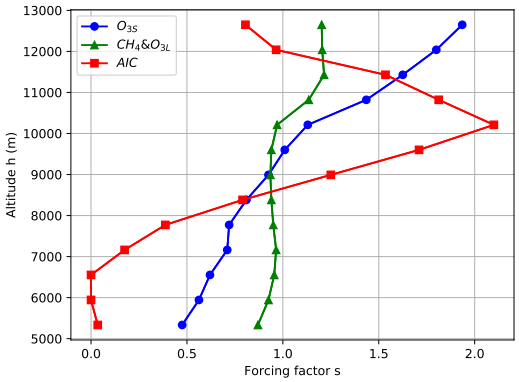

Figure 16.13: Radiative forcing factors as a function of altitude (reproduced from [27])

16.3.2. ATR Model Workings

The ATR_H of a given aircraft in units of Kelvin over an arbitrary time horizon H in years is defined in Equation 16.1. A time horizon of 100 years is chosen, which according to P. Proesmans enables accounting for both short- and long-lived climate agents [78]. The ATR_H computes the time-normalised integral of the emissions-induced surface temperature change $\Delta T(t)$ in year t, which in turn is defined by the convolution integral in Equation 16.2.

$$\mathrm{ATR}_H = \frac{1}{H}\int_0^H \Delta T(t)dt \qquad (16.1) \qquad \Delta T(t) = \int_{t_0}^{t} G_T\left(t-t'\right)\cdot RF^*\left(t'\right)dt' \qquad (16.2)$$

In Equation 16.2, $G_T(t)$ corresponds to the impulse response function provided in Equation 16.3 and $RF^*(t)$ represents the cumulative, normalised radiative forcing in year t (see Equation 16.4). Note that the ATR may also be evaluated at any intermediate year, simply by integrating up to and normalising by that very year; in this way, the ATR evolution over time can be plotted (see Section 16.3.3) The normalisation is performed with respect to the pre-industrial radiative forcing due to CO_2 RF_{2xCO_2}. The summation encapsulates all climate agents considered in this model, as listed in Table 16.14.

$$G_T(t) = \frac{2.246}{36.8}\mathrm{e}^{-t/36.8} \qquad (16.3) \qquad RF^*(t) = \sum_{i}^{\text{all species}} RF_i(t) = \sum_{i}^{\text{all species}} \left[\mathrm{Eff}_i \cdot \frac{RF_i(t)}{RF_{2\times CO_2}}\right] \qquad (16.4)$$

In the following, the contribution of each climate agent to Equation 16.4 shall be derived, and finally integrated to obtain the overall values of ATR_H.

CO_2

The change in atmospheric CO_2 concentration $\Delta\chi_{CO_2}(t)$ in year t is given by Equation 16.5, where $E_{CO_2}(t)$ represents the total mass of CO_2 emitted in year t by the considered aircraft. This term is derived via the TSFC and thrust obtained from the propfan engine model, combined with the mission profile yielded by the SUAVE tool and the corresponding emission index from Table 16.14. Depending on whether the ATR of a single flight or of all flights performed by a given aircraft during its operational lifetime is desired, this quantity takes on different values. In the former case, it constitutes an array featuring the CO_2 emitted during a single flight in year 1, and zeros for the remaining $H-1$ years. In the latter case, based on data of 7 American airlines' wide-body fleet in 2019 suggesting 12.49 average daily airborne hours and the estimated flight time for this project's design mission, the expected number of yearly flights can be computed, and therewith the yearly emitted CO_2 mass [6]. The impulse response function coefficients α_i and τ_i are provided in Table 16.15.

$$\Delta\chi_{CO_2}(t) = \int_{t_0}^{t} G_{\chi CO_2}\left(t-t'\right)\cdot E_{CO_2}\left(t'\right)dt' \quad \text{with} \quad G_{\chi CO_2}(t) = \sum_{i=1}^{5}\alpha_i\cdot \mathrm{e}^{-t/\tau_i} \qquad (16.5)$$

The radiative forcing contribution $RF^*(t)$ of CO_2 to Equation 16.4 in year t is computed via Equation 16.6, where $\chi_{CO_2,0}$ = 380 ppmv = 0.404 kg m^{-3} denotes the atmospheric background CO_2 concentration, which is assumed to be invariant with time [78].

[6] `http://web.mit.edu/airlinedata/www/2019%2012%20Month%20Documents/Aircraft%20and%20Related/Widebody/Average%20Daily%20Airborne%20Hours%20of%20Total%20Widebody%20Fleet.htm` (last accessed on 16/05/2021)

$$RF^*(t) = \frac{1}{\ln 2} \cdot \ln\left(\frac{\chi_{CO_2,0} + \Delta\chi_{CO_2}(t)}{\chi_{CO_2,0}}\right) \tag{16.6}$$

NO_X

NO_X is not a greenhouse gas in its own right, but depletes a number of other gases, which have a net positive global warming effect, including methane (CH_4), and short- and long-lived ozone (O_{3S} and O_{3L}, respectively).

CH_4 and O_{3L} have a net cooling effect and a long atmospheric residence time, as computed via the convolution integral in Equation 16.11. The so-called perturbation factor τ_n is set to 12 years, and the altitude-dependent forcing factors s_{CH_4} and $s_{O_{3L}}$ can be read off Figure 16.13, which linearly interpolates the displayed data points. The total mass of emitted NO_X in year t is computed in the same vein as outlined in the foregoing section on CO_2, however, this time the emission index EI_{NO_X} is not constant, but described by the following relations:

$$EI_{NO_X} = 0.0986 \cdot (\frac{p_{T3}}{101325})^{0.4} \cdot e^{\frac{T_{T3}}{194.4} - \frac{H_0}{53.2}} \quad (16.7) \qquad H_0 = \frac{0.62198 \cdot \Phi \cdot p_v}{p_{amb} - \Phi \cdot p_v} \quad (16.8) \qquad P_v = 0.014504 \cdot 10^{\beta} \quad (16.9)$$

$$\begin{aligned}\beta = {} & 7.90298 \cdot \left(1 - \tfrac{373.16}{T_{amb}+273.16}\right) + 3.00571 + 5.02808 \cdot \log\left(\tfrac{373.16}{T_{amb}+273.16}\right) + \\ & 1.3816 \times 10^{-7} \cdot \left[1 - 10^{11.344 \cdot \left(1 - \frac{T_{amb}+273.16}{373.16}\right)}\right] + 8.1328 \times 10^{-3} \cdot \left[10^{3.49149 \cdot \left(1 - \frac{373.16}{T_{amb}+273.16}\right)} - 1\right]\end{aligned} \tag{16.10}$$

Besides the total temperature $T_{T3}(t)$ and pressure $P_{T3}(t)$ at the high-pressure compressor, EI_{NO_X} depends on the specific humidity H_0, which itself is function of the relative humidity Φ (assumed to equal 60%), the saturation pressure P_v in psia (dependent on the ambient temperature T_{amb} in Kelvin only) and the ambient static pressure p_{amb} in psia. Ambient conditions as a function of altitude are straightforwardly obtained by interpolating ISA tables [7]. Please note that Equation 16.7 from [78] erroneously contains a negative sign in front of the exponential term, which has been rectified here.

The radiative forcing contribution of NO_X-depleted CH_4 and O_{3L} to Equation 16.4 is computed as follows:

$$RF_i(t,h) = s_i(h) \int_{t_0}^{t} G_i\left(t - t'\right) \cdot E_{NO_x}\left(t'\right) dt' \text{ with } G_i(t) = A_i \cdot \mathrm{e}^{-\mathrm{t}/\tau_i} \text{ for i} = \mathrm{CH_4, O_{3\,L}} \tag{16.11}$$

Short-lived ozone (O_{3S}) has a net warming contribution and a short atmospheric lifetime, meaning that no convolution integral is required to obtain its radiative forcing contribution (see Equation 16.12). $s_{NO_x - O_{3\,S}}(h)$ may again be read off Figure 16.13. Similar to CH_4 and O_{3L}, this result may directly be added to Equation 16.4.

$$RF_{NO_x - O_{3\,S}}(t,h) = s_{NO_x - O_{3\,S}}(h) \cdot \left(\frac{RF_{ref}}{E_{ref}}\right)_{NO_x - O_{3\,S}} \cdot E_{NO_x}(t) \tag{16.12}$$

H_2, SO_4 and Soot

Similar to O_{3S}, H_2, SO_4 and soot have short atmospheric residence times. Furthermore, their radiative forcing contribution may be approximated as altitude-independent, allowing the following simplified relation to be employed:

$$RF_i(t) = \left(\frac{RF_{ref}}{E_{ref}}\right)_i \cdot E_i(t) \text{ for } i = \mathrm{Soot, H_2O, SO_4} \tag{16.13}$$

All relevant quantities may be extracted from Table 16.14.

AIC

The subsequent analysis shall be restricted to the effect of linear contrails. Although several authors recommend that contrail-promoted cirrus cloud formation be taken into account, there is still a significant uncertainty associated with this effect. In favour of a more accurate ATR analysis, Equation 16.14 only considers the linear contrail length $L(t)$ and the linear contrail formation factor $s_{contrails}(h)$ (see Figure 16.13).

$$RF_{contrails}(t,h) = s_{contrails}(h) \cdot \left(\frac{RF_{ref}}{L_{ref}}\right)_{contrails} \cdot L(t) \tag{16.14}$$

[7] `https://onlinelibrary.wiley.com/doi/pdf/10.1002/9781118534786.app1` (last accessed on 12/06/2021)

16.3.3. ATR Model Results

In this section, the precise ATR footprint of the envisioned low-ATR aircraft is computed employing the method detailed in Section 16.3.2. To this purpose, the airframe and engine sizing process is conducted for the design point conditions to be identified in Section 16.5, namely a Mach number of 0.63 and an altitude of 5000 m. Please note that the motivation for choosing this cruise design point was postponed to a later section, in favour of a detailed demonstration of the foregoing ATR model. The global warming impact over time is subsequently plotted against that of the Airbus A330-200 reference aircraft flying at a cruise Mach number of 0.82 and an altitude of 11 250 m. As mentioned in Section 16.3.1 and schematised in Figure 16.1, the respective mission profiles were obtained from SUAVE via time-ordered arrays containing altitude, Mach number and throttle setting. The flight time for the 8000 km route Tokyo-Vancouver required by the present aircraft equals 11 hours and 25 minutes, compared to a reference flight time of 9 hours and 44 minutes. As presented in Table 16.17, the total mission fuel mass of the designed aircraft equals 37.40 tonnes, whereas the reference aircraft consumes 59.12 tonnes. The following choices were made as to the computed ATR footprint: a single aircraft is assumed to operate for 35 years and 12.49 average daily airborne hours [8]. Based on the aforementioned flight times obtained from SUAVE, this results in a certain number of flights per year, based on which the ATR footprint per aircraft resulting from 35 years of sustained operation can be computed. Table 16.17 contains the time-averaged Mach number, altitude, T_{T3} and P_{T3}, the TSFC at cruise, as well as the overall mission time and fuel mass are presented. It deserves mentioning how close the computed TSFC value of 11.85 g kN^{-1} s at cruise is to the 11.8 g kN^{-1} s obtained from SUAVE (see Figure 16.5), giving confidence as to the validity of the respective propfan models. Similarly, the burned fuel masses reported in Table 16.17 are close to the values reported in Table 16.7 for the converged take-off mass case, considering the uncertainties present in the thrust variation behaviour with altitude and Mach number of the two models.

Table 16.17: Own design mission and A330-200 reference mission parameters

Mission parameters	t_{tot} (hours)	Ma_{tavg} (-)	h_{tavg} (m)	$m_{fuel_{tot}}$ (kg)	$TSFC_{cruise}(\frac{g}{kNs})$	$T_{T3_{tavg}}$ (K)	$P_{T3_{tavg}}$ (Pa)
Own aircraft	11.41	0.61	4666.99	37403.21	11.85	780.50	$2.18 \cdot 10^6$
A330-200	9.73	0.77	9946.46	59117.43	17.27	730.89	$1.34 \cdot 10^6$

Figure 16.14 reports the results from applying the in-house ATR model to the case of a single aircraft performing 400 yearly flights for 35 years. This value stems from the computed flight time of the low-ATR aircraft assuming 12.49 average daily airborne hours. To avoid any artificial penalisation of the A330-200 due its shorter block time and thus higher yearly flight count, it shall also adopt this value (the reverse would presumably not be possible, as the propfan engines are not capable of operating under the A330-200's cruise conditions). As expected based on Table 16.14, CH_4, O_{3l} and SO_4 have a net cooling effect, whereas O_{3S}, CO_2 and soot are the dominant global warming agents. Interestingly, the net ATR contribution of NO_X changes sign for the low-ATR aircraft after about 55 years (Figure 16.14c), whereas it remains positive for the A330-200 (Figure 16.14f). As mentioned in Section 10.2, this primarily due to the CF6-80E1's larger high-pressure compressor outlet pressure (see Table 16.17), increasing the effective emission index of NO_X by depleting twice as much O_{3S} at equal CH_4 and O_{3L} emissions. Considering the altitude-independent relation between fuel burn and CO_2 (Equation 16.5), it appears reasonable that the ATR_{100} of CO_2 is nearly twice as high for the reference aircraft (Figure 16.14f) compared to the present low-ATR design (Figure 16.14c). The same observation holds for H_2O, SO_4 and soot, whose radiative forcing factors also scale with the burned fuel mass [21]. Finally, based on the Schmidt-Appleman criterion the ATR contribution of AIC strongly scales with the temperature difference between the engine exhaust stream and the ambient air [78]. In that sense, the lower turbine exit temperature of the CF6-80E1A3 engine decreases the probability of contrail formation. However, this is overcompensated by the significantly higher cruise altitude and therewith lower ambient air temperature, resulting in an overall higher radiative forcing contribution for the A330-200 (compare Figure 16.14b and Figure 16.14e). Compared to other studies such as the one by E. Schwartz Dallara [28], the AIC contribution obtained in this work is relatively low. As mentioned in Section 16.3.2, this is because contrail-induced cirrus cloud formation is excluded from the analysis, given the high uncertainty attributed to this relationship by multiple authors [78] [21]. Therefore, the ATR footprints reported in this work may underestimate the actual global warming footprints of both aircraft considered.

To conclude, the increased accuracy of the foregoing ATR results compared to the simplified method used to identify the mission design point (see Section 16.5) is small: after 100 years, the relative ATR gain of the present low-ATR aircraft is 80.0%, as compared to the 85% found in Section 16.5. This gives confidence to the validity of the assumption that both aircraft traverse the entire mission distance in cruise, which will be employed in Section 16.5 to determine the optimum cruise conditions.

[8] `http://web.mit.edu/airlinedata/www/2019%2012%20Month%20Documents/Aircraft%20and%20Related/Widebody/Average%20Daily%20Airborne%20Hours%20of%20Total%20Widebody%20Fleet.htm` (last accessed on 16/05/2021)

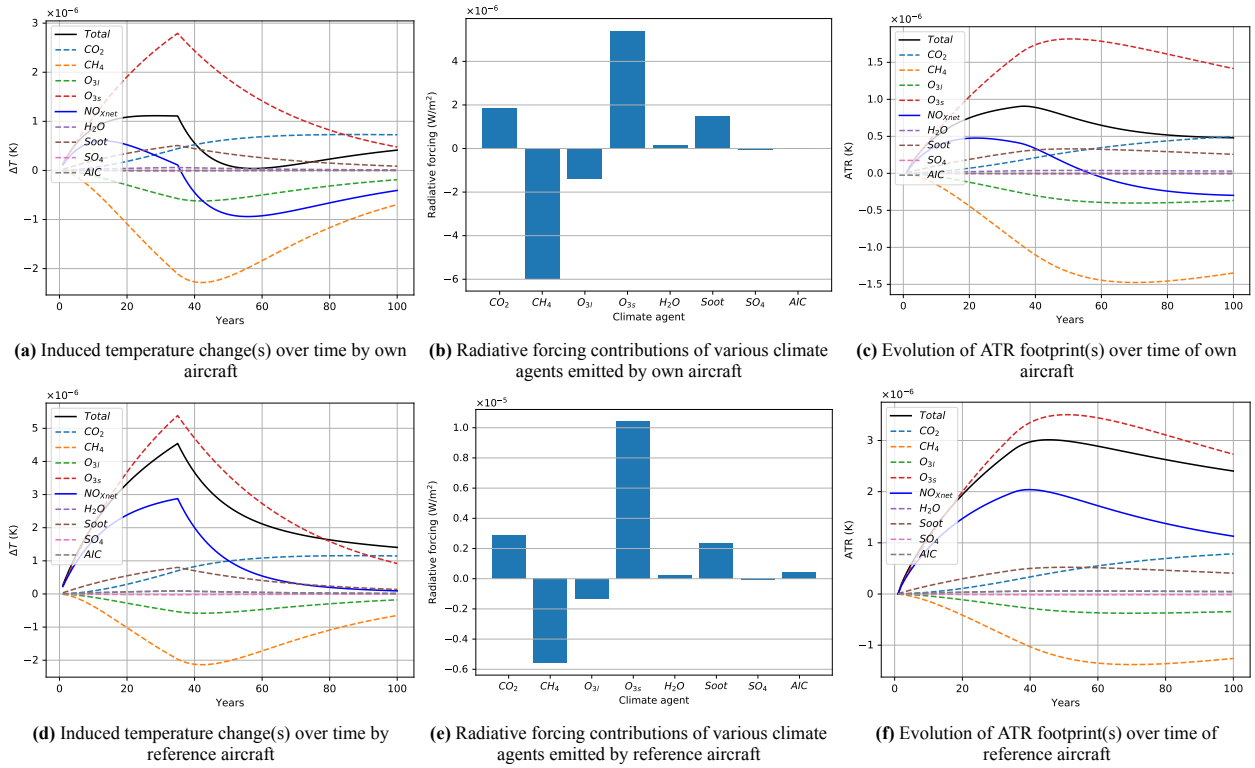

(a) Induced temperature change(s) over time by own aircraft

(b) Radiative forcing contributions of various climate agents emitted by own aircraft

(c) Evolution of ATR footprint(s) over time of own aircraft

(d) Induced temperature change(s) over time by reference aircraft

(e) Radiative forcing contributions of various climate agents emitted by reference aircraft

(f) Evolution of ATR footprint(s) over time of reference aircraft

Figure 16.14: Climate impact parameter variation over time for project and reference aircraft

Finally, one may also want to compute and plot the ATR footprint of both aircraft per kilometer, as done in Figure 16.15. This is done by evaluating Equation 16.1 for each year and normalising it by the cumulative kilometer count up to that year. In practice, this means that one can only obtain a meaningful graph whilst the aircraft is still operational, i.e., for the first 35 years. However, the relative ATR gain of the project aircraft over the A330-200 is unimpacted and remains at 80%.

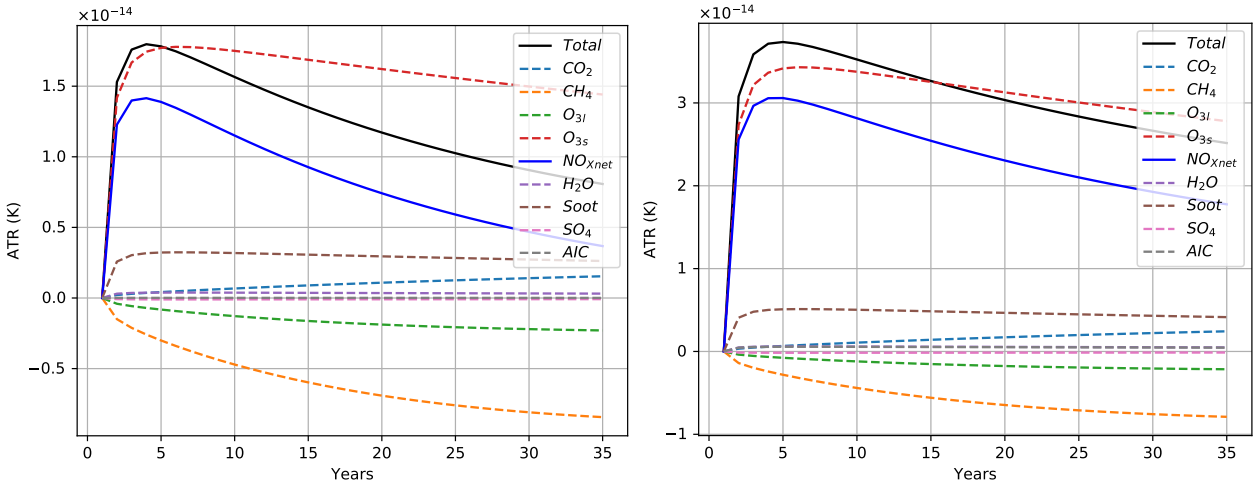

(a) ATR per kilometer of own aircraft

(b) ATR per kilometer of A330-200

Figure 16.15: ATR footprint of considered aircraft over operational lifespan

16.3.4. ATR Model Verification

In this section, the ATR model devised in Section 16.3.2 and employed in Section 16.3.3 and subsequent sections shall be verified by comparison with a reference study performed by P. Proesmans [78]. Said work considers a maximum fleet size of 15600 aircraft, a production time of 30 years and an operational lifetime of 35 years, resulting in the fleet size evolution over time displayed in Figure 16.16a. Two mission scenarios/optimisation objectives are considered: a minimum-fuel-mass scenario characterised by the parameters in the second row of Table 16.18, and a minimum-ATR_{100} scenario corresponding to the parameters in the third row of Table 16.18. The considered mission profile entails a 3200 km cruise

phase at the respective altitudes and Mach numbers indicated in Table 16.18, followed by a 460 km diversion segment at cruise conditions and finally a 35 minute loiter phase at 1500 feet (457 m) altitude. P. Proesmans employs the GE90 engine as a baseline propulsion system, the detailed parameters of which can be looked up in Table 16 of [78]. For the purpose of this verification task, the turbofan engine model devised in Chapter 10 is adapted to model the GE90 engine. It deserves mentioning that the employed model could not handle the very high BPRs of the GE90 engine, the presumed effects of which shall be discussed hereafter. For both scenarios, the maximum permissible BPR is indicated in brackets behind the reference value (fourth column of Table 16.18).

Table 16.18: Mission and engine design parameters for two reference cases from P. Proesmans [78]

Optimisation aim	h_{cr} (m)	Ma_{cr}	BPR	Π_{fan}	Π_{lpc}	Π_{hpc}	T_{T4} (K)
Fuel mass	10800	0.735	9.89 (7.1)	1.7	1.7	20	1600
ATR_{100}	8640	0.605	10.3 (9)	1.59	1.64	13	1560

As can be inferred from Figure 16.16b, the initial slope of the minimum-fuel-mass scenario (orange curves) agrees very well with the reference curve obtained by P. Proesmans. The difference in the long-term behaviour is attributed to discrepancies in the model input parameters, particularly with regards to the emission of CO_2, which is a long-term climate agent and directly scales with the fuel consumption [78]. In turn, the fuel consumption is a function of the BPR, which could not be modeled accurately due to aforementioned reasons. The minimum-ATR_{100} scenario (blue curves) displays a higher discrepancy with the reference curve. One possible reason relates to uncertainty in cruise throttle setting, which also P. Proesmans raises concerns about. In case of the minimum-fuel-mass scenario, one would assume the engine to operate at a higher throttle setting compared to the lower and slower flying ATR_{100}-optimised aircraft (assuming that the increase at lower altitudes is overcompensated by the thrust lapse of the GE90 engine at high altitudes), hence the greater over-estimation. Overall, given the uncertainty in climate and engine model input data, as well as in relation to the assumptions P. Proesmans' turbofan model is based on, the general behaviour of the ATR model devised in Section 16.3.2 may be considered verified. Any impact on the accuracy of the relative ATR results obtained in this report (which are arguably more representative in light of the relative project objective) is deemed small, considering that the relative ATR_{100} performance of the two mission scenarios predicted by P. Proesmans (27% lower ATR for "ATR_{100}" mission) and the present model (26.5% lower ATR for "ATR_{100}" mission) is small.

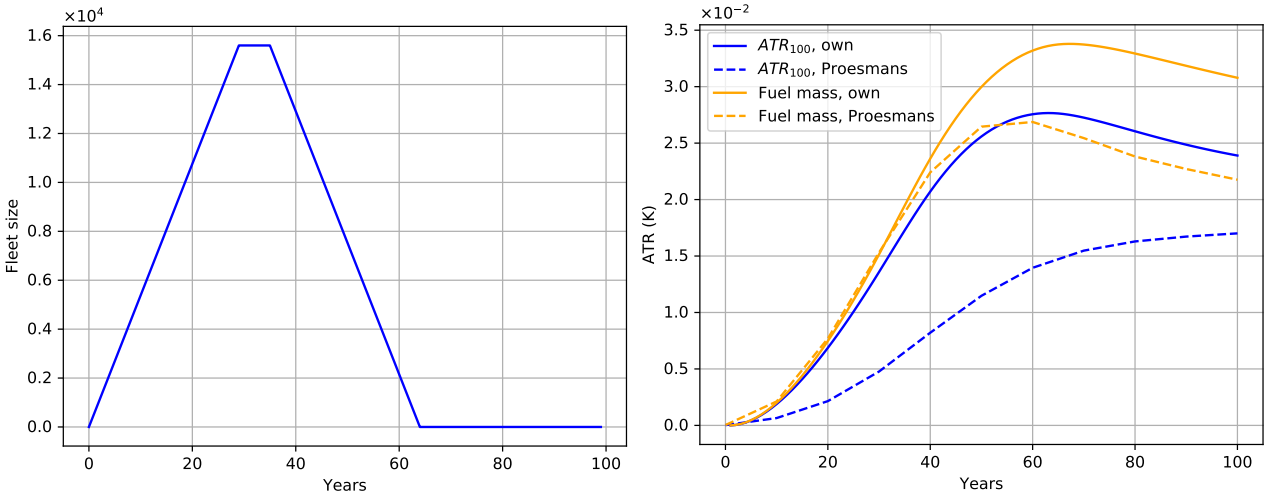

(a) Fleet size evolution over time employed by reference study

(b) ATR footprint for two reference mission scenarios [78]

Figure 16.16: Verification of ATR climate model with two reference mission scenarios elaborated upon in [78]

16.4. DOC Performance

The DOC model was devised and described in Section 22.2, which is based on the method presented in Roskam Part VIII "Airplane Cost Estimation" [92]. This same model is used in calculating the DOC of the present low-ATR aircraft.

The DOC model introduced in Roskam aims to split up the DOC into different parts, firstly the DOC of flying which takes into account the fuel cost, the crew cost, and the insurance. For this part the cost of fuel is most important, and the fuel mass per flight is the largest contributor to this cost.
The DOC is furthermore also split up into the cost of maintenance, which is further divided into labor costs and true material cost of maintaining the airframe and engines. For this analysis the size of the engine, and its maximum available thrust are used to estimate how much the engine costs and therefore how much the maintenance will cost. In Equation 16.15 the

cost per engine (Cer) is calculated based on a statistical relationship with respect to the thrust (T) in Roskam [92]. Where the thrust is the single engine maximum thrust in lbf, and the cost in 1990 US dollar, which will be converted to 2020 euro at the end of the cost analysis.

$$Cer = 10^{2.3044+0.8859 \cdot \log_{10} T} \tag{16.15}$$

Also a higher MTOW will result in larger maintenance costs. As the total aircraft cost is estimated using a statistical relationship with respect to the MTOW, which can be seen in Equation 16.16, where the MTOW is calculated in lbs and the cost in 1990 US dollars.

$$Aep = 10^{3.3191+0.8043 \cdot \log_{10} MTOW} \tag{16.16}$$

The cost of depreciation, is quite evidently the value loss of components due to their use. The cost of landing fees and taxes, and finally the cost of financing the aircraft is relatively similar for both the low-ATR aircraft and the airbus A330-200 and will not be elaborated on further. Now that a deeper understanding of the DOC model is provided, the relative DOC performance of the low-ATR aircraft and Airbus A330-200 can be discussed.

In Figure 16.17, the relative DOC of an Airbus A330-200 compared to its standard mission is plotted as a function of cruise altitude and cruise Mach number. The design mission altitude of 11 250 m and design mission Mach number of 0.82 is the reference mission for the Airbus A330-200, and is also the mission to which DOC is compared in this plot. One can observe that for the design mission the DOC is obviously equal to one, whereas if the aircraft flies slower its DOC will increase, in particular for Mach numbers less than 0.55. However, decreasing the altitude does not affect the DOC as greatly as decreasing the cruise Mach number, which is in excellent agreement with [54].

In Figure 16.18, the relative DOC of the low-ATR aircraft compared to itself is provided. The same behaviour with altitude and Mach number is observed as in Figure 16.17, however the relative DOC is smaller in magnitude than that of the Airbus A330-200 relative to itself. This is due to the Airbus A330-200 having a higher design Mach number and altitude, and therefore comparing it to itself at a much lower Mach number will result in a larger relative DOC. Therefore, for the low-ATR aircraft, since its design Mach number and altitude are lower and more central in the considered range of Mach numbers, the relative magnitude is lower. The altitude has very little effect on the DOC performance of the aircraft, therefore the large variation in cruise altitude between the Airbus A330-200 in Figure 16.17, and the low-ATR aircraft in Figure 16.18 does not result in a observable difference in relative DOC magnitude.

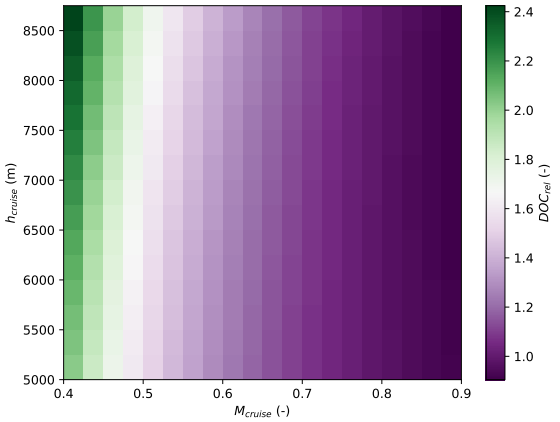

Figure 16.17: Variation of DOC with altitude and mach number of an Airbus A330-200, relative to itself.

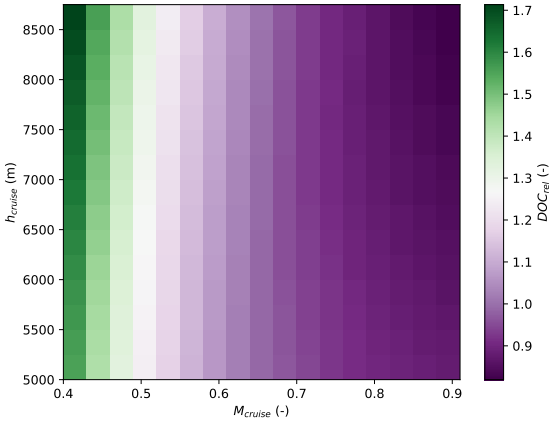

Figure 16.18: Variation of DOC with altitude and mach number of the low-ATR aircraft, relative to itself.

16.5. Synthesising ATR and DOC Performance - Design Point

In this section, the design cruise altitude and Mach number are established, which constitute the starting point for the entire aircraft sizing process. These values are chosen such that the DOC increase relative to an Airbus A330-200 is limited to 15%, whilst the ATR is to be minimised. Figure 16.19 and Figure 16.22a display the relative ATR and DOC performance of the present low-ATR airliner for a given cruise Mach number and altitude compared to the Airbus A330-200 reference aircraft flying at a Mach number of 0.82 and altitude of 11 250 m [54]. On a different note, Figure 16.21 and Figure 16.22b represent the relative performance of the low-ATR aircraft and the A330-200 flying at the same combination of Mach number and altitude. Given the limitations imposed by computing power, the total mission fuel, which is an input to both the ATR model (see Section 16.3.1) and the DOC model (see Section 16.4), is computed by assuming both aircraft to traverse the entire mission distance of 8000 km at their respective cruise Mach number Ma and altitude h. Seeing that this assumption is adopted for both aircraft, its effects on the accuracy of this analysis are expected to cancel. This simplified approach is captured by the following formula, where it should be noted that $T_{inst_{(h,Ma)}}$ is set equal to the overall aircraft drag at a certain Mach-altitude combination. The drag is estimated from the Class II drag model discussed in Chapter 12, where the effect of wave drag is not accounted for due to the large uncertainty associated with this drag

component. Hence, the ATR and DOC performance of the NLF airfoil-equipped low-ATR aircraft at high Mach numbers shall be considered with care (no wave drag factor would have to be applied to the A330-200, whose supercritical airfoils are assumed to operate below their critical Mach number for the Mach number range considered here).

$$m_{fuel_{(h,Ma)}} = \frac{SFC_{(h,Ma)} \cdot T_{inst_{(h,Ma)}} \cdot d}{Ma \cdot a_h} \tag{16.17}$$

The two primary contributors to ATR, namely the amount of emitted climate agents (proportional to the burned fuel mass) and the climate impact per unit mass (proportional to the altitude) shall now be investigated. The ATR colour map in Figure 16.19 and Figure 16.22a suggests a strong trend of diminishing ATR at lower altitudes, which can be understood from the forcing factors presented in Figure 16.13. The ATR variation with Mach number has a bucket-shaped appearance, particularly a high altitudes, which agrees with the results obtained by A. Koch (see Figure 16.20a). The higher thrust lapse of the employed propfans with Mach number compared to the CF6-80E1 engines causes the peak in the top right corner of Figure 16.22a, whereas the peak at Mach 0.4 and 8500 m altitude is due to the excessive C_L and thus induced drag predicted by the drag model devised in Chapter 12. Unsurprisingly, the graph has a local minimum for any fixed altitude, which corresponds to the Mach number of optimum lift-to-drag ratio (equivalent to the NLF airfoil's critical Mach number). As can be seen from Figure 16.19, this optimum Mach number reduces with altitude. Overall, one can conclude that the relative ATR varies less with cruise Mach number than with altitude, implying that the burned fuel mass, which scales with mission time and is proportional to the emitted mass of CO_2, H_2O, SO_4 and soot, is less driving than the altitude-dependent forcing factors of these and other gases. This observation is confirmed in [54] and [27].

From the relative DOC maps in Figure 16.19 and Figure 16.22a one can infer that the reference DOC would be matched for a Mach number of about 0.6 at any altitude, supporting the aforementioned prevalent time-dependency of DOC. Any Mach number above this value results in a relative DOC decrease. The 15% DOC limit would be matched for a Mach number of around 0.5, however, this would not permit an ATR reduction compared to higher Mach numbers, which are in any case preferable from the perspective of DOC. In light of the NLF airfoil's critical Mach number of 0.63 (see Section 9.1), flying above this threshold would result in a substantial wave drag penalty, requiring a a higher thrust and therewith a larger rotor diameter, which would be detrimental for ground clearance and aeroelasticity. For a design cruise point of Mach 0.63 and 5000 m, an ATR reduction of 85% compared to an A330-200 flying at Mach 0.82 and 11 250 m is achieved at a relative DOC decrease of 5%. As mentioned earlier, this design point constitutes the starting point for the entire aircraft sizing process, however, it also paves the way for a more accurate ATR and DOC computation based on the mission profile output by SUAVE, which, besides the aircraft's technical specifications, takes the design cruise Mach number and altitude as inputs.

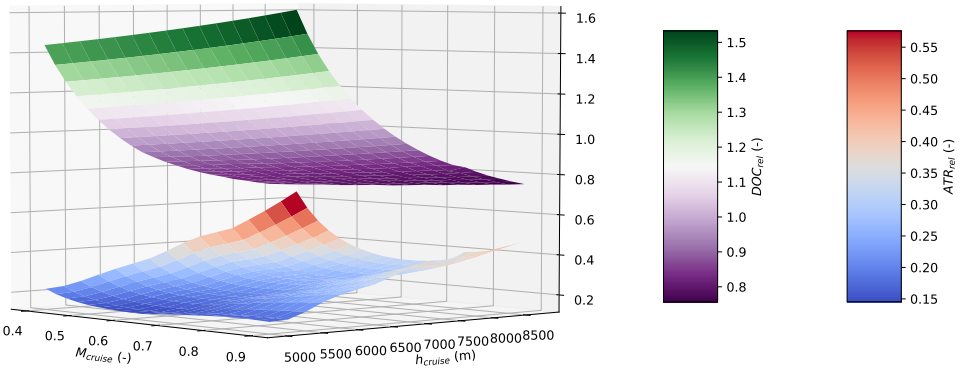

Figure 16.19: Relative ATR and DOC as a function of cruise Mach number and altitude for fixed reference mission

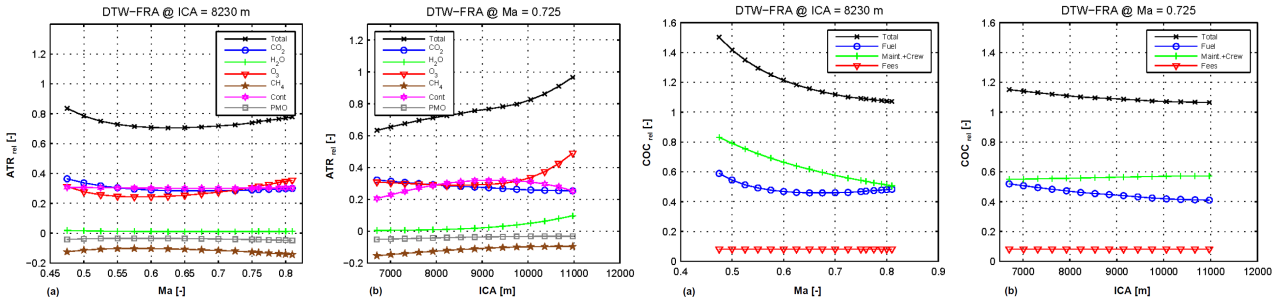

(a) ATR as a function of Mach number and altitude

(b) COC as a function of Mach number and altitude

Figure 16.20: ATR and DOC variation for fixed Mach number and varying altitude and vice versa [54]

One may take the preceding analysis one step further to compare the ATR and DOC performance of the present aircraft to the A330-200 operating on the same mission profile, for example, under the established design cruise conditions. This case is visualised in Figure 16.21 and Figure 16.22b, which differ from Figure 16.19 and Figure 16.22a in multiple aspects: unsurprisingly, the performance benefit of the propfan reduces with increasing Mach number, which is due to the model limiting the rotor's rotational speed to not exceed the design disk loading $(\frac{P_{fan}}{A_{fan}})_{design}$. For the lower density at high altitudes, the same rotational speed results in a smaller disk loading, hence the performance of the propfan increases in relative terms. This is because a larger proportion of the overall thrust stems from the bypass flow as opposed to the core flow, decreasing the TSFC. Also, the ATR gain increases slightly with altitude as a result of the propfans' lower OPR, and thus lower NO_X emissions [78]. The relative DOC behaves similarly, given that also here the propfan performs best where it is not limited by the maximum disk loading criterion. Obviously, the present low-ATR aircraft looses its competitive edge at high cruise speeds at any altitude, which in reality is expected to be even higher as a result of the wave drag penalty not accounted for in this model.

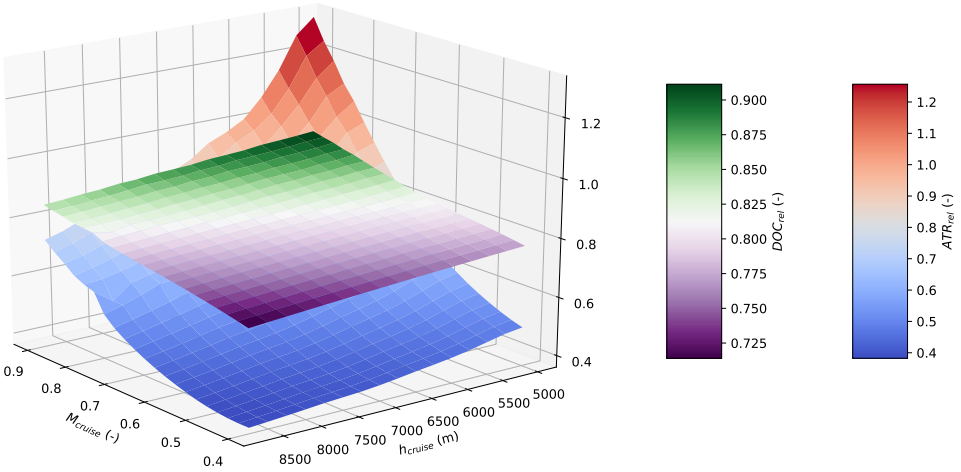

Figure 16.21: Relative ATR and DOC as a function of cruise Mach number and altitude for varying reference mission

In Figure 16.22a below the design point is denoted by a black cross, corresponding to the cruise condition for which the present aircraft achieves its minimum ATR at a 5% relative DOC decrease. As mentioned earlier, Figure 16.22b highlights the relative ATR reduction which could be achieved if the A330-200 reference aircraft were to fly at the same altitude and Mach number, but is not used for design point selection purposes. The latter is due to the difficulty to extrapolate to the absolute aircraft performance (to be investigated hereafter), which after all is what an aircraft designer is typically interested in.

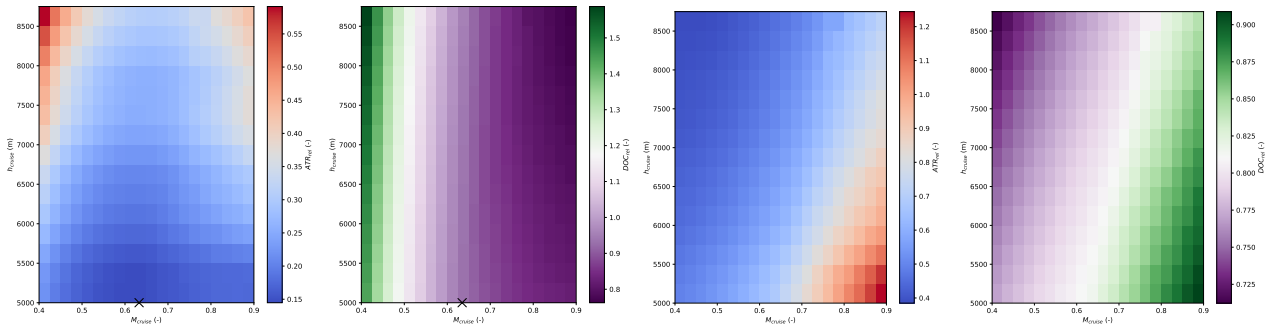

(a) Relative ATR and DOC for fixed reference

(b) Relative ATR and DOC for varying reference

Figure 16.22: ATR and DOC of project aircraft compared to A330-200 flying a fixed reference mission (a) and the same mission as the project aircraft

As anticipated in the introductory paragraph to this section, the absolute ATR and DOC performance per km of both aircraft shall now be investigated. The values displayed along the colour bars of Figure 16.23a and Figure 16.23b have been normalised with respect to the kilometers flown throughout the aircraft's operational lifetime. Comparing the absolute ATR maps of the present aircraft and the A330-200, one can observe that the low-ATR aircraft achieves a minimum ATR value at a lower cruise Mach number than the A330-200 reference aircraft, whose turbofan engines are designed to work in a higher Mach number regime. Also, the low-ATR aircraft sees an ATR peak at high Mach numbers and altitudes, where it clearly operates at a suboptimal life-to-drag ratio. The absolute DOCs of the low-ATR aircraft and Airbus A330-200 exhibit the same behaviour as the relative DOC graphs, namely a steep rise with Mach number. The reference aircraft has a very similar absolute DOC in the higher Mach number range (Mach 0.6 to 0.8), however at low Mach numbers the DOC

increases more rapidly due to the higher fuel burn, as neither the engines nor the aircraft geometry are designed for this flight regime.

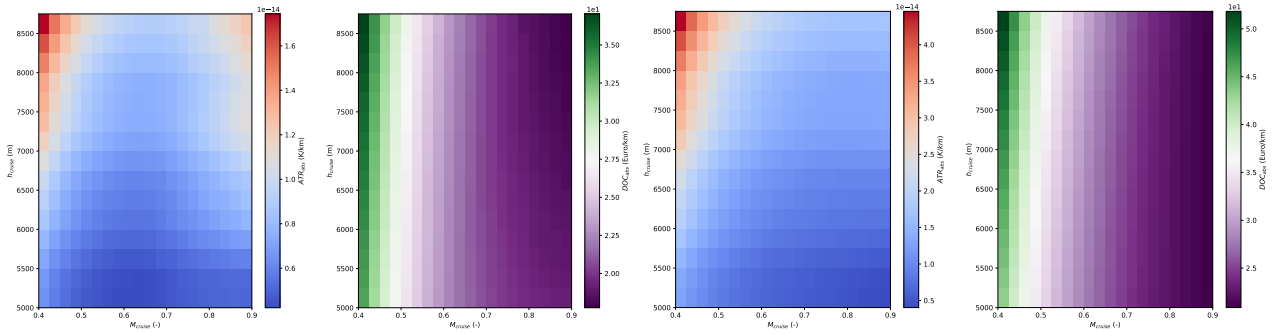

(a) Absolute ATR and DOC of own aircraft

(b) Absolute ATR and DOC of A330-200

Figure 16.23: Absolute ATR and DOC variation of project and reference aircraft with altitude and Mach number

Finally, the ATR-saving potential of the design mission profile itself shall be investigated. This scenario is crucial, as it is supposed to justify the efforts that were put into designing a new aircraft, instead of just operating the A330-200 on a different mission profile. To this purpose, Figure 16.24 and Figure 16.25 display the ATR and DOC of the A330-200 reference aircraft at various (Ma, h) combinations relative to its standard mission profile at 11 250 m and Mach 0.82. The maximum achievable ATR saving amounts to 70%, however, this would demand a DOC increase of 80%, which is way beyond the 15% limit imposed by the current project objective. This raises the need for the technological innovations implemented into the present low-ATR aircraft to concomitantly meet the DOC criterion and achieve a significant ATR reduction. To not leave the graphs' behaviour uncommented, note that the relative DOC in Figure 16.25 experiences a steep increase at lower Mach numbers and a much shallower decrease with altitude, as one can deduce from Figure 10.4 by assuming a constant throttle setting. Conversely, the relative ATR graph sees a clear increase with altitude, as well as with Mach number at higher altitudes. This is because at high Mach numbers (large air mass flow) and altitudes (low ambient temperature) a rather large difference between the ambient air temperature T_{amb} and the total burner temperature T_{T4} must be bridged, requiring more fuel as compared to flying at lower Mach numbers and the same altitude. This circumstance spurs a higher TSFC, and therewith a higher ATR.

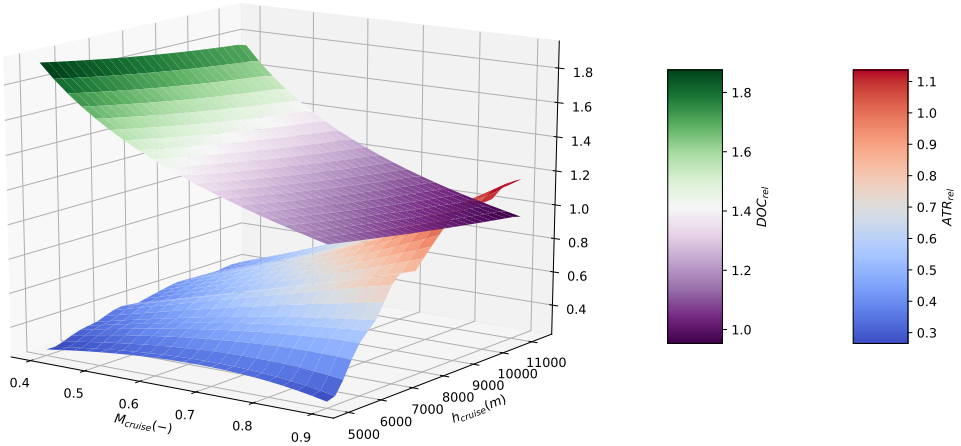

Figure 16.24: Relative ATR and DOC of reference aircraft for varying altitude compared to reference design point

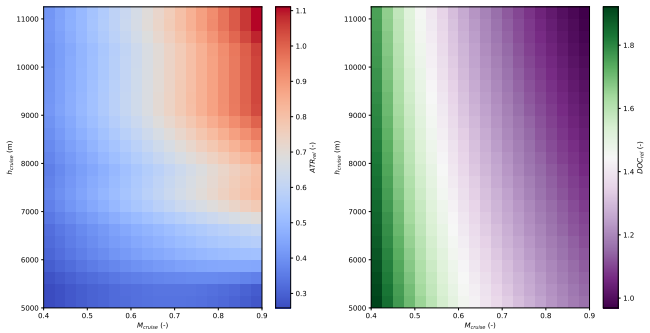

Figure 16.25: Relative ATR and DOC of reference aircraft for varying altitude compared to reference design point

16.6. Towards a Relative ATR vs. DOC Graph per Technology

This section outlines a roadmap towards a relative ATR vs. DOC graph displaying the respective gain/penalty in ATR/DOC per technology featuring in this aircraft design with respect to the A330-200. More accurately, the aim is to create two such graphs: one for the case where each technology (propfan engines, riblets, NLF control and synthetic kerosene) is applied individually, thereby visualising their stand-alone gain, and another for the case where they are sequentially combined. In order to transition from a 3D plot of ATR/DOC as a function of Ma and h (see Section 16.5) to a 2D plot of ATR vs. DOC, one must select a locus of (Ma, h) combinations for which the aforementioned technologies shall be evaluated. Ideally, this is done by establishing a so-called "Pareto front", as displayed in Figure 16.26.

The points on the Pareto front (the collection of outermost points on the convex side of the graph) represent an optimum trade-off between climate impact reduction and cost minimisation, depending on the ATR and/or DOC requirement proposed by the customer. In the context of this project, one would opt for a relative DOC increase of 15% and minimise the relative ATR footprint accordingly. Unlike previous ATR and DOC maps as a function of Mach number and altitude, every point on this graph demands an entire aircraft sizing process to be performed; in a sense, the aircraft is tailored to each (Ma, h) combination, thus representing the configuration of choice for a customer interested in said (Ma, h) combination. Figure 16.26 corresponds to the low-ATR aircraft featuring all of the aforementioned technological innovations. Note that due to the infeasibility of performing the full aircraft iterations discussed in Section 8.2 many times, the aircraft was sized for the 12 possible combinations of the Mach numbers (0.45, 0.60, 0.75) and altitudes (5.00, 6.33, 7.67, 9.00) km, and interpolated in between. In future research, it is intended to produce such a Pareto front for various technological combinations, thereby shedding light on their individual and combined performance. Also, one should spend more time on automating the iterations in order to be able to consider many more points than the ones obtained here, without having to rely on coarsely meshed interpolation increasing the results' uncertainty.

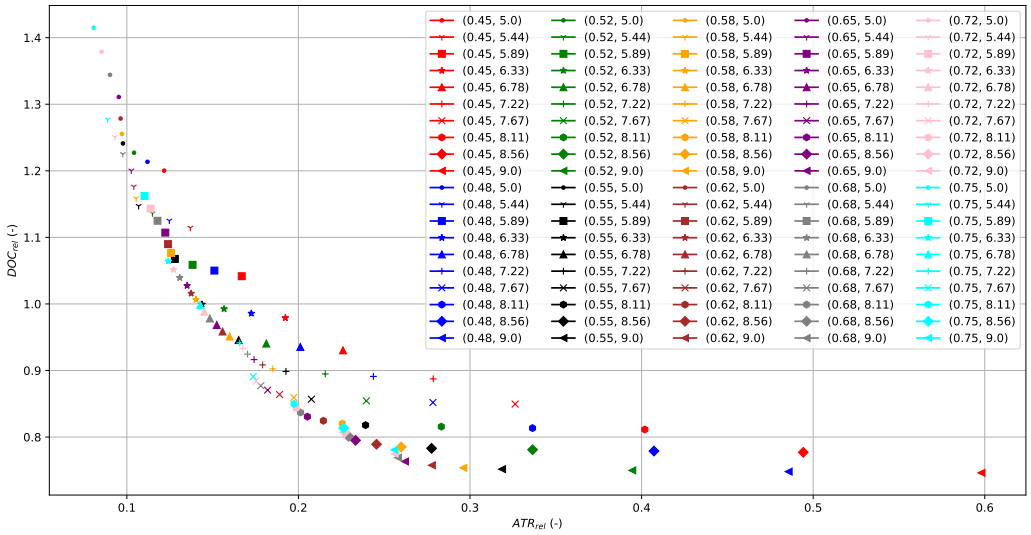

Figure 16.26: Pareto front of relative ATR and DOC for combined technologies with legend containing (Ma_{cruise} (-), h_{cruise} (km))

Table 16.19: Technological combinations and their influence on the ATR of the low-ATR aircraft. P = Propfan, R = Riblets, F = Sustainable aviation fuels, NACA.OPT = ATR using drag model for optimised airfoil, NACA = ATR using drag model for NACA airfoil, SC = ATR using drag model for supercritical airfoils

ATR (μK km^{-1})	Combination	Ref. mission: h = 11250 m, M = 0.82 ATR reduction (%)	Low-ATR mission: h = 5000 m, M = 0.63 ATR reduction (%)
4.2958E-09	**PRF**	80.00	30.59
4.4217E-09	**PR**	79.41	28.56
4.5562E-09	**P**	78.79	26.38
4.4264E-09	**PF**	79.39	28.48
4.5585E-09	**PRF.NACA.OPT**	78.77	26.35
4.6922E-09	**PR.NACA.OPT**	78.15	24.19
4.6281E-09	**PF.NACA.OPT**	78.45	25.22
4.7638E-09	**P.NACA.OPT**	77.82	23.03
4.5065E-09	**PRF.NACA**	79.02	27.19
4.6386E-09	**PR.NACA**	78.40	25.06
4.5762E-09	**PF.NACA**	78.69	26.06
4.7103E-09	**P.NACA**	78.07	23.90
5.0265E-09	**PRF.SC**	76.60	18.79
5.1739E-09	**PR.SC**	75.91	16.41
5.0961E-09	**PF.SC**	76.27	17.66
5.2455E-09	**P.SC**	75.58	15.25

As constructing the Pareto front for various technological combinations was not possible in the intended timeframe of the DSE, a new approach is taken to convey the effect of the different technologies on the ATR of the aircraft. The technologies considered in Table 16.19 are, the aircraft covered in riblets, the introduction of sustainable-aviation-fuels, the effect of having the optimised, non optimised laminar flow control airfoils and supercritical airfoils. In the first row the reference ATR is provided for the Airbus A330-200 reference mission, flying at an altitude of 11 250 m and Mach number of 0.82. In the first column the different combinations of technologies are presented. For example, ”PRF” stands for a propfan, with riblets and sustainable aviation fuel and a natural laminar flow control airfoil. If a letter is removed it indicates the technology is also removed from the calculation. The natural laminar flow control airfoil that is used when no indication is provided, such as in the first 4 rows, is using the classical class-II drag estimation formulas devised in Chapter 12. While the airfoils later denoted with the NACA.OPT, NACA and SC are calculated using a slightly different method, based on a more analytical approach which can be read about in Chapter 12. The baseline is the propfan with riblets and sustainable aviation fuels, as this is the design which was come up with during this DSE. It has a relative ATR reduction of 80% compared to the Airbus A330-200 flying its own reference mission. If the riblets are removed from the ATR computation, the ATR reduction is reduced to 79.39%, or in other words the reduction was reduced by 0.76%. If SAF’s are removed from the computation the reduction is reduced to 79.41, meaning the reduction is reduced by 0.74%. If a turbofan is used, the relative ATR reduction is 62.81% compared to the Airbus A330-200 flying at its own mission profile. What can be observed is that when the relative ATR reduction is decreased, the percentage increase of removing or adding SAF and riblets increases.

When the reference mission is changed for the Airbus A330-200 to the mission of the low-ATR aircraft in the second column of Table 16.19. The reference ATR drops dramatically, as does the relative ATR reduction, which is reduced to 30.59% for the low-ATR compared to the Airbus A330-200 flying at the same mission profile.

What can also be seen from the table is that the optimised NACA airfoil performs worse than the non optimised NACA airfoil in terms of ATR, due to it having a higher profile drag at cruise. Also the supercritical airfoil performs worse than both the optimised and non optimised NACA airfoils as for example with the riblets and sustainable aviation fuel applied, the ATR reduction goes from 79.02% as the highest for the NACA airfoil, it drops by 0.3% for the optimised airfoil, a very small difference. It drops by 3.1% if the supercritical airfoil is used on the low-ATR aircraft. The relative differences are again magnified for the case where the Airbus A330-200 flies at the low-ATR mission profile.

16.7. ATR and DOC Sensitivity

In this section a sensitivity analysis is performed on the ATR model and DOC model, which have been outlined in Section 16.3 and Section 16.4. This sensitivity analysis could be vital in determining the input parameters which have the largest effect on the ATR and DOC. A small change of 1% is applied to each of the input parameters considered in the discussion below.

In Figure 16.27 the change in relative ATR is considered for a range of cruise mach numbers and cruise altitudes. From this it can be seen that a 1% change in the thrust specific fuel consumption, increases the relative ATR by 1.08e-3 for the

mission profile chosen in Section 16.5, where the design point was chosen (M_{cr} = 0.63, h_{cr} = 5000 m). The fuel mass parameter provides the amount of fuel which is burned during a single flight. Increasing it with 1% changes the total fuel burnt by 1% as well.

In Figure 16.28, the change in relative ATR is considered due to a 1% change in the mission range which is designed for. Changing the mission range will manifest itself in the amount of flights the aircraft can have in a single year, which will decrease for an increase in mission range. Flying longer means it takes off and lands less, than for a shorter mission profile. The increase of the range, while keeping the mass flow parameter constant will mean that the aircraft can fly longer while burning the same amount of fuel, therefore reducing the relative ATR compared to the Airbus A330-200. The reduction for the mission profile of M = 0.63 and h = 5000m, is -1.07e-3, so a slightly lower decrease than the increase for changing the thrust specific fuel consumption. Changing the range will mean the cruise will be a smaller percentage of the flight, where the thrust specific fuel consumption is low, whereas the take-off and loitering phases are still the same regardless of the length of the flight. Therefore changing the specific fuel consumption by 1% at every step of the flight increases the relative ATR more than increasing the range by 1%.

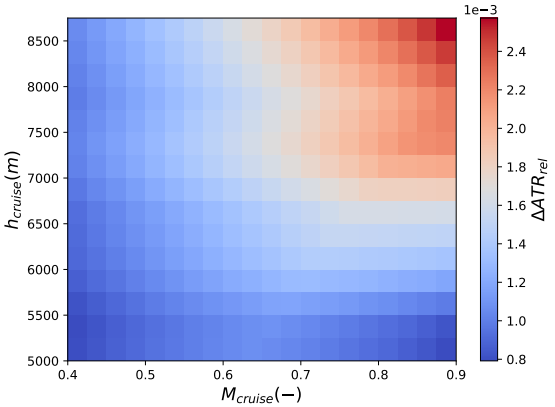

Figure 16.27: Relative ATR sensitivity to a change in the thrust specific fuel consumption.

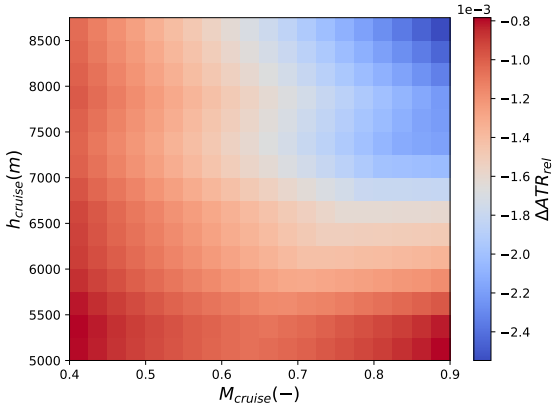

Figure 16.28: Relative ATR sensitivity to a change in the mission range.

In Figure 16.29 and Figure 16.30 the change in relative ATR is given for a 1% increase in the total temperature and pressure after the compressor respectively. For both parameters, the relative ATR decreases for an altitude below 7000 m and increases above 7000 m. Also for both parameters the magnitude of the increase and decrease in relative ATR is magnified for increasing Mach number. What also can be seen is that the relative ATR is almost 10 times more sensitive to an increase in total compressor exit temperature than the total pressure.

In Figure 16.31 the relative sensitivity of the direct operating cost is observed for a change in the fuel mass per flight of 1%. Multiple parameters flow into the fuel mass per flight. The drag the aircraft has at a specific altitude, the thrust specific fuel consumption and the total time flown. The fuel mass per flight scales linearly with all these parameters and grouping them into one parameter makes for a concise way of representing the data, as a 1% change in fuel mass could be due to any of these effects. The observed trend is that for an increase in the amount of fuel per flight, the DOC will increase. It will increase more at lower altitudes and Mach numbers, and less for higher altitudes and Mach numbers. This due to the DOC coming closer to the DOC value of the Airbus A330-200 and therefore the relative increase, is smaller for these altitudes and Mach numbers.

In Figure 16.32, the change in relative DOC is plotted for a 1% change in the total range flown by the aircraft. A higher range will result in a lower relative DOC, this is because if the fuel mass per flight is held constant, the aircraft will fly more kilometers for the same price, and thus have a lower DOC relative to the Airbus A330-200.

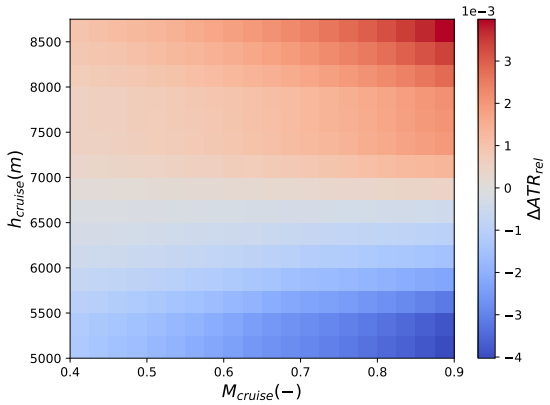

Figure 16.29: Relative ATR sensitivity to a change in the compressor exit total temperature T_{T3}

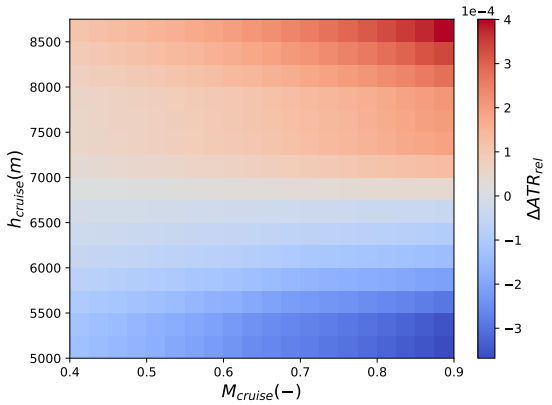

Figure 16.30: Relative ATR sensitivity to a change in the compressor exit total pressure P_{T3}

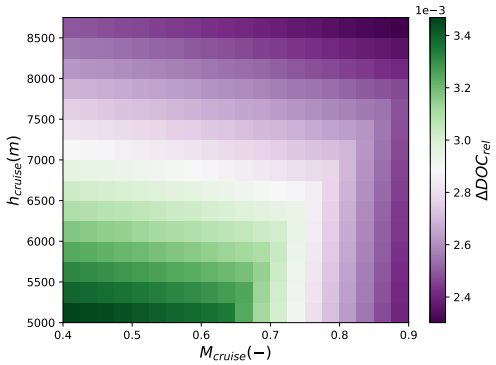

Figure 16.31: Relative DOC sensitivity to a change in fuel mass per flight.

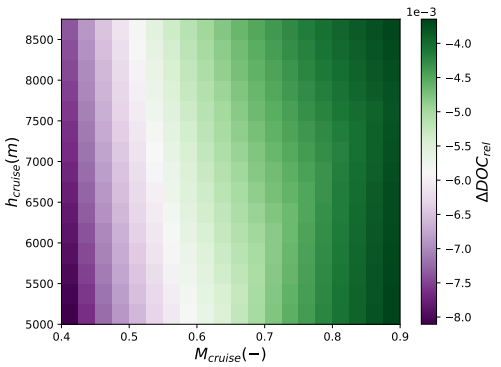

Figure 16.32: Relative DOC sensitivity to a change in range.

Figure 16.33 shows the change in relative DOC for an increase in the MTOW of the low-ATR aircraft. The aircraft shows that the relative DOC increases for an increase in MTOW, which has the largest effect at lower cruise mach numbers. This can be understood when looking at Figure 16.18, where the relative DOC is plotted of the low-ATR aircraft relative to itself. There the relative DOC increases compared to itself flying at its design mission profile, meaning the aircraft is already more expensive to run at lower Mach numbers, meaning the difference with respect to the Airbus A330-200 increases.

In Figure 16.34 the change in relative DOC for an increase in the MTOW of the low-ATR aircraft is shown. For an increase in the required take-off thrust and increase in DOC is observed. This is due to larger take-off thrust requirements, require a larger more expensive engine, and therefore a higher cost. Again the largest change in relative DOC is observed at the lower Mach numbers, which follows the same reasoning as for the DOC sensitivity with MTOW, which is explained above.

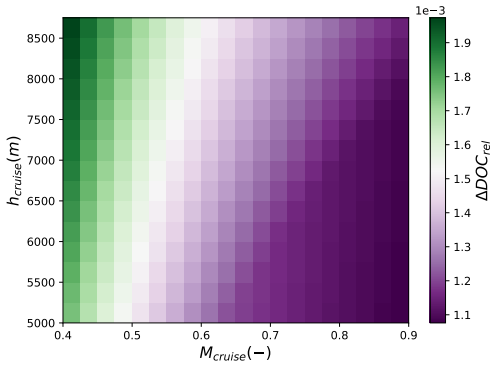

Figure 16.33: Relative DOC sensitivity to change in MTOW.

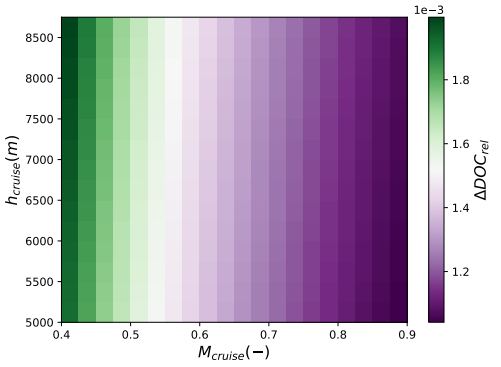

Figure 16.34: Relative DOC sensitivity to a change in required take-off thrust.

16.8. Flight Performance Recommendations

Until this phase of the design and therefore also in this report, the focus regarding flight performance mainly lay on finding the optimum mission profile to minimise ATR, and the aircraft characteristics on this profile. However, other flight performance characteristics should be assessed as well and are left as recommendations for the next stage of the design. First of all, the noise characteristics of the aircraft including airframe and especially the propfan should be looked into. Furthermore, the climb and descent segments have not been optimised yet, which is recommended to potentially reduce the ATR footprint of the aircraft even further, or to reduce the residence noise of the aircraft by means of a steeper climb in the first climb segments.

Complementing the aforementioned recommendations is the fact that in the next design phase the flight performance requirements in Chapter 18 that have not been verified yet should be analysed. Due to time constraints there is not looked into some of these requirements as these were not deemed crucial or project breaking at this design phase. Research should be performed amongst others in the aircraft's turn performance and the aircraft's service ceiling. Also the requirements currently assumed verified by means of the thrust-to-weight and wing loading diagram developed in the Midterm Report [39], such as the take-off length of 2500 meter and the climb gradient requirements should be evaluated more in depth.

17. Budgets Allocation

In the baseline report [38] a resource allocation was performed. The parameters with their target value and contingency can be found in Table 17.1. The current design should be checked with the original budget allocation now that the first iteration has been performed.

Table 17.1: Contingency table [38]

Parameter / Phase	**MTOM** (kg)	***L/D*** (-)	$C_{L_{max}}$ (-)	***T/W***	**SFC** (g/kN/s)
Target values	163,980	20.8	2.778	0.3	16.79
Conceptual design phase contingency	40%	40%	40%	25%	25%
Current values	182,280 kg	20.8	2.85	0.2892	11.76

The L/D can be found in Table 12.2, the MTOM from Section 8.2, the $C_{L\text{max}}$ from Section 9.4, the T^T/W from [39] and the SFC from Section 10.6. It can be clearly observed that only the SFC meets this budget allocation with its contingency. It has become clear that due to the characteristics of this design that the methods used to determine the budget allocations are not representative for the low-ATR aircraft. The weight budget was determined using reference aircraft which are optimised for low DOC. The low-ATR aircraft is designed for low ATR which is fundamentally different. The increase in weight can mainly be explained by the large amount of fuel which it will need as it flies slower than ordinary aircraft. Next to this the contingencies are placed at rather high values. For example the $C_{L\text{max}}$ would have to be 3.89. This would most likely require additional HLD's, which would increase the weight and increase the weight permanently. This is also called the self-fulfilling prophecy and should be avoided.

Due to the time constraint given it is not possible to revise the budget allocation. Yet it is recommended that for further work the budget allocation should be revised completely such that it is more tuned to the specifics of the requirements used for the low-ATR aircraft.

18. Requirements and Constraints Compliance Matrix

In this chapter the compliance matrix is provided. Compliance of the design with every requirement is indicated in the tables. Requirements which have been validated to be met are denoted with ✓in the third column of the compliance matrices, indicated by comp. (compliance). The last column shows where the requirement has been verified (ref. for reference), the section number has been noted in this column. An "O" means that the requirement has not been able to be verified or is not possible to be verified at this stage. An X indicates the requirement has not been met.

18.0.1. User Requirements

Table 18.1: Compliance of user requirements

Identifier	Requirement	Comp.	Ref.
MATRA-USER-PER-01	The maximum operating range at maximum payload shall be 8000 km.	✓	16.2.5
MATRA-USER-PER-02	The flight time associated with the maximum operating range specified in MATRA-USER-PER-03 shall not exceed 16 hours.	✓	16.2.2
MATRA-USER-PER-04	The aircraft shall be designed to seat 250 passengers.	✓	16.2.5
MATRA-USER-PER-05	The aircraft shall be able to operate from existing airports.	✓	
MATRA-USER-PER-06	The aircraft shall be able operate from runways of 2500 m length.	✓	
MATRA-USER-PER-07	The aircraft shall be able operate in cross winds of 20 kts.	✓	11.8.2
MATRA-USER-PER-08	The aircraft shall be able to operate in all-weather conditions specified in CS-25.	O	
MATRA-USER-PER-09	The aircraft shall be able to perform CAT-II landings.	O	
MATRA-USER-PER-10	The aircraft shall be able to perform diversions during CAT-II landing maneuvers.	O	
MATRA-USER-SAR-01	The aircraft shall comply with the standard part 25 certification requirements.	✓	
MATRA-USER-SAR-02	The passive flow control devices shall not require additional safety certification under CS-25.	✓	
MATRA-USER-SUS-01	The aircraft shall employ laminar flow control to delay laminar-to-turbulent transition.	✓	
MATRA-USER-SUS-02	The aircraft shall use riblets to reduce turbulent skin-friction drag.	✓	
MATRA-USER-SUS-03	The aircraft shall use sustainable materials during manufacturing.	✓	14.7
MATRA-USER-SUS-04	The aircraft shall have a holistic end of life plan.	✓	
MATRA-USER-BUD-01	The weight budget shall be finalised in the concept development phase.	✓	
MATRA-USER-BUD-02	The drag budget shall be finalised in the concept development phase.	✓	
MATRA-USER-COS-01	The development costs shall be less than 15 Billion € if pre-existing engines can be utilised.	✓	22.2
MATRA-USER-COS-02	The development cost shall be less than 20 Billion € if new engines must be developed.	✓	22.2
MATRA-USER-COS-03	The manufacturing cost per aircraft shall be less than 150 Million €.	✓	22.2
MATRA-USER-COS-04	The aircraft's ATR shall be minimised with a 15% DOC increase constraint compared to an Airbus A330-200.	✓	

18.0.2. Stakeholder Requirements

Table 18.2: Compliance of stakeholder requirements

Identifier	Requirement	Comp.	Ref.
MATRA-STA-TUD-01	The conceptual design phase shall be completed in 10 weeks time.	✓	
MATRA-STA-TUD-02	The development costs shall not exceed 600,000 €, given a per capita salary of 150 €/hour.	X	
MATRA-STA-AL-01	The aircraft shall seat 250 passengers.	✓	
MATRA-STA-AL-02	The cabin layout shall provide sleeping coaches for crew and pilots.	O	
MATRA-STA-AL-03	The aircraft shall be competitively priced.	✓	22.3
MATRA-STA-AL-04	The aircraft shall have an operational lifetime of at least 35 years.	✓	
MATRA-STA-AL-05	The aircraft shall be operable on short trans-pacific routes, such as Tokyo-Vancouver.	✓	
MATRA-STA-AL-06	Pilot training costs for type rating shall be minimised, provided pilots have already attained such type rating for comparable aircraft such as the A330-200 or B777-200.	O	
MATRA-STA-AP-01	Costs resulting from additional ground services, besides those required for operating an Airbus A330-200, shall be minimised.	✓	22.2
MATRA-STA-RES-01	The aircraft shall have low emissions during ground operations.	O	
MATRA-STA-RES-02	The noise level experienced by residents living around the airport shall be equal or less than that of an Airbus A350-800.	X	
MATRA-STA-REG-01	The aircraft shall be operable under all weather conditions, including CAT II landing- and diversion capabilities.	O	
MATRA-STA-REG-02	The aircraft shall adhere to all CS-25 safety requirements.	O	
MATRA-STA-GP-01	The aircraft shall have a significantly lower environmental footprint compared to its competitors.	✓	
MATRA-STA-PAS-01	The airplane shall be comfortable and pleasant to be transported in.	✓	11.8.5
MATRA-STA-PAS-02	The relative increase in ticket price, compared to an Airbus A330-200 with the same cabin configuration, shall be minimised.	✓	22.4

18.1. System Requirements

Table 18.3: Compliance of system requirements

Identifier	Requirement	Comp.	Ref.
MATRA-SYS-01	The aircraft shall transport 250 passengers.	✓	
MATRA-SYS-02	The aircraft shall have a maximum operating range of 8000 km.	✓	16.2.5
MATRA-SYS-03	The aircraft shall require at most 16 hours to cover a range of 8000 km.	✓	16.2.2
MATRA-SYS-04	The aircraft shall be able to operate from existing runways with a length of 2500 m.	✓	[39]
MATRA-SYS-05	The aircraft shall be able to operate in crosswinds of at least 20 kts.	✓	11.8.2
MATRA-SYS-06	The aircraft shall be able to operate under all weather conditions, including CAT II landings with diversion capabilities.	O	
MATRA-SYS-07	The aircraft shall pass all CS-25 certification requirements.	O	
MATRA-SYS-08	The aircraft's ATR shall be minimised with a 15% DOC increase constraint compared to an Airbus A330-200.	✓	25
MATRA-SYS-09	The aircraft shall have a manufacturing cost of less than 150 Million €.	✓	22.2
MATRA-SYS-10	The aircraft shall use passive flow control devices to reduce drag.	✓	12.5
MATRA-SYS-11	The development cost shall be less than 15 Billion € if pre-existing engines can be utilised.	✓	22.2
MATRA-SYS-12	The development cost shall be less than 20 Billion € if new engines must be developed.	✓	22.2

18.2. Sub-System Requirements

Table 18.4: Compliance of operational requirements

Identifier	Requirement	Comp.	Ref.
MATRA-SSYS-OPS-01	(a) The aircraft shall have an A-class maintenance interval of TBD hours.	O	
	(b) The aircraft shall have a C-class maintenance interval of TBD hours.	O	
	(c) The aircraft shall have a D-class maintenance interval of TBD hours.	O	
MATRA-SSYS-OPS-02	The aircraft shall have a minimum operational lifetime of 35 years.	✓	14
MATRA-SSYS-OPS-03	The cabin crew shall comprise of at least 5 flight attendants.	O	
MATRA-SSYS-OPS-04	The crew rest compartment shall accommodate 5 flight attendants and 2 pilots.	O	
MATRA-SSYS-OPS-05	The aircraft shall provide seats for all (reserve) crew members.	O	
MATRA-SSYS-OPS-06	The overhead storage space per passenger shall be 25 liter.	✓	8.6.1
MATRA-SSYS-OPS-07	The aisle height shall be 1.93 m.	✓	8.6.1
MATRA-SSYS-OPS-08	The aisle width shall be 0.558 m.	✓	8.6.1
MATRA-SSYS-OPS-09	The seat width shall be 0.635m in business and 0.457 m in economy class.	✓	8.6.1
MATRA-SSYS-OPS-10	The seat armrest width shall be 5.5 cm in economy and 7 cm in business class.	✓	8.6.1
MATRA-SSYS-OPS-11	The minimum legroom shall be 0.74 m.	✓	8.6.1
MATRA-SSYS-OPS-12	The aircraft shall require no additional type-rating for pilots type-rated on the Airbus A350.	O	
MATRA-SSYS-OPS-13	The cabin shall accommodate 7 seats abreast.	✓	8.6.1
MATRA-SSYS-OPS-14	The aircraft shall have at least two aisles.	✓	8.6.1
MATRA-SSYS-OPS-15	The aircraft shall allow for zero-carbon taxiing.	X	
MATRA-SSYS-OPS-16	The aircraft shall be able to operate from runways of 2500 m length at MTOW .	✓	
MATRA-SSYS-OPS-17	The cabin oxygen tank capacity shall be TBD kg.	O	
MATRA-SSYS-OPS-18	The fresh water tank capacity shall be TBD l.	O	
MATRA-SSYS-OPS-19	The waste water tank capacity shall be TBD l.	O	

Table 18.5: Compliance of power and propulsion requirements

Identifier	Requirement	Comp.	Ref
MATRA-SSYS-PP-01	The propulsion system shall provide enough thrust to maintain a cruise speed of 400 knots.	✓	10.6
MATRA-SSYS-PP-02	The propulsion system shall provide enough thrust to perform a take-off which adheres to CS25 regulations [26].	✓	10.6
MATRA-SSYS-PP-03:	The propulsion system shall provide enough thrust to climb at a climb angle of TBD %.	✓	[39]
MATRA-SSYS-PP-04	In case of OEI, the propulsion system shall not create a moment larger than 3.1 MNm.	✓	11
MATRA-SSYS-PP-05	The propulsion system shall be able to provide incremental thrust variations with an accuracy of TBD N.	O	
MATRA-SSYS-PP-06	The propulsion system shall be provided a flow of fuel at a rate and pressure needed for proper engine functioning under each operating condition.	O	
MATRA-SSYS-PP-07	The fuel tank shall be able to safely store fuel.	✓	13.2
MATRA-SSYS-PP-08	The fuel tank shall be able to withstand structural, vibrational, inertial and fluid loads.	✓	13.2
MATRA-SSYS-PP-09	The lifetime of a single engine shall be at least 0.15e6 hours.	✓	14
MATRA-SSYS-PP-10	The propulsion system shall have a total weight of a maximum of 6000 kg.	✓	10.6
MATRA-SSYS-PP-11	In case new engines have to be developed, the development cost shall not exceed 5 Billion €.	✓	22.2
MATRA-SSYS-PP-12	The aircraft shall have a fuel capacity of TBD kg.	✓	16.2.5
MATRA-SSYS-PP-13	The combined fuel consumption of all engines shall not exceed 8 kg/s.	✓	10.6
MATRA-SSYS-PP-14	The power system shall provide 82 kW of electrical power.	O	
MATRA-SSYS-PP-15	The power system shall provide redundancy in case components of the system fail.	✓	13.1
MATRA-SSYS-PP-16	The power system shall be able to store TBD J of electrical energy.	O	
MATRA-SSYS-PP-17	The power system shall have a distribution unit to regulate the provided power to each component of the system.	✓	13.1
MATRA-SSYS-PP-18	The power system shall provide 25 kW of electrical power when all engines are inoperative.	O	
MATRA-SSYS-PP-19	The propulsion system placement shall allow for 5 deg of lateral ground clearance.	✓	8.4

Table 18.6: Compliance of stability and control requirements

Identifier	Requirement	Comp.	Ref.
MATRA-SSYS-SAC-01	The aircraft shall be statically longitudinally stable.	✓	11.3
	(a) A pull of the control stick shall be required to obtain and maintain speeds below the trim speed.	✓	11.3
	(b) A push of the control stick shall be required to obtain and maintain speeds above the trim speed.	✓	11.3
	(c) The airspeed shall return to 10% of the original trim speed under climb, approach and landing conditions when the control force is slowly released.	O	
	(d) The gradient of the stick force versus airspeed shall be larger than 4 N per 11.2 km/hours.	O	
	(e) The airspeed shall stabilise below or above the trim speeds specified in MATRA-SSYS-SAC-04 (c) without requiring exceptional piloting skills.	O	
MATRA-SSYS-SAC-02	The aircraft shall be statically directionally stable.	✓	11.8.2
	(a) The aircraft shall have the tendency to raise its lower wing in sideslipping flight at any airspeed.	✓	11.8.2
	(b) In straight, steady, side-slips in regular operation, the aileron and rudder control movements and forces shall be proportional to the angle of sideslip in a stable sense.	✓	11.8.2
MATRA-SSYS-SAC-03	The aircraft shall be dynamically stable.	✓	11.8.2
	(a) Any short period oscillation shall be heavily damped with the primary flight controls being free.	✓	11.8.2
	(b) Any short period oscillation shall be heavily damped with the primary flight controls being fixed.	✓	11.8.2
	(c) Dutch roll shall be positively damped with controls being free.	✓	11.8.2
MATRA-SSYS-SAC-04	The aircraft shall be stable and controllable up to, during and after a stall.	O	
MATRA-SSYS-SAC-05	The aircraft shall not have an uncontrollable tendency to nose over in any reasonable operating condition.	✓	11.3.1
MATRA-SSYS-SAC-06	The aircraft shall not have uncontrollable ground-looping tendencies in 90 deg crosswinds, up to a wind velocity of 37 km/hours or 0.2 $V_{S_{R0}}$.	✓	11.8.2
MATRA-SSYS-SAC-07	The aircraft shall be directionally and laterally controllable.	✓	11.4
	(a) It shall be possible, with wings level, to yaw into the inoperative engine and to safely make a reasonably sudden change in heading of up to 15 deg in the direction of the critical inoperative engine.	✓	11.4
	(b) It shall be possible to make 20 ° banked turns, with and against the inoperative engine, from steady flight at a speed equal to 1.3 $V_{S_{R1}}$.	✓	11.4
	(c) No more than 2/3 of the rudder area shall be shielded by the horizontal stabiliser in the event of an aggravated spin with 45 deg angle of attack.	✓	11.5

Table 18.7: Compliance of requirements dealing with safety and regulations

Identifier	Requirement	Comp.	Ref.
MATRA-SSYS-ST-01	The aircraft shall be evacuable in 90 s using 50% of the available exits.	✓	8.6.2
MATRA-SSYS-ST-02	The number and types of (different) emergency exits shall permit compliance with MATRA-SSYS-ST-01, while comprising of at least two Type I or larger exits on each side of the fuselage.	✓	8.6.2
MATRA-SSYS-ST-03	Pressurised cabins and compartments to be occupied shall be equipped to provide a cabin pressure altitude of not more than 2438 m (8000 ft) at the maximum operating altitude of the aircraft under normal operating conditions.	✓	13.4
MATRA-SSYS-ST-04	The aeroplane shall be capable of continued safe flight and landing during and after any thrust reversal in flight.	O	
MATRA-SSYS-ST-05	The materials inside the cabin shall be fire retardant.	✓	14.1

Table 18.8: Compliance of aerodynamics and flight performance requirements

Identifier	Requirement	Comp.	Ref.
MATRA-SSYS-AFP-01	The aircraft shall create enough lift to balance its weight during take-off and landing.	✓	9.4
	(a) The aircraft shall have a maximum C_L in critical take-off configuration of 2.7.	✓	9.4
	(b) The aircraft shall have a maximum C_L in critical landing configuration of 2.8.	✓	9.4
MATRA-SSYS-AFP-02	The aircraft shall have adequate stall characteristics for take-off and landing.	✓	9.1
	(a) The aircraft shall have a minimum stall speed in critical take-off configuration of 100 kts^{-1}.	✓	9.4
	(b) The aircraft shall have a minimum stall speed in critical landing configuration of 80 kts^{-1}	✓	9.4
MATRA-SSYS-AFP-03	In normal take-off configuration, with gears retracted, the climb gradient may at no point in the take-off flight path be less than 1.2% for twin-engined aircraft, 1.5% for triple-engined aircraft and 1.7 % for quadruple-engined aircraft.	✓	[39]
MATRA-SSYS-AFP-04	The aircraft shall be able to climb.	O	
	(a) The steady climb gradient at MTOW with OEI and deployed landing gear shall be no less than 0.3% for twin-engined aircraft, and 0.5% for triple- and quadruple-engined aircraft.	O	
	(b) The steady climb gradient at MTOW with OEI and retracted landing gear shall be no less than 2.4% for twin-engined aircraft, and 2.7% for triple-engined aircraft and 3.0% quadruple-engined aircraft.	✓	[39]
MATRA-SSYS-AFP-05	The stall speed in icing conditions at MTOW shall exceed that in non-icing conditions by 3% V_{SR}.	O	
MATRA-SSYS-AFP-06	In landing configuration, the steady gradient of climb shall not be less than 3.2%, with all engines at the power or thrust that is available 8 seconds after initiation of movement of the power or thrust controls from the minimum flight idle to the go-around power or thrust setting.	✓	[39]
MATRA-SSYS-AFP-07	In the en-route configuration and with OEI, the steady gradient of climb shall not be less than 1.2% for twin-engined aircraft, 1.5% for triple-engined aircraft and 1.7% for quadruple-engined aircraft.	✓	[39]
MATRA-SSYS-AFP-08	The landing distance shall include a wind component safety factor of 50%.	O	16.8
MATRA-SSYS-AFP-09	In non-icing conditions, the landing reference speed V_{ref} shall not be less than $1.23V_{SR}$.	O	
MATRA-SSYS-AFP-10	The aircraft shall be able to perform CAT-II landings including diversions.	O	
MATRA-SSYS-AFP-11	The aircraft shall be able to loiter for 30 minutes.	✓	16.2.5
MATRA-SSYS-AFP-12	The aircraft shall have enough reserve fuel on board to perform an approach and missed approach. Afterwards, it should still be able to fly to an alternate airport 200 nm away from the original airport, fly at 450 m for 30 minutes at holding speed above the new airport and still have TBD l of additional fuel to account for increased fuel consumption due to any contingencies. [7]	✓	16.2.5
MATRA-SSYS-AFP-13	The aircraft shall have a maximum operating altitude of TBD m.	O	16.8
MATRA-SSYS-AFP-14	The aircraft shall be able to cruise in a speed range of TBD kts.	O	16.8
MATRA-SSYS-AFP-15	The aircraft shall be able to cruise in an altitude range of TBD m.	O	16.8
MATRA-SSYS-AFP-16	The aircraft shall have a turnaround time of no more than TBD seconds.	O	
MATRA-SSYS-AFP-17	The aircraft shall have a turn radius of no more than TBD m.	O	16.8
MATRA-SSYS-AFP-18	The aircraft shall be able to roll 30 deg in 1.5 s	O	16.8
MATRA-SSYS-AFP-19	The aircraft shall have adequate adverse yaw performance such that the aircraft can be flown without exceptional pilot skill.	O	16.8
MATRA-SSYS-AFP-20	The aircraft shall not have aileron reversal characteristics up until the dive speed V_D	O	16.8

Table 18.9: Compliance of guidance, navigation, control and communication requirements

Identifier	Requirement	Comp.	Ref.
MATRA-SSYS-GNCC-01	The cockpit instrumentation shall adhere to CS25 regulations.	O	
MATRA-SSYS-GNCC-02	The cockpit instrumentation shall be optimised for easy use.	O	
MATRA-SSYS-GNCC-03	All the onboard guidance, navigation, control and communication systems shall adhere to CS25 regulations.	O	
MATRA-SSYS-GNCC-04	The GNCC system shall include all navigation systems necessary for IFR flights.	O	
MATRA-SSYS-GNCC-05	The GNCC systems shall include all navigation systems necessary for CAT II landings.	O	

Table 18.10: Compliance of requirements on structural, material and manufacturing aspects

Identifier	Requirement	Comp.	Ref.
MATRA-SSYS-SMM-01	The most aft c.g. position specified in the loading diagram shall be located in front of the main landing gear.	✓	8.4
MATRA-SSYS-SMM-02	All structural elements shall be designed for an operational lifetime of 35 years.	✓	15.5
MATRA-SSYS-SMM-03	An evaluation of parts used in the aircraft structure shall show that these parts will not fail due to fatigue or corrosion during their operational lifetime.	✓	14.1
MATRA-SSYS-SMM-04	The aircraft fuselage structure shall be designed for TBD number of take-off and landing cycles.	✓	14.1
MATRA-SSYS-SMM-05	The aircraft structure shall be designed for lightning strikes.	✓	14.3
MATRA-SSYS-SMM-06	Any structure shall be protected from a loss of strength due to weathering, corrosion and abrasion.	✓	14.1
MATRA-SSYS-SMM-07	It shall be possible to inspect critical aircraft structures.		
MATRA-SSYS-SMM-08	The aircraft structure shall be designed to be free from negative aeroelastic effects.	✓	15.4
MATRA-SSYS-SMM-09	The structural modes of the aircraft wings shall be stable at speeds in the aeroelastic envelope.	✓	15.4
MATRA-SSYS-SMM-10	The aircraft structure shall be designed to be free of negative flutter effects within the aeroelastic envelope.	✓	15.4
MATRA-SSYS-SMM-11	The aircraft structure shall be designed such that it can be manufactured using currently available methods.	O	
MATRA-SSYS-SMM-12	The aircraft structure shall be designed such that it can sustain limit loads without permanent deformation of any structure.	✓	15.5
MATRA-SSYS-SMM-13	The aircraft structure shall be able to sustain ultimate loads without any permanent deformation for at least 3 s.	✓	15.5
MATRA-SSYS-SMM-14	The positive limit manoeuvring load factor ”n” which shall be designed for up to V_D may not be less than $2.1 + \frac{24000}{W+10000}$ with W the MTOW in lbs.	✓	15.5
	(a) ”n” may not be less than 2.5 .	✓	15.5
	(b) ”n” may not be greater than 3.8 .	✓	15.5
MATRA-SSYS-SMM-15	The negative limit load factor which shall be designed for may not be less than -1 at speeds up to V_c.	✓	[39]
MATRA-SSYS-SMM-16	The aircraft structure shall sustain an ultimate load factor of 1.5 times the highest load factor of the combined maneuver and gust envelope.	✓	[39]
MATRA-SSYS-SMM-17	The aircraft wing structure under ultimate design loads shall have limited deflections.	O	
	(a) The vertical wing tip deflection under ultimate loads shall be limited to TBD m.	O	
	(b) The horizontal wing tip deflection under ultimate loads shall be limited to TBD m.	O	
MATRA-SSYS-SMM-18	The fuselage shall sustain an ultimate pressure difference of 1.33 times the pressure difference at maximum operating altitude.	✓	14.3
MATRA-SSYS-SMM-19	The aircraft structure shall be designed for the unsymmetrical loads which stem from an engine failure.	O	
MATRA-SSYS-SMM-20	The ultimate control surface hinge loads parallel to the hinge line shall not exceed 1.5 times those stipulated by CS25.	✓	15.5
MATRA-SSYS-SMM-21	The landing gear shall sustain touch-down velocities in level attitude between V_{L1} and 1.25 V_{L2}.	✓	8.5
MATRA-SSYS-SMM-22	The materials used in the aircraft structure shall be chosen to minimise DOC, weight, ATR and climate impact.	✓	14.1
MATRA-SSYS-SMM-23	The aircraft structure shall be designed to house anti-icing systems.	O	
MATRA-SSYS-SMM-24	The materials used during manufacturing shall be safe to handle.	✓	14.1

18.3. Constraints

Table 18.11: Compliance of cost constraints

Identifier	Requirement	Comp.	Ref.
MATRA-CON-COS-01	The total development costs shall not exceed	✓	
	(a) 15 Billion € if pre-existing engines can be utilised.	✓	
	(b) 20 Billion € if new engines must be developed.	✓	
MATRA-CON-COS-02	The manufacturing cost per aircraft shall be less than 150 Million €.	✓	
MATRA-CON-COS-03	The direct operating costs per aircraft shall not exceed a 15% increase compared to an A330-200 on the same flight.	✓	
MATRA-CON-COS-04	The hourly operating costs shall not exceed 10252 €.	✓	
MATRA-CON-COS-05	The yearly maintenance costs shall not exceed 2302 €.	✓	
MATRA-CON-COS-06	The overall dismantling costs shall not exceed TBD €.	O	
MATRA-CON-COS-07	The overall recycling costs shall not exceed TBD €.	O	

Table 18.12: Compliance of sustainability constraints

Identifier	Requirement	Comp.	Ref.
MATRA-CON-SUS-01	Transport of raw materials for construction shall be optimised for sustainability.	O	
MATRA-CON-SUS-02	The acquisition of raw materials shall be optimised for sustainability.	O	
MATRA-CON-SUS-03	Scarcity of raw materials shall be considered in the material selection process.	✓	14.1
MATRA-CON-SUS-04	Manufacturing shall be done as centralised as possible.	✓	21.1
MATRA-CON-SUS-05	Energy used for manufacturing shall be minimised.	✓	14.7
MATRA-CON-SUS-06	Emissions caused by manufacturing shall be minimised.	✓	14.7
MATRA-CON-SUS-07	Toxicity caused by manufacturing shall be minimised.	✓	14.7
MATRA-CON-SUS-08	The aircraft shall have a minimised ATR footprint.	✓	16
MATRA-CON-SUS-09	Damage to wildlife as a result of operating the aircraft shall be minimised.	O	
MATRA-CON-SUS-10	The aircraft shall produce less than TBD dB of noise in take-off configuration.	O	10.9
MATRA-CON-SUS-11	The aircraft shall make less than TBD dB of noise in landing configuration.	O	10.9
MATRA-CON-SUS-12	The aircraft shall have an end of life plan for every system component.	✓	23.4
MATRA-CON-SUS-13	Recycling of components shall be maximised.	✓	23

Table 18.13: Compliance of ethical constraints

Identifier	Requirement	Comp.	Ref.
MATRA-CON-ETH-01	Manufacturing of the aircraft shall be performed under labour conditions conforming to the declaration of human rights.	O	
MATRA-CON-ETH-02	During the aircraft design and operation, safety shall be prioritised above financial gain.	O	
MATRA-CON-ETH-03	The people working on the design of the aircraft shall conform to the NSPE code of ethics [79]	O	

Part III
Practical Applications

19. Operations and Logistics

This chapter covers the operations and logistics of the low-ATR aircraft. First, a general operations and logistics overview is given in Section 19.1. Thereafter, the more specific operations regarding the low-ATR aircraft is discussed in Section 19.2, considering the riblets and the low-ATR mission profile.

19.1. General Operations and Logistics Overview

In Figure 19.1 a logistical flow block diagram is presented in order to visualise the logistical steps to be taken during the operational life of the low-ATR aircraft [39]. Note that these steps are no different from other long-range commercial aircraft and that the possibility of the use of a taxi-bot to significantly reduce the fuel burn on ground has been considered

[1] [39].

The operational life have been split-up in four phases: manufacturing, ground operations, flight operations and End of Life (EOL) operations. However, it should be noted that the aircraft will spend the vast majority of its lifetime in the second and third phase, when it is in operation for an aircraft operator as the aircraft is designed to have an operational life of at least 35 years (MATRA-STA-AL-04).

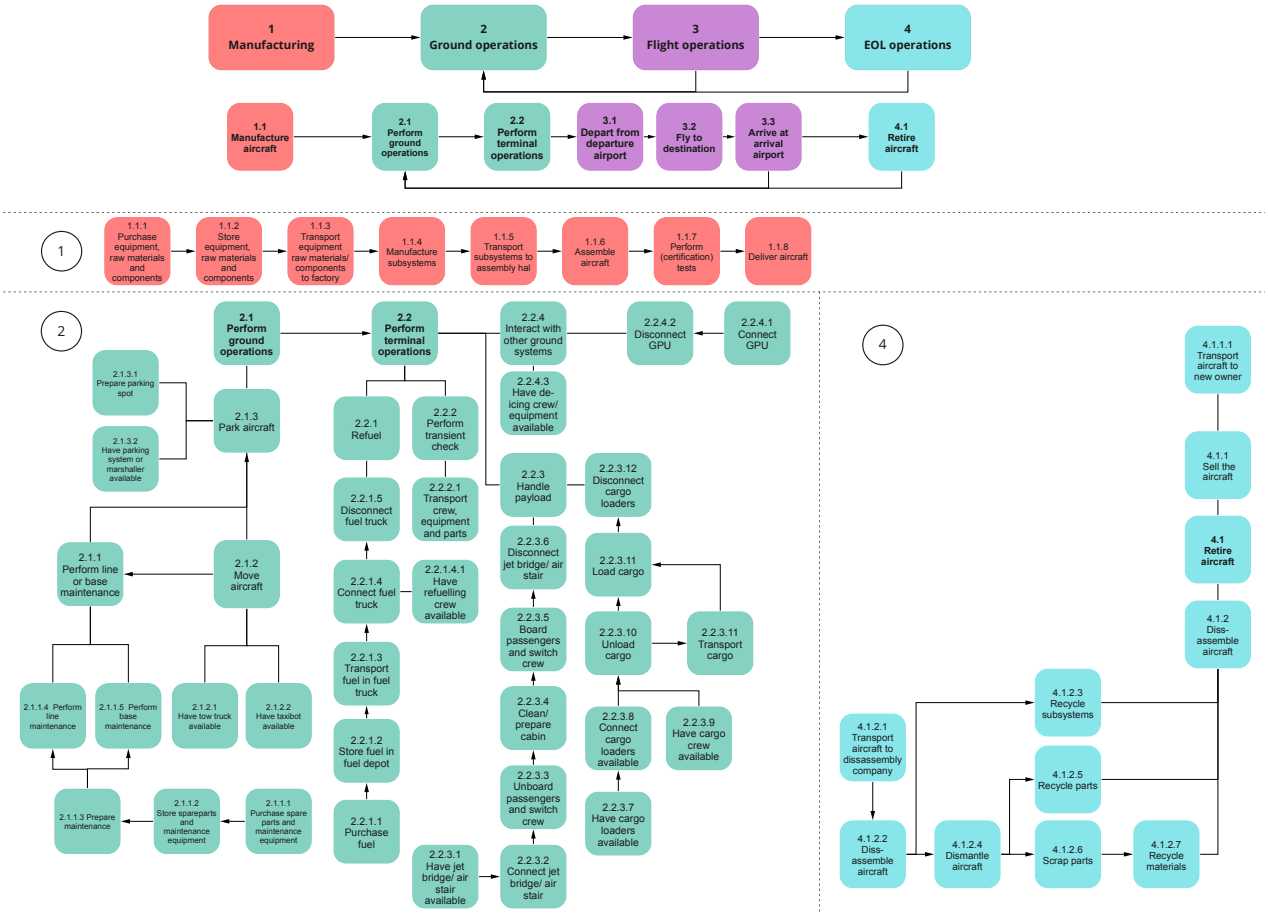

Figure 19.1: Logistical flow block diagram [39]

Figure 19.1 shows the logistics that is required during the life-time of the low-ATR aircraft and helps identifying the aircraft should be compatible with. The logistics of the manufacturing phase is no different than currently done by other aircraft manufacturers. Special attention should be given to the manufacturing of the riblets. A more detailed discussion on this and manufacturing in general can be found in Figure 21.3 and Chapter 21, respectively. A distinction in line and base maintenance has been made inFigure 19.1. Line maintenance, that includes amongst other trouble shouting and the A and B checks, does generally not require long term planning, while the more heavy base maintenance, that includes amongst other aircraft painting and the C and D checks, requires planning well in advance and is usually performed by a Maintenance, Repair and Overhaul (MRO) company, hence more logistically intensive. Maintenance is covered more in depth in Section 20.3. It is decided to not elaborate on the logistics regarding the flight operations, as this is the responsibility of the aircraft operator. After its operational life the aircraft enters its final phase: the End of Life (EOL) operations. Depending on the strategy of the aircraft operator and the state of the aircraft itself, the aircraft will either be sold to another operator or be disassembled in order to recycle the (sub)systems and materials. A detailed discussion on the EOL operations including EOL plans for the different aircraft systems can be found in Section 23.4. Finally, the reader is referred to Section 23.3 for a discussion on operational sustainability.

19.2. Operations of the Low-ATR Aircraft

This section covers the operations specific to the low-ATR aircraft. First, the operational considerations regarding the riblets is discussed in Section 19.2.1, followed by the considerations regarding the low-ATR mission profile in Section 19.2.2.

[1] https://www.iamsterdam.com/en/business/news-and-insights/news/2020/schiphol-airport-sustainable-taxibot-scheme (last accessed on 12/05/2021)

19.2.1. Operational Considerations Regarding Riblets

One of the most significant differences between the low-ATR aircraft and the aircraft currently on the market is the use of riblets on the aircraft skin to reduce skin friction drag in turbulent boundary layers. The following discussion on the operational considerations regarding the use of riblets has been taken from the Midterm Report [39]. Potential operational considerations are the exposure to external factors such as strong UV radiation, high temperature and pressure fluctuations and the exposure to de-icing fluid. In 2021 Lufthansa Cargo successfully applied riblets by means of a special film and found solutions to the aforementioned problems in collaboration with BASF [2] [39]. These films are also acting dirt repellent [15], resulting in no expected extra cleaning of the riblets with respect to normal aircraft cleaning schedule.

In order to make the riblets economically feasible for aircraft operators, the riblets should have a durability equivalent to the time between two paint jobs, which is approximately 4-5 years [61]. Besides the start of operations of Lufthansa Cargo with riblets, implying an economic advantage, Reference [42] supports the retention of the aerodynamic performance of the riblets for a sufficient time period. The proposed riblet paint application process in Reference [42] is suitable to commercial aircraft. Figure 19.2 shows a maximum drag reduction of 5.1% for freshly applied riblet paint and a 3.8% reduction for riblets samples after both 6 and 12 months in service. The y-axis of Figure 19.2 shows $\Delta\tau/\tau_0$, which is linearly proportional to skin friction drag, and the x-axis displays s^* which is a Reynolds number [42]. It is interesting to note that the aerodynamic performance is the same after operating either 6 or 12 months, implying a stable performance for the first period in-service and therefore significant durable performance of the riblets. However, further research should be performed into the exact durability and deterioration of the riblets in order to allow the aircraft operator to make a deliberate choice between replacing the riblets potentially earlier than at a regular paint job, resulting in additional cost, or flying longer with the deteriorated riblets hence resulting in relatively more skin friction drag and therefore more fuel burn and thus cost.

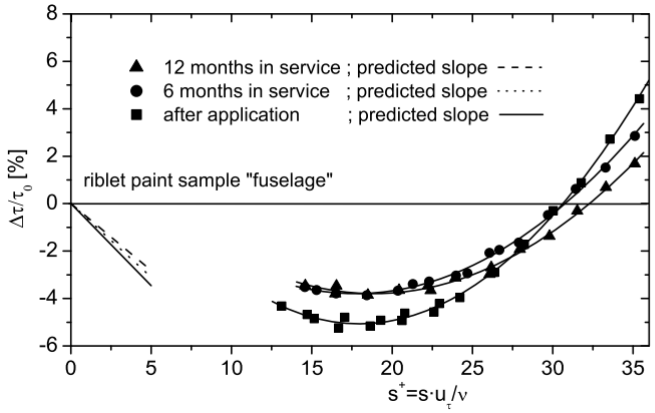

Figure 19.2: Drag reduction data of riblet samples from free flight tests after 0,6 and 12 months of application, obtained using oil channel experiments [42]

19.2.2. Operational Considerations Regarding the Low-ATR Mission Profile

The low-ATR aircraft's mission profile differs rather significantly from the high Mach and high altitude profiles commercial aircraft operate at nowadays, hence requiring certain operational considerations. First of all, as the flight time of the low-ATR aircraft for the design range is about 19% longer, as determined in Section 16.2.2, compared to an A330-200 flying the same range on its reference profile, the aircraft operator can operate less flights with a given low-ATR aircraft fleet compared to an A330-200 fleet of the same size. Furthermore, the crew cost, if paid per flight hour, increases for the same number of passengers transported. However, all these effect have been included in the DOC of the aircraft, which is not higher than 15% compared to an A330-200. Nevertheless, airlines have to review their network and corresponding flight planning and crew planning, as these longer flight times will introduce discrepancies in this respect.

Besides the lower cruise Mach number, also the lower cruise altitude poses some operational concerns which require further attention. The advantage of flying at higher altitudes such as the A330-200 reference mission is that the aircraft flies over the majority of turbulent cloud formations such as nimbostratus and cumulus clouds. These however are typically felt on the climb and descent phases of flight and are not of much concern. The cloud formation which is of concern is the cumulonimbus since strong upward air currents and thunderstorms are generated within, and flying through these is prohibited due to safety regulations. These cloud formations are typically very tall, with bottoms below 6500 ft and tops above 23 000 ft. For typical airliners, protocols are in place, and procedures dictate either to clear the top of the cumulonimbus by 5000 ft and or laterally clear the cloud formation by 200 nm. Current airliners are not concerned by these protocols since they are designed to fly at high altitudes in the troposphere. However, since the envisioned aircraft is being designed to fly at low altitudes, it will not be able to meet the vertical clearance requirement and will have to

[2] `https://www.basf.com/global/en/media/news-releases/2021/05/p-21-204.html` (last accessed on 17/05/2021)

divert horizontally around the cloud formation to avoid damaging the aircraft structure. This ultimately translates into an increase in fuel burn and a higher workload for the flight crew.

As the aircraft will encounter clouds throughout its whole mission profile, also during the cruise phase, the aircraft will have to cope with the effects resulting from this. Modern aircraft are already equipped with anti-icing systems, but in the further design of the low-ATR aircraft special attention should be given to the fact that the aircraft will be exposed to icing conditions much more frequently, potentially harming the airframe or engine. Furthermore, as the aircraft will fly through clouds more regularly, maintenance practices might have to be revised to account for the fact that the aircraft is exposed more often to relatively high moisture levels, potentially resulting in more corrosion effects or other forms of material degradation.

20. RAMS Analysis

RAMS or Reliability, Availability, Maintenance and Safety is an operational philosophy for hazard prevention. The main required formulas are displayed and a list of general product hazards is given as well. Section 20.1 covers the reliability, Section 20.2 the availability, Section 20.3 the maintainability and finally, Section 20.4 the safety.

20.1. Reliability

Reliability can be defined as the probability that a product will perform it's purpose successfully for a given amount of time. Equation 20.1 depicts the reliability equation for a given distribution f(t) and Equation 20.2 depicts the hazard function, the probability that a product which has not failed up to time x will fail. For aircraft systems, a constant failure rate with an exponential distribution is assumed as this best models random failures in complex systems; Equation 20.3 shows the reliability equation of this distribution where θ is the mean time to failure (MTTF). Another failure rate that is sometimes used is the bath-tub distribution, which describes wear-in at the begin of life and wear out at the end of life and these distributions are modelled with Weibull distributions [35].

$$R(t) = S(t) = 1 - F(t) = 1 - \int_0^t f(t)dt \qquad (20.1) \qquad h(x) = \frac{f(x)}{R(x)} \qquad (20.2)$$

$$R(t) = 1 - F(t) = 1 - \int_0^t f(t)dt = 1 - \int_0^t \frac{1}{\theta} e^{-t/\theta} = 1 - \left[-e^{-t/\theta}\right]_0^t = e^{-t/\theta} \qquad (20.3)$$

In subsequent phases of the design project, each component will be assigned a failure distribution so that the reliability over time can be computed. This reliability procedure will then be continued in a bottom to top manner. Note that sometimes a system as a whole will not fail if only a single subsystem fails. This means that the system reliability is not the multiplication of all its subsystem reliability and more detailed knowledge on which combination of subsystems a system needs to operate is required. For each system and sub-system a fault tree analysis will be constructed.

20.2. Availability

The availability of the aircraft is closely related to maintainability and reliability of the aircraft. The systems engineering field defines different types of availability, with operational availability being the most relevant, as it takes into account all the parameters available. Operational availability is defined as the percentage of time that the aircraft is available for its use. It accounts for maintainability, reliability and MTBM, and can be calculated using Equation 20.4 [1]. MTBM is defined as the average time between maintenance activities, both corrective and preventive [2]. MMT is the average maintenance time needed for both corrective and preventive actions [3]. Finally, MLDT is the average time needed for the logistics around the maintenance of the aircraft [4].

$$A_O = \frac{\text{MTBM}}{\text{MTBM} + \text{MMT} + \text{MLDT}} \qquad (20.4)$$

On the other hand there is also achieved availability, which ignores MLDT [5], and inherent availability that ignores MLDT and time losses from preventive maintenance [6].

At this stage of the design an estimation of the availability will not be accurate enough, and therefore this is left as a recommendation for further research in more detailed design.

[1] https://web.archive.org/web/20130312154509/https://dap.dau.mil/glossary/Pages/Archived/1476.aspx (last accessed on 18/06/2021)
[2] https://web.archive.org/web/20130309034113/https://dap.dau.mil/glossary/Pages/2234.aspx (last accessed on 18/06/2021)
[3] https://web.archive.org/web/20130309034104/https://dap.dau.mil/glossary/Pages/2232.aspx (last accessed on 18/06/2021)
[4] https://web.archive.org/web/20130309030824/https://dap.dau.mil/glossary/Pages/2231.aspx (last accessed on 18/06/2021)
[5] https://web.archive.org/web/20170624180658/https://dap.dau.mil/glossary/Pages/1380.aspx (last accessed on 18/06/2021)
[6] https://web.archive.org/web/20170624144513/https://dap.dau.mil/glossary/Pages/2045.aspx (last accessed on 18/06/2021)

20.3. Maintainability

According to [13], the maintainability of an aircraft is its ability to fulfill the operational requirements with a minimum investment in maintenance. This maintenance includes preventive (scheduled maintenance) and corrective (unscheduled) activities. Scheduled maintenance is performed at regular intervals, including annual and progressive inspection alongside preflight checks. Unscheduled maintenance is considered part of the reliability of the aircraft. These inspections and operations are meant to ensure the airworthiness of the aircraft [7].

According to the MATRA-SSYS-OPS-01 requirements, the aircraft is to receive A-class, C-class, and D-class. A-class checks are less exhaustive, while C-class and D-class maintenance includes heavier checks [53]. An aircraft undergoes A-class maintenance every 400-600 flight hours, which takes between 50 to 70 man-hours of work [53]. It includes change of filters, lubrication of hydraulics and inspection of the emergency equipment. Heavier maintenance are much more expensive for the companies, as they take more time and personal to be completed, as well as more space. C-class checks are done every 18 to 24 months, and take between 1 to 3 weeks to be completed. It includes checks like light structural maintenance or inspection for corrosion [25]. Finally, for the D-class checks, all the systems of the aircraft are dismantled and put back together, and when necessary a part is repaired or replaced after inspection. D-class maintenance is the most expensive type of check, resulting in an aircraft inoperative for a long time (3-6 weeks and between 30000-50000 man-hours [8]), so this maintenance needs to be planned years in advance. The high costs of this maintenance are often underestimated by manufacturers [9]), but luckily, newer aircraft need less of this type of checks. On the other hand, lighter regular airport maintenance includes inspection of wheels, brakes and fluid levels, as well as checking the alerts from the aircraft sensors. [10]

A measure of the maintenance is the MTBM. It can be calculated using Equation 20.5 [44] [11]. The MTBF can be calculated as shown in Equation 20.6 [18], where $R(t)$ is the reliability function and λ is the failure rate.

$$\text{MTBM} = \frac{1}{\frac{1}{\text{MTBF}} + \frac{1}{\text{MTBPM}}} \tag{20.5}$$

$$\text{MTBF} = \int_0^\infty R(t)dt = \frac{1}{\lambda} \tag{20.6}$$

In further stages of the design, this method can be used to calculate the maintainability of the aircraft. Currently, the design is not mature nor detailed enough to make an accurate MTBM prediction, so this is left as a recommendation for further research.

20.4. Safety

Safety is what keeps people and equipment separated from hazards. Figure 20.1 shows the general safety design philosophy of the ATR project [62], based on the ARP4761 system. The hazard identification follows a top to bottom approach starting with the preliminary aircraft safety assessment and ending with the system safety assessment. The hazards are then mitigated by implementing them into the requirements. The main aircraft safety hazards were identified during the risk assessment, see and asterisk denotes that the risk is also a safety hazard. A preliminary mitigation plan is also included in this section and the main hazards are incorporated into the requirements.

[7] `https://doublemaviation.com/aircraft-maintenance/` (last accessed on 17/06/2021)

[8] `https://web.archive.org/web/20140926151241/http://www.lufthansa-technik.com/overhaul` (last accessed on 17/06/2021)

[9] `https://www.aircraftvaluenews.com/maintenance-reserves-need-to-account-for-realistic-d-check-costs/` (last accessed on 17/06/2021)

[10] `https://www.qantasnewsroom.com.au/roo-tales/the-a-c-and-d-of-aircraft-maintenance/` (last accessed on 17/06/2021)

[11] `https://www.weibull.com/hotwire/issue147/hottopics147.htm` (last accessed on 17/06/2021)

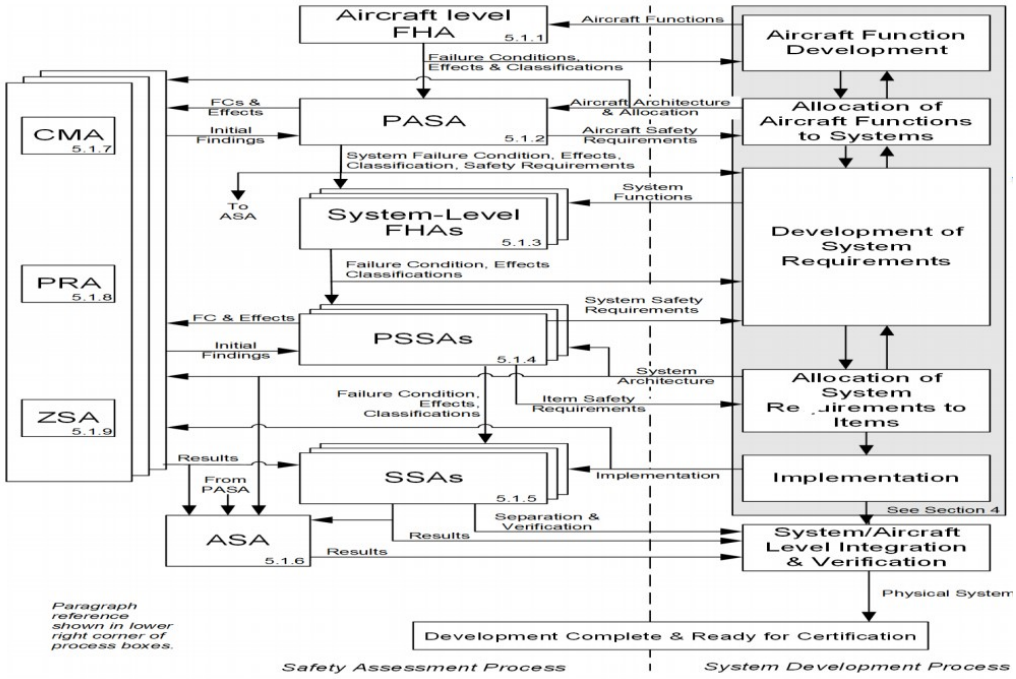

Figure 20.1: Incorporating safety into an aircraft design process [62]

21. Production, Manufacturing & Integration

The manufacturing section consists of three sections, one covering the general aircraft production plan in Section 21.1 and two covering the manufacturing of as of this point in time unconventional technology; propfans and riblets in Section 21.2 and Section 21.3 respectively.

21.1. Production Plan

In order to get an idea of how the aircraft will be made and put together a production plan is made. This can be seen in Figure 21.2 on the next page. First the individual parts will be made in batches. These will than be assembled in subassemblies such as the wing, the fuselage and so on. The fuselage will be assembled first as other subassemblies will have to be attached to it. Per subassembly that needs to be attached the fuselage will move on a station this way the same crew can make the same aircraft. The efficiency will therefor increase and the time it takes will go down over time. So first the empennage will be mounted then the wing. After this the landing gear will be attached. Finally the engine can be mounted. Now wit the aircraft complete the riblets can be applied and the area where no riblets are placed are painted. At this point the aircraft only needs a test flight and is ready to be used. This kind of manufacturing is called line production and is ideal for the amount of aircraft that need to be produced per month. This is also the most used method in aviation.

Not everything for the aircraft will be made by the manufacturer. Some parts will be outsourced to other companies as they often have greater experience and more knowledge about those parts. The fixed equipment: instrumentation, avionics, hydraulics, furnishing, APU, airco, pressurization-, oxygen-, electrical-, anti icing- and flight control system will be outsourced as these require a more specific expertise and equipment. Furthermore, some of the engine systems are also outsourced, the fuel system, oil systems, bladder support, engine control and starting systems Finally, the riblets will also be outsourced as this is a very new technique, which would require extensive design and certification time and cost. It is also important to note that unlike most aircraft companies the Engine will be produced in house as there are no such engines available at this time.

21.2. Propfan Blade Manufacturing

The most unconventional part of a propfan compared to turbofans are the blades, which are now not inside a cowling. Unlike the engine core, which will be made of an intermediate steel, the blades will be made of composite (an HM cyanate ester); adhering to the production plan of figure 21.1. For the detailed design, CIM is implemented. A single program can then be used for FEM, CAD and CAM, which improves total design accuracy and further support the concurrent engineering philosophy. The eventual blades will then consist of several two and three dimensional plies produced by multiple-axis machines and water knifes [94]. Whether current propfan design software also work with cyanate esters, which is considered to be used for the propfan blades, would have to be further investigated.

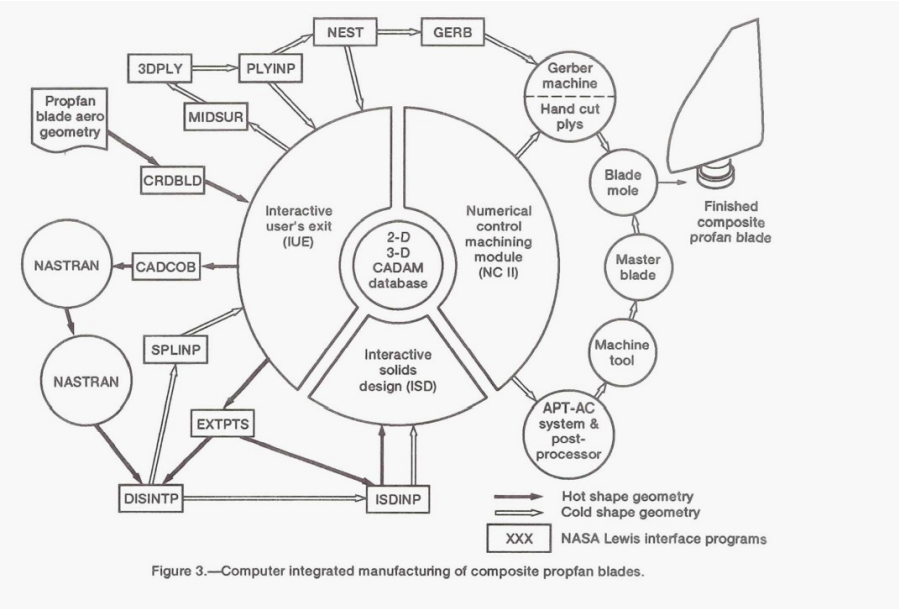

Figure 3.—Computer integrated manufacturing of composite propfan blades.

Figure 21.1: Digital manufacturing of composite propfan blades [94]

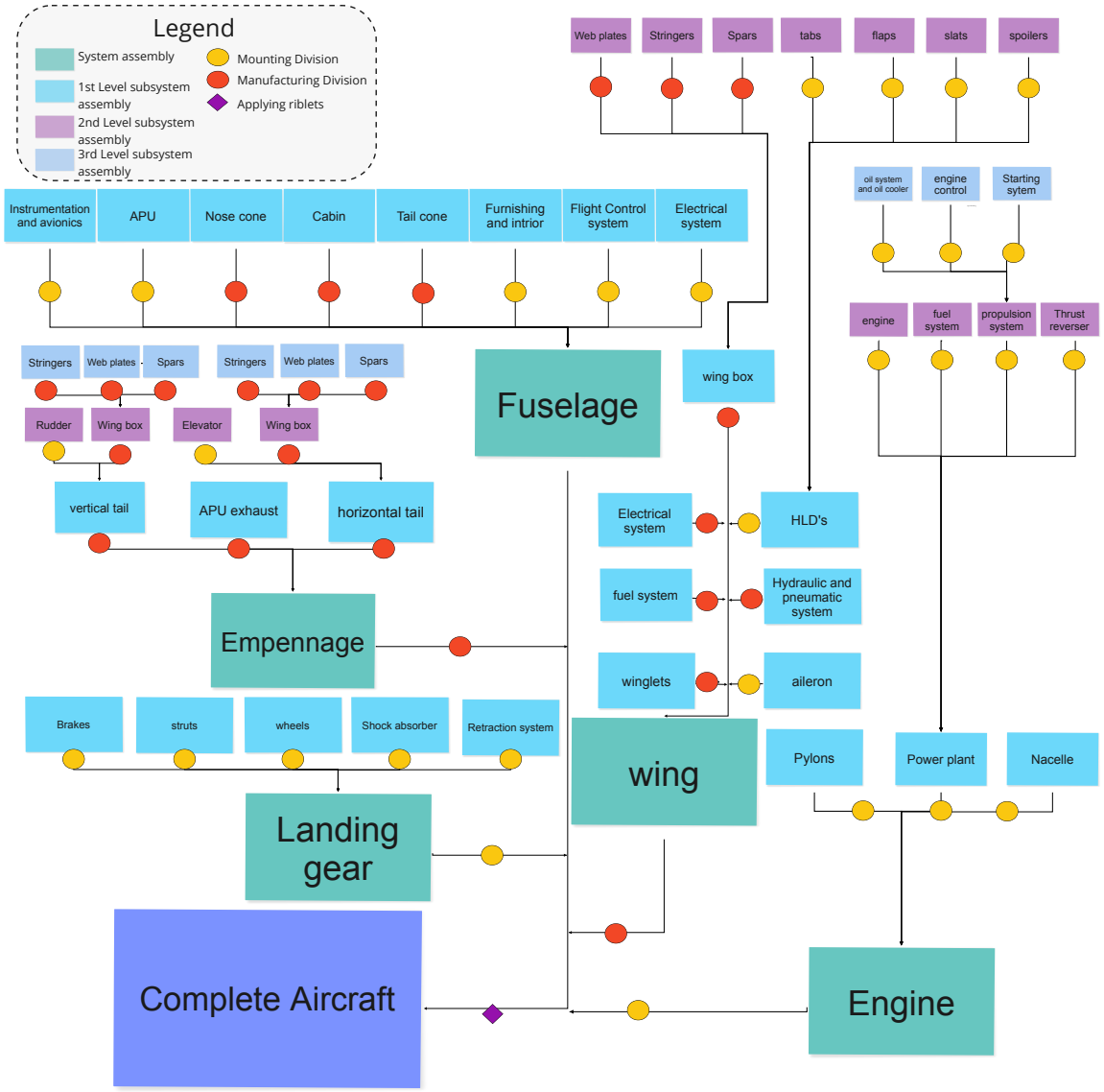

Figure 21.2: Production plan

21.3. Riblet Manufacturing

As seen in the production plan, the aircraft riblets will be applied as a coating after the aircraft is fully assembled. Figure 21.3 shows how the coating is applied through 'Direct Contactless Microfabrication', a type of photolithography developed by the Australian company Microtau [16]. First the aircraft skin is covered in a UV curable resin. This coating is then partially exposed to UV light, which causes only the exposed parts to harden and the unexposed parts to remain soft. Finally, after the soft parts are removed, only the hard parts remains, which has the desired riblet shape. The riblet shapes can be three dimensions, have dimensions of 5-90 μm and an accuracy of $\pm 1 \mu m$. The technology has previously been applied to a Boeing 767 and reduced skin friction drag by 6-7% [17]. Ideally, a partnership with Microtau can be established as developing similar technology in-house increases design time and cost. Another third party company option for a partnership would be BASF, which uses similar technology and has already had success with Aeroshark [1]. Producing riblets through water jet cutting was also researched to no avail as this method proved not economically feasible [23].

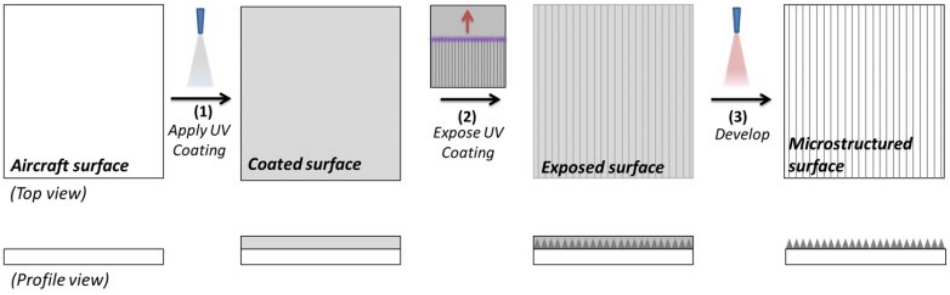

Figure 21.3: Riblet manufacturing [17]

22. Financial Overview

This section can be split up into two parts: manufacturer finances and airliner finances. Both operate with different models and therefore each business model is analyzed separately. As the client of this project is a manufacturer, the manufacturing finances are covered more thoroughly. The manufacture financial overview consists of Section 22.1, Section 22.2, Section 22.3 while the airliner financial overview consists of Section 22.4 and finally, Section 22.5 covers the complete verification and validation of the cost model.

22.1. Total & Conquerable Market Share

Figure 22.1a shows that an aircraft carrying 250 passengers with a 4300 nautical mile range (8000 km) is located inside a saturated market. This is a good sign as the large supply means that there is plentiful demand. Figure 22.1b shows that there are 727 operational A330 aircraft in 2019, the most similar operational aircraft compared to the design. The main advantage of the design aircraft is that it is designed to adhere to long term climate policies while the current aircraft fleet is not. The A330-200 neo for example, improved fuel burn efficiency compared to the previous A330-200 by 14% in 10 years [1], while the CORSIA scheme requires a fuel efficiency increase of 2% per year [71]. This means that it is difficult to modify the A330 line to meet CORSIA requirements. Therefore, the ATR aircraft can potentially beat most current competitors so that the market share is purely dependent on demand. To still be conservative, only the A330 market size is, adjusted for demand increase (4% per year on average [56]), is assumed conquerable. Furthermore, only aircraft located in countries that singed the CORSIA program are taken into account (this at the time of writing the entire A330 fleet), which is 920 aircraft in 2025. The average A330 production rate was 10 aircraft per month in 2019, which leads 13 aircraft per month in 2025 when production is scaled with demand increase.

[1] https://www.basf.com/global/en/media/news-releases/2021/05/p-21-204.html (accessed on 16-06-2021)
[1] https://simpleflying.com/a330neo-changing-aviation/ last accessed on 15-06-2021

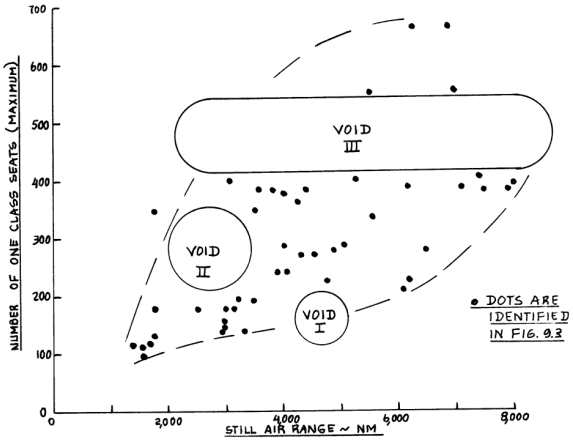

(a) Total market segmentation [92]

(b) A330 market share

Figure 22.1: Aircraft market shares [2]

Normally in transitions not all operational models are instantly replaced. Assuming only new aircraft will have to adhere to emission regulations this would lead to 727 * (0.03 + 0.04) = 51 aircraft per year (where 0.03 is taken from the fact that each year 3% of aircraft retire [3]). This will however, have to be larger due to the climate policies. Model predictions suggest that far more drastic measures than those done previously are required in the period from now until 2030 to meet pathways that lead to the 1.5 ° C global average temperature increase in 2050 [63]. 13 * 12 = 157 aircraft per year is therefore a more realistic value in this scenario. As a final note, there were 864 Boeing 787 operational in 2019 [4], another potentially conquerable market segment.

22.2. Cost Analysis

The total aircraft manufacturer costs in Figure 22.2 can be sub divided into the development cost and the manufacturing & acquisitions cost. The development cost are all the costs necessary to design the product, in this case the aircraft; while the Manufacturing & Acquisitions cost are all the cost necessary to sell a fully functional product. The breakdown is derived from the Roskam method [92]. The operating cost are explained in a later section as there are airliner cost, not manufacturer. For all costs, the values are converted to euros and scaled with inflation, which is assumed to be 3% per year, by computing all the values in 2021 euros. the Roskam model equations date back from 1990 and it is assumed that all costs and labor rates are time invariant when inflation scaled.

Overall, the development cost from Figure 22.2 meets the requirement of being 20 billion euros by merely being 5.13 billion. The air frame engineering and design cost of 1.04 billion and the development support and testing cost of 0.257 billion are the cost necessary for a team of engineers to come up with a feasible design and test it. These costs heavily depend on the program difficulty (1.0 is standard aircraft, 2.0 extremely unconventional such as blended wing, the ATR aircraft is set at 1.5) and company experience (moderate CAD experience was assumed, assigning a factor 1.0). The main component of the development cost are the flight test aircraft coming in at 1.57 billion. Their cost is much higher than for a production aircraft because there is no assembly line and the manufacturing process has not yet been optimised; hence the manufacturing and tooling cost make up 1.248 billion together. Conventional values were assumed for the number of test aircraft at 4 dynamic and 2 static. The certification and additional testing cost are included in the Flight test operations, coming in at 0.157 billion. For aircraft design, the costs are usually not paid directly by the developer but through a loan and a conventional value of 10% of the development cost is assumed. Furthermore, some of the operations and processes will be outsourced and these other parties will require a profit margin for their services, which is in this case also set at the conventional value of 10% of the development cost. Finally, the test and simulation facilities cost of 1.51B are extra costs which cover the design and certification of propfan engines; riblet technology is assumed to be outsourced.

[3] https://www.boeing.com/resources/boeingdotcom/market/assets/downloads/2020_CMO_PDF_Download.pdf (accessed on 15-06-2021)
[4] https://www.planespotters.net/operators/Boeing/787?refresh=1 (accessed on 15-06-2021)

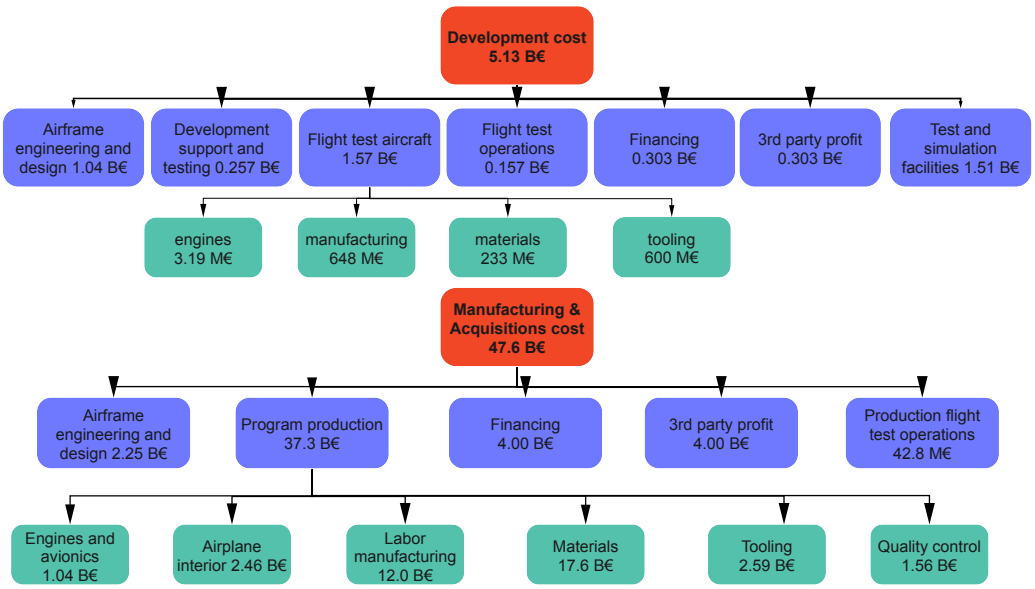

Figure 22.2: Cost Breakdown Structure

The other main component of the cost breakdown structure from Figure 22.2 is the manufacturing and acquisitions cost. The figure shows the total manufacturing cost of 47.6 billion, which covers all 920 production aircraft. The reason to give this value as a total and not as a single aircraft value is due to a phenomenon called the learning curve. Over time the aircraft producers gain experience on the manufacturing of the ATR aircraft, which inevitably results in aircraft number one hundred costing less time and resources than aircraft number one [92]. The lean manufacturing philosophy will also be applied and this will inevitably lead to processes becoming more efficient with time and experience (as the whole company actively seeks to reduce waste, costs lower) [101]. The mean value of one aircraft would be 51.6 million and this easily meets the requirement of a 150 million production cost. The Airframe engineering and design cost comes in at 2.25 billion, this is the engineering support required during production (for example, the Boeing 737 max that required updated software while it was already flying). The vast majority of the Manufacturing and Acquisitions cost comes from actually building aircraft: the program production, which is 37.3 billion and includes engines and avionics, interior, labor, materials, tooling and quality control. Note that the tooling cost in the development phase are on average 34.74 times higher aircraft, showing the cost reduction potential of a assembly line. Financing and third profit have a similar rationale as for the development cost and come in at 10% of the total cost each. Finally, each aircraft is flown by the manufacturer before being delivered to the customer as a means of inspection; the cost for these flights is 42.8 million, assuming two hours of test flight per aircraft. It is assumed that the manufacturing rate matches the demand so that 13 aircraft are produced each month. This is logical because otherwise there would be a shortage in supply and thus profit is left on the table or too aircraft would be produced, resulting in waste of resources (the ladder would also be in violation of lean manufacturing).

22.3. Return on Investment

Table 22.1 depicts all useful financial values for an aircraft manufacturer for both the ATR aircraft and an A330-200. The A330 values for obtained from both a database [5] and by plugging non financial values into the Roskam method and thus Roskam method values were acquired as well.

Table 22.1: Investment values

2021 value	ATR AC	A330
market price Roskam in million euros	57.3	73.3
listing price million euros	203.4*	259.9
market volume	920	-
Achievable market share	920	-
Development cost in billion euros	5.135	6.507
Production Cost per AC in million euros	51.72	66.27
Direct Operating Cost million euros per aircraft per year	20.5	16.8
RoI per year in %	9.79	9.73
* data fitted		

[5] https://modernairliners.com/airbus-a330/airbus-a330-specs/ accessed on 17-06-2021

The first anomaly to note is that the A330 listing price is 3.55 times higher than the predicted Roskam price. Such a price difference can be explained with a market that is in either a monopoly or oligopoly (a few companies controlling a vast majority of a market) as these models allow companies to have great control over the product price. This model theory is supported by Airbus owning a 45% market share and Boeing a 43% [6]. The airbus price control is further supported by the discounts given to airliners who buy multiple aircraft during the development phase; on average the discount is 50% [7]. A business is only able to give such a discount if the profit margin if large enough (otherwise, selling a plane would cost money) and in competitive markets the profit margin is negligible, hence the support for the aircraft manufacturer market being an oligopoly. To give an estimation, the Roskam ATR aircraft market price is multiplied by 3.55 to return a value of 203.4 million (the data fitting is mentioned because this value is derived from the A330 value). In the future it would be recommended to base this multiplier on more aircraft than just the A330-200. The low listing price is also to a minor extent a consequence of the bottom to top approach and is in accordance with literature [114].

The market volume, achievable market share, development cost and production cost were already extensively discussed in the previous sections of this chapter and therefore just the return on investment or RoI remains to be discussed. The values for both aircraft are expected as they are very similar to the RoI of the SP500 index (500 largest companies on the American stock market) of 8% [8]. What is rather remarkable however, is that the ATR aircraft has a higher return on investment than the A330-200, 9.79% compared to 9.73% (note that the Roskam values are taken); meaning Airbus would make more profit producing the ATR aircraft than the A330. The exact reason of this result would have to be further investigated but it is most likely caused by the ATR aircraft being lighter and thus having lower costs. More importantly, the A330-200 is most likely not optimized for generating profit (the ATR aircraft is not optimized for profit and has the best RoI). Most likely in an attempt to beat Boeing, the A330-200 is optimized for direct operating cost reduction, making it more attractive for customers. The direct operating cost will be further discussed in the section below.

22.4. Airliner Financial Overview

In order for any aircraft to be successfully, it needs to generate profit for airliners. This section investigates the feasibility of an ATR aircraft by analysing the operating cost and attainable profit margins; the main findings are displayed in Figure 22.3.

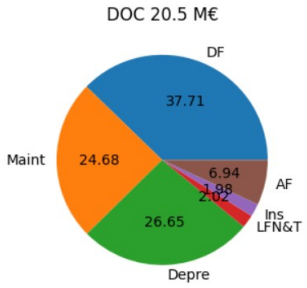

(a) Direct operating cost

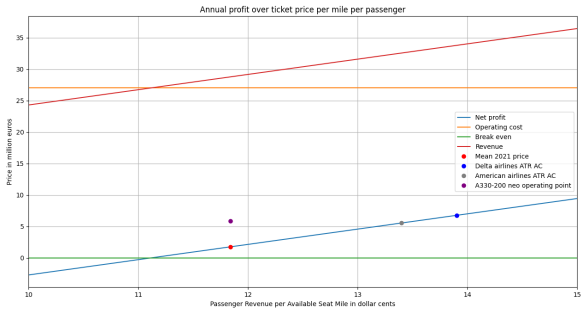

(b) Airliner profit per passenger rate

Figure 22.3: Airliner operations

The direct operating cost are given by Figure 22.3a for a single aircraft per year in 2021 million euros and are 20.5 for the ATR aircraft. The largest share of costs are the DF costs at 37.71%. This includes cockpit crew, fuel and oil costs and for the fuel mixture of 50% kerosene with 1.4 2021 DgP [9] and 50% bio fuel with 0.532 2021 DpG [56] is taken (the Roskam model has a fuel price input unit of 1990 DgP). The oil price is set at 21.54 1990 DgP [10] and the average cockpit crew salary at 80000 1990 dollars per year [92]. Next up is the Depre at 26.65% , which uses depreciation rates and initial price values from Roskam for each major system value wise [92]. The Maint of 24.68,l of LFN& T 2.02% and AF of 6.94% are all configured for international intercontinental flights meaning they are relatively higher compared to their respective mean values. Finally, the Ins cost is 1.98% of the total cost and if often considered to be part of the DOC. The total operating cost also consists of the indirect flight cost, which is assumed to be 52% of the DOC [92], resulting in a total operating cost of 31.15 2021MEpY per ATR aircraft.

Figure 22.3b shows some valuable data on the profit margin of the ATR aircraft. At the current average market ticket price of 11.84 DCpNM [11], a single ATR aircraft will make a profit of 1.75 MEpY, while an A330-200 will make a profit of

[6] https://www.flightglobal.com/insight-from-flightglobal-flight-fleet-forecasts-single-aisle-outlook-2016-2035/121497.article accessed on 17-06-2021

[7] https://simpleflying.com/airbus-reveals-on-average-airlines-get-50-off-airline-list-prices/ accessed on 17-06-2021

[8] https://www.investopedia.com/ask/answers/042415/what-average-annual-return-sp-500.asp accessed on 17-06-2021

[9] https://www.investopedia.com/ask/answers/042415/what-average-annual-return-sp-500.asp accessed on 17-06-2021

[10] $https://www.energy.gov/sites/prod/files/maprod/documents/nepdg_8501_8750.pdf accessed$ on 17-06-2021

[11] http://web.mit.edu/airlinedata/www/2019%2012%20Month%20Documents/Revenue%20and%20Related/Passenger%20Revenue/System%20Passenger%20Revenu accessed on 17-06-2021

5.83 MEpY. The ATR aircraft would require a ticket price of 11.12 DCpNM to break even and a price of 13.52 DCpNM to reach the A330-200 profit margin, meaning average ticket prices would have to increase 13.5% for the ATR aircraft to reach A330 profit margins. Furthermore, among current American airlines, only Delta (13.9 DCpNM) and American (13.4 DCpNM) airlines operate on ticket prices around the ATR aircraft hypothetical A330 profit margin . To conclude this section, the RoI for an airliner with one ATR aircraft is 11.86% for the 57.3 million euros Roskam market price and Delta net operating income of 6.76 MEpY (see Figure 22.3b for a value of 13.9 DCpNM).

22.5. Roskam Cost Model Verification & Validation

In order to assess the accuracy of the Roskam model both verification and validation are performed. For verification the model output was compared to values within the Roskam book itself [92] and with literature that also used this method [112] and once results were promising validation was initiated. While the Roskam method is widely used and validated by various external sources it was still deemed necessary to perform an in house validation of the model. The DOC play a vital role is the user requirements and therefore the model accuracy is a valuable asset. The Roskam model output for the ATR aircraft and an A330-200 are compared to reference aircraft. As the model follows a bottom-to-top approach, comparison between the top values will provide sufficient information on the maximum deviation. For each of the three costs, a trend that best fits the data is selected and the R^2 is computed to analyze the data variance, it shows the strength of dependence between two variables. Finally, the Roskam values are compared to the trend so that their model deviation can be analyzed. The main findings are depicted in Figure 22.4.

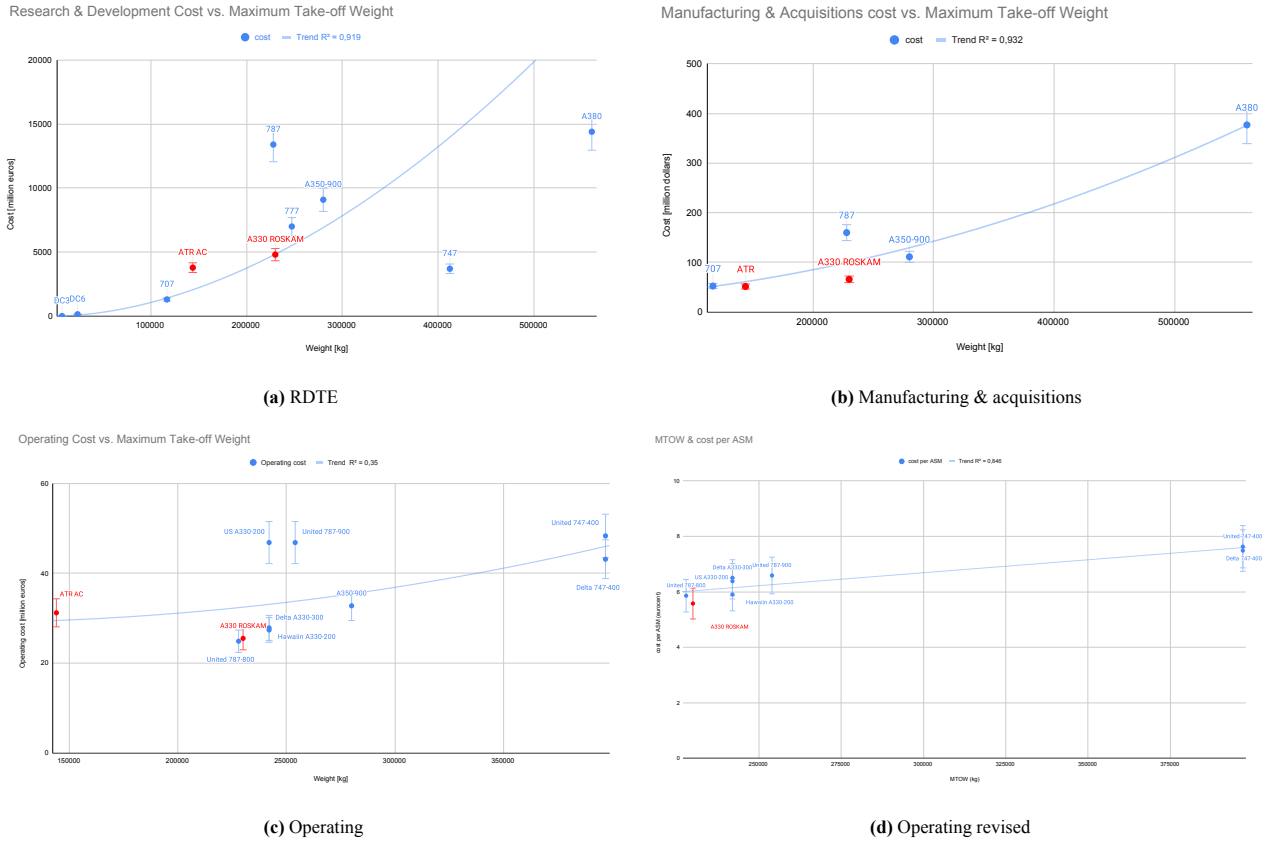

(a) RDTE

(b) Manufacturing & acquisitions

(c) Operating

(d) Operating revised

Figure 22.4: Roskam cost model validation

The first cost analyzed is the Development cost of Figure 22.4a, which design uses design cost values of several comparable modern aircraft [12] [20]. The data has an R^2 value 0.919 when a power series is used as trend line. Therefore, there is a clear correlation between maximum take-off weight and design cost, meaning the Roskam output data can be properly analyzed. The A330 output data lies exactly on the trend with variance of roughly 10%. The actual A330 is unfortunately confidential but the current data provides sufficient proof that the model is accurate for an A330 aircraft. The ATR aircraft has a slightly higher cost than the trend. This could however, be explained by the need for extra facilities to develop the propfan. Subtracting the 1.151 billion extra facilities cost (note that this extra engine cost is still lower than the allowable 5 billion) from the 5.31 billion design cost returns a value of 3.62 billion and this lies right on the trend line. Based on

[12] https://simpleflying.com/airbus-a350-break-even/#: :text=The%20projected%20cost%20to%20Airbus,m%20on%20each%20aircraft%20sold. accessed on 19 June

these conclusions, the development cost part of the Roskam model is considered sufficiently validated. This also means that the assumptions of 1.03% inflation per year and time invariant inflation adjusted costs are accurate.

The manufacturing and acquisitions cost validation is given by Figure 22.4b [13] [14] [15] and has a R^2 value of 0.932 for a polynomial function meaning there is a strong correlation between aircraft weight and production cost. The Roskam A330 has a significantly lower production cost than other aicraft but is still closer to the trend than the Boeing 787 and therefore the model output is still deemed acceptable. The ATR aircraft is spot on on the hand. Overall, the manufacturing part of the Roskam model is also deemed sufficiently validated.

Figure 22.4c is shows the final cost, the operational cost (note that the operating cost are assumed a factor 1.52 of the direct operating cost [92]) [16] [17]. The best R^2 achieved is 0.35 for a polynomial function, meaning there is no strong relation between aircraft weight and operating cost. This is further supported by the same aircraft, the A330-200 having roughly twice as high operating cost when operating by US airlines then when by Delta. Both Roskam outputs lie however, well within in the data set meaning the unpredictability is probably primarily caused by the weak relation and not the Roskam model. As a recommendation, further research could look if there is a stronger correlation between the operating cost and other variables (block speed in particular). This would however, require more data on the reference aircraft, which is difficult to acquire.
Figure 22.4d shows the operating cost per ASM on the vertical axis with the MTOW on the horizontal axis. Now the trend is much stronger with $R^2 = 0.846$. The Roskam predicted A330 cost is on the low side but within error margin similar to those found in literature [36].

23. Sustainable Development Strategy

This chapter devises a detailed sustainability strategy for the envisioned low-ATR aircraft. The foregoing Project Plan [40], Baseline Report [38] and Midterm Report [39] investigated sustainability from the standpoints of lean design and project management, technical (sub-) system sustainability and operational sustainability, respectively. The aim of this chapter is to synthesise these complementary aspects into a sustainable life-cycle strategy. The following approach shall be adopted: firstly, pre-operational sustainability during detailed design, manufacturing and certification is addressed in Section 23.2. Secondly, Section 23.3 is devoted to sustainability throughout the system's operational lifetime, which is typically 35 years for a commercial transport aircraft [78]. Lastly, a detailed end-of-life plan is devised in Section 23.4 in order to minimise the system's post-operational adverse environmental impact.

23.1. Sustainable Group Performance Evaluation

During the Project Plan phase the group identified the status quo in terms of lean design/project management and set its goal for the end of this DSE. Figure 23.1 compares the group's initial, targeted and achieved performance related to a number of organisational waste forms. The group was able to meet its goal on four out of five criteria, with only waiting time lacking behind the expectations. This is primarily due to the final sub-system integration and design iterations, which turned out to be more time-demanding and error-prone than expected. As a result, the final converged design was available later than planned, necessitating a reallocation of tasks to allow certain group members to make effective use of the waiting time. Miscommunication and waste of physical resources can practically be considered as eliminated. Regarding the former, the group vigorously followed an established meeting format (three times per day, starting with a discussion of the results and outlook per engineering department, followed by interface management and finally planning the communication with tutors/coaches/teaching assistants) and made consistent use of dedicated communication channels. The primarily online setting of the exercise already minimised the waste of physical resources (the group refrained from paper-based work and contacted faculty staff and external experts remotely). Moreover, the group was able to meet its goal regarding under-utilisation of its members, since during the technical design phase almost everyone could be allocated to their engineering department of choice. The amount of reworking was reduced from "infrequent" to "occasional", as a common basis for reporting style and quality, notation and referencing could be established. Lastly, as was to be expected, all group members but one typically met up three times a week on campus, unless it was deemed beneficial to work from home (for example, to practice for an upcoming online review). Seven out of ten people commuted by bike, one by public transport, one by car, and one worked entirely from home.

[13] https://www.airlinercafe.com/page.php?id=72 (accessed on 19 June)
[14] https://www.planestats.com/bhsw_2014sep (accessed on 19 June)
[15] https://www.assemblymag.com/articles/95910-last-airbus-a380-superjumbo-assembled-in-france#:~:text=The%20Airbus%20A380%20was%20developed,produced% (accessed on 19 June)
[16] https://epsilonaviation.wordpress.com/2018/04/28/how-large-is-the-market-for-the-airbus-a350-900ulr-and-how-much-does-it-cost-to-operate-it/ (accessed on 19 June)
[17] https://www.planestats.com/bhsw_2014sep accessed on 19 June

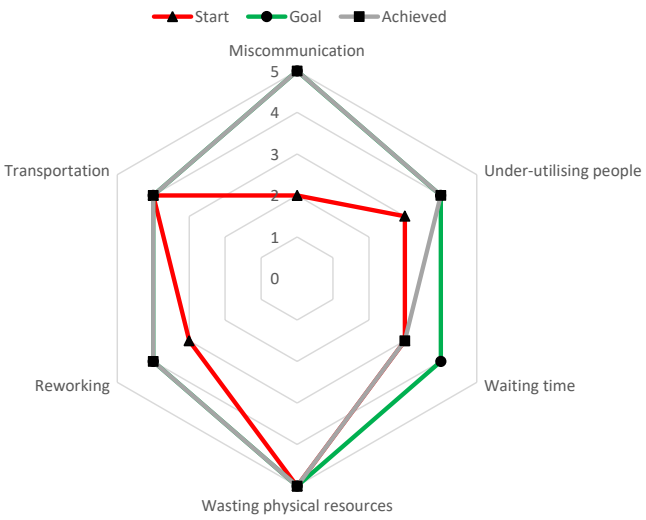

Figure 23.1: Outcome of lean design/project management performance - 1: Common, 2: Occasional, 3: Infrequent, 4: Rare, 5: Eliminated

23.2. Pre-Operational Sustainability

A holistic sustainability strategy incorporates all phases of a project, from the design phase until the system's end of life. Since this report marks the end of the preliminary design phase, the present section is concerned with the subsequent detailed design phase and aircraft manufacturing, assembly and certification. These stages shall be based on the concept of "Lean Thinking", which describes the "dynamic, knowledge-driven and customer-focused process through which people in an enterprise continuously eliminate waste with the goal of creating value" [100].

23.2.1. Post-DSE Preliminary Design Phase

During the forthcoming preliminary design phase, the "5S Approach", which was devised as part of the successful "Toyota Production System" and targeted at eliminating waste from any industrial process [100], shall be employed. In the following, for each stage concrete examples shall be provided as to how this approach will surface during the preliminary design phase, for which reference shall be made to the diagrams in Chapter 24.

1. **Seiri (Sort):** During this phase, higher fidelity design tools compared to the ones employed throughout this DSE will be employed. It is expected that the current Python-based design process will gradually shift towards more dedicated, sub-system specific analysis tools, such as FEM, CFM and CAD software packages. This necessitates a good integration of said tools with a common database accessible to all design groups. Also, during this phase it is advisable to allocate one system engineer to each design group, who is tasked with gathering and sorting his/her group's data and communicating it to the other groups' system engineers. Similarly, this phase will likely see a closer contact with the customer, for which a customer relations officer should be appointed, as well as a person responsible for managing the (sub-) contractor network.
2. **Seiton (Simplify):** Similar to the foregoing conceptual and preliminary design phase, limiting the number of design and organisational tools to a bare minimum is key to maintain a good overview at all times. For example and where applicable, the same flutter analysis tool should be applied to the propfans' rotor blades as to the aircraft's wings (see Figure 24.1), which also limits the modelling discrepancies. With regards to organisational and communication tools, a balance between the increased complexity of multi-functional tools and the benefits of fewer communication channels ought to be found. Potential bottlenecks, for example wind-tunnel facilities for experimental testing, ought to be identified, and the performance of non-critical design features ought to be assessed via simulation.
3. **Seiso (Scrub):** One way to think about "scrubbing" relates to the stability and control/autopilot system design; one should simplify the model as much as constraints on accuracy allow, for example by linearising the equations of motion. From an organisational viewpoint, obsolete or outdated data should either be archived or discarded, for which the appointment of a dedicated file manager per design group would be beneficial.
4. **Seiketsu (Standardise):** Even though the design methods and tools will inevitably vary between subsystems, formalities should be standardised as much as possible. This includes meeting hours, frequency and minutes keeping, but also more technical aspects such as a common quality control approach. Also, by offering regular training opportunities to employees, a common skill level can be ensured.
5. **Shitsuke (Sustain):** Ultimately, once a functional and efficient 5S design approach has been established, it ought to be sustained and, where possible, improved upon. For suggested areas of improvements related to group organisation/management, please refer back to Figure 23.1.

23.2.2. Manufacturing and Assembly

In Chapter 14, a detailed material trade-off for each major aircraft component was conducted. Sustainability, in this case related to recyclability and primary CO_2 per kg, was weighted with 3/5, highlighting its relative importance for the present aircraft design. Next, in Chapter 21 a holistic production plan aimed at minimising the aircraft's list price was devised. This goes hand in hand with the high level "15% DOC increase at minimum ATR" objective, striving to make sustainable flight economically viable for both airlines and customers. In this section, further suggestions for sustainable manufacturing inspired by Lean Thinking shall be provided.

A high level of material recyclability was targeted during the material selection process. This was one of the primary reasons why the aluminium-infused carbon composite material was discarded, despite is superior carbon footprint. Also, the feasibility of using a thermoplastic composite as fuselage material was investigated. However, given the lack of large, proven structural components made from thermoplastic composites combined with the due entry into service date, a traditional thermoset design was opted for. Both material options shall undergo re-evaluation in the nearer future, and potentially be incorporated into the production process. Moreover, materials shall be be acquired from local suppliers at the cost of slightly higher prices, and the usage of scarce materials is sought to be avoided during the selection process (nickel-, chromium-, and/or cobalt alloys/coatings are only used where inalienable, such as for the landing gear struts and engine components). Finally, care was taken to ensure a low material corrosiveness, both with regards to external agents (e.g., salt water, which is particularly relevant for the considered reference mission) and galvanic corrosion.

In line with the foregoing detailed design phase, lean thinking shall feature prominently throughout the production process, with the aim of eliminating waste and creating value. As mentioned in Chapter 21, an aerospace-typical line production system shall be employed. Particularly during the early production stage, establishing a JIT system, where the right amount of components are manufactured and delivered at the right time (the opposite of batch production) aids in reducing storage and depreciation costs [100]. In order to mitigate the resultant risk of bottlenecks in the (sub-) contractor network, all components shall be outsourced to at least two (sub-) contractors, further allowing a more rapid response to changes in market demand. As explained in Chapter 21, the propfan engines, which are arguably the most costly sub-system, shall be developed and manufactured JIT in-house. Furthermore, in-house production shall be centralised, reducing the carbon footprint caused by transporting components between their manufacturing and assembly location (contrary to Airbus' highly decentralised production network). Cellular manufacturing shall be employed during assembly, where the same crew repeatedly performs the same work package within self-contained workstations. This approach leverages the learning effect developed over time, however work packages shall be designed to span several days and involve varying tasks to prevent boredom. A moving belt (sub-) assembly transportation system, inspired by the pioneering Beoing 777X final assembly line [1], shall be employed to cut assembly times by more than 30%. The sustainability of the envisioned manufacturing processes for the materials chosen in Chapter 14 was quantified by their CO_2 footprint. With the ATR model from Section 16.3.2 at hand, these emissions shall be associated with a sea-level ATR estimate in Section 23.5. Note, however, that unlike the operational ATR footprint determined in Section 16.3, only CO_2 is accounted for. This section on manufacturing sustainability shall be concluded by focusing on the two principle ATR-reducing technologies investigated in this project: propfan engines and riblets. The CIM method employed for manufacturing the propfan blades in Section 21.2 gives a flavour of the significant cost reductions and purpose-tailored designs that can be achieved with novel manufacturing methods. Despite the primary structural materials and manufacturing selection method being rather conservative, by the expected EIS date techniques such as AM are expected to have reached full operational maturity. AM cabin interior elements such as wall panels, seat frameworks and air ducts may already be considered proven as of today, facilitating substantial wait savings [108]. The "Direct Contactless Microfabrication" of riblets detailed in Section 21.3 is an excellent example of a low-energy, low-processing-waste manufacturing process. The excessive, uncured resin is fully reusable for application on subsequent aircraft, the local UV curing process neither exposes workers to hazardous chemicals nor radiation, and features excellent repair properties. From these viewpoints, this photolitographic technique is superior compared to BASF's "Aeroshark" foil, which has already been proven in flight.

23.2.3. Certification

Incorporating the topic of sustainability into aircraft certification is a difficult endeavour, given the immutable guidelines that need to be followed. However, it is suspected that with the ongoing advent of high-fidelity simulations, more and more certification tasks become obsolete, until one day entire aircraft can be conceived, designed and certified from one's desk. Currently, each major subsystem/structural component undergoes major in-house certification tests (e.g., engine blade containment tests, fuselage pressure tests or wing limit load bending tests, as shown in Figure 24.2) carried out by its manufacturer, before being integrated with the other subsystems. The complete aircraft is then tested under extreme operational conditions, ranging from high- to low-altitude and temperature, varying runway conditions etc. Even though it would obviously be beneficial from a sustainability point of view to bundle all certification tasks in one and the same location, this is not practically feasible and will likely continue not to be for some time to come.

[1] `https://www.boeing.com/news/frontiers/archive/2010/april/i_ca01.pdf` (last accessed on 20/06/2021)

23.3. Operational Sustainability

Considering the project objective, namely ”to design a long-range airliner employing laminar flow control and riblet technologies which achieves a low ATR”, it is clear that the emphasis of operational sustainability lies on minimising the aircraft’s global warming footprint. This goal has been extensively discussed in Section 16.3 and shall therefore not be repeated here. Also, the reader may again want to be referred back to Section 10.1 for a brief note on sustainable aviation fuels. The present section shall instead touch upon other operational sustainability aspects, including noise and mission infrastructure, which is a very broad term, as will become apparent.

23.3.1. Noise

A propfan engine configuration emerged from the trade-off process conducted as part of the Midterm Report [39], where ATR reduction was prioritised over noise reduction. The market analysis conducted in Chapter 3 further backed up this decision with governmental policy trends. Nonetheless, the final aircraft design presented in this report is required to meet the December 2017 ICAO Chapter 14 noise standards [2], which scale with MTOW and specify an upper bound for the EPNdB measured at any of the following three reference points: during approach at 2000 m from the runway, assuming a 3° approach angle, at a 450 m sideline reference point at takeoff, and after 6500 m at cutback thrust. For the converged MTOW of 182.28 tonnes, a Chapter 14 noise bound of 277±2 EPNdB applies to the present aircraft (see Figure 23.2a). In comparison, the best-performing Airbus A330-200 equipped with Rolls Royce Trent 772-60 engines and with a MTOW of 242 tonnes is certified at a cumulative 286.1 EPNdB, thus ranging 17.9 EPNdB below the applicable ICAO Chapter 3 noise limit based on its 1999 certification date [3]. State-of-the-art airliners, such as the A350-900 equipped with the Rolls Royce Trent XWB-84, comfortably meet the Chapter 14 requirements (certified at 21 EPNdB below Chapter 4 standards [3], translating into 267±2 EPNdB for an MTOW of 280 tonnes).

Thanks to the latest insights gained into the unsteady aerodynamics of open rotor engines, recent conferences and studies were confident that counter-rotating configurations can fulfil Chapter 14 noise regulations [27]. A scaled model study conducted by Hoff et al. [46] actually found counter-rotating propfan engines to be 0.5 dB quieter than reference turbofan models, and a further 2.5 dB gain can be achieved from employing single-rotor configurations. Another study by Guynn et al. employs the ANOPP noise prediction model to compute the certification noise of a 151000 lbs (68.49 tonnes) aircraft propelled by two 22140 lb (94.3 kN) geared, counter-rotating open rotor engines at the three locations depicted in Figure 23.2. A cumulative open-rotor certification noise of 272.1 EPNdB is reported, which does not account for additional noise sources such as the core jet and airframe interactions. On the other hand, the authors emphasise that the study is based on early 1990s propfan technology, which does not reflect recent advances in low-noise-signature rotor design, leading to expectantly lower noise levels with 2021 technology. A number of noise mitigation strategies which could not be incorporated into the propfan engine model due to time constraints devised in Chapter 10 were formulated as recommendations for the forthcoming detailed design phase in Section 10.9. A noise reduction strategy suggested by E. Schwartz Dallara [27] which has been implemented into the current preliminary design phase relates to the climb and descent gradient. In SUAVE, a steeper climb and descent segment compared to the standard A330-200 mission profile based on literature has been implemented, trading a higher throttle setting and fuel consumption for a reduced noise impact on residents around airports.

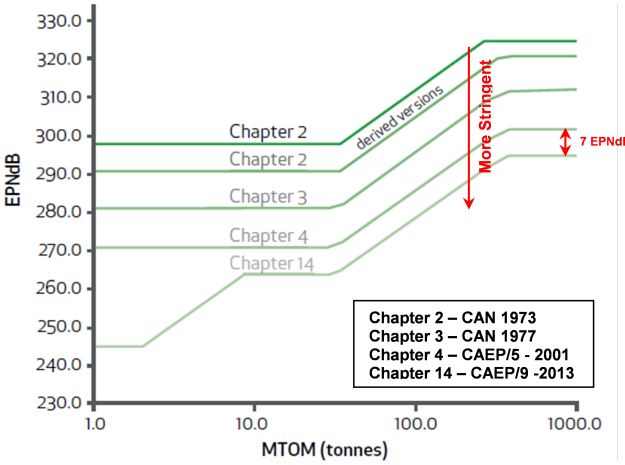

(a) ICAO noise limit scaling with MTOW[2]

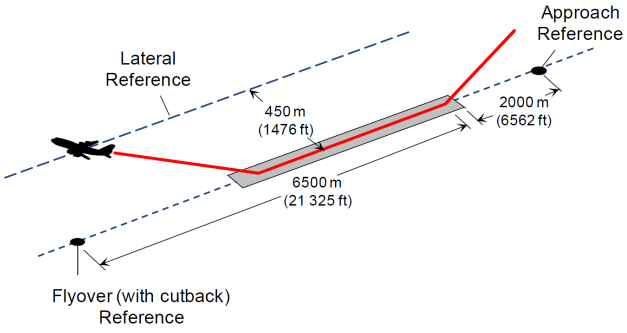

(b) Observer arrangement relative to hypothetical combined takeoff and landing aircraft trajectories [41]

Figure 23.2: Noise certification levels and observer arrangement during measurements

[2] https://www.icao.int/environmental-protection/pages/reduction-of-noise-at-source.aspx (last accessed on 17/06/2021)

[3] https://www.easa.europa.eu/eaer/system/files/ftab_files/EAEr%20Figure%202.3%20Certified%20aircraft%20noise%20levels%20(160122).xlsx (last accessed on 17-06/2021)

23.3.2. Mission Infrastructure

The design cruise conditions identified in Section 16.5 themselves enable a considerable ATR reduction of 80% (updated in Section 16.3.3) for the envisioned aircraft. The optimum altitude of 5000 m is dictated by short-lived climate agents, such as NO_X, which depletes short-lived ozone at high altitude, and contrails, whose formation is enhanced by the low ambient air temperatures in the upper troposphere. As mentioned in Section 16.5, the chosen cruise Mach number of 0.63 corresponds to the critical Mach number of the NLF airfoil, above which a wave-drag, and thus fuel-burn-penalty results. It concomitantly corresponds to the point of highest $\frac{L}{D}$, thus following the same mission design approach as P. Proesmans for his A330-200 [78]. As a side-effect, the wing may have less sweep and a higher thickness, increasing the fuel tank volume and thus compensating for the reduction in range [39].

Another noteworthy benefit of the envisioned low-ATR aircraft is that it can be operated from runways of 2500 m length, enabling it to serve a wider selection of airports than its competitors (e.g., the Airbus A350-800). As a consequence, passengers will have to travel shorter distances to reach their final destination after arrival, since they are not bound to the major hubs (e.g., London Heathrow, Paris Charles de Gaulle, Frankfurt am Main, etc.), thus producing fewer emissions [39].

Although an all-electric propulsion system was discarded during the most early trade-off stage in the Baseline Report [38], zero-carbon ground operations are realisable with today's technology. Besides a fuel-saving potential of up to 4%[4], electrical taxiing capabilities would improve on-ground autonomy, as well as the air quality and background noise level around airports. For large airports like Frankfurt, potential emission savings as high as 19% and noise savings of up to 100% were claimed [83]. This raises the need for both an advanced, green electrical airport ground power network, and a powerful on-board electrical energy storage system. The ground propulsion system demonstrator tested by the German Aerospace Center DLR, Airbus and Lufthansa Technik in July 2011 was integrated into the nose gear of an A320, producing a maximum torque of 5 kN m at a power consumption of 50 kW [83]. For the present aircraft's MTOW of 182.28 tonnes, one would require one such motor per tire pair, the total power consumption of which would amount to $3 \cdot 50 = 150$kN m at an estimated weight penalty of $3 \cdot 600 = 1800$kg [83] [98]. These two parameters have been accounted for in the weight budget (Section 8.1) and power budget (Section 13.1). Despite concerns raised by Safran about the economic feasibility of ETSs on long-haul aircraft[5], the 7.5% DOC decrease found in Section 16.3.3 leaves sufficient room to pursue the ATR minimisation goal further down this road. Besides this, an electrical taxiing system can be regarded as a concession to residents around airports, for whom the marginally higher propfan noise level would be compensated by an improved air quality.

Several on-board systems may be tailored to sustainability, such as OLED-based cabin lighting and no-bleed power-generators [39]. With their 787 "Dreamliner", Boeing's engineers have electrified functions such as anti-icing, engine starting, hydraulic pumping and the cabin environmental control system[6].

Air traffic management has a big impact on aircraft fuel efficiency through airspace design and mission optimisation. "Flexible routing" is already employed in uncrowded airspace (e.g., to exploit favourable air streams), however, surveillance techniques such as GPS have the potential of extending this procedure to crowded air spaces, such as The Netherlands [4] [39].

The "free route airspace" concept, allowing aircraft to be seamlessly navigated on direct routes across borders, is facilitated by the increasing harmonisation of airspace. Studies by the Geneva-based Air Transport Action Group have shown that aggregating the 45 European Air Navigation Service Providers (ANSPs) into a "Single European Sky" could save up to 16 million tonnes of carbon emissions annually[4] [39].

In order to realise "performance-based navigation", the envisioned low-ATR aircraft shall follow continuous, high-accuracy routes to cut flight times and obliterate the need for zig-zagging between ground-based radar posts[1] [39]. For such routes, the mission profile obtained from SUAVE may be deemed rather accurate.

A novel approach technique called "continuous descent operations" allows aircraft to glide into the airport at low/idle engine setting, saving fuel and reducing noise pollution. However, the conceived low-ATR aircraft ought to be equipped with the latest weather and traffic monitoring systems to permit such highly optimised approach procedures[7] [39].

A potential downside of a relatively low cruise altitude, is that an aircraft will not be able to take advantage of the naturally prevailing jet streams that occur between 8 and 16 km. Jet streams are strong currents of air moving from west to east that form when cold and warm air masses interact. There exist three main circulation cells known as the Hadley, Ferrel and Polar cells, and it is these which circulate air within the troposphere from the hotter equator to the cooler poles [8]. The strength and position of the jet streams are strongly correlated to the seasons. In the winter there exists a steeper

[4] https://aviationbenefits.org/environmental-efficiency/climate-action/infrastructure-efficiencies/ (last accessed on 06/05/2021)

[5] https://www.safran-landing-systems.com/systems-equipment/electric-taxiing-0 (last accessed on 28/06/2021)

[6] https://www.boeing.com/commercial/aeromagazine/articles/qtr_4_07/article_02_2.html (last accessed on 06/05/2021)

[7] https://aviationbenefits.org/environmental-efficiency/climate-action/operational-improvements/ (last accessed on 06/05/2021)

[8] https://www.weather.gov/jetstream/circ (last accessed on 21/05/2021)

temperature gradient between the equator and the poles than in summer resulting in stronger air currents. Additionally, since the inclination of the Sun also drifts towards the North Pole during winter, the position of hot air also shifts northwards, and with that, the average latitude of the jet stream drifts north [9]. In summer and autumn, the speed of these currents range from 80 - 150 kts, however in the winter due to the steeper temperature gradients, they can reach speeds over 200 kts.

Aircraft when travelling from west to east will try to benefit from the added tailwind by flying within the jet stream. Understandably, aircraft flying from east to west will try to avoid them. When an aircraft flies with the jet stream, its relative ground velocity increases without any change in propfan setting, thereby reducing DOC. This allows pilots to reduce flight times and consequently lower fuel burn and ATR. If airlines operating the envisioned aircraft wish to minimize DOC by making use of the jet streams when flying west to east, then the cruise altitude will need to increase from 5 km to a minimum of 8 km. The shorter flight time will result in a lower fuel burn and ATR, however, since NO_X emissions scale sharply with altitude, increasing the altitude would instead be unfavorable for reducing ATR [27].

23.4. Post-Operational Sustainability: End-of-Life Plan

The end of life is the final stage of a sustainable aircraft. A poor end of life plan can undo many good which has been done in terms of sustainability, therefore in this subsection an end of life plan is proposed for each system level component, which is in line with the projects goal of building a more sustainable aircraft for future generations.

Before the year 2000, aircraft were stored in landfills around the world [85]. Whereafter Boeing and Airbus started developing end of life strategies for their aircraft. Airbus launched PAMELA (Process for Advanced Management of End-of-Life of Aircraft), which demonstrated that 85% of aircraft, by weight, could be re-used, recycled and recovered[10]. If more and more aircraft will be stripped and recycled, new businesses may arise which find sustainable and profitable ways to manage, redistribute and also use the decommissioned parts of aircraft. This was also demonstrated by the PAMELA process which gave rise to a new company TARMAC Aerosave, and it is suspected more and more companies will start with similar objectives. Aircraft may also be sold or provided to educational institutions which can use these to educate the next wave of engineers. Carefull consideration must be taken when selling old aircraft parts on the market. Firstly if the part is sold due to it not meeting regulation standards it must be carefully marked that it cannot be used anymore. Furthermore, if aircraft parts are sold, the control over the End-of-Life is lost, as the next owner might not have the same End-of-Life sustainability goals in mind. The first step in making the aircraft End-of-Life plan sustainable is making sure all retired aircraft end up in a End-of-Life treating facility, and do not end up in landfills. To do this facilities will need to be made across the globe to minimise the need for transport after retirement. A global collaboration between airliners, manufacturers and safety agencies could be set up to disassemble aircraft for re-use and recycling. These facilities will dismantle and strip the retired aircraft if necessary and sort the material and components for their future use. The reuse of a component might require further maintenance, cleaning, certification and/or shipment. The recycling of a component may require the component to be disassembled first, for which specialised tools and personnel might be needed. Therefore the facilities are versatile and privatising these facilities could be an opportunity for business.

The decision to reuse a component, recycle the materials making up a component or scrapping the component, which have been listed in the order of highest importance, is essential in the end-of-life plan. There are many reason why an aircraft at End-of-Life is still valuable, and can contribute to sustainability. First of all there are always parts on aircraft which are still worth money to the owner of the aircraft, they can reused or maybe even sold. If a part is reused it is also beneficial as a new part will not have to be made, saving money, time and emissions. As airlines and companies are still motivated most with making money, this is the main reason to look at the End-of-life. Secondly if a parts cannot be reused the material making up the component might still be salvageable and usable. The recycling of used materials will require less emissions than the making of raw material [85], and therefore beneficial for ATR. In Figure 23.3 a flowchart is presented guiding one through the End-of-Life process. The goal illustrated in this flowchart is to have 0% of the aircraft weight ending up on a landfill, and just like PAMELA recycling, reusing at least 85% of the aircraft total weight.

[9] `https://www.metoffice.gov.uk/weather/learn-about/weather/types-of-weather/wind/what-is-the-jet-stream` (last accessed on 21/05/2021)

[10] `https://www.airbus.com/newsroom/news/en/2006/03/the-airbus-led-pamela-recycling-project-receives-an-a300-for-experimentatio` `html` (last accessed on 16/06/2021)

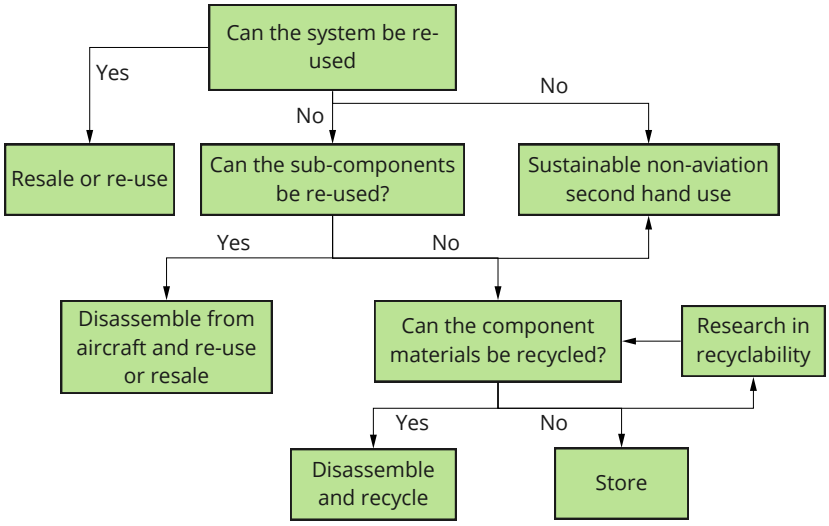

Figure 23.3: Flowchart End-of-Life strategy for each aircraft system

Below an End-of-Life plan is proposed for each of the components making up the aircraft.
Electronics, hydraulics

Component	End-of-Life plan
Wiring	The metal from the wiring can be reused or recycled as copper is a valuable material. The polymer protections can be melted down to be recycled as well.
Air conditioning	Material recycled for reuse.
Fuels, oils and liquids	Fuel and oil are drained from the tanks and possibly filtered for further use.

Interior components

Component	End-of-Life plan
Seats	It is hard to know whether aircraft seats will evolve to more modern or different designs. The most sustainable option would be to remove the seats from an End-of-Life aircraft and re-use these in a new aircraft. Minimising the amount of energy needed to make a new aircraft, if this can also result in a reduction in cost, there is no reason why this should not be done. The aircraft seats should be designed to easily renew the appearance by changing the fabric or other covering material, but also swapping out the infotainment system to a more modern version (larger, better display, lower energy usage,...) and keep the frame of the seats. This way the seats can be reused in new airliners while still appearing ”new”. Moreover, if seats were standardised across different aircraft versions, say a short range version of the low-ATR aircraft, any seats taken from a low-ATR aircraft could be reused in any other low-ATR aircraft. If reusing is not an option, due to damage, outdated design or not meeting new safety standards of the new aircraft, a partnership with a company like AIRA (Aircraft Interior Recycling Association) [11] could also be looked into. It recycles aircraft interiors with the goal of reducing the airlines carbon footprint. It promises to recycle 100% of the aircraft interior components with no components ending up on a landfill. Cockpit seats can be sold or used in training simulators for future pilots.
Aircraft Windows	The aircraft window consists of an interior part which is usually made from plastic, which will be disassembled and recycled, to be used for the production of new aircraft. The exterior part is made from thermally tempered glass, which is not considered recyclable at this moment. Again ideally these windows would be re-used in future aircraft.
Overhead luggage compartments	Disassembled and material recycled.
Galleys and Lavatories	Galleys include the storage compartments on the aircraft. Lavatories include the cabin, sink, and actual toilet and its mechanism. These will be disassembled from the aircraft, and if still in a good condition reused on aircraft. If the condition does not allow re-use, the component is scrapped for material and recycled.

Structural Parts

Component	End-of-Life plan
Rivets, nuts and bolts	While disassembling bolts, nuts and rivets which are loosened are collected and recycled.
Wing	The wing skin is made from Cyanate esters/HM modulus carbon fibre, UD prepreg, QI lay-up (Chapter 14), or in short, a carbon fibre composite. Carbon fibre is usually more difficult to recycle, but for example airbus has said that they plan on recycling 95% of their carbon fibre waste by 2020-2025 [12]. As the industry is tending towards higher carbon fibre production in aircraft, also more carbon fibre will have to be recycled. There are many companies now who specialise in carbon fibre recycling and it is believed that in the future more companies will arise which can safely and ecologically process the carbon fibre structure at the End-of-Life of the aircraft. The riblets which are on the skin outer surface are made from a urethane-acrylate photopolymer sprayed on the skin, there is currently no research on the effect of this material sprayed on the wing surface towards the recyclability or End-of-Life of the material it is coated on. Therefore two scenarios are considered, the coating poses a threat to the reuse of the skin, then the photopolymer will be removed and scrapped, and the skin reused. In the other case where it does not pose any difficulties, the riblets coating is recycled together with the skin.
Fuselage	The wing skin is made from Epoxy/HS carbon fiber, UD prepeg, UD lay-up (Chapter 14), which is also a type of carbon fibre. A similar strategy is proposed for the fuselage as has been explained for the wing. Also the riblets which are painted on the fuselage are planned to be recycled in the same manner.
Landing Gear	Landing gears are extremely durable and can usually be used again in another aircraft. Only as a last resort is it recycled for second use of the material.

Propulsion system

Component	End-of-Life plan
Blades	As has been provided in Section 21.2, the propfan blades will be made from carbon fibre composites. The blades are incredibly valuable and with proper maintenance can be used untill the part is no longer desired or does not meet regulations. Therefore, the plan for if the aircraft goes out of service but the blades are still in good condition, is to re-use the blades on other aircraft engines, store the blades as spare parts, or sell them to other manufacturers. If the part is no longer certified for aviation, due to the large diameters of the propfan blades, the blades might have a secondary use as propellers for small scale wind turbines. The other options are to store the blade for when better research is available on recycling of composites.
Engine core parts	The engine core parts are usually made from valuable metals, and can if the part is not reused in other engines, or stored for spare parts, be melted down and used again.
Engine mounting structure	If permitted, used in other aircraft as spare parts. Else it can be melted down and reused.

23.5. Life-Cycle ATR Footprint

This section shall investigate the ATR footprint per aircraft resulting from life-cycle phases other than operations, where the latter have been extensively discussed in Chapter 16. In particular, the relative ATR contribution of the manufacturing and end-of-life phases to the overall life-cycle ATR footprint shall be assessed for both the envisioned airliner and the A330-200.

Figure 23.4 displays the ATR impact per aircraft and total mass of emitted climate agents during the three aforementioned life-cycle stages on a semi-log scale. In case of the manufacturing and end-of-life phase, the total amount of emitted or ”stored” CO_2 in year one is considered, which has been determined via the Ansys Granta EduPack software leveraged for the materials selection in Chapter 14. The operational ATR footprint has been computed in line with Section 16.3.2 and Section 16.3.3, thus for 35 years of sustained operations and including the full spectrum of emission agents. Therefore, the computed ATR footprint of the manufacturing and EOL phase is expected to be an underestimation of the true value, which ought to be kept in mind when comparing the relative contributions per phase to the overall life-cycle ATR footprint. Also note that due to the log-scale the EOL ATR potential, which turns out to be negative for both aircraft and can be understood as the CO_2-storage capability of the airframe materials, was plotted in absolute terms. In theory, this means that future aircraft require less pristine material for manufacturing, however, in practice the recycling and/or disposal emits a certain amount of CO_2/ATR, thus reducing the net gain to be extracted from the airframe structure.

Table 23.1 suggests that the overwhelming majority of an aircraft’s life-cycle ATR footprint stems from its operational phase, which is in good agreement with [9]. The rightmost column displaying the relative gain of the envisioned low-ATR

aircraft over the A330-200 is of particular interest: one can infer that the project aircraft achieves a 35.24% lower ATR footprint during manufacturing compared to the A330-200, while boasting a more than six times greater EOL potential. In combination with the 80% operational ATR reduction computed in Section 16.3.3, an invariant life-cycle ATR footprint of 80% is obtained. This is due to the staggering ATR fraction attributed to the operational phase. Overall, it may be concluded that the manufacturing and end-of-life phases of the envisioned low-ATR airliner live up to its impressive operational ATR reduction potential, highlighting the holistic sustainability ambition of this design.

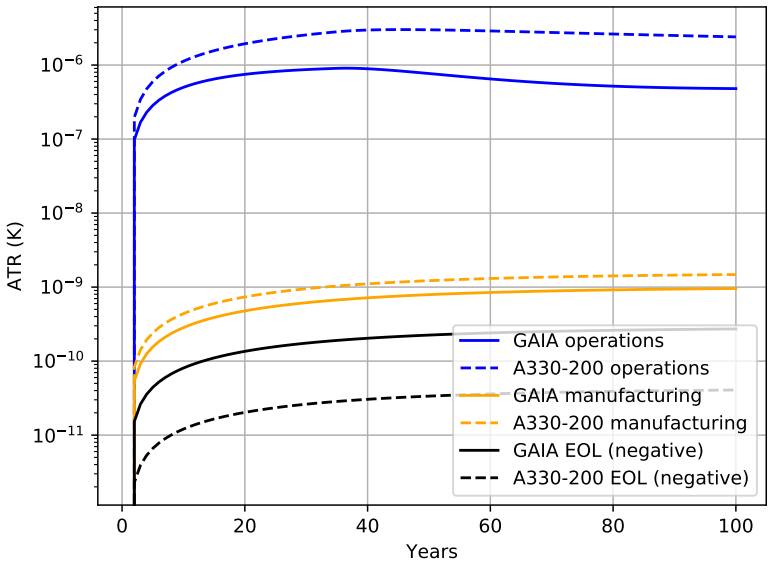

Figure 23.4: Life-cycle phase ATR contributions

Table 23.1: Life-cycle ATR contributions

Life-cycle phase	Low-ATR Aircraft	A330-200	Relative Reduction
Manufacturing (%)	0.20	0.06	35.24
Operations (%)	99.86	99.94	80.00
End-of-life (%)	-0.06	-0.002	668.05
Overall ATR (µK)	0.48	2.40	80.00

Part IV
Outlook

24. Project Design and Development Logic

The aircraft design process typically consists of 5 main phases: conceptual design, preliminary design, detailed design, certification and testing, operations and end-of-life procedures [105]. The intent of the DSE is to replicate the initial phase of a real-world aerospace engineering project, with the aim of developing a proof-of-concept over a period of 11 weeks. For this reason, the DSE begins with covering the conceptual design phase followed by the initial phase of the preliminary design in the final report. This chapter therefore introduces a breakdown and logic for the tasks to be executed upon completion of the DSE to get the aircraft into service, and ultimately then out of service during the EOL phase. Once the DSE is completed, the preliminary design phase shall be resumed and completed. Following the preliminary design phase, the detailed design phase will take place before which the certification and testing phase will ensure the aircraft is deemed airworthy. Finally, this chapter will outline the operations and EOL phase of the the project. To make the time schedule of the aircraft design process easy to visualize, the following sections will be displayed graphically on a gantt chart.

24.1. Preliminary Design Phase

During the baseline and midterm stages of the DSE, the tasks performed were aimed at performing the conceptual design phase of the project. This stage of the engineering design process concerns itself with the initial brainstorming and aircraft concept development. It aims to arrive at a final baseline aircraft configuration with a general understanding of the high-level systems as well as the technical aspects which make it superior to current aircraft in the market. The final report

phase of the DSE then aims to take the baseline aircraft configuration, and conduct preliminary analysis on the main aircraft systems using low fidelity models and empirical relations to quantify performance.

Upon completion of the DSE, there still remains work to be completed on the initial phase of the preliminary design. Namely, ensuring that all the low fidelity models have been verified and validated, and any recommendations are looked into. Following this, the concept's individual systems will need to undergo more in-depth analysis. This will be done by means of developing dedicated in-house models or using software that employ higher fidelity models. Where necessary, experiments may also need to be carried out to validate the models and software being used. As an example, consider the aerodynamic and structural departments. For the envisioned aircraft, due to the high span and low wing sweep, the wing is highly susceptible to aeroelastic phenomena. For this reason, it will be required to either develop high fidelity in-house models or make use of software such as NEOCASS or SHARPy to conduct the fluid-structure interaction simulations. However, it will also be necessary to conduct experiments that reproduce the numerical simulations to validate the software or models for the given application.

Once the individual systems have been analyzed an iterated on a system level, they can be integrated into a complete system and checked for compliance with the requirements outlined in the conceptual design phase. If there are requirements which have not been complied with, which should have been, then the design needs to be further iterated. Otherwise, the aircraft characteristic systems can be designed. Torenbeek estimates that the preliminary design phase should last between 12 - 16 months [105]. However, due to the use of innovative technologies and new engine development, a time of 24 months will be assumed. The final overview of the tasks to be completed during the preliminary design phase can be found in Figure 24.1.

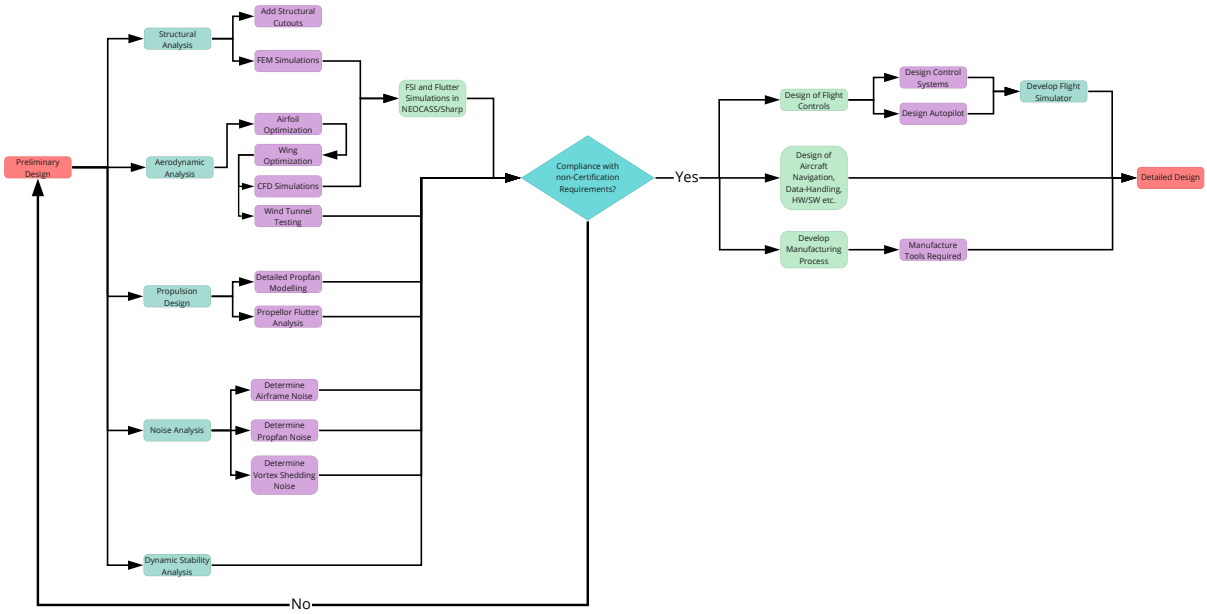

Figure 24.1: Preliminary design phase overview

24.2. Detailed Design Phase

Upon finalizing the design iterations and freezing the aircraft configuration at the end of the preliminary design phase, the detailed design phase may commence. This stage of the process is intended to define the geometry of each component, develop their manufacturing processes, and lastly develop the instructions for the production and manufacturing departments on the full-scale assembly procedure [105]. A typical detailed design phase lasts between 2 and 3 years, however, due to the innovative technologies the envisioned aircraft will employ, it will be assumed that a length of 3.5 years is appropriate.

24.3. Certification and Testing Phase

Before an aircraft can be deemed eligible for entry into service, it must undergo a rigorous set of certification and flight tests. Without passing these certification tests, the aircraft will not be authorized to operate in certain regions. The main two certification standards for long-range passenger aircraft are the FAR 25 regulations for the United States of America and JAR 25 regulations for the European Union. For this stage, first a series of prototypes must be manufactured: 2 static and 4 dynamic. From Roskam's 8th book on aircraft design, a valid estimate for the manufacturing time of the prototypes is 20 months [92]. An overview of this stage in the engineering process can be found in Figure 24.2, displaying the most

common destructive and non-destructive testing methods, followed by the later flight test campaigns to demonstrate the aircraft's operational performance in a variety of extreme circumstances. Once the aircraft is certified and airworthy, the aircraft is authorized to be sold and thus the operations phase of the engineering process commences. For new aircraft, the certification and testing phase typically lasts between 5-9 years. Once more, the use of innovative technologies will potentially shift the actual time spent towards the upper limit, hence it is assumed that the certification and testing phase will last 8 years [1].

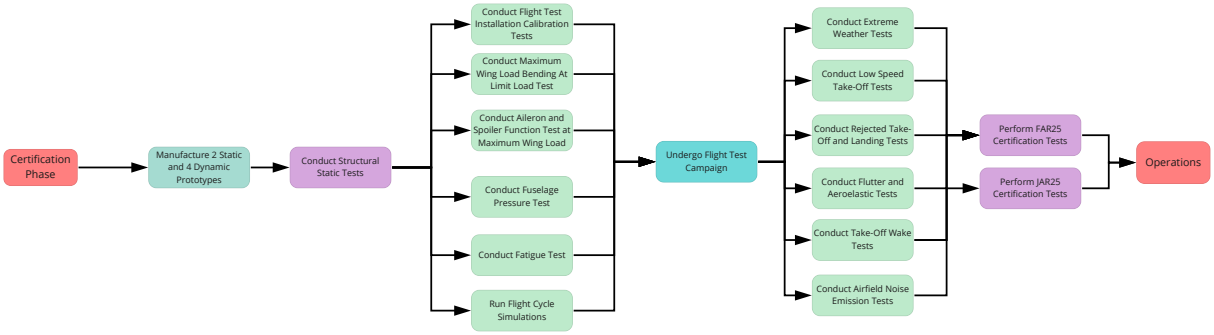

Figure 24.2: Certification and flight testing overview

24.4. Operations and End-of-Life Phase

Once the aircraft has been certified, it is then ready to enter into service. As the aircraft manufacturer, the initial stage of the operational phase involves production and delivery of the aircraft to customers. A detailed overview as to the production and manufacturing procedure can be found in Chapter 21. Since each aircraft has their own intricacies and nuances, it is important to train the new flight crew specifically for operating the envisioned aircraft. This is extremely important when considering training the pilots for the new stability and controllability characteristics of the aircraft. Negligence of this process can and has previously proved to be catastrophic as experienced with the crash of Ethiopian Airlines Flight 302's Boeing 737 MAX [2]). The 737 MAX sported a slightly modified engine configuration, however, since Boeing deemed the aircraft similar enough to its predecessor, it was not required for the pilots to undergo extensive training. For this reason the pilots were unaware of the maneuvering characteristics augmentation system (MCAS) which due to a malfunctioning sensor, was causing the aircraft to pitch downwards, ultimately bringing down the aircraft. If the pilots had previously been extensively trained, they would have known about the MCAS software, how to disable it, and likely prevent the death of 157 passengers and crew.

With respect to aircraft maintenance, since the aircraft is adopting innovative technologies including riblets and propfans, it is therefore the responsibility of the manufacturer to ensure that maintenance is conducted on the riblets and engines to ensure optimal operational performance. Lastly, during the operational phase it is likely that there will be a need to make changes to the software onboard the flight electronic systems, and so updates will need to be made available as soon as bugs are identified. These different processes are outlined in Figure 24.3.

From research into literature, it will be assumed that each aircraft will have an average operational lifetime of 35 years [78]. Each service as presented in Figure 24.3 will therefore be available throughout the entirety of the operational lifetime of the aircraft. Once the aircraft has completed its 35 years of service, it is then required to remove the aircraft out of service. For this, an end-of-life procedure which retains the ongoing sustainability philosophy has been previously formulated in Section 23.4.

[1] `https://www.faa.gov/aircraft/air_cert/airworthiness_certification/` (last accessed on 18/06/2021)

[2] `https://www.airport-technology.com/features/ethiopian-airlines-crash-what-happened-last-two-years/` (last accessed on 18/06/2021)

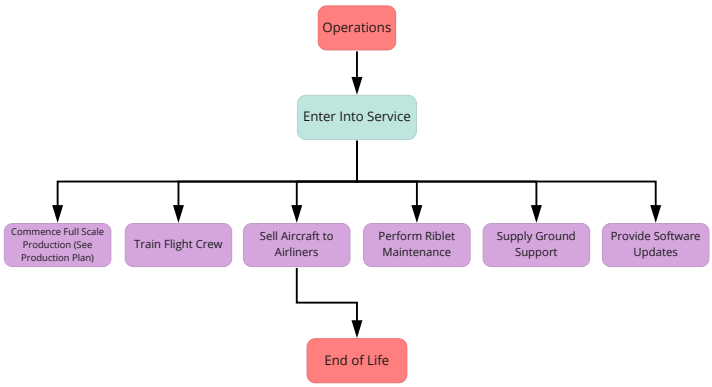

Figure 24.3: Operations to end of life overview

24.5. Project Gantt Chart

In the previous sections, the general overview of the tasks that must be completed in order to bring this aircraft into service have been outlined. Although each section gave an estimate to the time required to complete a given phase of the engineering process, it may still be unclear as to the scheduling of each of the phases. For this reason, it is useful to display the post-DSE activities in a Gantt chart format. Gantt charts are dynamically changing diagrams used for project management that show the current project timeline. Figure 24.4 shows the preliminary Gantt chart for the post-DSE activities. Note that as the project unfolds and delays arise, the Gantt chart will need to be modified to update dependencies between tasks, and display the latest timeline. From the Gantt chart, key years relating to the project timeline are: 2021, preliminary design starts; 2035, entry into service; 2070, start of the end of life phase.

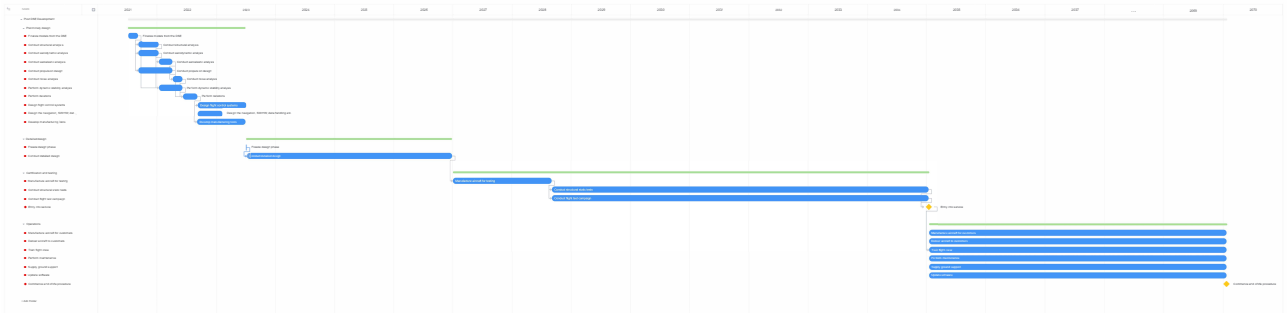

Figure 24.4: Gantt chart for the post-DSE aircraft design process.

25. Conclusion

Now that all loose ends have been nicely tied up, a final conclusion from this report and the project as a whole shall be drawn. After having updated the initial project objective from minimising DOC for a 40% ATR reduction to minimising ATR for a 15% DOC increase, which was motivated by novel market insights, the final design achieves a staggering 80% ATR decrease at a 7.5% DOC reduction. In view of this performance, it does not only outdistance the A330-200, but is also optimally positioned to gain a strong foothold in the long-haul commercial airliner market until 2050 and beyond. In that sense, it bridges the gap between present day fossil fuel-based airliners and future zero-emission concepts, whilst inheriting the valuable capability to promptly respond to policy changes in times of political turmoil.

In the following, the key points addressed in this report shall be reviewed. First of all, a comprehensive market analysis identified the bearable DOC increase of a sustainable aircraft to be 10%, resulting in a new design objective. Based on literature, it was clear that one would be aiming to fly lower and slower in order to minimise one's ATR. This unlocked a plethora of evolutionary technologies, of which the following were considered in this project: open-rotor engines, riblets, NLF airfoils, biofuels and and recyclable materials. A NACA 663-418 airfoil was chosen as a compromise between NLF-promoting characteristics and a gentle stall behaviour. The wing planform was designed such as to maximise the Oswald efficiency factor, and therewith minimise the induced drag. Finally, the nose design was optimised to minimise the skin friction drag by promoting laminar flow. With these geometric features established, riblets were applied to 70% of the wetted turbulent surface area, thereby achieving a 3.16% overall drag reduction in cruise. The arguably most innovative

feature of the envisioned low-ATR aircraft are its 5.3 m diameter, synthetic kerosene-powered propfan engines, which achieve a 32% TSFC reduction in cruise compared to the A330-200's CF6-80E1 engines. Besides the TFSC, the overall installed thrust T_{inst}, the total compressor outlet pressure P_{T3} and the total compressor outlet temperature T_{T3} are the primary outputs of both engine models. The final low-ATR targeted technology, namely the recyclable materials, were selected based on the vast Ansys Granta EduPack aerospace database and their ATR footprint during manufacturing and EOL was computed. Based on an iterative mission design point analysis involving the ATR and DOC per kilometer, an optimum cruise Mach number of 0.63 and an altitude of 5000 m was established. Overall, the low-ATR aircraft designed in this project achieves a 35% ATR reduction during manufacturing, 80% during operations and 668% during EOL, all relative to the A3302-200. Now, there were of course a number of practical requirements our aircraft needed to comply with in order to constitute a feasible product, most notably that it should be stable and controllable, and not suffer from flutter issues. The technical design and performance evaluation was followed by an outlook to the post-DSE life-cycle stages, including the preliminary and detailed design phase, the certification and testing phase, and finally the operational and end-of-life phase. This report was concluded with a holistic sustainable life-cycle strategy, which covered all stages considered during the post-DSE analysis, with special emphasis on the EOL stage. This emphasised the central role played by sustainability in the present airliner design.

26. Task Division

Table 26.1: Final Report task distribution per section (please refer to Table of Contents for numbers)

NB: Nils, **MCA:** Martin, **OC:** Oscar, **GDS:** Gianni, **BG:** Basthian, **LG:** Luca, **MSG:** Mustafa, **VM:** Vincent, **AR:** Austin, **PR:** Patrick																						
Section	ES	1	2	3.1	3.2	3.3	3.4	3.5	3.6	3.7	4.1	4.2	4.3	5.1	5.2	6	7.1	7.2	8.1	8.2	8.3	8.4
Name	NB	NB	PR	MSG AR	MSG	MSG	MSG	MSG	MSG AR	AR MSG	AR	AR	AR	PR VM	PR VM	GDS VM	GDS	GDS	PR AR	GDS LG	PR	PR
Section	8.5	8.6	8.7	9.1	9.2	9.3	9.4	9.5	10.1	10.2	10.3	10.4	10.5	10.6	10.7	10.8	10.9	10.10	11.1	11.2	11.3	11.4
Name	PR AR	VM	MCA	MSG MCA LG	MCA MSG	LG	MCA	MCA LG	VM, NB	VM, NB	VM, NB	VM, NB	VM, NB	VM, NB	VM, NB	VM, NB	VM, NB	VM, NB	PR	PR	PR	PR
Section	11.5	11.6	11.7	12.1	12.2	12.3	12.4	12.5	13.1	13.2	13.3	13.4	13.5	14.1	14.2	14.3	14.4	14.5	14.6	14.7	14.8	15.1
Name	GDS	PR	PR	MSG MCA LG	LG	MSG MCA LG	LG	LG	OC GDS	OC GDS	OC GDS	OC GDS	OC GDS	AR OC	AR OC	AR OC	AR OC	AR OC	MCA	AR OC	AR	AR OC MCA
Section	15.2	15.3	15.4	15.5	15.6	15.7	16.1	16.2	16.3	16.4	16.5	16.6	16.7	16.8	17	18.1	18.2	18.3	19.1	19.2	20.1	20.2
Name	AR OC	AR OC	AR	AR OC	AR	AR	BG	BG	NB, VM	NB, VM	NB, VM	NB, VM	NB, VM	BG	OC	GDS	GDS	GDS	BG	BG LG	AR	MCA
Section	20.3	20.4	21.1	21.2	21.3	22.1	22.2	22.3	22.4	22.5	23.1	23.2	23.3	23.4	23.5	24	Conclusion	11.8	-	-	-	
Name	MCA	AR	AR	AR	AR	AR	MSG AR	AR	AR	AR	NB, VM	NB, VM	NB, VM, LG	NB, VM	NB, VM	LG	NB	GDS	-	-	-	

References

[1] Airbus. *A330 Aircraft Characteristics- Airport and Maintenance Planning*. Tech. rep. June 2020.

[2] Airbus. *A330-200 Weight and Balance Manual*. Tech. rep. June 1998.

[3] Airbus. *A350 Family: Shaping the Future of Air Travel*. Airbus Facts and Figures (PDF); accessed on 06/05/2021. Apr. 2021.

[4] Airbus. *Aircraft Characteristics Airport And Maintenance Planning*. Tech. rep. Jan. 2020.

[5] Desiderio SÁNCHEZ-BRUNETE ÁLVAREZ. "Leading edge for aircraft made of reinforced composite material". US 8,146,865 B2. Mar. 2008.

[6] J. Anderson. *Introduction to flight*. 8th ed. McGraw-Hill Higher Education, 2005.

[7] *Annex 6 to the Convention on International Civil Aviation, Operation of Aircraft, Part II International General Aviation, Aeroplanes*. 10th ed. Canada: International Civil Aviation Organisation, 2018.

[8] Anon. *MIL-F-8785C, Military Specification, Flying Qualities of Piloted Airplanes*. Nov. 1980.

[9] M.F. Ashby, H. Shercliff, and D. Cebon. *Materials: engineering, science, processing and designs*. 3rd ed. Oxford, United Kingdom: Butterworth-Heinemann, 2014.

[10] GE Aviation. *CF6-80E1 high-bypass turbofan engines*. Tech. rep. June 2014.

[11] J. Bachmann, C. Hidalgo, and S. Bricout. "Environmental analysis of innovative sustainabe composites with potential use in aviation sector-A life cycle assessment review". In: *Science China* 60 (Oct. 2016), pp. 1301–1317. DOI: 10.1007/s11431-016-9094-y.

[12] J. Bachmann et al. "Towards a Circular Economy in the Aviation Sector Using Eco-Composites for Interior and Secondary Structures. Results and Recommendations from the EU/China Project ECO-COMPASS". In: *Aerospace* 8.5 (2021), p. 131.

[13] B.R. Ramesh Bapu. *Evaluation of Aircraft Maintainability and Aircraft Maintenance*. Conference Paper. Chennai, India, 2007.

[14] BASF. *BASF Report 2019*. Tech. rep. Ludwigshafen am Rhein, Germany, 2019.

[15] D.W. Bechert and W. Hage. “Drag reduction with riblets in nature and engineering”. In: *WIT Transactions on State of the Art in Science and Engineering* 4 (2006), pp. 457–469.

[16] H.C. Bilinsky, R.N. Wilson, and M.J. Dvorchak. “Direct Contactless Microfabrication for Application of Drag Reducing Riblets onto Aerospace Vehicles Utilizing UV Curable Allophanate Structures”. In: (2018).

[17] H.C. Bilinsky et al. “Advanced Direct Contactless Microfabrication of Drag-reducing Riblets: Rapid Prototyping, Robotic Scale-up and Materials Development”. In: (Jan. 2021).

[18] A. Birolini. *Reliability Engineering: Theory and Practice*. Berlin, Germany: Springer, 2013.

[19] Boeing. *Statistical Summary of Commercial Jet Airplane Accidents*. Tech. rep. June 2011.

[20] J. Bowen. *The Economic Geography of Air Transportation: Space, Time, and the Freedom of the Sky*. Tech. rep. Routledge, London, 2010.

[21] M. Braun-Unkhoff, U. Riedel, and C. Wahl. “About the emissions of alternative jet fuels”. In: *CEAS Aeroneutical Journal* (2016).

[22] Martijn Brons et al. “Price Elasticites of Demand for Passenger Air Travel: A Meta-Analysis”. In: *Tinbergen Institute Discussion Paper* (2001).

[23] D.M. Bushnell. “Aircraft drag reduction review”. In: *Journal of Aerospace Engineering: 25th Anniversary Collection* 217 (Oct. 2002).

[24] H. Canaday. “European Aviation Environmental Report 2019”. In: *European Union Aviation Safety Agency* (2019).

[25] H. Canaday. “Major maintenance due for A380s”. In: *MRO Network* (2015).

[26] *Certification Specifications and Acceptable Means of Compliance for Large Aeroplanes CS-25*. 26th Amendment. Kortenberglaan 100, 1040 Brussel: European Union Aviation Safety Agency, 2020.

[27] E. Schwartz Dallara, I.M. Kroo, and I.A. Waitz. “Metric for Comparing Lifetime Average Climate Impact of Aircraft”. In: *AIAA Journal* 49.8 (Aug. 2011).

[28] E. Schwartz Dallara, I.M. Kroo, and I.A. Waitz. “Metric for Comparing Lifetime Average Climate Impact of Aircraft”. In: *AIAA Journal* 49.8 (Aug. 2011).

[29] A.M. Dorsey and A. Uranga. “Design Space Exploration of Future Open Rotor Configurations”. In: (2020). DOI: 10.2514/6.2020-3680.

[30] M. Drela. “XFOIL: An analysis and design system for low Reynolds number airfoils”. In: *Low Reynolds number aerodynamics*. Springer, 1989, pp. 1–12.

[31] W.F. Durand et al. *Aerodynamic Theory*. 2nd ed. Berlin: Julius Springer, 1935.

[32] J. Fransson. “Transition to turbulence delay using a passive flow control strategy”. In: *Procedia IUTAM* 14 (2015), pp. 385–393.

[33] R. Garcia-Mayoral and J. Jimenez. “Hydrodynamic stability and breakdown of the viscous regime over riblets”. In: *Journal of Fluid Mechanics* 678 (2011), p. 317.

[34] A. Gary and Sr. Crowell. *The descriptive geometry of nose cones*. 1996.

[35] E. Gill. *Systems Engineering and Aerospace Design (AE3211-I)*. Tech. rep. unpublished. Tu Delft, Feb. 2018.

[36] C. Goldberg et al. “Economic Viability Assessment of NASA’s Blended Wing Body N3-X Aircraft”. In: (2017). DOI: 10.2514/6.2017-4604.

[37] Goodyear. “Goodyear Aviation Data Book”. In: *Global Aviation Tyres* (2021).

[38] Spring DSE 2021 Group 15. *Design of a Low-ATR, Long-Range Aircraft Using Passive Flow Control - Baseline Report*. Tech. rep. Delft University of Technology, Faculty of Aerospace Engineering, 2021.

[39] Spring DSE 2021 Group 15. *Design of a Low-ATR, Long-Range Aircraft Using Passive Flow Control - Midterm Report*. Tech. rep. Delft University of Technology, Faculty of Aerospace Engineering, 2021.

[40] Spring DSE 2021 Group 15. *Design of a Low-ATR, Long-Range Aircraft Using Passive Flow Control - Project Plan*. Tech. rep. Delft University of Technology, Faculty of Aerospace Engineering, 2021.

[41] M.D. Guynn et al. “Initial Assessment of Open Rotor Propulsion Applied to an Advanced Single-Aisle Aircraft”. In: *Journal of Aerospace Engineering: 25th Anniversary Collection* 217 (Oct. 2002).

[42] W. Hage, V. StenzeL, and T. Vynnyk. “Investigation of the Wear Properties of a Riblet Paint Structure on an Airbus A300-600ST Beluga”. In: *New Results in Numerical and Experimental Fluid Mechanics VII* 121 (2013), pp. 185–192. DOI: 10.1007/978-3-642-35680-3_23.

[43] C. Hall et al. “How to improve open rotor aerodynamics at cruise and take-off”. In: *The Aeronautical Journal* 118.1208 (2006), pp. 1103–1123.

[44] R.J. Hamann and M.J.L. van Tooren. *Systems Engineering and Technical Management Techniques - part 2*. LR Ch. System Integration: Aircraft Design, 2004.

[45] B. Hemmings et al. "Taxing Aviation Fuel in Europe. Back to the Future?" In: *Transport & Environment* (2020).

[46] G.E. Hoff et al. *Experimental performance and acoustic investigation of modern, counterrotating blade concepts*. Tech. rep. NASA Lewis Research Center, 1990.

[47] S. Hulshoff and D. Modesti. *Design Synthesis Excercise Project Guide: A low-ATR, Long-Range Aircraft using Passive Flow Control*. 1st ed. Kluyverweg 1, 2629 HS Delft, Nederland: TU Delft, 2021.

[48] S. J. Hulshoff. *Course AE4930 Aerolasticity*. 11.1. Delft: Faculty of Aerospace Engineering, 2011.

[49] F.T. Jane. *Jane's all the world's aircraft*. 6th. New York: McGraw-Hill, 1900.

[50] L.R. Jenkinson, P. Simpkin, and D. Rhodes. *Civil Jet Aircraft Design*. London, UK: Arnold, 1999.

[51] K. R. V. Kaza et al. "analytical and experimental investigation of mistuning in propfan flutter". In: - (1987). Published. DOI: https://doi.org/10.2514/6.1987-739 .

[52] M. K. A. Khan et al. "An overview of methods for investigation of aeroelastic response on high aspect ratio fixed-winged aircraft". In: *IOP Conference Series: Materials Science and Engineering* 899 (Sept. 2020), p. 012002. DOI: 10.1088/1757-899x/899/1/012002.

[53] H.A. Kinnison and T. Siddiqui. *Aviation Maintenance Management*. 2nd ed. McGraw-Hill Education, 2013.

[54] A. Koch. "Climate Impact Mitigation Potential given by Flight Profile and Aircraft Optimization". PhD dissertation. Technische Universität Hamburg-Harburg, 2015.

[55] K. Kosar, S. Durmaz, and E.M. Jafarov. "Longitudinal Dynamics Analysis of Boeing 747-400". In: *Proceedings of the 9th WSEAS International Conference on Automatic Control, Modeling and Simulation*. Istanbul Technical University, May 2007.

[56] J.J. Lee et al. "Historical and Future and Future Trends in Aircraft Performance, Cost and Emissions". In: *Annual Review of Energy and the Environment* 26:167-200 (2001).

[57] Granta Design Limited. *CES EduPack software*. Cambridge, UK, 2009.

[58] T. Lin et al. "Aluminum with dispersed nanoparticles by laser additive manufacturing". In: *Nature Communications* (Sept. 2019).

[59] L. Loftin and W. Bursnall. "The effects of variations in Reynolds number between 3.0 x 10sub6 and 25.0 x 10sub6 upon the aerodynamic characteristics of a number of NACA 6-series airfoil sections". In: (1950).

[60] P. Luchini, F. Manzo, and A. Pozzi. "Resistance of a grooved surface to parallel flow and cross-flow". In: *Journal of fluid mechanics* 228 (1991), pp. 87–109.

[61] F.T. Lynch and M.D. Klinge. "Some Practical Aspects of Viscous Drag Reduction Concepts". In: *SAE Transactions* 100 (1991), pp. 2493–2504.

[62] Jim Marko. *Safety Assessment Processes of ARP4761: Major Revision*. Tech. rep. Canada transport, Nov. 2018.

[63] V. Masson-Delmotte et al. *Global warming of 1.5° C*. Tech. rep. IPCC, 2018.

[64] J.D. Mattingly, W.H. Heiser, and D.T. Pratt. *Aircraft Engine Design*. 2nd ed. Alexander Bell Drive, Reston VA: Institute of Aeronautics and Astronautics, Inc., 2002.

[65] T.H.G. Megson. *Aircraft Structures for Engineering Students*. sixth edition. Elsevier, 2017.

[66] P. T. Millhouse, S.C. Kramer, and P.I. King. "Identifying Optimal Fan Compressor Pressure Ratios for the Mixed-Stream Turbofan Engine". In: *JOURNAL OF PROPULSION AND POWER* 16.1 (2000), pp. 123–456.

[67] D. Modesti et al. "Dispersive stresses in turbulent flow over riblets". In: *Journal of Fluid Mechanics* 917 (2021).

[68] D. Modesti et al. "Kelvin–Helmholtz rollers in turbulent flow over riblets". In: (2018).

[69] J. Morgado et al. "XFOIL vs CFD performance predictions for high lift low Reynolds number airfoils". In: *Aerospace Science and Technology* 52 (2016), pp. 207–214. ISSN: 1270-9638.

[70] J.A. Mulder et al. *Flight Dynamics*. 1st Amendment. 2600 AA Delft: Faculty of Aerospace Engineering, 2013.

[71] multiple. *Destination Green The Next Chapter*. Tech. rep. ICAO, 2019.

[72] M. Nita and D. Scholz. *Estimating the Oswald factor from basic aircraft geometrical parameters*. Deutsche Gesellschaft fur Luft-und Raumfahrt-Lilienthal-Oberth eV, 2012.

[73] A. Lyckegaard O. T. Thomsen E. Bozhevolnaya. *Sandwich Structures 7: Advancing with Sandwich Structures and Materials*. Aalborg, Denmark: Springer, 2005.

[74] F. Oliviero. *AE2111-II Aerospace Design and Systems Engineering Elements II: Aircraft aerodynamic analysis - Lift & Drag*. Delft University of Technology, 2019.

[75] F. Oliviero. “Aircraft aerodynamic analysis”. Lecture slides from course Aerospace Design and Systems Engineering Elements II - AE2111. Sept. 2019.

[76] B. Peerlings. “A review of aerodynamic flow models, solution methods and solvers and their applicability to aircraft conceptual design”. In: *Delft University of Technology, Delft* (2018).

[77] D. Prederi, A. Parrinello, and A. Gadda. “Environmental analysis of innovative sustainabe composites with potential use in aviation sector-A life cycle assessment review”. In: *Science China* 60 (Oct. 2016), pp. 1301–1317. DOI: 10.1007/s11431-016-9094-y.

[78] P. Proesmans and R. Vos. “Airplane Design Optimization for Minimal Global Warming Impact”. In: *Aircraft Configuration Design and Trade Studies IV* (2021). DOI: 10.2514/6.2021-1297.

[79] The National Society of Professional Engineers. “NSPE Code of Ethics for engineers”. In: *JOM* 1.2 (1993), pp. 14–16.

[80] G. Ramanujam and H. Ozdemir. “Improving airfoil lift prediction”. In: *35th Wind Energy Symposium*. 2017, p. 1999.

[81] G. Ramanujam, H. Ozdemir, and H. Hoeijmakers. “Improving airfoil drag prediction”. In: *Journal of aircraft* 53.6 (2016), pp. 1844–1852.

[82] D. Raymer. *Aircraft design: a conceptual approach*. 6th ed. American Institute of Aeronautics and Astronautics, Inc.

[83] F. Re. “Model-based Optimization, Control and Assessment of Electric Aircraft Taxi Systems”. PhD dissertation. Technische Universität Darmstadt, 2017.

[84] Thomas Reynaert et al. “Destination 2050 - A road to net zero European Aviation”. In: *European Union* (2019).

[85] J.S. Ribeiro and J.O. Gomes. “Proposed framework for End-Of-Life aircraft recycling”. In: *Elsevier* 1.2 (2015), pp. 1–6.

[86] J. Roskam. *Airplane Design: Part II: Preliminary Configuration Design and Integration of the Propulsion System*. Lawrence, Kansas, USA: DARcorporation, 1997.

[87] J. Roskam. *Airplane Design: Part III: Layout design of cockpit, fuselage, wing and empennage: cutaways and inboard profiles*. 3th ed. Lawrence, Kansas, USA: DARcorporation, 2002.

[88] J. Roskam. *Airplane Design: Part IV: Layout Design of Landing Gear and Systems*. Lawrence, Kansas, USA: DARcorporation, 1989.

[89] J. Roskam. *Airplane Design: Part V: Component Weight Estimation*. 4th ed. Lawrence, Kansas, USA: DARcorporation, 2011.

[90] J. Roskam. *Airplane Design: Part VI: Preliminary Calculation of Aerodynamic, Thrust and Power Characteristics*. Lawrence, Kansas, USA: DARcorporation, 2004.

[91] J. Roskam. *Airplane Design: Part VII: Determination of Stability, Control and Performance Characteristics: FAR and Military Requirements*. Lawrence, Kansas, USA: DARcorporation, 2002.

[92] J. Roskam. *Airplane design: Part VIII: Airplane Cost Estimation: Design, Development, Manufacturing and Operating*. Lawrence, Kansas, USA: Roskam Aviation and Engineering Corporation, 1990.

[93] J.J. Ruijgrok. *Elements of Airplane Performance*. 2nd ed. Delft, The Netherlands: Delft Academic Press, 2013.

[94] K. M. Downey S. A. Thorp. *Computer Aided Design and Manufacturing of Composite Propfan Blades for a Cruise Missile Wind Tunnel Model*. Tech. rep. National Aeronautics and Space Administration Lewis Research Center, Sverdrup Technology, Inc. Lewis Research Center Group, Sept. 1992.

[95] A.A. Sabaruddin et al. “Engine Optimization by Using Variable Valve Timing System at Low Engine Revolution”. In: *ARPN Journal of Engineering and Applied Sciences* 10.20 (Nov. 2015).

[96] H.I.H. Saravanamuttoo, H. Cohen, and G.F.C. Rogers. *Gas Turbine Theory*. 5th ed. London: Pearson, 2001.

[97] W. Saric, A. Carpenter, and H.Reed. “Passive control of transition in three-dimensional boundary layers, with emphasis on discrete roughness elements”. In: *Philosophical Transactions: Mathematical, Physical and Engineering Sciences* 369.1940 (2011), pp. 1352–1364.

[98] M. Schier, F. Rinderknecht, and H. Hellstern. “Electrical Wheel Hub Motor for Aircraft Application”. In: *International Journal of Renewable Energy Research, IJRER* 1.4 (Oct. 2011).

[99] C. Silva et al. “SUAVE: An Open-Source Environment for Multi-Fidelity Conceptual Vehicle Design”. In: (July 2015). DOI: 10.2514/6.2015-3087.

[100] J. Sinke. *Lean Manufacturing*. Kluyverweg 1, 2629 HS Delft, Nederland: TU Delft, 2021.

[101] Jos Sinke. *17510Lean Manufacturing*. Tech. rep. Delft University of Technology, Feb. 2018.

[102] R. C. Smith and A. D. Levin. “Propfan Installation Aerodynamics of a Supercritical Swept Wing Transport Configuration”. In: *17th Joint Propulsion Conference* (1981). Published.

[103] P. Spalart and J. McLean. “Drag reduction: enticing turbulence, and then an industry”. In: *Philosophical Transactions of the Royal Society A: Mathematical, Physical and Engineering Sciences* 369.1940 (2011), pp. 1556–1569.

[104] J. Staley and D. Lege. “Advances in aluminium alloy products for structural applications in transportation”. In: *Journal de Physique IV Proceedings, EDP Sciences* 3.C7 (Aug. 1993), pp.C7-179-C7–190. DOI: 10.1051/jp4:1993728.

[105] E. Torenbeek. *Advanced aircraft design: conceptual design, analysis and optimization of subsonic civil airplanes*. John Wiley & Sons, 2013.

[106] E. Torenbeek. *Synthesis of Subsonic Aircraft Design*. Kluwer Academic Publishers, 1982, pp. 50–53.

[107] Ministry of Transport Singapore. *Runway Excursion Incident Boeing 777-200 Registration 9V-SRG Singapore Changi Airport 24 January 2004*. Tech. rep. Apr. 2005. DOI: AIB/AAI/CAS.016.

[108] E. Uhlmann et al. “Additive manufacturing of titanium alloy for aircraft components”. In: (2015).

[109] Andre van Velzen, Sander de Bruyn, and Amanda Bachaus. “Costs of EU ETS and CORSIA for European aviation”. In: *Transport & Environment* (2019).

[110] Prof. P. van Vollenhoven et al. *Crashed during approach, Boeing 737-800, near Amsterdam Schiphol Airport*. May 2010.

[111] A. Wendorff et al. *SUAVE: An Aerospace Vehicle Environment for Designing Future Aircraft*. Version 2.0. 2019.

[112] K. Wilocx. “16.885 Aircraft Systems Engineering”. In: (Sept. 2004).

[113] J. Hu X. Zhang Y. Chen. “Recent advances in the development of aerospace materials, Sikorsky Aircraft Corporation”. In: *Progress in Aerospace Sciences* 97 (Jan. 2018).

[114] S.O.L. Zijp. “Development of a Life Cycle Cost Model for Conventional and Unconventional Aircraft”. In: (June 2014).

A. Collection of Diagrams

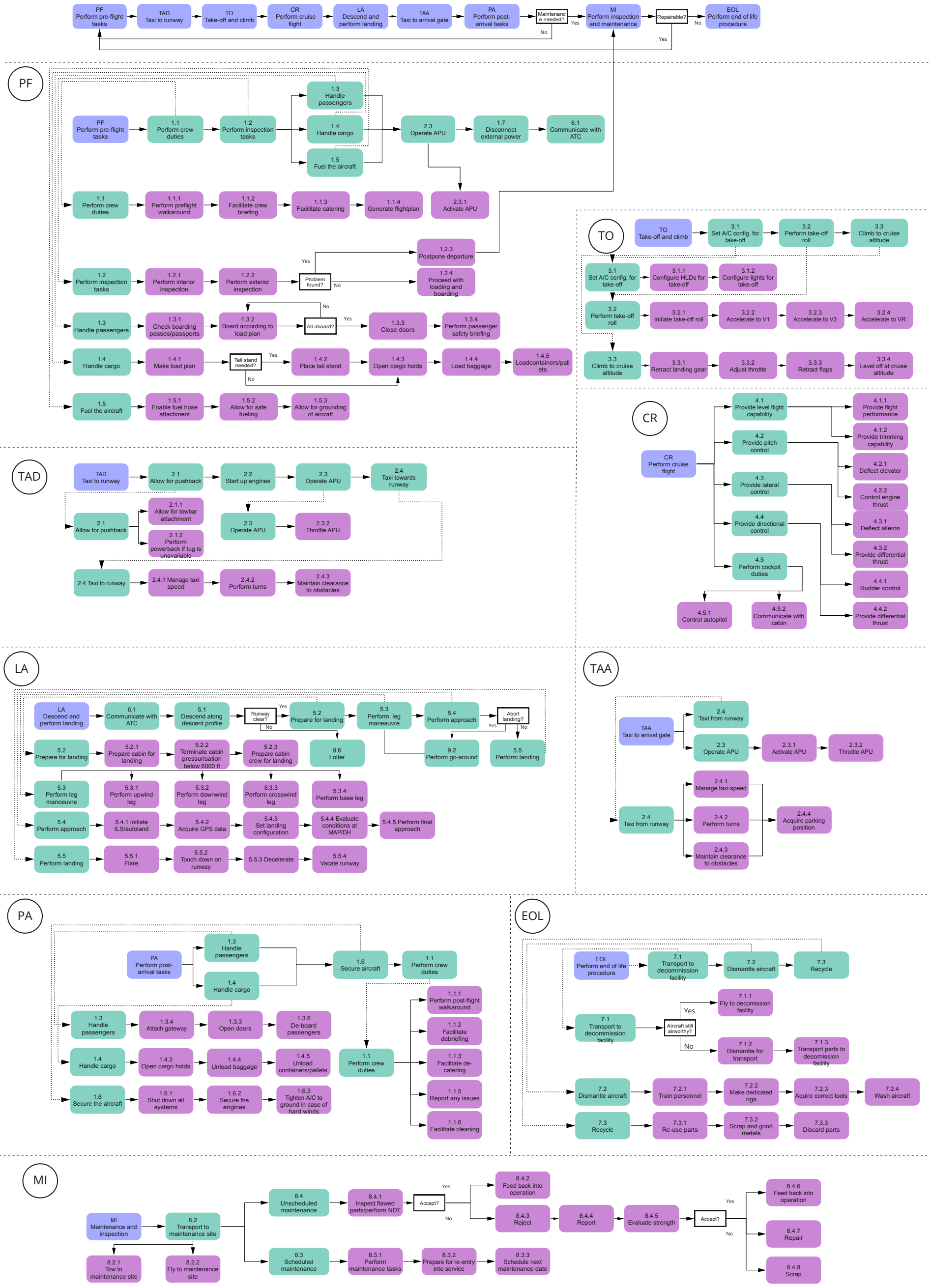

Figure A.1: Functional Flow Diagram

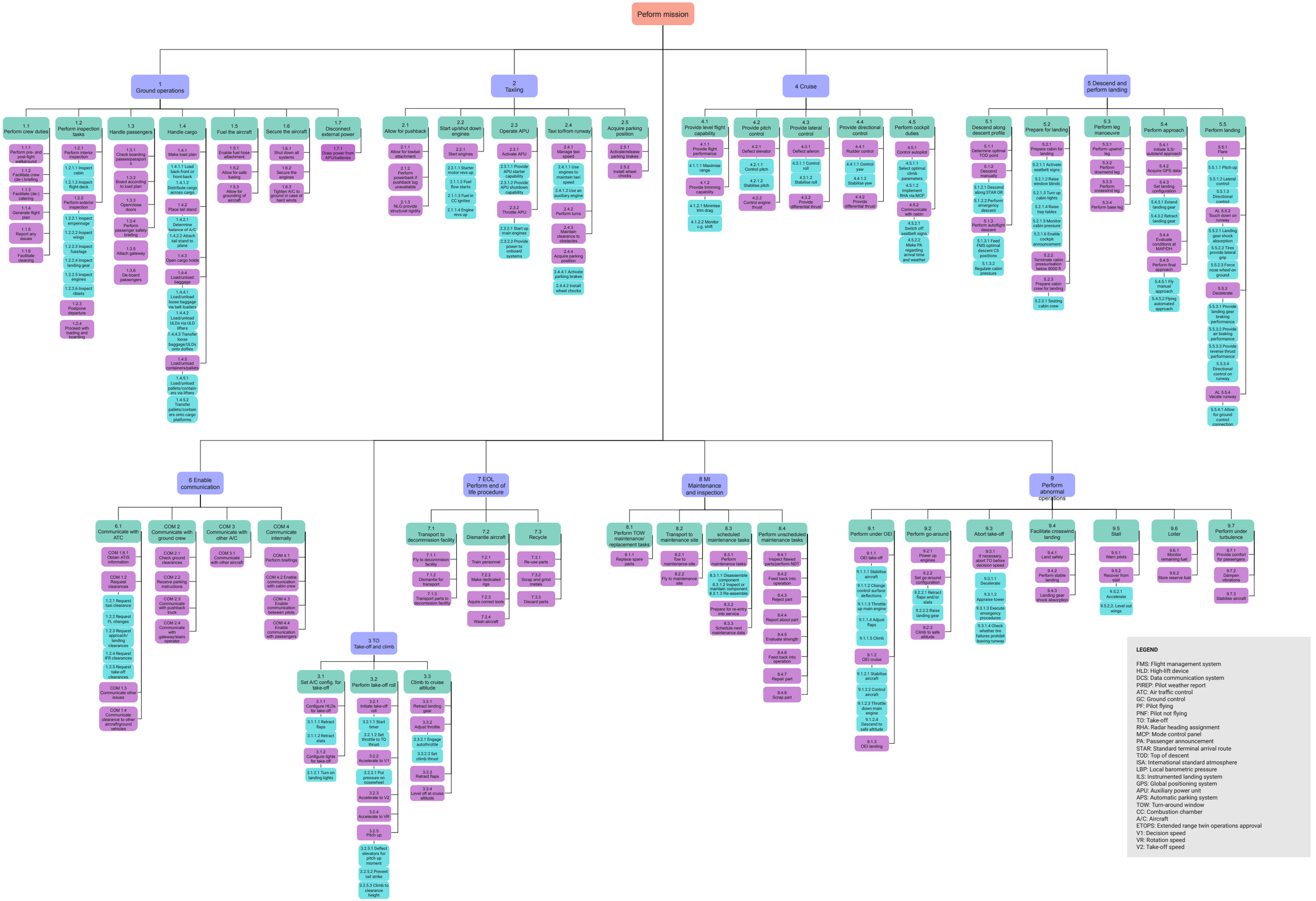

Figure A.2: Functional Breakdown Structure